A thesis submitted to the

University of London

for the degree of

Doctor of Philosophy

DIODE MIXERS WITH OPTICAL LOCAL OSCILLATOR INJECTION

Nathan Joseph Gomes

Department of Electronic and Electrical Engineering

University College London

Torrington Place

London WC1E 7JE

1988

ABSTRACT

The results of an investigation into the use of diodes as mixers with optical local oscillator injection are presented. Such 'optically pumped mixers' might be employed in complex microwave systems where the optical distribution of the local oscillator is attractive.

The photocurrent generation, through which the optical local oscillator is coupled into the device, the frequency conversion and noise mechanisms in optically pumped mixers are all investigated. Computer models of optically pumped mixing have been developed, and are shown to give very good agreement with experimental measurements.

A novel optically pumped mixer structure using the tunnelling nonlinearity in a metal contact to heavily doped gallium arsenide has been investigated theoretically and experimentally. The prototype device has been found to be limited to relatively low frequencies ($\simeq$100MHz) as an optically pumped mixer, although for a device of smaller area low conversion loss may be achieved at frequencies up to 1GHz. The structure is limited by the large capacitance per unit area, the generally poor responsivity, and the dependence of the responsivity on relatively slow, minority-carrier diffusion, current transport mechanisms.

The results from the above investigation have enabled an improved, Mott diode structure to be proposed for optically pumped mixers. Predictions from the accurate computer model indicate efficient operation should be achievable at X-band frequencies and beyond using gallium arsenide lasers of moderate output power ($\geqslant$3mW average). Similar performance at lower power levels should be achievable with shorter wavelength illumination.

Due to the simplicity of using a single device, it is shown that optically pumped mixers may be more attractive than photodetector-mixer combinations in many complex microwave systems.

ACKNOWLEDGEMENTS

The author would like to express his fullest thanks for the support, guidance, and encouragement given to him by his supervisor Dr. A.J. Seeds.

The author would also like to acknowledge valuable discussions with many members of staff and colleagues at University College London (UCL) and Queen Mary College, London (QMC). Special mention must go to Dr. H. Griffiths, but the following also deserve specific thanks: Dr. C. Parini, Dr. G. Parry, M.C. Carvalho, I.D. Blanchflower, B. Lenoir, Dr. R. Brown, A. Sloper, R. Fatah, Dr. P. Radmore, and (for word-processing hints) Dr. D. Kreit. The author is also very grateful to A. Overbury for assistance with the Nd:YAG laser system at UCL.

The following have provided valuable practical assistance: M. Gillett, A. Gorrod (mechanical workshop, UCL), E. Goose (mechanical workshop, QMC), A. Bruce (electronics workshop, QMC), and N. Kolb (for help in the laboratory at QMC).

The devices most extensively investigated in this work were provided by D. Esdale of RSRE, Malvern; the author is grateful for the devices and for the results of some useful measurements made on them at RSRE which were made available to him. Fast photodiode structures were provided by Dr. D. Parker of GEC Hirst Research Centre where they were mounted by A. Hansom.

Finally, the author would like to acknowledge the Science and Engineering Research Council who provided financial support through a research studentship.

To

my Mother and Father

and

my Sister.

CONTENTS

LIST OF PRINCIPAL SYMBOLS 8

LIST OF TABLES 11

LIST OF FIGURES 12

CHAPTER ONE: INTRODUCTION **22**

1.1 Aims of this thesis 23

1.2 Optical/electrical mixing 24

1.3 Optically pumped mixing mechanisms 32

1.4 Performance parameters 39

1.5 Generation of high-frequency intensity-modulated optical signals 41

1.6 Chapter summary and structure of thesis 44

CHAPTER TWO: OPTOELECTRONIC MIXER THEORY **46**

2.1 Illumination effects 47

2.2 Analytic mixer theory 64

2.3 Noise 71

2.4 Chapter summary 86

CHAPTER THREE: COMPUTER MODELLING OF OPTICALLY PUMPED MIXERS 88

3.1 Introduction 89

3.2 Overview of computer models 91

3.3 Nonlinear analysis in the frequency domain 95

3.4 Nonlinear analysis in the time domain 101

3.5 Performance of frequency domain model 109

3.6 Performance of time domain model 112

3.7 Chapter summary 118

CHAPTER FOUR: TUNNELLING METAL-SEMICONDUCTOR CONTACT: DEVICE CHARACTERISATION 120

4.1 Device physics 121

4.2 Modelling the I-V characteristics 125

4.3 Equivalent circuit 135

4.4 Effect of illumination 146

4.5 Chapter summary 155

CHAPTER FIVE: TUNNELLING METAL-SEMICONDUCTOR CONTACT: DEVICE PERFORMANCE 157

5.1 Preliminary predictions 158

5.2 Conversion loss measurements using semiconductor lasers 166

5.3 Conversion loss measurements using Nd:YAG laser 177

5.4 Other parameters 185

5.5 Comparison with photodetector-mixer combination 201

5.6 Chapter summary 211

CHAPTER SIX: RECTIFYING SCHOTTKY STRUCTURES **214**

6.1 Proposed device structure 215

6.2 Current transport in Schottky/Mott diodes 218

6.3 Frequency response limitations 234

6.4 Predicted performance 245

6.5 Chapter summary 256

CHAPTER SEVEN: CONCLUSIONS AND FURTHER WORK **258**

7.1 Summary of major results 259

7.2 Applications and comparison with alternative approaches 264

7.3 Suggested topics for further work 268

7.4 Chapter summary 276

REFERENCES 278

APPENDICES

A: The photocurrent contribution of carriers generated outside the depletion region 291

B: Mixer linear analysis 294

C: Mixer noise analysis including correlated shot noise 298

LIST OF PRINCIPAL SYMBOLS

This list is for quick reference; all symbols are defined in the appropriate places in the text.

A	device area [cm^2 or μm^2]
A', A*	modified Richardson constants [$A.cm^{-2}.K^{-2}$]
B	bandwidth [Hz]
C	capacitance; various subscripts, e.g. barrier cap., C_b, parasitic/package cap. , C_p. [F]
c	velocity of light [$cm.s^{-1}$ or $m.s^{-1}$]; small-signal capacitance [F]
D	carrier diffusion constant [$cm^2.s^{-1}$]
E_b	bias voltage [V]
E_{BH}	barrier height [eV or V]
E_{OO}, E_O, $\mathcal{E}'$	energy parameters [eV]
$\mathcal{E}$	electric field [$V.m^{-1}$ or $V.cm^{-1}$]
e_n	rms noise voltage [V]
F	noise factor; also noise figure, $10\log_{10}$(noise factor) [dB]
F_{SSB}, F_R , F_{IF}	noise factors: single-sideband, receiver and i.f. amplifier, respectively.
f	frequency [Hz]
G	conductance [S]
g	small-signal conductance [S]
h	Planck's constant [J.s]
$\mathcal{I}_n$	modified Bessel function of order n
I	current; subscripts defined in text [A]
i	small-signal current [A]
i_n	rms noise current [A]
J	current density; subscripts defined in text [$A.cm^{-2}$ or $A.m^{-2}$]
k	Boltzmann's constant [$J.K^{-1}$]
L, L_c	loss, conversion loss
L_D	Debye length [cm or μm]

L_p	hole-minority-carrier diffusion length [μm]
L_s	series inductance [H]
m	capacitance-voltage law exponent
m_0, m^*	electron rest mass, effective mass [kg]
n	diode ideality factor; no. of harmonics
n_e	electron concentration [cm^{-3}]
N	noise spectral density [$W.Hz^{-1}$ or $dBm.Hz^{-1}$]; donor doping density (also N_D) [cm^{-3}]
N_C	density of states in conduction band [cm^{-3}]
P_{opt}	optical power [W or dBm]
p	hole concentration [cm^{-3}]
p_{n0}	equilibrium conc. in n-type material [cm^{-3}]
q	elecronic charge [C]
R	responsivity [A/W]
R	resistance [Ω]; reflectance
R_b	barrier resistance [Ω]
r, r_s, R_s	series resistance [Ω]
S	device area [cm^2 or μm^2]
S_i, S_o	input, output signal levels [dBm]
T	temperature [K] (T_0 standard noise temp.=290K)
t_r, t', t''	noise-temperature ratios
t	time [s]
V	voltage [V]; subscripts defined in text
v	small-signal voltage [V]; velocity [$cm.s^{-1}$] Subscripts may be similar too, e.g. diode voltage and diffusion velocity, v_d. All are defined in the text.
w	depletion/barrier width [μm or nm]
x	distance [m]
Y	admittance [S]
Y_{mn}	admittance matrix element (integer m,n) [S]
y_s, y_{IF}	input source, output i.f. load admittances[S]
z	distance [m]
Z	impedance (see admittance symbols above) [Ω]
$Z_{IF,opt}$	optimum i.f. output impedance [Ω]

α	optical absorption coefficient [m^{-1} or cm^{-1}] (1/α ≡ optical absorption length [cm or μm]); diode exponential coefficient (≡q/nkT) [V^{-1}]
δ	convergence parameter
ε	permittivity [$F.m^{-1}$ or $F.cm^{-1}$]; accuracy parameter
θ	phase angle [radians]
λ	wavelength [nm or μm]
μ	carrier mobility [$cm^2.V^{-1}.s^{-1}$]
τ	carrier lifetime; transit-time [s]
τ_p	hole-minority-carrier lifetime [s]
Φ	diode contact potential [V]; illumination photon flux density [$photons.s^{-1}.cm^{-2}$]
φ	electron quasi-Fermi level potential [V]
χ_1	Fermi level penetration into conduction band [eV or V]
ψ	conduction band potential [V]
ω	angular frequency [$rad.s^{-1}$]; ω_p pump freq.

LIST OF TABLES

Table	page no.
Table 3.1 Input parameters example for frequency domain model.	110
Table 3.2 Typical output from frequency domain model.	111
Table 3.3 Typical input parameter set for time domain large-signal analysis.	114
Table 4.1 Optical current generation in tunnelling contacts using lasers of different emission wavelengths, and expected optical absorption coefficients at these wavelengths.	148
Table 4.2 Optical current generation dependence on bias.	150

LIST OF FIGURES

Title page no.

Fig. 1.1 Optoelectronic mixer principle. 28

Fig. 1.2 Optically pumped mixing mechanism in rectifying Schottky-type devices. 34

Fig. 1.3 Optically pumped mixing mechanism in reverse-biased tunnelling devices. 34

Fig. 1.4 Optically pumped mixing mechanism in variable capacitance diode. 37

Fig. 1.5 Optically pumped mixing mechanism for an APD. 37

Fig. 1.6 Optical phase-locked loop. 43

Fig. 2.1 Band diagrams illustrating photocurrent generation in (a) tunnelling metal-semiconductor contact, and (b) p-n diode photodetectors. 48

Fig. 2.2 Photocurrent generation considerations with barriers of widths, w_1= 25.5nm, w_2= 0.25μm and minority-carrier diffusion length = 0.4μm (a) absorption length, $1/\alpha$ = 0.1μm, (b) $1/\alpha$ = 0.75μm 51

Fig.2.3 Geometry used to analyse transit-time effects of carriers generated in the depletion region of a semiconductor by intensity-modulated light. 57

Fig.2.4 Minority-carrier diffusion current profile for $L_p = 0.4\mu m$, $D_p = 9cm^2/s$, $1/\alpha = 0.25\mu m$ (w = 25.5nm) 57

Fig.2.5 $[F_1(x)/J_{diff}(w)]$ for $1/\alpha = 0.1\mu m$, $L_p = 0.4\mu m$ and $D_p = 9cm^2/s$, with barrier width, w = 25.5nm, for frequencies 5GHz to 50GHz in 5GHz steps. 62

Fig.2.6 $[F_1(x)/J_{diff}(w)]$ for $1/\alpha = 0.75\mu m$, $L_p = 0.4\mu m$ and $D_p = 9cm^2/s$, with barrier width, w = 25.5nm, for frequencies 600MHz to 6GHz in 600MHz steps. 63

Fig.2.7 Notation used for sideband frequencies in linear analysis[59]. (Named frequencies correspond to upper-sideband down-conversion.) 69

Fig.2.8 Equivalent 3-port network representation of a distortionless mixer. 69

Fig.2.9 Reduced 2-port network representation of a distortionless mixer. 74

Fig.2.10 Noise sources in a semiconductor barrier device: (a) representation of barrier shot noise and series resistance thermal noise, (b) reduced Thévenin equivalent. 74

Fig.3.1 Basic circuit for large-signal analysis of optically pumped mixer problem. 90

Fig.3.2 Formulation of the large-signal problem in Gwarek's analysis[82]. 92

Fig.3.3 Equivalent circuit for frequency domain large-signal analysis. 96

Fig.3.4 Flow-chart showing calculation sequence in frequency domain large-signal analysis. 100

Fig.3.5 Equivalent circuit for the multiple-reflection transmission line model used in the time-domain analysis. 102

Fig.3.6 Separate circuits formed in the time domain model analysis. 102

Fig.3.7 Flow-chart showing calculation sequence in time domain large-signal analysis. 105

Fig.3.8 Diode waveforms over a local oscillator cycle predicted by the time domain model - 500μA average photocurrent generated in a tunnelling contact optically pumped mixer... 116

Fig.3.9 Part of a typical output file from the time domain computer program. 117

Fig.4.1 Structure of a tunnelling metal-semiconductor contact of the type investigated in this thesis. 122

Fig.4.2 Current transport mechanisms in metal-semiconductor contact for moderate to heavy doping levels, and n-type material. 124

Fig.4.3 Experimentally measured I-V characteristic of a tunnelling metal-semiconductor contact. 129

Fig.4.4 I-V plot of exact form of forward bias thermionic-field emission relationship... 129

Fig.4.5 Dependence of E_0 and n (ideality factor) on E_{00} at 300K. (E_0 and E_{00} are characteristic energy parameters of the barrier defined in the text.) 132

Fig.4.6 Fit of reverse characteristic to field emission equation of Padovani's theory. 133

Fig.4.7 Tunnelling metal-semiconductor contact: comparison of modelled and experimentally measured I-V characteristics. 136

Fig.4.8 Equivalent circuit for a semiconductor diode 138

Fig.4.9 Cole-Cole plot of impedance of tunnelling contact. 138

Fig.4.10 Typical variation of the dynamic resistance of a tunnelling contact with diode voltage bias. 141

Fig.4.11 Barrier capacitance of a 25 x 25 μm^2 contact calculated from network analyser measurements. 143

Fig.4.12 Barrier capacitance of a 50 x 50 μm^2 contact calculated from vector voltmeter measurements. 143

Fig.4.13 Plot of C_b^{-2} (C_b is the barrier capacitance) against diode bias voltage, from the vector voltmeter measurements. 144

Fig.4.14 Measured I-V characteristics of tunnelling contact under illumination (broken line) and in the dark (solid line)... 151

Fig.4.15 Predicted response (normalised to dc level) of tunnelling contact to modulated incident light versus the modulation frequency, taking into consideration transit-time limitations only. 154

Fig.5.1 Conversion loss variation with source resistance predicted by frequency domain model. Average photocurrent of 500µA, 100% modulation, constant external bias. 161

Fig.5.2 Conversion loss variation with source resistance predicted by frequency domain model. Constant (-150mV) diode voltage. 161

Fig.5.3 Conversion loss dependence on diode bias predicted by frequency domain model. Source resistance 750Ω, average photocurrent 500μA, 100% sinusoidal modulation. 162

Fig.5.4 Variation of fundamental component of diode (dynamic) conductance with bias as predicted by results from the time domain model. Source resistance 750Ω, average photocurrent 500μA, 100% sinusoidal modulation. 164

Fig.5.5 Conversion loss dependence on diode bias predicted by time domain model. Source resistance 750Ω, average photocurrent 500μA, 100% sin. mod. 165

Fig.5.6 Basic test arrangement for measurement of conversion loss of optically pumped mixer. 168

Fig.5.7 Optical output power of HL7801E laser versus the a.c. drive power with constant laser bias current of 55mA. 168

Fig.5.8 Measured conversion loss variation with diode bias voltage in unmatched 50Ω system. 171

Fig.5.9 Experimental circuit arrangement for the tunnelling contact optically pumped mixer. 172

Fig.5.10 Experimental conversion loss variation with intensity modulated semiconductor laser

illumination, and predictions for experimental arrangement from time and frequency domain models. 175

Fig.5.11 Experimental conversion loss variation with mode-locked frequency-doubled Nd:YAG laser. 179

Fig.5.12 Comparison of Gaussian and $sech^2$ pulse shapes of same (unity) pulse width. 179

Fig.5.13 Predicted conversion loss variation with $sech^2$ photocurrent pulses, effect of change in peak current. 181

Fig.5.14 Example of predicted diode waveforms with pulse excitation at (a) forward-bias and (b) reverse-bias conversion loss minima. 183, 184

Fig.5.15 Conversion loss variation with diode bias using Nd:YAG laser. {Comparison of experimental and predicted results} 186

Fig.5.16 Output noise-temperature (T_n) of an optically pumped tunnelling contact mixer. 189

Fig.5.17 Noise figure of receiver employing tunnelling contact optically pumped mixer using frequency domain model predictions. 190

Fig.5.18 Comparison of noise factors of receivers employing optically pumped and equivalent (same

conversion loss, bias, etc.) electrically pumped tunnelling contact mixers. 191

Fig.5.19 Diode impedance predictions from time domain model for test arrangement conditions. 194

Fig.5.20 Measured compression points for tunnelling contact optically pumped mixers: (a) laser drive level at 13dBm, and (b) at 10dBm 198

Fig.5.21 Conversion loss variation with l.o. frequency predicted by time domain model taking into account the decrease in the a.c. photocurrent. 200

Fig.5.22 Circuit for the analysis of the optical power requirements of a photodiode-mixer combination 203

Fig.5.23 Comparison between performance of (a) optically pumped mixer and (b) photodetector-mixer combination. 208

Fig.6.1 Proposed structure of an optically pumped Mott mixer diode... 216

Fig.6.2 Conduction band profile and electron quasi-Fermi level for a contact to n-type semiconductor under forward bias. The quasi-Fermi level variations according to the two extreme ideal situations of the thermionic emission theory and the diffusion theory are shown. 220

Fig.6.3 Electron energy levels in contact to n-type semiconductor used to determine the current flow under forward bias from the combined thermionic emission-diffusion theory. 227

Fig.6.4 Current-voltage characteristics for contacts of barrier height 0.8eV to GaAs (for different donor concentrations). 230

Fig.6.5 Computed conduction band and quasi-Fermi level variations for contacts of barrier height 0.8eV ... 232

Fig.6.6 Current-voltage characteristics of contacts to n-type GaAs as given in Fig.6.4 but with the current density plotted against the difference between the applied voltage and the built-in potential. 233

Fig.6.7 Theoretical maximum cutoff frequencies with the transit-time limitation calculated according to the inequality expressed in (6.19). 235

Fig.6.8 Predicted transit-time-limited cutoff frequencies for contacts of barrier height 0.8eV and with epilayer widths made equal to the absorption length at the corresponding illumination wavelength. 239, 240

Fig.6.9 Cutoff frequencies for contacts of barrier height 0.8eV and with epilayer widths equal to the absorption length at the

corresponding illumination wavelength, under sufficient forward bias to give a barrier current = 500μA. 243, 244

Fig.6.10 Conversion loss variation with diode voltage for optically pumped Mott mixer from time domain model predictions. Upper-sideband down-conversion with l.o. frequencies of 2.2GHz (i.f.= 60MHz) and 9.9GHz (i.f.= 270MHz). 247

Fig.6.11 Diode voltage waveforms over a l.o. cycle corresponding to the situations at the conversion loss minima shown in Fig.6.10. 249

Fig.6.12 Diode impedance with optical l.o. producing 500μA average photocurrent (100% modulation) at l.o. frequencies of 2.2GHz (i.f.= 60MHz) and 9.9GHz (i.f.= 270MHz). 254, 255

Fig.7.1 Receiver configuration for a phased-array radar employing optically pumped mixers. 266

Fig.7.2 Stacked tunnelling junction structure. 273

Fig.7.3 Schematic diagram of band profiles in modulated barrier photodiode. 273

CHAPTER ONE

INTRODUCTION

1.1 Aims of this thesis 23

1.2 Optical/electrical mixing 24
- 1.2.1 Optical heterodyning 25
- 1.2.2 Frequency conversion with an optical output 26
- 1.2.3 Optoelectronic mixers 27
- 1.2.4 Optically pumped mixers 30

1.3 Optically pumped mixing mechanisms 32
- 1.3.1 Resistive mixing (1): Schottky-type devices 33
- 1.3.2 Resistive mixing (2): reverse-bias tunnelling 35
- 1.3.3 Photocapacitive mixing 36
- 1.3.4 Avalanche nonlinearity 38

1.4 Performance parameters 39

1.5 Generation of high-frequency intensity-modulated optical signals 41

1.6 Chapter summary and structure of thesis 44

1.1 Aims of this thesis

In this thesis the results of a theoretical and experimental investigation into the use of semiconductor diode structures as electronic mixers with optically provided local oscillator signals will be presented. Such 'optically pumped mixers' might be employed in complex microwave systems where the optical distribution of the local oscillator may be attractive.

The use of optical techniques in microwave-frequency communications, for the control, generation and distribution of signals has been extensively investigated in recent years[1-4]. Such techniques are attractive because of the ultimately short response times of optoelectronic interactions (and, hence, the high modulation rate capabilities), and the high degree of isolation that can be achieved between the optical control and microwave signals. Advances in optical device technology can only open up the possibilities of more applications. Also, the field is interesting because of the suitability of GaAs for active optical devices, optical waveguides, and microwave devices, potentially leading to a whole range of new developments in the area of microwave monolithic integrated circuits (MMICs)[5]. Functions such as switching, oscillator tuning and phase locking have already been performed with microwave devices such as TRAPATTs, IMPATTs, bipolar transistors and MESFETs as well as photodiodes and photoconductors[1, 6-15]. This has prompted interest in the participation of optical signals in another common microwave device function, that of mixing or frequency conversion.

In the next section (1.2) a general introduction to optoelectronic mixers will be given. The term 'optoelectronic mixing' will be defined, the different

types of optoelectronic mixing will be described and a review given of reported instances. Special attention will be given to 'optically pumped' mixers, which form a particular category of optoelectronic mixer, since these form the principal concern of this thesis.

The remainder of this introductory chapter is concerned with some fundamental concepts involved in optically pumped mixing, which are usefully considered before the more detailed theory is presented in Chapter 2. In section 1.3 different nonlinear mechanisms which could give mixing action, and their modes of operation are briefly described.

In section 1.4 mixer performance parameters are defined and applied to optically pumped action. These parameters are important as they will be used later in the thesis to describe the actual and predicted performance of optically pumped mixers.

In section 1.5 the provision of the optical l.o. is considered, and various schemes for the generation of high-frequency signals on optical carriers are reviewed.

Finally, in section 1.6 a brief summary of this chapter will be given and the structure of the remainder of the thesis described.

1.2 Optical/electrical mixing

Generally, the basic function of a mixer is to produce an output signal at the sum or difference frequency of two input signals. In order to do this the mixer must employ a nonlinear device since this causes multiplication of the input signals rather than just simple addition; the products of the input signals then form sum and difference

frequency components which can be selected by suitable tuning of the embedding network.

In this section the different mixing or frequency conversion processes involving optical and electrical signals will be reviewed.

1.2.1 Optical heterodyning

A photodiode is a square-law device since the photocurrent generated is proportional to the incident optical power and, hence, to the square of the amplitude of the optical field. It can be shown, therefore, that the amplitudes of the fields of two beams of light of optical frequencies f_1 and f_2 will be multiplied due to the square-law detection, and a difference frequency output will result if the wavefronts are superposed (e.g. if the beams are well aligned), and if the difference frequency falls within the bandwidth of the photodiode.

This type of photomixing, or optical heterodyning, has been performed with a large variety of optical sources and detectors. For example, Patel and Sharpless observed beats in the region of 14GHz and 17.7GHz between the closely spaced transitions in a bromine-argon laser around 844.6nm using a germanium point-contact diode[16]. Hall and Morey detected a 51.3GHz beat frequency between transitions near 1.15μm in a pure neon gas laser using a Schottky diode[17]. Beats between different laser sources have also been observed using Schottky and point-contact diodes. Daniel et al. observed beat frequencies of up to 430GHz between the lines of a krypton ion laser at 568nm and a tunable dye ring laser using a point-contact diode[18]. Donald et al. have detected signals up to 80GHz by heterodyning the outputs of a HeNe laser and a dye laser in a GaAs Schottky barrier diode[19].

A variety of other devices have also been used as optical heterodyne detectors. The technique is of interest in optical telecommunication systems[20] and here the devices typically used are PIN[21] and avalanche[22,23] photodiodes. Burghardt et al. used an avalanching point-contact diode to observe an 80GHz beat-frequency between a HeNe laser and a dye laser oscillating at 633nm[24].

Very high beat frequencies have been detected with metal-insulator-metal (MIM) diodes. For example, Drullinger et al. observed a 2.5THz beat-frequency between visible cw dye lasers[25], using electrical down-conversion of the heterodyne signal .

BARITT diodes[26] and MESFETs[15,27] have also been used as optical heterodyne detectors.

1.2.2 Frequency conversion with an optical output

In some crystals frequency conversion can be obtained, due to the nonlinear electro-optic effect[28], in which the output signal is optical[29]. Bay and Luther have generated sum- and difference-frequencies between a 633nm HeNe laser transition and microwave signals of up to 25GHz in KDP crystals[30]. Much of this type of work, however, can be regarded as optical mixing since the lower frequency source is in the far-infrared or infrared region of the spectrum. For example, Kaminow et al. obtained the sum- and difference-frequencies between the 339 and 311μm lines (≃ 900GHz) of a HCN laser and a 0.633μm HeNe laser using lithium niobate ($LiNbO_3$)[31]. However, the efficiency was poor, of the order of 10^{-5} ; Midwinter and Warner obtained efficiency better than 1% using a ruby laser pump to convert 1.7μm radiation to green light[32]. Proustite (Ag_2AsS_3)[33] has been found to be very suitable for the frequency up-conversion of CO_2 laser radiation at 10.6μm, using a 0.633μm HeNe laser drive[34], and pulsed ruby laser

drive[35].

1.2.3 Optoelectronic mixers

The optical and optical/electrical mixing described in sections 1.2.1 and 1.2.2 could be described as optoelectronic mixing if both optical and electrical signals are present at some stage of a frequency conversion process. However, the type of device of interest in this thesis is one which would be used in an electronic, microwave system; the frequency up-converting crystals of section 1.2.2 could not be used as such electronic mixers. The optical heterodyning described in section 1.2.1 can be performed by any photodiode and, therefore, a definition including such action as optoelectronic mixing must be considered too vague; further, it can be said that in such a device it is two optical signals which are being mixed rather than both optical and electrical ones. For the purposes of this thesis an optoelectronic mixer will be defined as a device in which the output is electrical, and one of the two inputs is an intensity-modulated optical signal and the other an electrical signal. A schematic diagram for such a device is shown in Fig.1.1.

A mixer can be employed to down-convert a signal to a lower, intermediate frequency or up-convert a signal to a higher frequency, although in the latter case it is usually specified as an up-convertor. In both cases a local oscillator of relatively high power is used to modulate the nonlinear admittance, while the received signal and the sum- and difference-frequency (or sideband) components are of much lower level. It can be seen then that two types of optoelectronic mixer exist[36]: those in which the local oscillator, or pump, is the electrical input and those in which it is the optical input.

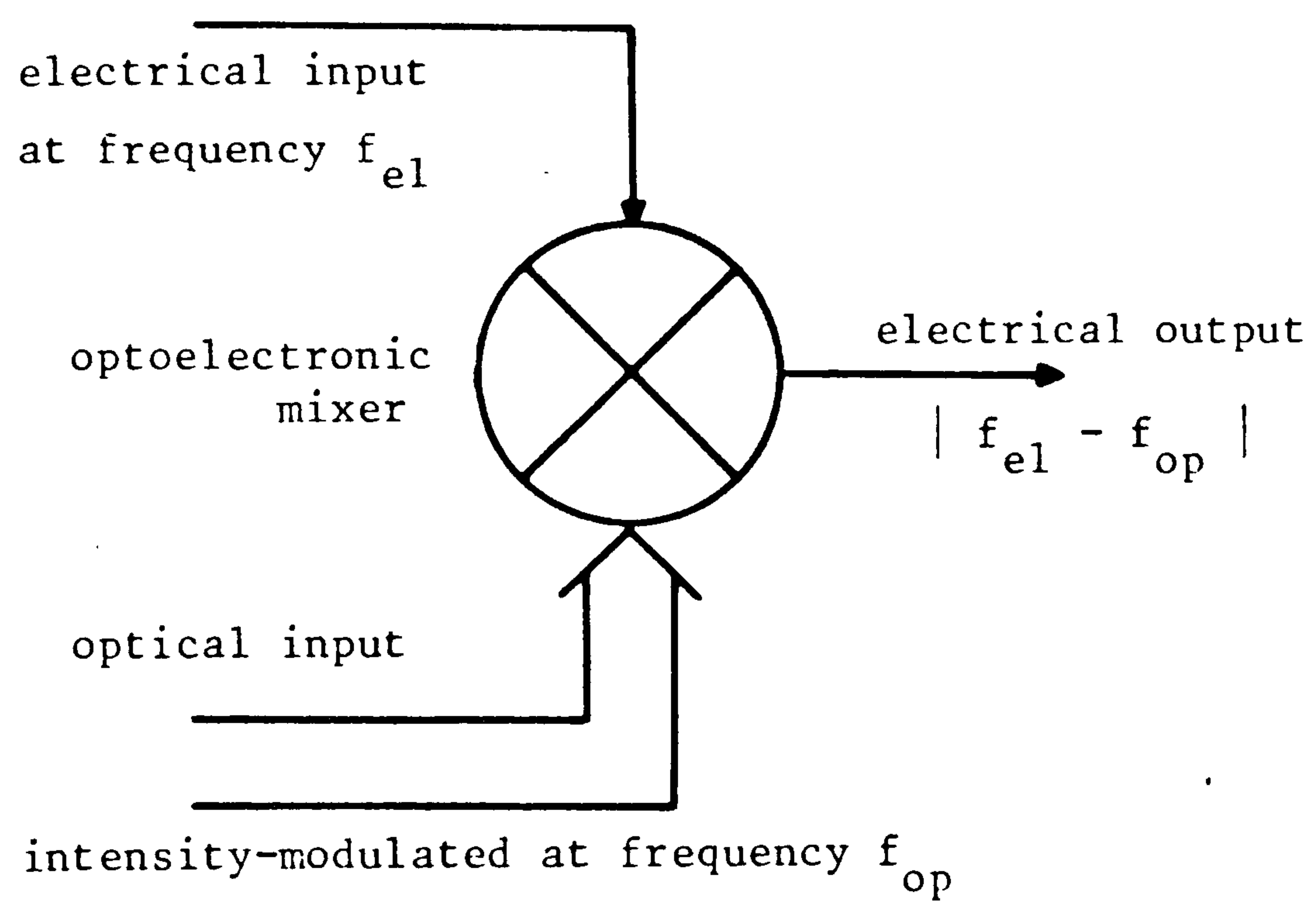

Fig. 1.1 Optoelectronic mixer principle.

In many laser frequency measurements (although certainly not all) the high-frequency beat signal between two laser lines is down-converted to a lower microwave frequency by applying an electrical l.o. to the detecting device. Two stages of mixing are then occuring, the second of which, according to the definition above, can be described as optoelectronic mixing. This has been performed in many of the heterodyne laser frequency measurements described in section 1.2.1 (see, for example, references [16]-[18], [25]). Of course, the efficiency of the conversion process is not that important for the laser frequency measurements, and only Hall and Morey[17] discuss it. However, Donald et al.[19] did discuss this aspect since they proposed the technique for heterodyne receivers. By modulating the forward conductance and capacitance nonlinearities of their fast Schottky photodiodes they obtained a conversion loss (difference between the detected RF signal strength and IF signal strength) estimated to be 5dB.

Lower conversion loss has been achieved by employing avalanche photodiodes as such electrically pumped opto-electronic mixers. This was first demonstrated by Davis and Kulczyk[37]. Subsequently, the advantages that this type of operation may bring were demonstrated by MacDonald and Hill[38], and by Yakovlev[39], and by Seeds and co-workers[40,41] who have used the APD as a harmonic mixer.

Chu and co-workers have demonstrated optical and optoelectronic mixing in GaAs MESFETs[27]. Below 20GHz the difference frequency between a HeNe laser and a dye laser was directly detected by coupling the two optical signals into the gate region of the transistor. At higher frequencies, optoelectronic mixing was employed to down-convert the difference frequency; relatively high pump power was necessary, but difference frequencies of up to

300GHz were down-converted. This performance is surprising since the cutoff frequency f_T of the devices used was approximately 25GHz. Chu et al. discuss likely mechanisms behind this performance[27].

Lam and MacDonald have demonstrated electrically pumped optoelectronic mixing[42] in photoconductive devices similar to those used as electrically gated optoelectronic switches[7]. It is easier to explain the operation in terms of switching between 'on' and 'off' states; operated as a mixer the device would be varied between states that approach these, corresponding to low and high impedance states, respectively. In the devices, the optical input signal is turned 'off' at low bias voltages when the field and, hence, carrier velocity are sufficiently low that the transit times of the photo-generated carriers exceed the recombination time. Müller and Hanke[43] have also demonstrated electrically pumped photoconductive mixing.

Finally, photoparametric up-conversion in variable capacitance diodes has been demonstrated by Roulston[44].

1.2.4 Optically pumped mixers

In this thesis attention will be concentrated on optically pumped mixers. The principles involved in optically pumped mixing will be proven and, hence, the fundamental design considerations for optically pumped diode mixers explained. It is not the object of this thesis to prove the viability of the devices in any particular application; rather, the performance of the devices will be compared with that of the photodetector-mixer combinations they would replace. In Chapter 7, however, some possible applications for optically pumped mixers will be discussed.

Apart from the author's previous publications on the topic[36,45-47], no other published work on optically pumped mixer diodes is known. However, optically pumped mixing[48] has been demonstrated by Foyt and Leonberger using photoconductive devices developed from optically gated switches[6]. In these devices the resistance presented by a gap in a gold microstrip on a high resistivity indium phosphide (InP) substrate is dramatically reduced under illumination. A focussed, modulated laser light source can therefore modulate the resistance presented to an electrical signal input at one end of the microstrip. The mixer devices are substantially improved by using interdigitated contacts with very narrow gap spacing. Good performance was obtained at low frequencies (100MHz) with projections indicating that the InP photoconductive mixers could prove efficient up to about 20GHz if the carrier lifetime could be reduced; beyond this frequency the optical power requirements are likely to become too demanding[48]. The limitations likely with these devices are discussed further and compared with those of diode mixers in Chapter 7.

Although this thesis will concentrate on the use of semiconductor diodes as optically pumped mixers, the use of alternative structures should not be ruled out - this is considered further in Chapter 7. In the following section some mechanisms by which optically pumped mixing may be achievable in diode structures are described.

1.3 Optically pumped mixing mechanisms

A variety of devices are now employed as mixers at radio to millimetre-wave frequencies; these include junction diodes, MESFETs, and bipolar transistors, but one of the most commonly used is the Schottky-barrier diode. The Schottky-barrier diodes are pumped in forward bias where their nonlinear I-V characteristic is used as the mixing mechanism. The mixing is basically resistive, i.e. the conductive part of the admittance is modulated. Previously this form of resistive mixing employed point-contact diodes[49], which can be considered to be hybrids between Schottky and p-n diodes. Backward p-n diodes[50], which rely on a nonlinear reverse characteristic due to tunnelling, are still used in some applications, although the advantages of low noise and low local oscillator power they offered over point-contact diodes can now be obtained with Schottky structures.

Mixing can also be performed by varying the reactive part of the diode admittance. Such action is frequently used in up-converting mixers, commonly called 'parametric up-convertors', employing variable capacitance diodes, since conversion gain can easily be achieved in this mode of operation[51]. Down-convertors with gain have now been demonstrated[52]. The diodes are used in reverse bias where their conductance is low, and they may be of the p-n or Schottky-barrier variety.

In this section a brief description of some likely optically pumped mixing mechanisms in differing diode structures is given.

1.3.1 Resistive mixing (1): Schottky-type devices

Fast photodetectors are now made using either Schottky or p-i-n diode structures. In reverse bias both types of device can combine efficient detection, low capacitance and small transit-time limitations; however, their characteristics are not nonlinear. In forward bias the characteristics are nonlinear but, due to the narrow depletion width, detection becomes less efficient and the capacitance increases. The latter is especially true for semiconductor-semiconductor junctions such as PIN (p-i-n) diodes, since minority-carrier storage gives rise to a large diffusion capacitance. For Schottky-contacted structures, however, the possibility exists of making some compromises and fabricating a device which will remain 'punched through' even in forward bias, and hence retain efficient photodetection and low capacitance properties. The details of such a device will be described more fully in Chapter 6; for now its existence will be assumed and a brief look at its mixing mechanism will be taken. For the purposes of this work, optically pumped operation is considered more important and attention will be concentrated on this type of mixing. With electrically pumped operation the device will behave in a very similar manner to an ordinary mixer down-converting an input current signal.

The mixing mechanism is best described with reference to Fig.1.2. The I-V characteristic used is of the form of the typical diode equation[53]:

$$I = I_s \{ \exp(qV/nkT) - 1 \} \qquad (1.1)$$

where q is the electronic charge, k Boltzmann's constant, T the absolute temperature, and n the diode ideality factor $\geqslant 1$.

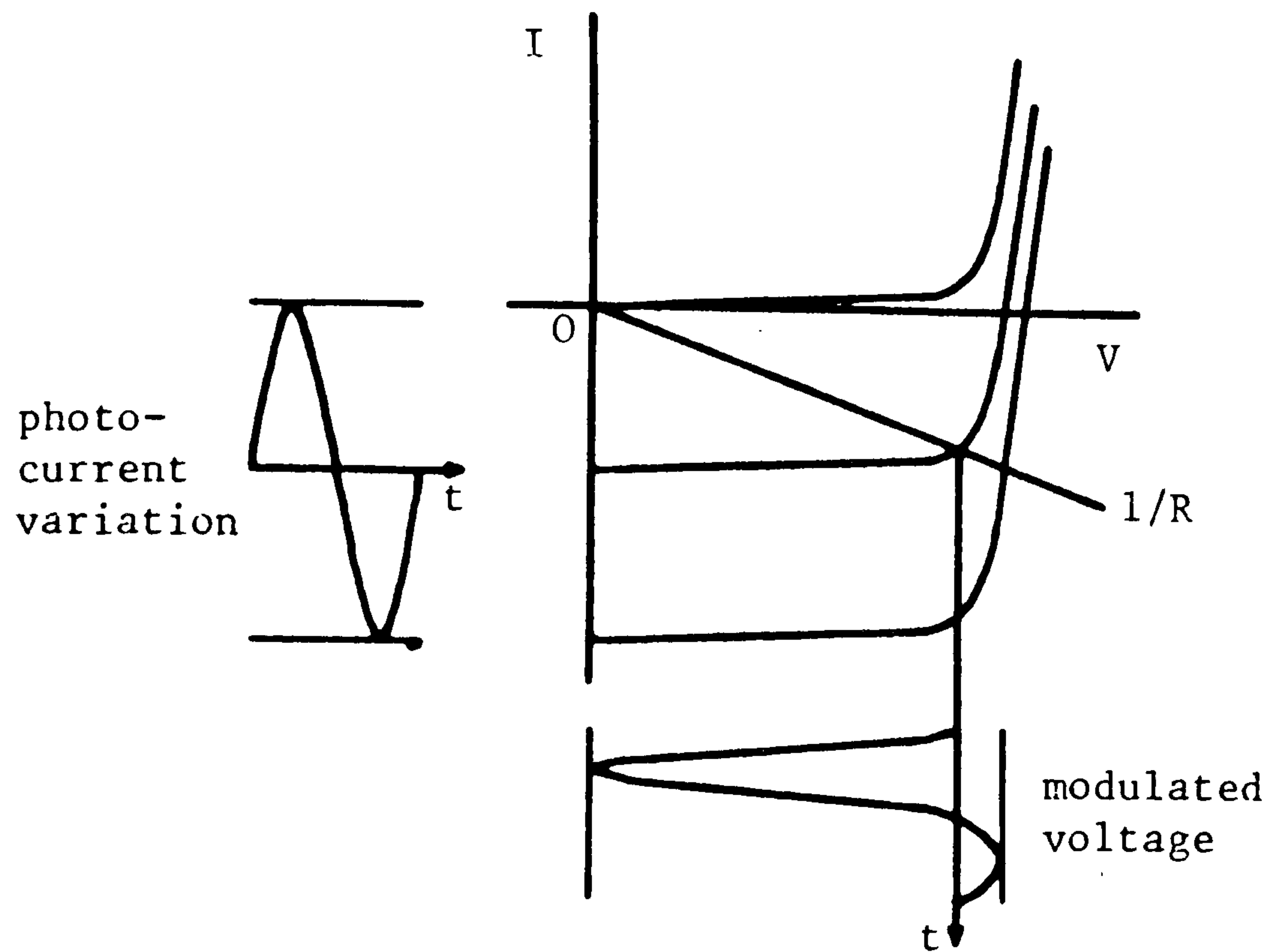

Fig. 1.2 Optically pumped mixing mechanism in rectifying Schottky-type devices.

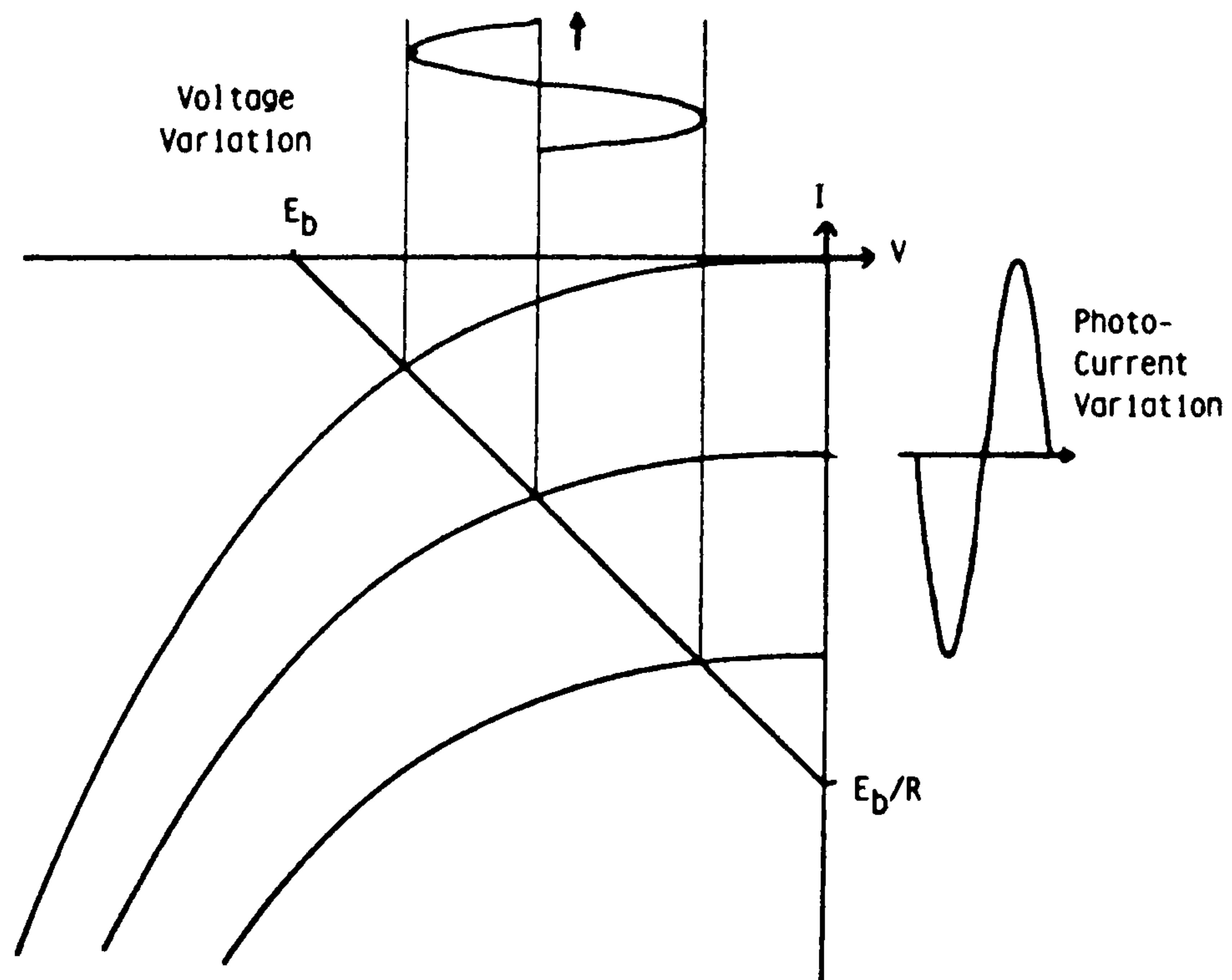

Fig. 1.3 Optically pumped mixing mechanism in reverse-biased tunnelling devices.

The diode is pumped using sinusoidally varying illumination which it is assumed produces photocurrent directly proportional to the incident optical power (the generation of this photocurrent is described in section 2.1). This simple, illumination-dependent, and voltage-independent, current generator model is used throughout this thesis; qualifications regarding its use are described in section 2.1. The photocurrent variation is shown on the left of Fig.1.2 and its effect on the I-V characteristic is also shown. With a resistive load-line it can be seen how the voltage across the diode varies with illumination. The differential (slope) conductance of the diode which is defined by the diode voltage is, therefore, also modulated.

The load-line shown assumes that the diode and embedding circuit are matched at the l.o. frequency so that the sinusoidally varying optically generated current sees a purely resistive path. Reactive components in this path would tend to open the line up into an ellipse. Also, in a real mixer the d.c. and a.c. load lines, which are shown as being the same in Fig.1.2 for simplicity, will be separate.

1.3.2 Resistive mixing (2): reverse-bias tunnelling

In reverse bias most diode characteristics are not sufficiently nonlinear to produce frequency conversion. An exception to this, mentioned at the beginning of section 1.3, is the backward diode, which relies on tunnelling in a reverse biased p-n junction. Tunnelling in metal-semiconductor contacts can also produce highly nonlinear reverse characteristics.

The tunnelling mechanism is dependent on the barrier being very thin so that the conduction electrons can penetrate it. The narrowness of the barrier will mean that

most photo-carriers are generated outside the barrier, causing the responsivity and transit-time limitations to be dependent on minority-carrier diffusion. The thin barrier also causes the capacitance per unit area of the devices to be large. Lower limits to the device area will be set due to the need to couple light into it effectively; this will be discussed further in section 2.1.

A load-line construction similar to that used for the Schottky type devices may be employed to illustrate the optically pumped resistive mixing mechanism, Fig.1.3. The action of the photocurrent on the diode voltage and, hence, slope conductance, is similar to that for the Schottky type devices, and the same qualifications about the use of the resistive load-line need to be borne in mind.

1.3.3 Photocapacitive mixing

If a photocurrent can be generated in a variable capacitance diode in a similar way to the previous cases, then the device can be used as a photocapacitive mixer. This can be seen with reference to Fig.1.4. The load circuit at the l.o. frequency is conjugate-matched to the diode, so the photocurrent sees a resistive bias circuit and a load-line model similar to those used before (especially Fig.1.2) can be used, Fig.1.4(a). The diode is operated in reverse bias since here the barrier conductance is low and the reactive components of the admittance can therefore dominate. The photocurrent variation can be seen to produce a voltage variation across the diode in Fig.1.4(a), which is transferred to the C-V characteristic in Fig.1.4(b) to demonstrate the capacitance modulation necessary in this type of mixer. The C-V characteristic used is of the form:

$$C = C_0 / [1 - (V/\Phi)]^m \qquad (1.2)$$

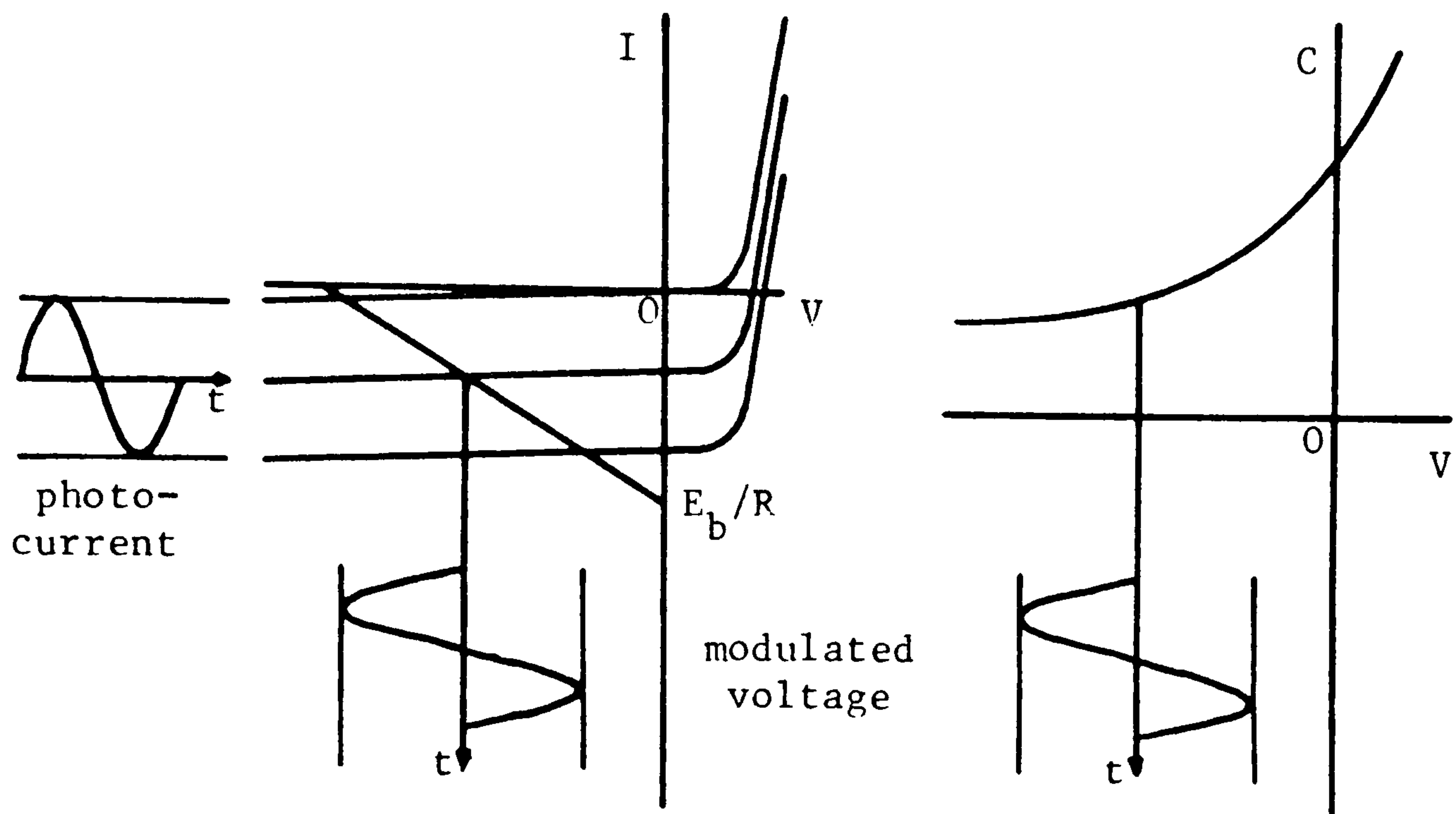

Fig.1.4 Optically pumped mixing mechanism in variable capacitance diode (a) load-line model
(b) modulation of C-V characteristic

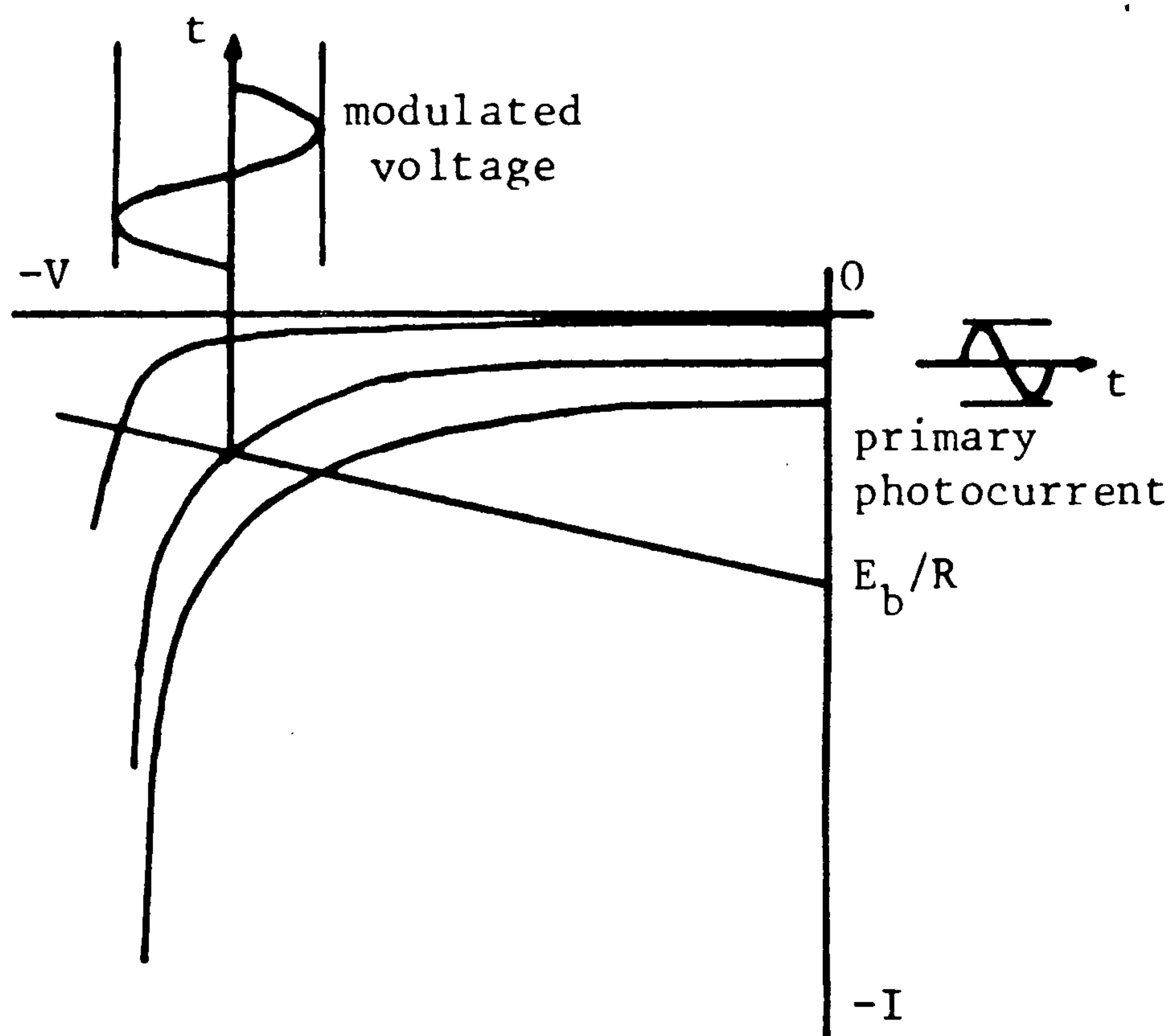

Fig.1.5 Optically pumped mixing mechanism for an APD

where C_0 is the zero bias barrier capacitance, Φ is the diode contact potential, and m the C-V law exponent. This exponent typically has values between 1/2 (for uniformly doped material) and 1/3 (for linearly graded doped material), although it can have much higher values ($\rightarrow$5) for specially fabricated 'hyper-abrupt' junctions[54].

1.3.4 Avalanche nonlinearity

Avalanche photodiodes (APDs) are a commonly used form of photodetector in which internal amplification of the optical signal is achieved as the primary photogenerated carriers, due to their high energy in the high fields that exist in such devices, ionise further carriers, which may again ionise further carriers; in this way the photocurrent is multiplied. The nonlinear characteristic of the device under high reverse bias could be used, in a similar way as before, as an optically pumped mixing mechanism as shown in Fig.1.5. However, with a typical APD, a very high resistance would be required in the l.o. circuit to obtain significant voltage modulation (perhaps $\gg$ 10kΩ); this could lead to problems with the frequency response if reactive parasitics are not effectively resonated, as well as problems in matching the mixer to the signal input which will be at a frequency close to that of the l.o. Also, if the device was being used to down-convert an electrical signal, the voltage variations caused by this signal will limit it to being of a very low level to prevent distortion. The statistical nature of the avalanche multiplication process makes it very noisy, and this is likely to be an opposing limitation on very low level signals which might be swamped by avalanche noise.

Since the avalanche multiplication factor is strongly bias-dependent, the APD optoelectronic mixer is best suited to electrically pumped action[36-41]. The electrical

l.o. applies a voltage variation across the diode which modulates the multiplication factor. Seeds and Lenoir have developed an analytic theory for the conversion loss and noise performance of APD harmonic optoelectronic mixers which is based on a linearisation of the $(M)^{-1}$ versus voltage curve[41], where M is the multiplication factor; excellent agreement with experimental results is obtained.

1.4 Performance parameters

Although a number of parameters describing the performance of a mixer device can be specified, mixers are generally employed in receivers and it is the receiver performance which is of greatest significance. Individual receivers will be affected to differing degrees by different mixer parameters. The most important measure of the performance of a receiver is the receiver overall noise factor, F_R, which can be defined as the ratio of the input signal-to-noise ratio of the receiver to the output signal-to-noise ratio, although the stricter definition will be given later in section 2.3.2. Assuming that the mixer is the first stage in the receiver and that it is followed by a low-noise amplifier of suitably high gain and noise factor F_{IF}, then the noise contributions of the following stages can be neglected and the receiver overall noise factor given by:

$$F_R = L_C(F_{IF}+t_r-1) \tag{1.3}$$

F_R, being a measure of the degradation of the signal-to-noise ratio, should be minimised. It can be seen that two mixer parameters affect F_R; the conversion loss, L_C, is the ratio of the available input power at the signal frequency to the available output power at the intermediate frequency; the noise-temperature ratio, t_r,

(or noise ratio) is the ratio of the available output noise power from the mixer diode under the specified operating conditions to the noise power available from a resistor equal to the diode equivalent resistance at the IF port under those operating conditions, and at standard noise temperature (290K). It can be seen from equation (1.3) why so much attention is paid to the conversion loss of the mixer; it multiplies the other parameters and, therefore, has a dominant effect on the overall noise factor.

The input (signal) and output (IF) impedances of the mixer are also important, (a) because mismatch with the source and/or load, respectively, will result in loss over and above that of the intrinsic conversion loss and (b) because the noise factors for IF amplifiers are generally specified for a given input impedance (which is the output impedance of the mixer in the usual configuration). The mixer impedance (which is time-varying) is determined by the bias and pump conditions at the diode and can thus be adjusted.

The dynamic range of a mixer is another important parameter, it being the difference between two important specifications of mixer operation: at the low signal level, the minimum detectable signal, and at the high signal level, the compression point or the third-order intercept (these will be defined in Chapter 5 - see section 5.4.3). All of these specifications will depend on the pump and bias conditions as well as the actual mixer device. They will be discussed in greater detail in section 5.4.3.

Finally, the frequencies at which the mixer can be used need to be defined. Although it will be related to the device frequency response, the mixer response will generally deteriorate at lower frequencies than the device

response, because of less efficient coupling of the l.o. power and, hence, increased conversion loss.

1.5 Generation of high-frequency intensity-modulated optical signals

The systems in which optically pumped mixers could be used would have optically distributed l.o. signals; since this distribution (using fibres or bulk-optics) would typically involve transmission distances of, at most, a few metres, signal dispersion and loss would not present significant problems even at millimetre-wave frequencies. The main problem would be in the generation of the high-frequency intensity-modulated optical signals.

The high-frequency signals could be generated by directly modulating semiconductor laser devices, but the maximum modulation frequencies of the fastest devices would limit this technique to frequencies below 20GHz at room temperature[55], although a -3dB bandwidth of 26.5GHz has been reported for a cooled (-60°C) laser[56]. External modulators possess similar bandwidth limitations: lithium niobate modulators with a -3dB bandwidth of 17GHz have been fabricated[57]; possibly of more interest, due to the possibility of integration, are GaAs modulators, and devices operating at up to 14GHz have recently been demonstrated[58]. However, a more important limitation for such modulators is the optical damage threshold (typically less than mW levels).

A number of techniques for optically generating microwave-frequency signals have been employed. For example, the nonlinearity of semiconductor lasers can be exploited to generate a high harmonic content by direct modulation[59]. Thus high-frequency signals can be generated by modulation at lower frequencies. Lasers may be mode-locked to generate short pulses which again are very rich

in harmonic content[28]; the spectra of such pulsed waveforms are 'combs', with separation equal to the repetition rate, which may be flat out to very high frequencies. Finally, use can be made of optical heterodyning, as described in section 1.2.1, in which very high frequency beats limited only by the detecting device can be generated. The technique may work well with gas and solid-state lasers, but for semiconductor lasers good bias current and temperature stabilisation is essential, and for reasonably narrow linewidths external cavities and/or devices such as distributed feedback lasers should be used[20].

Optical phase-locked loops (OPLLs)[60,23] have been demonstrated where the difference frequency between two semiconductor lasers is detected in a photodiode and then mixed (phase-detected) with a reference oscillator in a microwave mixer. The output is then applied to one of the lasers which acts as a current-controlled oscillator since its emission wavelength is thus varied. A simplified diagram of an OPLL is shown in Fig.1.6. The heterodyned optical output of an OPLL could provide a useful optically distributed reference signal.

A further form of high-frequency modulated optical signal generation employs optical injection locking, in which the FM modes of a modulated master laser are used to injection lock cavity modes of one or more slave lasers; high-frequency narrow-linewidth microwave signals have been obtained[61-64]. Several arrangements for the heterodyning are possible: heterodyning the master and slave laser outputs[61], or the outputs of two injection-locked slave lasers[62,63], or two cavity modes of the same slave laser[64]. The last case has produced a 35GHz signal with a linewidth of less than 10Hz.

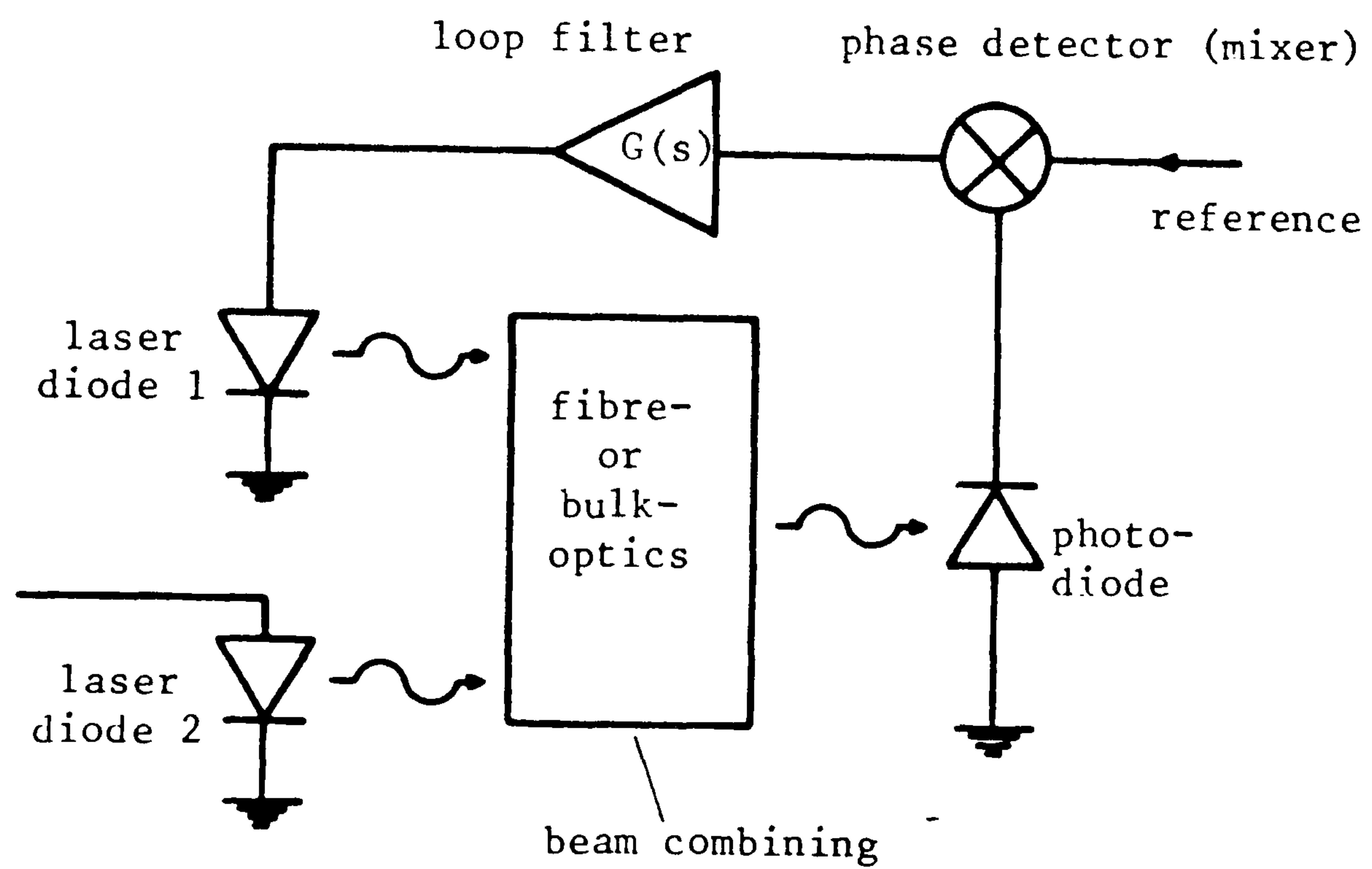

Fig. 1.6 Optical phase-locked loop (simplified diagram). Laser diode 1 is temperature-stabilised and bias current-controlled. Laser diode 2 is temperature- and bias current-stabilised.

1.6 Chapter summary and structure of thesis

In this chapter an introduction to optoelectronic mixers has been given. This has consisted of a review of the various types of mixing action that can involve optical and electrical signals. The review has resulted in the definition of an optoelectronic mixer and (according to this definition) the identification of two types: electrically pumped and optically pumped optoelectronic mixers. As this thesis will address optically pumped mixing in diode structures, a brief description of some likely mechanisms in such devices was given in section 1.3. In section 1.4 the parameters which will be used to describe the performance of optically pumped mixers were defined. In section 1.5, the chapter ended with a brief review of the different methods that might be employed to generate high-frequency intensity-modulated optical signals which are important as such signals provide the l.o. modulation for optically pumped mixers.

Chapter 2 contains the theory behind the mechanisms involved in optically pumped mixing. The coupling of the optical local oscillator into the mixer is of critical importance to the performance of an optically pumped mixer, and represents the novel aspect of such a device. In a diode mixer this coupling will be performed by photocurrent generation. The mechanisms behind this generation and their limitations (in terms of magnitude and speed of response) are described. Mixer theory is then described. Firstly, this involves an analytic description of the effects of l.o. pumping on nonlinear admittances; the frequency conversion theory is then explained. An important aspect of mixer performance is the noise performance, and factors relating to this performance are

covered after a general review of noise mechanisms and parameters has been given.

The analytic frequency conversion theory of Chapter 2 is generally inadequate to obtain accurate predictions of mixer performance. In Chapter 3 computer models of optically pumped mixing are described. The models have actually been implemented in Fortran programs, and indications of the performance of these programs are given.

Most of this thesis is concerned with an investigation of tunnelling metal-semiconductor contacts as optically pumped mixers. In Chapter 4 the device is characterised: its structure is first described, followed by an explanation of the current transport mechanisms at the barrier, the formulation of an equivalent circuit of the device, and a study of the effects of illumination. In Chapter 5 the performance of the device as an optically pumped mixer is described using the parameters defined in section 1.4. Both theoretical (from the computer models) and experimental results for the conversion loss performance are given and compared.

Although the performance of the tunnelling contacts can be used to describe some of the general aspects of optically pumped mixer behaviour, the devices themselves, as will be seen, are relatively inefficient. In Chapter 6 an improved optically pumped mixer diode structure is described, and predictions of the performance that should be achieved with typical devices are given.

The main conclusions that can be drawn from the work described in this thesis are stated in Chapter 7. Suggestions are made as to how the work could be usefully extended, and a brief description of the possible applications of optically pumped mixers is given.

CHAPTER TWO

OPTOELECTRONIC MIXER THEORY

2.1 Illumination effects 47

2.1.1 Photocurrent generation 47

2.1.2 Analytic expressions for the photocurrent 52

2.1.3 Transit-time limitations (1): drift current 55

2.1.4 Transit-time limitations (2): diffusion current 56

2.2 Analytic mixer theory 64

2.2.1 Large-signal analysis 65

2.2.2 Frequency notation 68

2.2.3 Small-signal analysis 68

2.3 Noise 71

2.3.1 Types of noise 72

2.3.2 Noise parameters 76

2.3.3 Noise in mixer diodes 78

2.3.4 Noise in optoelectronic mixer diodes 80

2.3.5 Mixer noise factor 82

2.3.6 Mixer noise-temperature ratio 85

2.4 Chapter summary 86

In this chapter the basic theory behind optoelectronic mixer action in diode structures is described. For an optoelectronic mixer, as defined in section 1.2, at least one of the inputs, l.o. or signal, is an intensity-modulated optical signal. The effect of illumination on diode structures therefore needs to be examined and this theory is summarised in section 2.1. In section 2.2 an analytic mathematical description of mixer theory is given, showing how a nonlinear device under large-signal l.o. excitation can be represented by linear relationships for the small signals involved in the mixing. Section 2.3 examines the noise sources present in an optically pumped mixer and their likely effect on the performance of a receiver employing such a device.

2.1 Illumination effects

2.1.1 Photocurrent generation

When light is absorbed in a semiconductor the incoming photons cause the generation of electron-hole pairs. This is shown using band diagrams for both a metal-semiconductor contact (Fig.2.1(a)) and a p-n junction (Fig.2.1(b)). The carriers generated in the depleted region of the devices are separated by the electric field in the barrier and, generally, can all be considered to contribute to the external current as they traverse this region; each electron-hole pair therefore contributes a charge q, where q is the electronic charge. Since it can be considered that all of the photo-excited carriers contribute to the external current, this is a highly efficient means of photodetection. The barrier cannot be made very wide because of carrier transit-time limitations (which will be discussed later), but even for fast

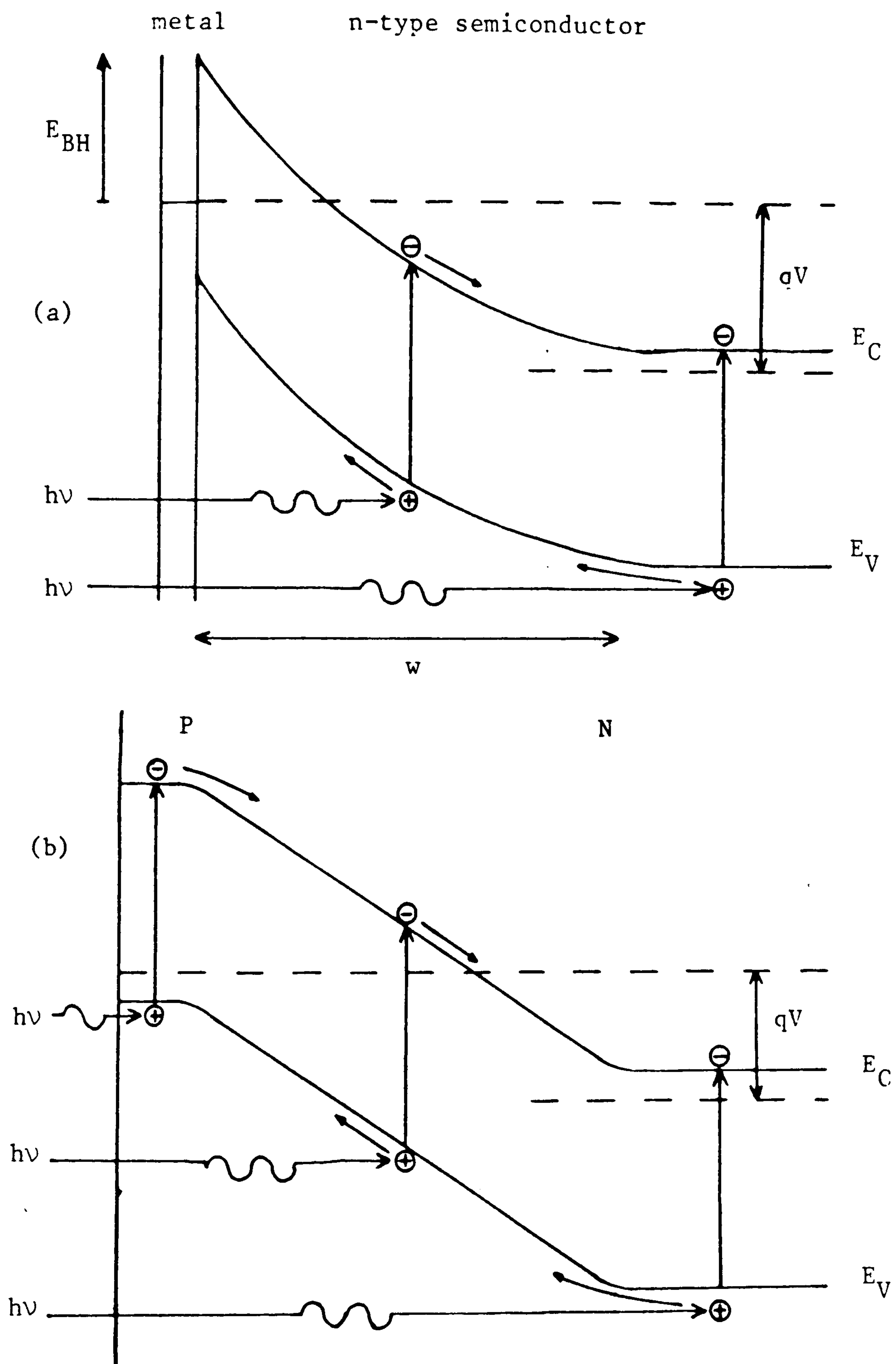

Fig. 2.1 Band diagrams illustrating photocurrent generation in (a) tunnelling metal-semiconductor contact, and (b) p-n diode photodetectors. (w is the depletion width)

photodetectors, with a commonly used compromise between the device responsivity and transit-time limitations, the barrier width is made $\geq 1/\alpha$, where $1/\alpha$ is the absorption length in the material at the illumination wavelength of concern. The absorption length will be wavelength dependent, but in materials such as GaAs can be very short (approximately 1μm or less) at visible and near infrared wavelengths, yielding short transit-times.

Apart from the compromise made between the device responsivity and carrier transit-times mentioned above, the device capacitance, which will cause an RC cutoff in the frequency response, must also be taken into consideration. The capacitance of a device of a given barrier width can be reduced by reducing the device area, although for smaller area devices parasitic capacitances tend to dominate. Very fast photodetectors have device capacitances less than 0.2pF, which would enable operation up to 16GHz and above assuming a 50Ω load. An optimised photodetector will typically give an RC cutoff at about the same frequency as that at which the transit-time limitations set in. The device area cannot be reduced indefinitely as it must be large enough for the optical input to be effectively coupled into the device. Devices of various areas have been investigated and are described in this thesis, but, in numerical examples, a lower limit of $10 \times 10 \mu m^2$ will usually be used for the device area. This represents an area somewhat greater than the core size of typical monomode fibre, and therefore sufficient for focussing onto in a mechanically stable environment, or for making a pig-tailed device. In order to maximise absorption in the barrier region, it is also necessary to make the metallisation of the Schottky contact for the metal-semiconductor diode, and the p layer for the p-n diode, as transparent as possible.

Carriers generated outside the depletion region will have to diffuse to the barrier in order to contribute to the current. The number that reach the barrier before recombining will depend on the diffusion length of the (minority) carriers in the material. Of course, the number generated outside the barrier in the first place will depend on the barrier width and the absorption length in the material at the wavelength of concern.

Figs.2.2(a) and (b) show the situation for two absorption lengths, one less ($1/\alpha$=0.1μm), the other greater ($1/\alpha$=0.75μm) than the diffusion length (L_p=0.4μm). In each of the figures the diffusion length curves can be regarded as the probability of carriers generated at a distance x reaching the barrier, for the two barrier widths (w_1=25nm, w_2=0.25μm) shown. The figures can be used to gain a qualitative understanding of the photocurrent generation. In Fig.2.2(a) in the wider barrier case, the situation is that present in most photodetectors, with most of the carriers being generated in the depletion region. In Fig.2.2(b) with the wider barrier, however, because of the longer absorption length most carriers will be generated outside the barrier and a substantial number of these will not contribute to the current. In both situations with the narrow barrier most carriers will be generated outside it, but it is obvious that in case (a) where the carriers are generated much nearer the barrier and their probability of reaching it is higher, the photocurrent will be greater. In case (b) with the narrow barrier it is interesting to note that because the barrier is so thin, small variations in the width will have negligible effect on the total current, since the probability of diffusing carriers generated around this distance contributing to the current is very high anyway. The narrow barrier cases correspond closely to the situation in tunnelling metal-semiconductor (GaAs)

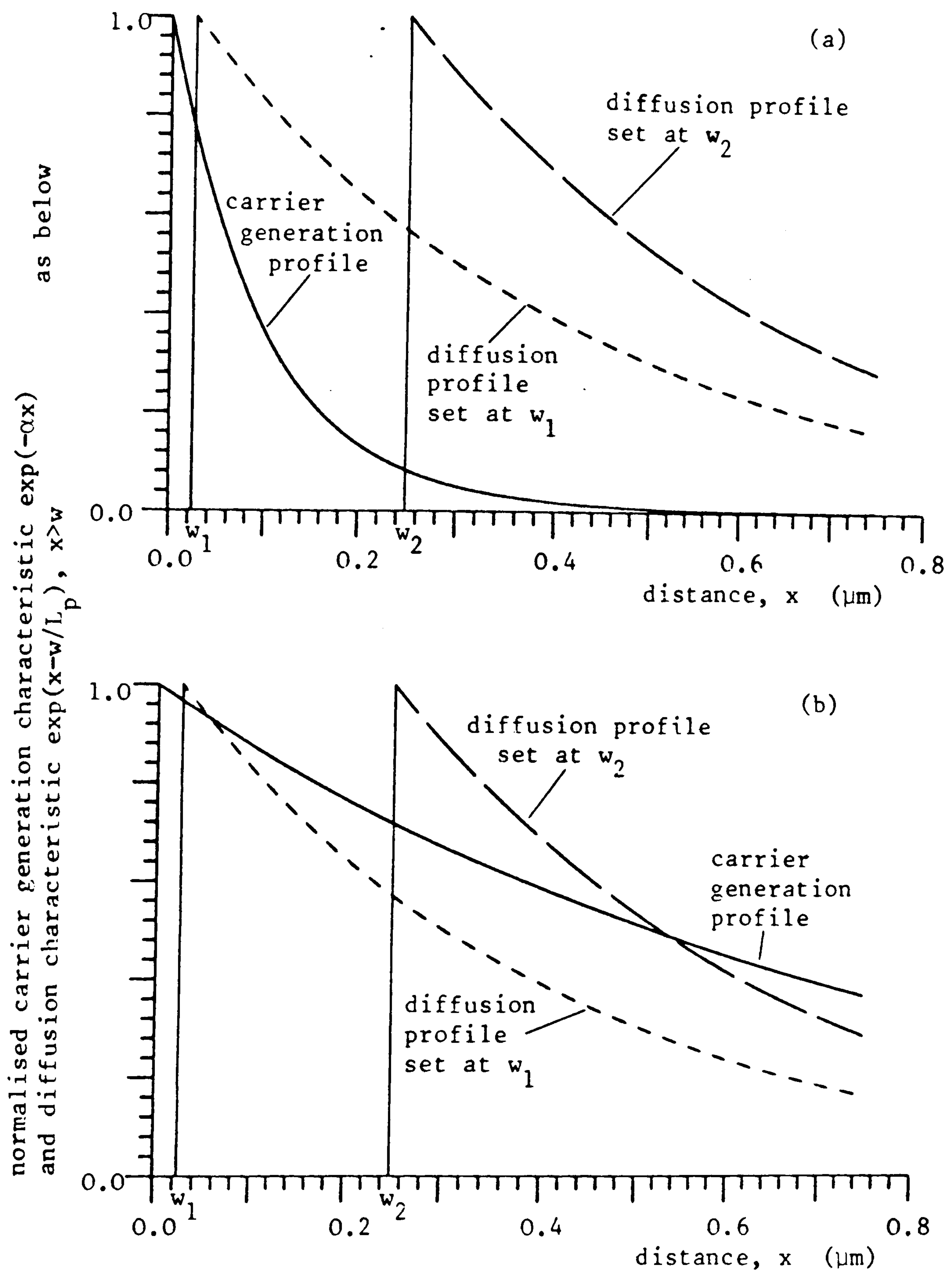

Fig. 2.2 Photocurrent generation considerations with barriers of widths, w_1= 25.5nm, w_2= 0.25μm and minority-carrier diffusion length = 0.4μm

(a) absorption length, $1/\alpha$ = 0.1μm, (b) $1/\alpha$ = 0.75μm

contacts investigated in this work, and will be discussed further in Chapter 4.

2.1.2 Analytic expressions for the photocurrent

Analytic expressions for the current (density) can also be derived. Carriers generated in the depletion region of a device will be separated by the barrier field; recombination in such a region is negligible and all of the generated carriers can be assumed to contribute to the current. For a depletion width, w, an incident photon flux density, Φ (in photons per second per unit area), and an absorption coefficient, α, the current generated in the depletion region, J_{dep}, is given by:

$$J_{dep} = q\Phi \{ 1 - \exp(-\alpha w) \} \qquad (2.1)$$

In the above, the photon flux density can take into account loss due to the reflectance, R, of the metallisation so that $\Phi=(1-R)P_{opt}\lambda/Ahc$, where P_{opt} is the incident optical power, λ the wavelength of the illumination, c the velocity of light, h Planck's constant, and A the active area of the device.

The corresponding diffusion current density from the carriers generated in the undepleted material is obtained by solving the (time-independent in this case) continuity equation; this solution is derived in Appendix A, and the result is given by:

$$J_{diff} = q\Phi \frac{\alpha L_p}{1+\alpha L_p} \exp(-\alpha w) \quad + \quad qp_{n0}\frac{D_p}{L_p} \qquad (2.2)$$

where L_p is the minority-carrier (hole, for n-type material considered here) diffusion length, D_p is the hole

diffusion coefficient, and p_{n0} is the equilibrium hole concentration in the n-type material.

The total current density is then:

$$J_{tot} = q\Phi \left[1 + \frac{\exp(-\alpha w)}{1 + \alpha L_p} \right] + q p_{n0} \frac{D_p}{L_p} \qquad (2.3)$$

In the above, the term containing p_{n0} can usually be ignored as it is very small and since p_{n0} represents the hole concentration in n-type material. In GaAs (in which the intrinsic carrier concentration is very low), even assuming low n-type doping ($10^{14}cm^{-3}$), and hence higher p_{n0}, the term is sufficiently small that even in a relatively large area device ($100x100\mu m^2$) the current due to it would still be only of the order of 10^{-20}A. The total current is therefore proportional to the photon flux.

The above result, that the photocurrent is proportional to the incident photon flux, agrees well with the current generator model assumed for the photoresponse mechanism as stated in section 1.3.1. However, the model also assumes independence of the photocurrent on the diode voltage; it can be seen from equation (2.3) that the total photocurrent depends on the depletion width, and will therefore, in general, depend on the diode voltage. The extent of this dependence will be affected by the extent of the depletion width variation to be considered, as well as the physical parameters of absorption length, minority-carrier diffusion length, etc. For example, in the discussion on Fig.2.2 at the end of section 2.1.1, it was shown that with a depletion width and absorption length much less than the diffusion length, the depletion width variation will have negligible effect on the total photocurrent.

The assumption used to derive the photocurrent contribution of carriers generated in the depletion region, namely that the carriers are separated by the barrier field and all contribute to the current, can be expected to be accurate for most diodes in reverse bias. In forward bias, however, the transport mechanisms within the barrier need to be reconsidered, as the above assumption predicts a current in the opposite direction to what is now the 'normal' direction of current flow. Simplistically, in an unilluminated barrier in forward bias the forward current diffusion effects in the barrier become more important than the reverse drift effects, since the electric field in forward bias is low (this is discussed in Chapter 6). The transport of the photo-generated carriers in the barrier will depend on the electric field in the barrier (and, hence, on the barrier height, doping level, and applied bias), and on the influence of the illumination on the electron concentration (and, hence, on the majority-carrier quasi-Fermi level - see Chapter 6). Heasell[65] has shown that a quasi-Fermi level shift due to illumination decreases the collection efficiency of photo-generated carriers in forward bias. The effect becomes most significant for low barriers on very lightly doped material, at high forward bias, and with strong illumination. Lavagna et al.[66] have considered the effect of recombination at the metal-semiconductor interface where the direct transfer of electrons into the metal causes a carrier flow in the opposite direction to the field-separated carriers. Again, this effect is most significant for low barriers to lightly doped material, in which the field is insufficient to 'drive' electrons away from the interface, and for strongly absorbed light, with which carriers are generated nearer the interface. The above analyses have been carried out for solar cell devices in Si and CdTe; further work is

necessary to determine the influence of these effects on the quantum efficiency of GaAs devices.

2.1.3 Transit-time limitations (1): drift current

In sections 2.1.1 and 2.1.2 it was shown that carriers contributing to the current may do so via two transport mechanisms. In devices with wide barriers the current will be mainly due to the carriers generated in the depletion region and for reasonably high electric fields these carriers will traverse the barrier region, of width w, at some (usually saturated) drift velocity, v_s. The carriers generated in the depletion layer will thus take a finite time to traverse this region and a phase difference will develop between the incident photon flux and the photocurrent when the light intensity is modulated. Obviously, at high modulation rates when the phase difference becomes significant, not all carriers will enhance the detected signal at the modulation frequency.

The simplest case to obtain a quantitative result for this effect is shown in Fig.2.3; the illumination is from the left and generation at the 'front' surface of the depletion layer only is assumed. For a photon flux density $\Phi_1 \exp(j\omega t)$ the conduction current density at a point x is

$$J_{cond}(x) = q\Phi_1 \exp[\, j\omega\,(t - x/v_s)\,] \qquad (2.4)$$

Since within the barrier $\nabla . J_{tot} = 0$, where J_{tot} is the total current density,

$$J = \frac{1}{w} \int_0^w \left(J_{cond} + \varepsilon_s \frac{\partial E}{\partial t} \right) dx \qquad (2.5)$$

where the second term in the parentheses represents the displacement current density; ε_s is the semiconductor permittivity, and E the electric field. Equations (2.4) and (2.5) give:

$$J_{tot} = \frac{j\omega\varepsilon_s V}{w} + q\Phi_1 \frac{1 - \exp(-j\omega\tau_r)}{j\omega\tau_r} \exp(j\omega t) \qquad (2.6)$$

where V is the sum of the built-in and applied (reverse) voltages, and $\tau_r = w/v_s$ is the transit-time of carriers through the depleted region. The above equation may be used to determine the short-circuit current density (V=0) or the open-circuit voltage ($J_{tot}=0$) of the photoresponse. Both show the same normalised response dependent on $[(1-\exp(-j\omega\tau_r))/j\omega\tau_r]$ and this response has been illustrated graphically by Gärtner[67]. The response is down by $\sqrt{2}$ at $\omega\tau_r=2.4$. The -3dB frequency is therefore:

$$f_{t1} = \frac{2.4}{2\pi\tau_r} = \frac{1.2v_s}{\pi w} \quad . \qquad (2.7)$$

If the field in the depleted region is insufficient to ensure saturated carrier velocity, v_s in the above equations should be replaced by an average velocity.

2.1.4 Transit-time limitations (2): diffusion current

For barriers which are narrow compared to the absorption length the photocurrent will be mainly due to carriers generated outside the depletion region and the transit-time limitations will be due to carrier diffusion. The diffusion current contribution to the total current is the diffusion current reaching the barrier, i.e. at x=w,

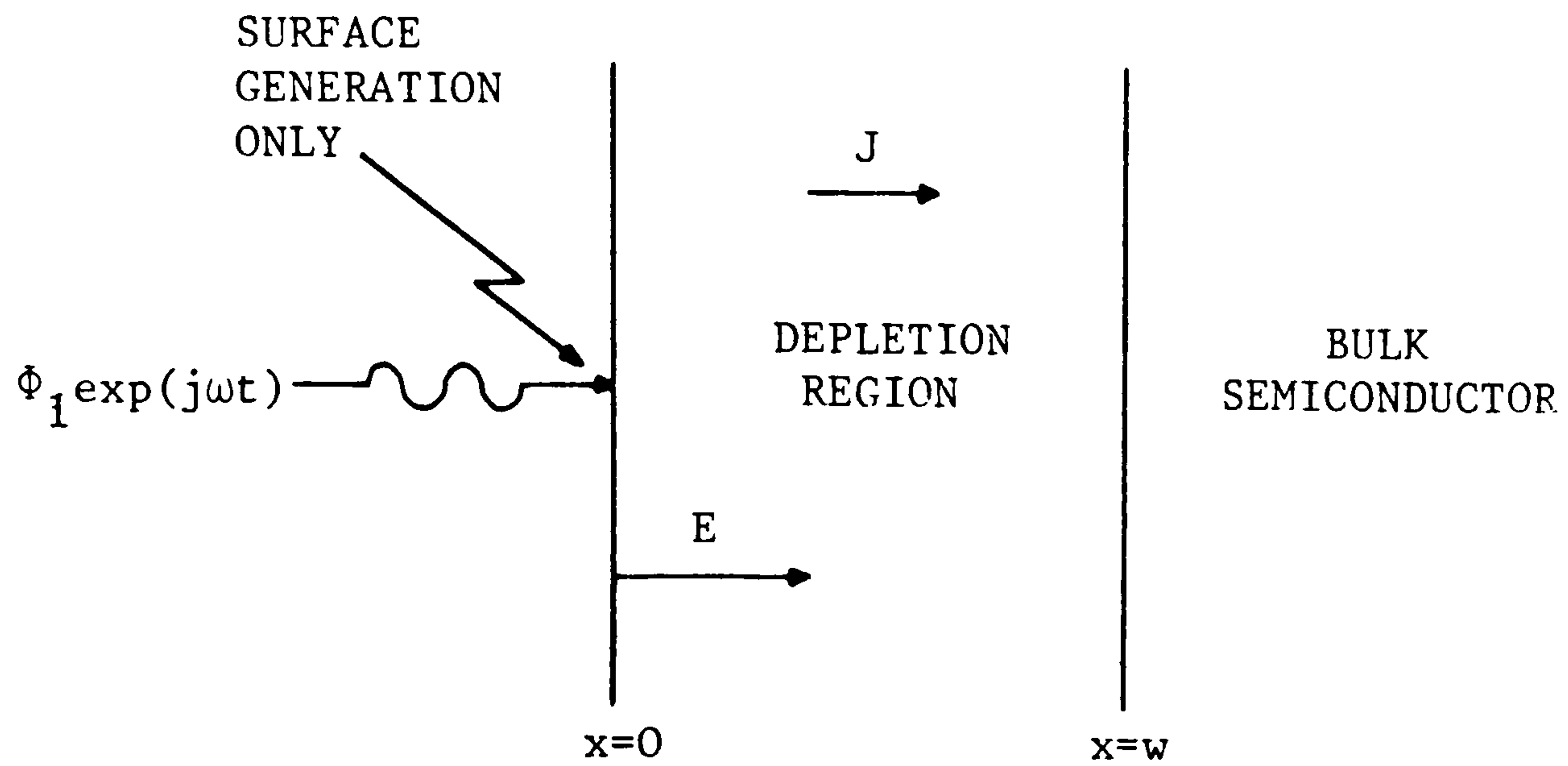

Fig.2.3 Geometry used to analyse transit-time effects of carriers generated in the depletion region of a semiconductor by intensity-modulated light.

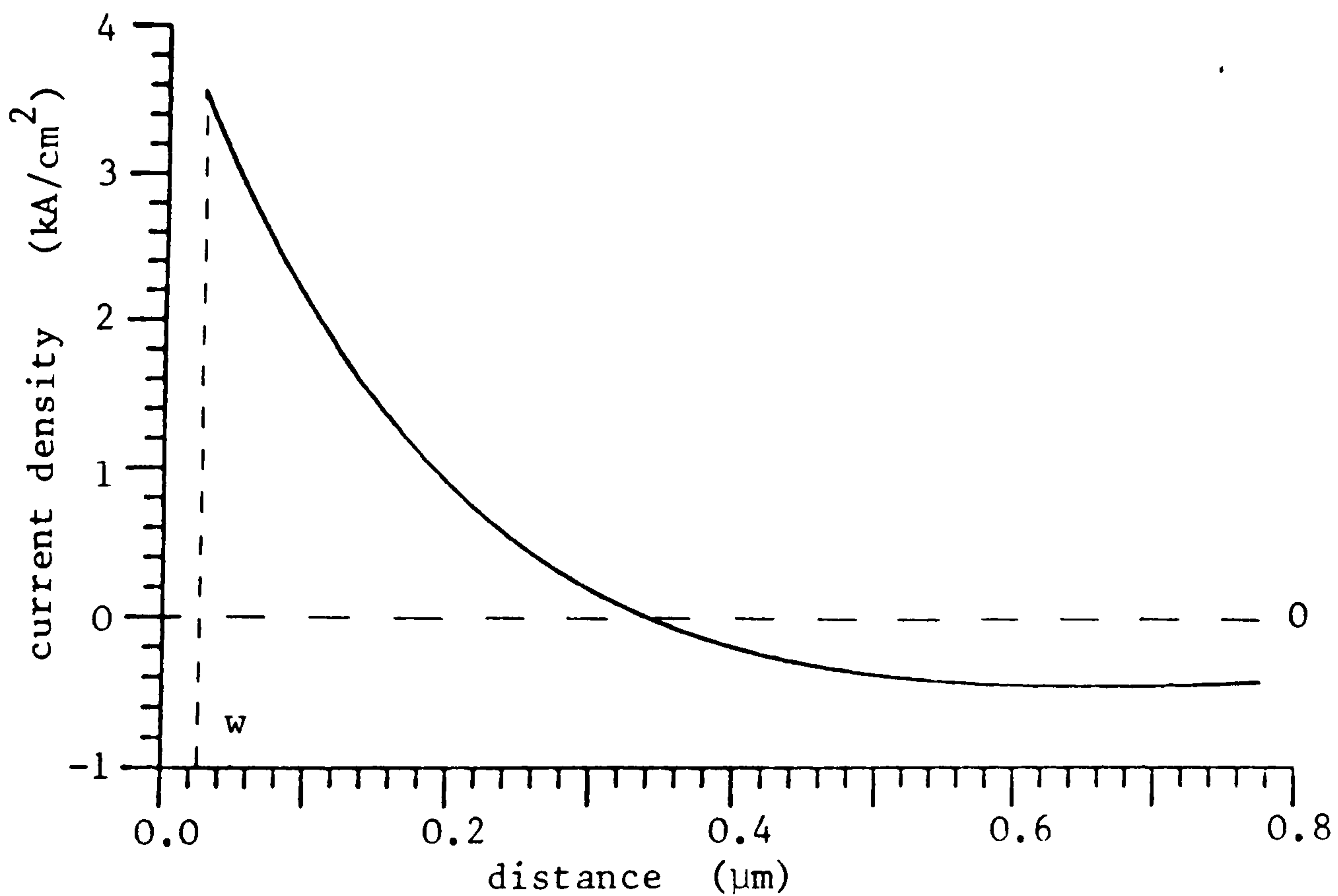

Fig.2.4 Minority-carrier diffusion current profile for $L_p = 0.4\mu m$, $D_p = 9cm^2/s$, $1/\alpha = 0.25\mu m$ ($w = 25.5nm$)

as expressed in eqn. (2.2). However, as derived in Appendix A, a more general equation exists for the minority-carrier diffusion current at a position x,

$$J_{diff}(x) = qD_p\{[(p_{n0} + C.\exp(-\alpha w)/L_p].\exp((w-x)/L_p) - \alpha C.\exp(-\alpha x)\} \quad (2.8)$$

where $$C = \frac{\Phi\alpha L_p}{D_p(1 - \alpha^2 L_p^2)}$$

If v is the average velocity due to diffusion at a distance x, then dt=dx/v is the time taken to traverse a distance dx. Using the general relation $J=qp_{n1}v$ where p_{n1} is the excess hole concentration, the transit time across a region from x=z to the barrier at x=w is:

$$\tau_{diff} = \int_z^w [v]^{-1}\,dx = \int_z^w \frac{qp_{n1}}{J_{diff}}\,dx$$

$$= \int_z^w \frac{[p_{n0} + C.\exp(-\alpha w)].\exp((w-x)/L_p) - C.\exp(-\alpha x)}{D_p\{[(p_{n0}+C.\exp(-\alpha w))/L_p].\exp((w-x)/L_p)-\alpha C.\exp(-\alpha x)\}}\,dx \quad (2.9)$$

In applications for which the transit-time limitations due to diffusion have been derived previously, such as the limitations caused by transport across the base region of a transistor[68], the distance over which the diffusion occurs is known. Sawyer and Rediker[69] have analysed the situation for the minority-carrier diffusion limitations to the frequency response of narrow-base germanium

photodiodes; however, in this case too, the distance over which the diffusion occurs is known, since the photodiodes are 'back-illuminated' and the relevant region is between the illuminated surface and the barrier which is at a known depth. In the case considered in this thesis the distance over which the average diffusion velocities must be integrated is not so easily defined.

The minority-carrier diffusion current itself can be considered to be made up of two components; a current that diffuses towards the barrier due to the extraction of the minority carriers at the barrier, and a current that diffuses away from the barrier due to the concentration gradient set up by the exponential generation profile. (The situation is clearly somewhat different to that analysed by Sawyer and Rediker in which the second component would enhance the first.) Obviously, the former component dominates near the barrier since there is a very sharp concentration gradient there, but further from the barrier the second component will dominate and there will be a diffusion current away from the barrier (the effect of this current on the external current can be neglected since it is assumed that the bulk region is much wider than the diffusion length of the minority carriers and these carriers will recombine before reaching the ohmic contact). The diffusion current profile shown in Fig.2.4 and calculated from eqn.(2.8) shows the minority-carrier diffusion current taking into account both components; the effective contribution can be seen to be that current between the barrier and the point at which the current is zero, that is, the point at which carrier motion in either direction is equally likely.

The transit-time as given by eqn. (2.9) is the effective transit-time for the current generated between w and z; an effective transit-time can be found for the contributing current at a range of distances between w and the point at which the diffusion current is zero, where the effective transit-time will be infinite since at this point the average velocity of the minority-carriers is zero. As has been said, this represents the point from which the total d.c. current can be considered to contribute. It can be inferred from this, that lesser proportions of the d.c. current can be considered to contribute from distances less than this point, where, for example, at a distance x, the contribution can be regarded as $(J_{diff}(w)-J_{diff}(x))$ from the diffusion current profile.

The response of the diffusion current to modulation will depend on the current contributing and on the transit-time effects on this contribution. It is obvious that for given values of absorption length and diffusion length, as the modulation frequency is increased only the current from within a shorter distance will be able to respond quickly enough to follow the modulating signal. The current contribution may become very small if this distance is very short. In analysing the situation a balance must be struck such that this distance within which carriers effectively respond to the modulation signal is not taken as too short such that the current contribution is too low, or too long such that the transit-time limitations become too severe. Since the transit-time given by eqn. (2.9) represents that for an average velocity for the total current contribution between x=w and x=z, this contribution can be multiplied by the magnitude of the transit-time effect function as derived by Gärtner, giving the function, F_1:

$F_1(x) =$

$$[J_{diff}(w) - J_{diff}(x)] \; \frac{1 - \exp(-j\omega\tau_{diff}(x))}{j\omega\tau_{diff}(x)} \qquad (2.10)$$

for the modulation frequency $f=\omega/2\pi$. The distance at which F_1 reaches a maximum is the distance at which the aforementioned balance is struck and, therefore, the distance within which the carriers can be said to contribute effectively. The magnitude of F_1 at this point will give the magnitude of the a.c. current at the modulation frequency.

Figs.2.5 and 2.6 show $[F_1(x)/J_{diff}(w)]$, that is $F_1(x)$ normalised to the d.c. photocurrent, for a range of frequencies at absorption lengths of $1/\alpha=0.1\mu m$ (in Fig.2.5) and $1/\alpha=0.75\mu m$ (in Fig.2.6). As expected, the distance from within which carriers respond and the proportion of a.c. to d.c. photocurrent both decrease with increasing modulation frequency. Since the a.c. photocurrent at any modulation frequency can be found, the frequency response of the minority-carrier diffusion mechanism can be determined from this analysis. A full solution of the time-dependent continuity equation would be useful in confirming the validity of the analysis, but such a solution would be a considerable mathematical task.

It is interesting to note that the results for the -3dB cutoff frequency obtained using the above analysis have been very similar to those obtained by taking z as the distance within which $1/\sqrt{2}$ of the current contributes according to the diffusion current profile, integrating to find the effective transit-time, τ', over this distance (z-w), and then defining the cutoff frequency as $f=1/2\pi\tau'$.

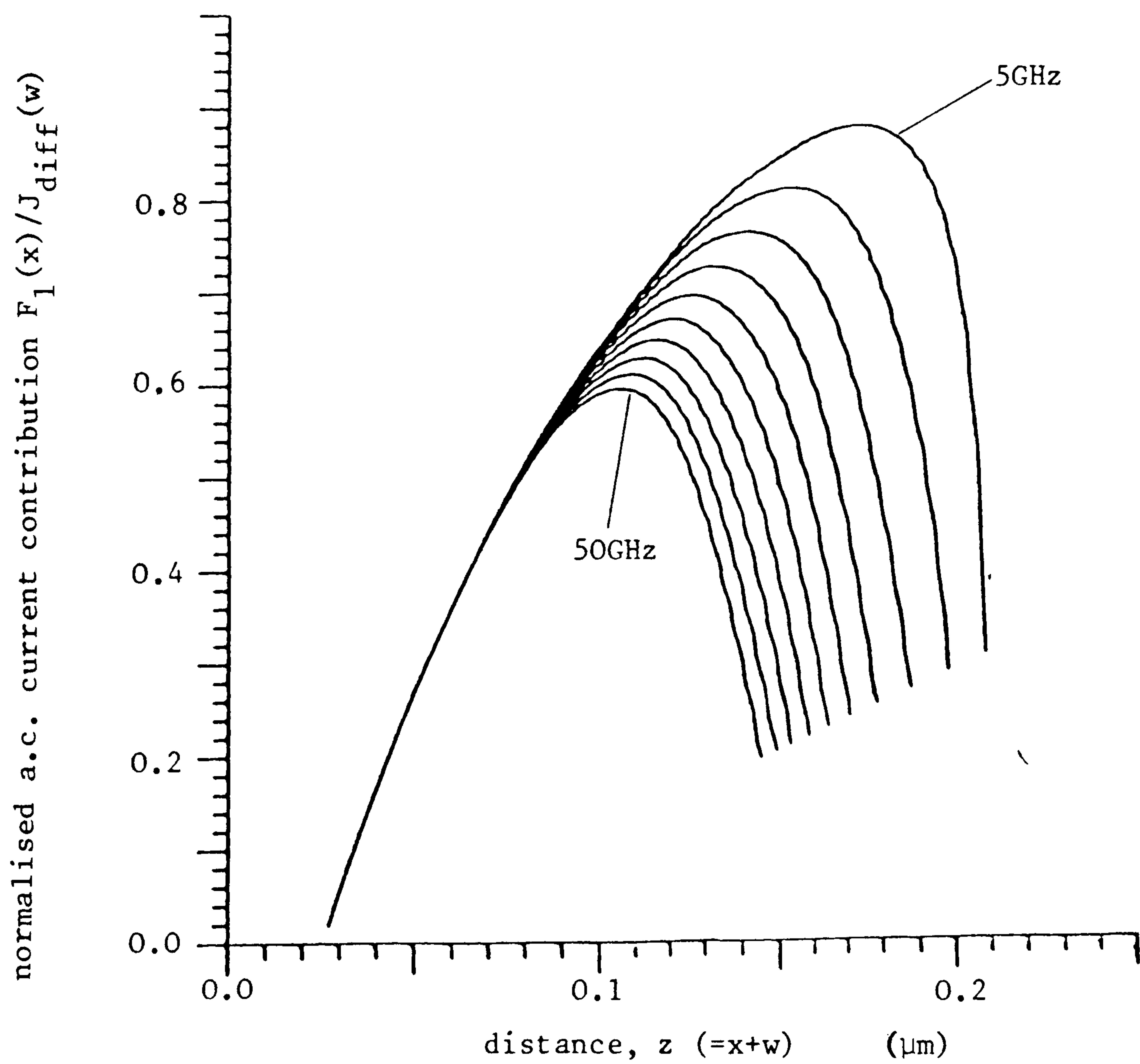

Fig.2.5 [$F_1(x)/J_{diff}(w)$] for $1/\alpha = 0.1\mu m$, $L_p = 0.4\mu m$ and $D_p = 9cm^2/s$, with barrier width, $w = 25.5nm$, for frequencies 5GHz to 50GHz in 5GHz steps.

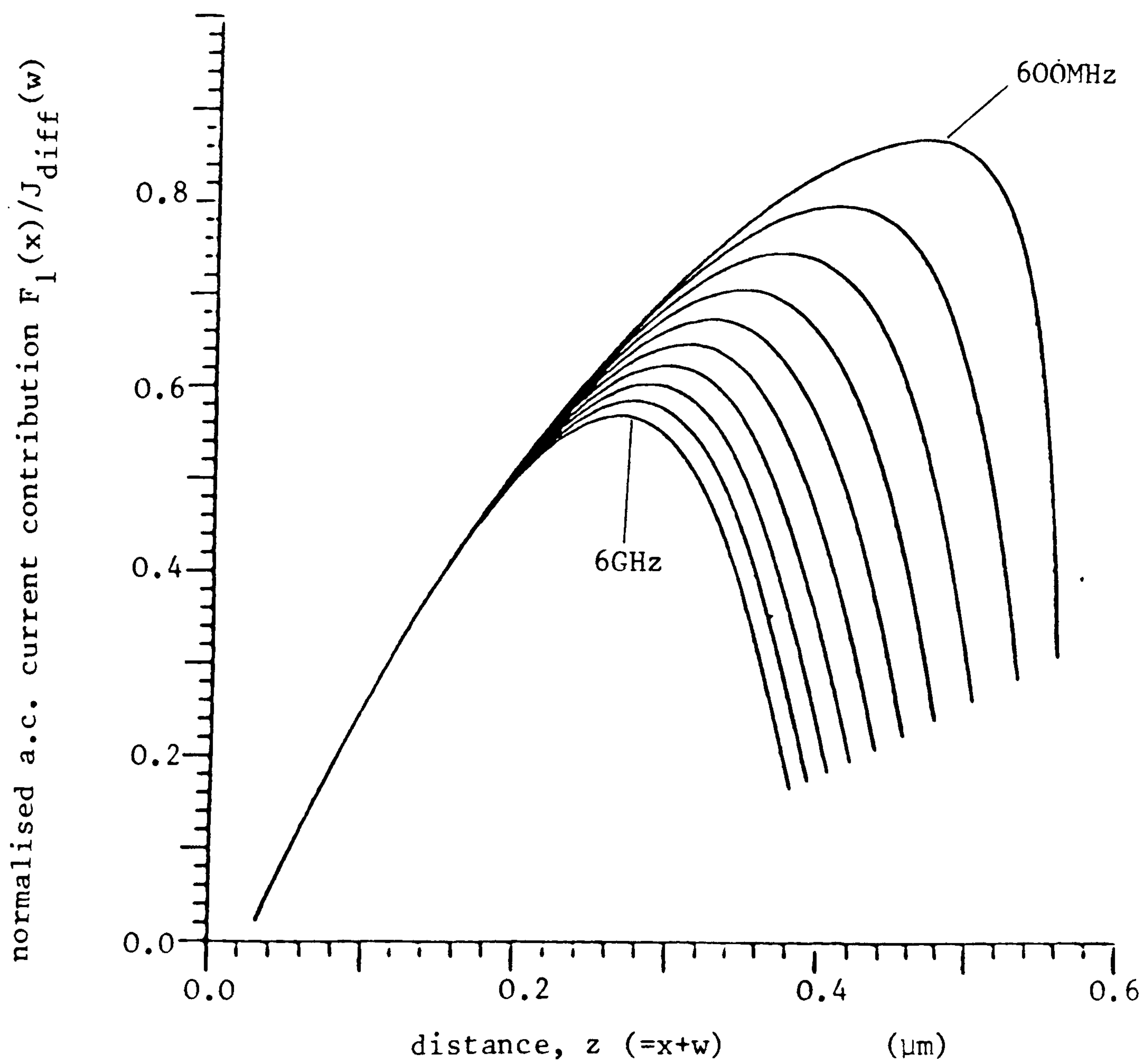

Fig.2.6 [$F_1(x)/J_{diff}(w)$] for $1/\alpha = 0.75\mu m$, $L_p = 0.4\mu m$ and $D_p = 9cm^2/s$, with barrier width, $w = 25.5nm$, for frequencies 600MHz to 6GHz in 600MHz steps.

Again, a full solution of the time-dependent continuity equation may clarify this point; in the absence of such a solution the more rigorous analysis described in the preceding paragraphs (rather than the simplified formula of this one) is used in the calculations in later chapters.

2.2 Analytic mixer theory

An analysis of mixer performance can be divided into two parts:

a. A large signal analysis which finds the solution satisfying the nonlinear diode characteristic equations and embedding circuit equations when the diode is driven by the local oscillator (l.o.), assumed to be the only 'large' signal imposed on the diode. The solution will give the diode voltage and current, and therefore differential conductance and capacitance, as functions of time.

b. A small-signal analysis in which it is assumed that the input signal and the output intermediate-frequency (i.f.) signal are much smaller than the l.o. and small enough to ignore the diode nonlinearities; this implies that the mixer is 'distortion-free'. In this case the Fourier coefficients of the differential conductance and capacitance found in the large signal analysis are used in a linear analysis to form an 'admittance matrix' of the diode under l.o. excitation; from this matrix parameters such as the conversion loss of the mixer may be determined.

Early analytic theories for the large signal problem, such as that of Torrey and Whitmer[49] assumed a sinusoidal driving voltage across the diode; i.e. all harmonics of

the l.o. were assumed short-circuited. Similarly, in the small signal analysis all frequency components except for the desired output i.f., the input signal frequency and, usually, the image frequency were assumed short-circuited - the image frequency was considered because it lies as near below the l.o. frequency as the signal frequency does above it for upper-sideband down-conversion (vice-versa for lower-sideband down-conversion).

2.2.1 Large-signal analysis

With the sinusoidal driving voltage assumption the diode voltage, v_d, is:

$$v_d(t) = V_{dc} + V_p \cos \omega_p t \qquad (2.11)$$

where V_{dc} is the d.c. bias voltage and V_p is the peak amplitude of the local oscillator voltage. The current is allowed to contain all the possible l.o. harmonic components.

Most analyses[49,70] have been concerned with ideal or near-ideal diode mixers, the I-V characteristics of which give the following expression for the diode current:

$$i_d(t) = I_s \left[\exp(\alpha v_d(t)) - 1 \right] \quad , \quad \alpha \equiv q/nkT \qquad (2.12)$$

The mixing action is caused by the modulated nonlinear differential conductance of the diode which can be expressed as:

$$g_d(t) = di_d \,/\, dv_d = \alpha I_s \exp(\alpha v_d) \qquad (2.13)$$

Replacing v_d in the above by the expression in eqn.(2.11), the conductance can then be expressed in terms of a series expansion, e.g.[49]:

$$g_d(t) = g_0 + \sum_{n=1}^{\infty} 2\, g_n \cos(n\omega_p t) \qquad (2.14)$$

$$g_n = \alpha I_s \exp(\alpha V_{dc}) . I_n(\alpha V_p)$$

where I_n is the modified Bessel function of order n, $I_n(x)=j^{-n}J_n(jx)$. The conductance waveform described above is that for an exponential diode mixer with perfect short-circuit terminations at the higher harmonics of the l.o. frequency (due to assuming the diode voltage variation to be purely sinusoidal). Saleh[71] has considered current and voltage pumped resistive mixers with a variety of short- and open-circuit terminations for the higher l.o. harmonics; the simplest classifications are the Z-mixer (higher l.o. harmonics open-circuited), the Y-mixer (higher harmonics short-circuited), the H-mixer (higher even harmonics short, odd open), and the G-mixer (higher even harmonics open, odd short). However, the case given above, corresponding to Saleh's Y-mixer, is likely to be closest to reality since the diode capacitance, which is neglected, will tend to short out higher frequencies.

For metal-semiconductor contacts and p-n diodes (the latter under reverse bias only) a voltage-dependent depletion capacitance can be assumed to exist – in forward bias, p-n diodes exhibit significant diffusion capacitance. The C-V relationship of the device, eqn.(1.2), will give the time-dependent capacitance as:

$$c_d(t) = C_0 \;/\; [1 - (v_d(t)/\Phi)]^m \qquad (2.15)$$

Still considering the case where the diode pump voltage is purely sinusoidal, expansions of this capacitance have been derived[54]:

$$c_d(t) = a_0 C_d + a_1 C_d \cos \omega_p t + a_2 C_d \cos 2\omega_p t$$

$$\ldots + a_n C_d \cos n\omega_p t \qquad (2.16)$$

where the coefficients a are dependent on the exponent in the C-V relationship and the relative pump swing (≡ $V_p/(\Phi - V_{dc})$) only, and C_d is the capacitance at the bias point. The evaluation of the coefficients requires numerical integration although Mortenson[54] has expressed $a_0 \ldots a_4$ in terms of standard complete elliptic integrals of the first and second kinds, and has plotted values of a_n/a_0 and a_n/a_0^2 against the relative pump swing with the C-V exponent equal to 1/2.

For an optically pumped mixer the l.o. modulation will consist of a photocurrent variation. In the simplest case this variation can be considered to be sinusoidal and with a suitable (resistive) l.o. source circuit will produce an equivalent pump voltage variation across the diode as described in the Introduction, section 1.3; this pump voltage will correspond to that used in the analyses described above.

The above cases assume the pump voltage across the diode to be purely sinusoidal, which requires perfect short-circuit terminations at the higher l.o. harmonic frequencies. In practice this will never be the case and the voltage occuring across the diode will be significantly modified. In order to take into account diode-circuit interactions, numerical analysis techniques are required.

2.2.2 Frequency notation

The frequency notation used for the linear mixer theory in this thesis is that generally used for microwave mixers since it was proposed by Saleh[71]; it leads to a considerable simplification of the analysis.

The large signal analysis is concerned with the l.o., or pump, frequency, ω_p, and its harmonics, $n\omega_p$, $n=0,1,2,$ etc. If the mixer can be considered distortion-free, the small-signal analysis is then concerned with the sideband frequencies given by:

$$\omega_n = \omega_0 + n\omega_p \qquad n = 0, \pm 1, \pm 2, \pm 3 \ldots \qquad (2.17)$$

With this notation negative frequencies will appear in the analysis which, obviously, correspond to positive frequencies in reality; it is important to note that with the subscript notation used, these negative frequencies are not such that $\omega_1 = -\omega_{-1}$ as is the case in many other signal analysis problems. The upper-sideband, i.f, and lower-sideband radian frequencies will be given by ω_1, ω_0, and $-\omega_{-1}$, respectively. Fig.2.7 may be useful in clarifying the notation used.

2.2.3 Small-signal analysis

For small signals the mixer device can be characterised as a linear network relating input signals at different frequencies to output signals at these frequencies. For example, for a distortionless mixer the admittance network relating current components to voltage components considering only the signal, intermediate, and image frequencies is shown in Fig.2.8 and can be represented by the relations:

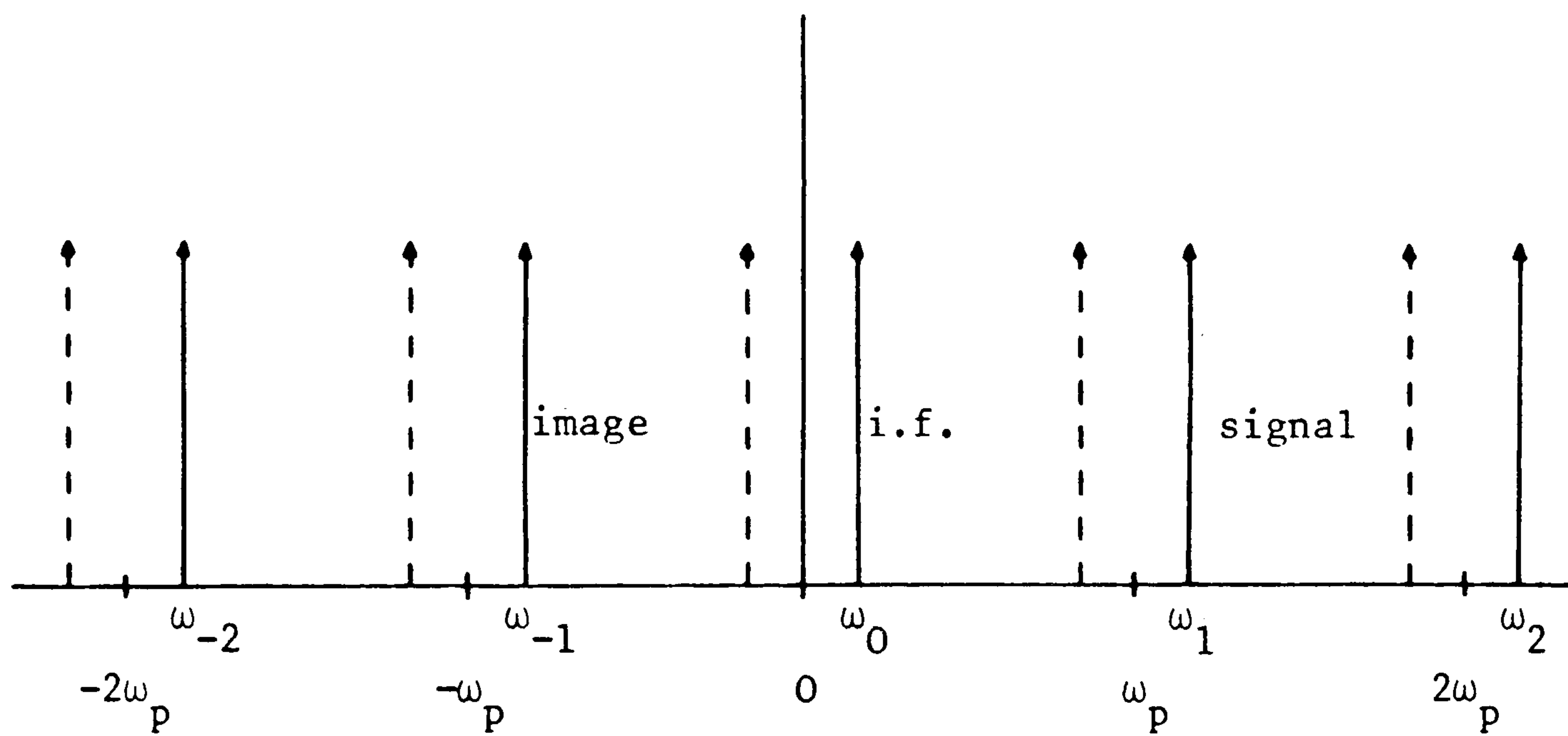

Fig. 2.7 Notation used for sideband frequencies in linear analysis[71]. (Named frequencies correspond to upper-sideband down-conversion.)

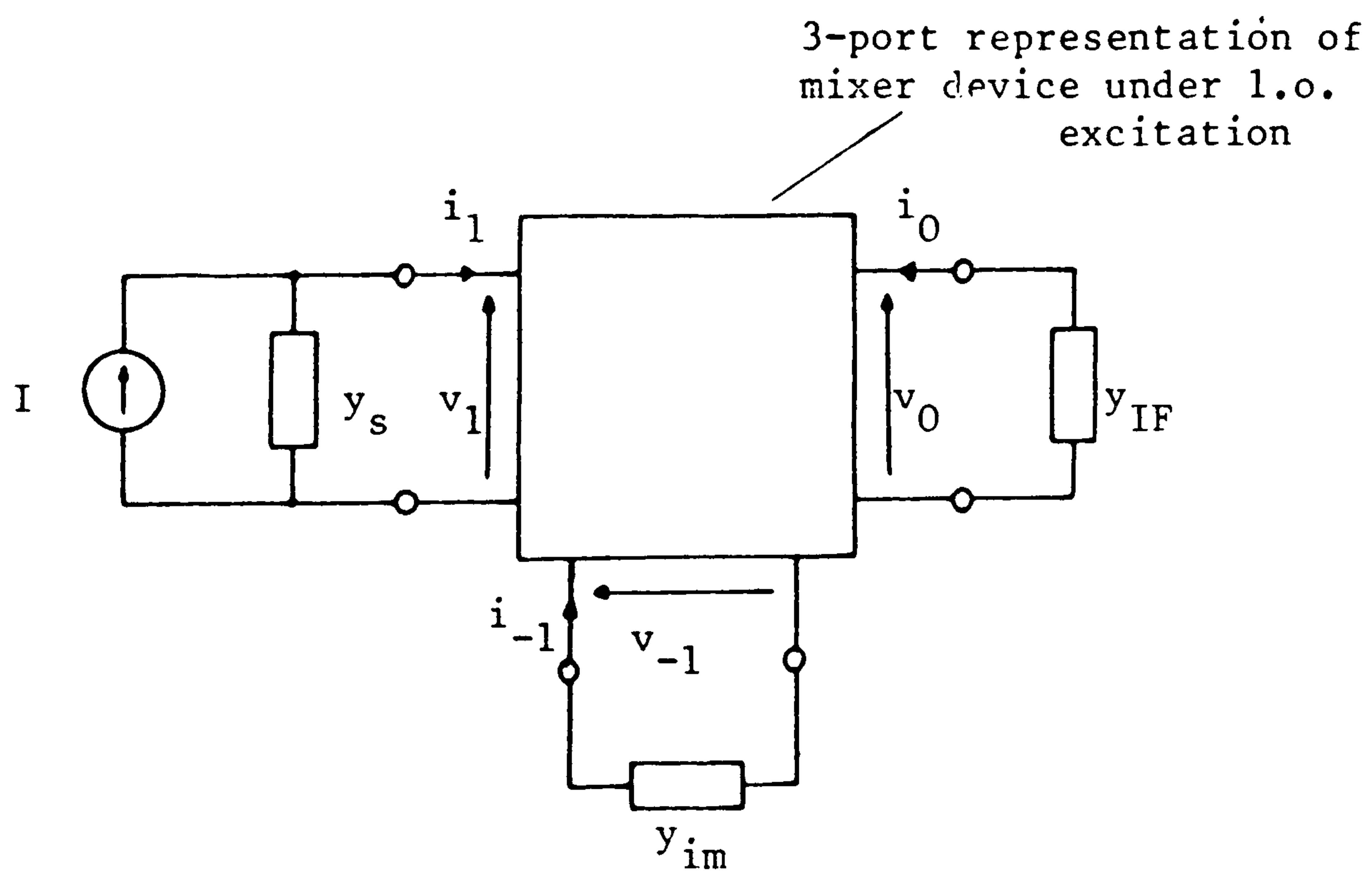

Fig. 2.8 Equivalent 3-port network representation of a distortionless mixer.

$$\begin{bmatrix} i_1 \\ i_0 \\ i_{-1} \end{bmatrix} = \begin{bmatrix} Y_{11} & Y_{10} & Y_{1-1} \\ Y_{01} & Y_{00} & Y_{0-1} \\ Y_{-11} & Y_{-10} & Y_{-1-1} \end{bmatrix} \begin{bmatrix} v_1 \\ v_0 \\ v_{-1} \end{bmatrix} \qquad (2.18)$$

Again, the assumption used to form the above admittance matrix is that frequencies above the input signal frequency are terminated by a short-circuit. The admittance matrix represents the mixer device under l.o. excitation and the components are the Fourier coefficients of the time-varying admittance derived in the large signal analysis:

$$Y_{mn} = G_{m-n} + j(\omega_0 + m\omega_p)\, C_{m-n} \qquad (2.19)$$

where G_{m-n} and C_{m-n} are the (m-n)th Fourier coefficients of the diode conductance and capacitance waveforms, respectively.

For example, in the case of the expansion for the purely resistive mixer given in section 2.2.1, the matrix components would be made up of the coefficients:

$$G_0 = \alpha I_s \exp(\alpha V_{dc}) \cdot I_0(\alpha V_p)$$

$$G_1 = \alpha I_s \exp(\alpha V_{dc}) \cdot I_1(\alpha V_p)$$

$$G_2 = \alpha I_s \exp(\alpha V_{dc}) \cdot I_2(\alpha V_p)$$

with $Y_{11} = Y_{00} = Y_{-1-1} = G_0$

$Y_{10} = Y_{01} = Y_{-10} = Y_{0-1} = G_1$

and $Y_{-11} = Y_{1-1} = G_2$

If the image termination is known then the three-port network can be reduced to a two-port one[49] (Fig.2.9); typically in analytic models this is done by assuming that one of three conditions exist[71] (although this is not necessary): (a) image short-circuited, (b) image open-circuited, (c) image broadband-matched. The first case simply results in the image components of the 3x3 matrix being zero and has no effect on the other components; however, the last case is the most realistic since, especially if $\omega_0 \ll \omega_p$, the signal and image frequencies will be very close. With the prime indicating that these are components of the reduced 2x2 matrix, the conversion loss can be expressed as:

$$L_c = \frac{Re(y_{IF})}{Re(y_s)} \frac{| Y'_{11} + y_s |^2}{| Y'_{01} |^2} \qquad (2.20)$$

where y_s is the source admittance, and y_{IF} is the optimum, conjugate-matched output admittance which can also be found from the two-port network. The above represents the intrinsic conversion loss of the nonlinear barrier only; parasitics will increase the loss still further.

2.3 Noise

In a receiver, a limit to the ability to recover information from a received signal is set by the fact that the received signal level must be greater than the background noise level, that is, it must be discernible. Noise in a communication system can come from two main sources: noise arising in the transmission of a signal (both in its generation and in its path), and noise

internally generated in the electronic receiver itself. Obviously, a receiver is better able to process signals, especially weak ones, the less internal noise it generates. In order to gain an idea of the noise levels generated in a receiver it is first necessary to define the types of noise that may be present; a brief resumé of the most important types of receiver noise is given below.

2.3.1 Types of noise

Flicker noise[72], or 1/f noise as it is sometimes called because of its characteristic frequency dependence, is typically encountered in non-equilibrium situations, i.e. where a direct current is flowing in electrical systems. It is generally a poorly understood phenomenon, no one theory exists to fit all occurences, but it can usually be considered unimportant at the frequencies involved in this work (MHz frequencies and above).

Thermal (or Johnson or Nyquist) noise is due to the random motion of electrons in a metal or semiconductor. The time-average voltage or current in a piece of resistive wire under open-circuit or short-circuit conditions, respectively, will be zero, because the probability of electron flow will be the same in all directions; the mean-square values, however, will be non-zero, and an ohmic resistor will act as a generator of noise power. Since this noise power is independent of frequency (at frequencies of practical interest) it is often called 'white' noise. The (random) electron motion which causes the noise is due to the thermal energy of the electrons and so thermal noise may be reduced by cooling. For thermal noise the noise spectral density, or noise per unit bandwidth, from a source at absolute temperature, T, is given simply by kT, where k is Boltzmann's constant. However, in electronic applications it is often convenient

to represent noise sources by equivalent current or voltage generators with their respective source conductances or resistances. For a source of conductance, G, the mean-square noise current, i_n^2, in an incremental bandwidth, df, is given by:

$$i_n^2 = 4kTG.df \qquad (2.21)$$

A similar expression for the mean-square noise voltage, e_n^2, in a source of resistance, R, holds:

$$e_n^2 = 4kTR.df \qquad (2.22)$$

Shot noise is due to the discrete, particle nature of electronic current, and is a consequence of the statistical manner in which charge-carriers cross a boundary. In contrast to thermal noise, therefore, shot noise arises only in systems which are not in equilibrium, i.e. a direct current is required. In this case, the time-averaged current is non-zero and equal to the direct current, I, and the statistical fluctuations are described by the mean-square noise current:

$$i_n^2 = 2qI.df \qquad (2.23)$$

where q is the electronic charge. Shot noise can only be reduced by reducing the quiescent current and not by cooling.

According to eqns.(2.21)-(2.23) both thermal and shot noise have (white) spectra extending to infinite frequency. This implies infinite noise power and so clearly cannot be the case. For thermal noise there is a quantum-mechanical correction[73] which limits the noise

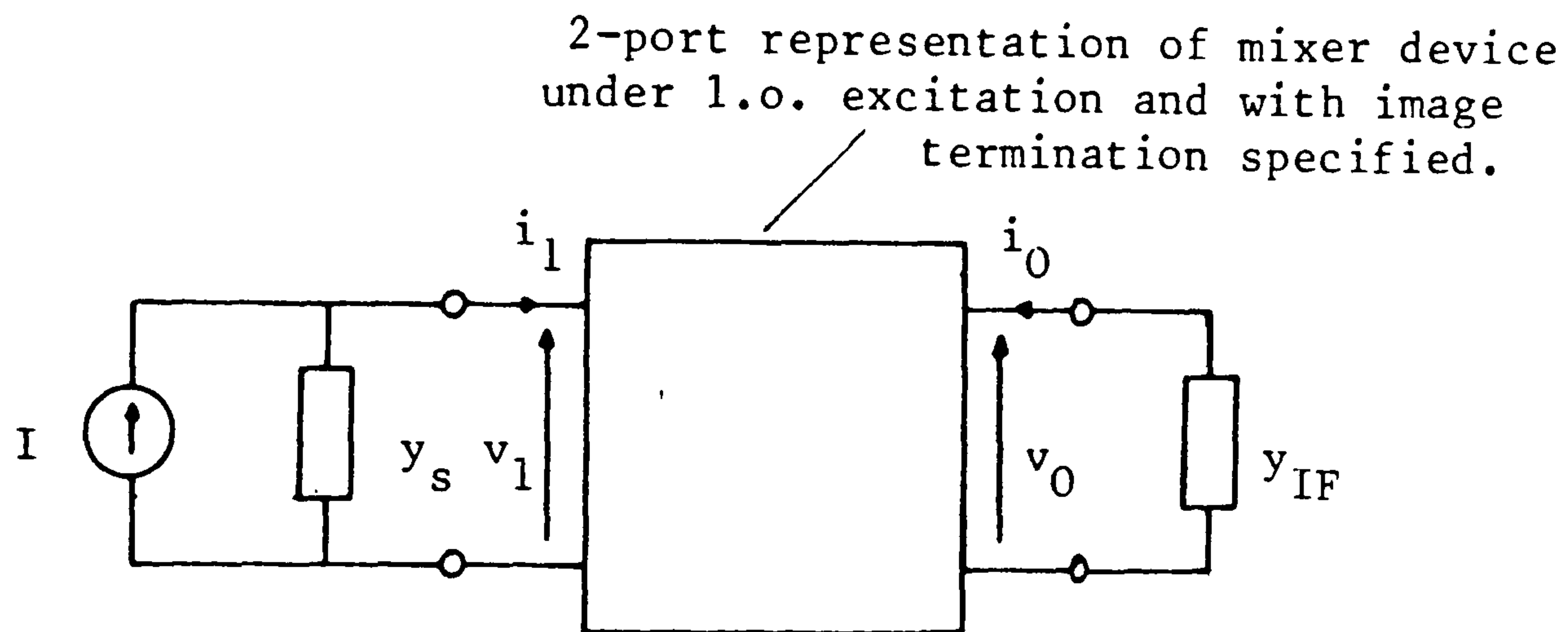

Fig.2.9 Reduced 2-port network representation of a distortionless mixer.

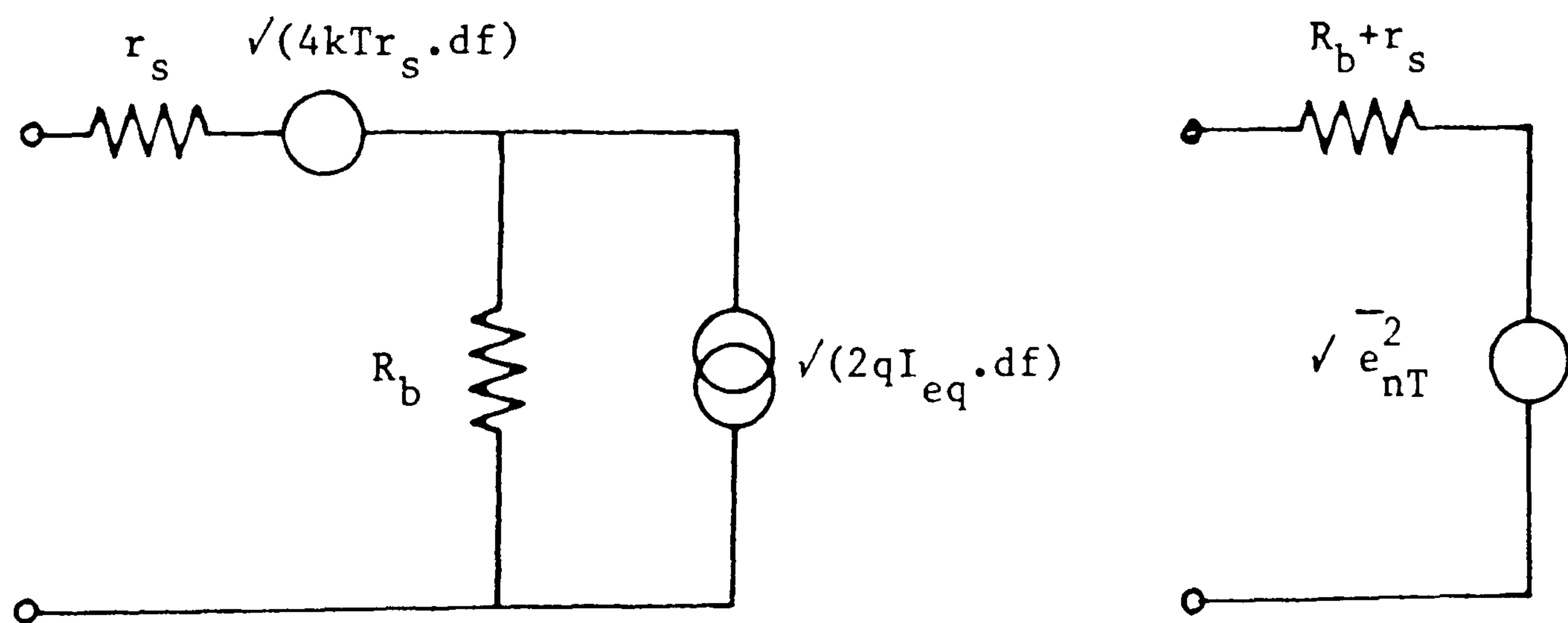

Fig.2.10 Noise sources in a semiconductor barrier device: (a) representation of barrier shot noise and series resistance thermal noise, (b) reduced Thévenin equivalent.

bandwidth, but, at room temperature, it will have negligible effect up to nearly 1.3THz. At cryogenic temperatures, however, it may be necessary to take this correction factor into account; at 3K, for example, the noise power spectrum cannot be modelled as white out to 12GHz. The finite transit times of carriers crossing a boundary will limit shot noise at high frequencies[72].

The fact that many high-frequency communication systems today use angle modulation is only one reason for the importance of phase noise. It is also important because the sources generally used for generating high-frequency signals tend to have large phase noise compared to amplitude noise, although the amplitude noise may be more widespread[74]. Multipliers, for example, can have little effect on amplitude noise (being nonlinear devices they may multiply amplitude noise, or due to limiting may suppress it) but inherently multiply phase noise power density by a factor n^2, where n is the frequency multiplication ratio[74]. Also, amplitude noise in a l.o., for example, may be suppressed by using a balanced mixer. Phase noise has the same origins as amplitude noise, i.e. the random fluctuations already discussed, but here the fluctuations affect the frequency defining characteristics of systems - fluctuations in the bias current of a laser diode, which will vary the emission wavelength, are a good example of this.

In a photodetector there will be noise due to the generation of electron-hole pairs, dependent not only on the average photocurrent but also on the dark current (due to the thermally generated pairs), and any background radiation which will contribute an average direct current. In most photodetectors, where all of the generated carriers can be considered collected, full shot noise can be applied to the photocurrent. (In the case of an optoelectronic mixer down-converting an optical signal,

these noise sources would be present anyway in the photodetector stage of a photodetector-mixer combination. With an optically pumped mixer, these noise sources will be additional to any other sources of l.o. noise.)

2.3.2 Noise parameters

A number of parameters are commonly used to define the noise performance of a device or network.

The noise factor of a network, according to the IRE definition[75], is the ratio of (a) the total noise power per unit bandwidth at a corresponding output frequency available at the output port when the input termination is standard (T_0=290K) at all frequencies (that is, it is 'white'), to (b) that portion of the above engendered at the input frequency by the input termination at the standard noise temperature of 290K.

It has also been defined by Friis[76] as the ratio of the available signal-to-noise ratio (SNR) per unit bandwidth at the signal generator terminals with the input termination at 290K, to the available SNR per unit bandwidth at the output terminals, in which case,

$$F = \frac{S_i / N_i}{S_o / N_o} = \frac{L\,N_o}{k\,T_0} \qquad (2.24)$$

where the second equality results only if the network is linear, that is if the loss, L, is the same for both signal and noise; in this latter case the IRE definition and Friis' definition are equivalent.

One can also consider the output noise spectral density, N_o, to be due to two sources: (a) the input noise generated by the source (N_i=kT_s) and (b) the excess noise

of the network itself ($N_{to}=kT_x$). If the network has loss, L, then,

$$N_o = \frac{kT_s}{L} + N_{to} = \frac{kT_s}{L} + kT_x \qquad (2.25)$$

The excess noise is then often referred to the input terminals - in effect, in this representation, the network is noise-free and a fictitious generator connected across its input terminals produces the observed excess noise. Then,

$$N_o = \frac{1}{L} \cdot k(T_s + T_e) \qquad (2.26)$$

where T_e is called the (effective) input noise temperature of the network,

$$kT_e = LN_{to} \qquad (2.27)$$

T_e is the input source temperature which when connected to a noise-free equivalent of the network would result in the same available output noise power per unit bandwidth, as the actual noisy network when connected to an input source at OK. It is more broadly defined than the noise factor since it does not rely on a specific reference temperature.

Another commonly used parameter, especially for diodes, is the noise-temperature ratio, t_r - also called the noise ratio or the output noise ratio. It is the ratio of the available output noise power of a device or network to thermal noise at the reference temperature, or in terms of noise-temperatures,

$$t_r = T_n / 290 \qquad (2.28)$$

where kT_n is the available output noise power per unit bandwidth.

2.3.3 Noise in mixer diodes

The calculation of the noise generated in a mixer diode will now be described. The concept of an incremental bandwidth is modified since for most systems some practical receiver bandwidth, B, can be specified over which the noise density (noise power per unit bandwidth) is integrated to give the receiver noise. For simplicity the case of an ideal rectifying barrier only will be taken first, and the calculation then corresponds to the standard derivation of noise in p-n and Schottky diodes[77]. The diode characteristic is assumed ideal, so the direct current can be expressed:

$$I = I_s \{ \exp(qV/kT_d) - 1 \} \qquad (2.29)$$

then the mean-square noise current is given by:

$$i_{n,d}^2 = 2qI_s \{\exp(qV/kT_d) + 1 \}.B \qquad (2.30)$$

A useful expression for this noise can be obtained by using the differential conductance of the diode:

$$G = dI/dV = (qI_s/kT_d).\exp(qV/kT_d) \qquad (2.31)$$

which leads to:

$$i_{n,d}^2 = 4kT_dGB - 2qIB \qquad (2.32)$$

In this case, it can be seen that with zero current flowing, i.e. with the diode in equilibrium, the noise reduces to the pure thermal noise expected in a conductance, G.

Many mixer diodes are unlikely to have such ideal I-V characteristics, this is certainly the case for the tunnelling contacts described in Chapters 4 and 5, and in such cases the standard derivation, above, is of limited value.

If the diode equation contains an ideality factor, n, as has been used earlier in this chapter (eqn.(2.12)), then the above analysis can be modified by replacing kT_d by nkT_d. In this case from eqns.(2.30) and (2.31), the mean-square shot noise current could be written:

$$i_{n,d}^2 = 2nkT_dGB \qquad (2.33a)$$

The thermal noise mean square current from the conductance, G, would be:

$$i_{n,T}^2 = 4kT_dGB \qquad (2.33b)$$

The above can be related so that the output noise power per unit bandwidth is given by:

$$N_o = nkT_d/2 \qquad (2.33c)$$

which can be seen to reduce to half thermal noise for the special case, n=1. Such a device therefore acts as a 'sink' to noise power.

If the non-ideal characteristic is assumed to be of the form[78]:

$$I = I_s \{\exp(qV/nkT_d) - \exp[(n^{-1}-1)qV/kT_d]\} \qquad (2.34)$$

then following similar arguments to those used to derive (2.32), the mean-square noise current is given by:

$$i_{n,d}^2 = 4kT_dGB - (2/n - 1).2qIB \qquad (2.35)$$

where I is positive for forward bias and negative for reverse bias. When n=1 it can be seen that eqn.(2.35) reduces to eqn.(2.32) (as eqn.(2.34) reduces to eqn.(2.29)).

For near ideal diode characteristics ($n \to 1$), at significant forward bias $G \simeq qI/kT$ and so the mean-square noise current will be given by 2kTGB, or, again, half thermal noise. In fact, from (2.35) the noisiest barriers would be those which have near symmetrical I-V characteristics ($n \simeq 2$), and the noise would then approach thermal noise. Barriers which conduct current in the 'reverse' direction only ($n \to \infty$) would have noise characteristics similar to the ideal diode. All of the above cases are rather idealised since many diodes have characteristics which cannot be fitted using single values of n; that is n, in the most general case, is voltage dependent itself.

2.3.4 Noise in optoelectronic mixer diodes

The optoelectronic mixers described in this work are basically types of photodetecting barrier for which, if it is assumed that shot noise dominates, the mean-square noise current can be modelled using eqn. (2.23). Applying full shot noise to the barrier dark current, I_g, and the optically generated current, I_{ph}, and assuming the two are uncorrelated so that their power spectra may be added, the

mean-square noise current is:

$$i_{n,b}^2 = 2q(I_g + I_{ph})B = 2qI_{eq}B \qquad (2.36)$$

If the I-V characteristic can be modelled by the double exponential diode equation (2.34), then the noise may also be given by the mean-square noise current:

$$i_{n,b}^2 = 4kT_dGB - (2/n - 1)2qI_gB + 2qI_{ph}B \qquad (2.37)$$

Not all diodes can be approximated by the double exponential relationship (see Chapter 4), and for the purposes of this analysis eqn.(2.36) is easier to use. However, the barrier current should actually consist of both the forward and reverse current flows which make up the total current. In equations (2.36) and (2.37) the additional contribution to the mean-square noise current of shot noise associated with the photocurrent is clearly expressed.

A useful relationship can be derived if the shot noise mean-square current due to the photocurrent is related to the thermal noise that would be present in the device, by using an effective noise-temperature ratio, t' (not the actual noise-temperature ratio as defined in section 2.3.2). Then putting

$$2qI_{ph}B = 4k(t'.T_d)GB$$

the device mean-square shot noise current defined in a similar way to eqn.(2.33b) is:

$$i_{n,b}^2 = 2kT_dG(n + 2t')B \qquad (2.38)$$

The equivalent expression to eqn. (2.33c) for the output noise spectral density is:

$$N_o = \frac{(n + 2t')}{2} kT_d \qquad (2.39)$$

Reactive parasitics will not contribute any noise but any diode series resistance may have to be taken into account. The equivalent noise circuit of the diode is shown in Fig. 2.10; for convenience a voltage source representation for the thermal noise contribution of the series resistance is used:

$$e_{n,r}^2 = 4kT_d r_s B \qquad (2.40)$$

The mean-square noise voltage of the Thévenin equivalent of the noise sources in the diode can be used to characterise the device noise:

$$e_{n,T}^2 = 2qI_{eq}R_b B + 4kT_d r_s B \qquad (2.41)$$

2.3.5 Mixer noise factor

As has been seen in the linear mixer theory of section 2.2.3, the mixer can be regarded as having a number of ports, one for each frequency of interest, although the physical terminals for many of these frequencies may be the same. The equations for the noise factor etc. derived in section 2.3.2 are easily applicable to networks with one input port and one output port. For networks which have multiple 'responses' (such as mixers) the noise at an output port may be due to input noise at many other ports, any number of which may carry an input signal. In the typical down-convertor case, only one input port carries

the signal, but noise at the other sidebands will be converted to the output i.f. This noise will consist of the thermal noise of the terminations at these frequencies, and the excess noise of the diode being reflected back from these terminations and being down-converted. A full analysis of these effects is a very complicated problem since the conversion losses from each of the sideband frequencies to the output frequency, and the terminations at each sideband must be known (see Appendix C). There is also a further complicating effect: the shot noise at each sideband frequency will itself be modulated by the l.o. and will therefore give modulation products at all of the other sideband frequencies. These modulation products will also be converted to the i.f. but their individual outputs will obviously be correlated. The properties of this modulated shot noise have been investigated by Dragone[79] and van der Ziel[80], among others. Down-converted thermal noise, originating in the diode series resistance, will have no correlated components if it is assumed that the l.o. does not modulate r_s (this may not always be true).

An idea of the noise considerations for a mixer can be gained, however, if a number of simplifying assumptions are made. The first is to assume that shot noise dominates and ignore the diode series resistance; further, the diode capacitance is assumed to be constant, so parametric effects can be neglected. Correlation between the shot noise components is also neglected. Then the output noise per unit bandwidth, if real power can flow at R input sideband ports (including the signal port) is

$$N_o = k \frac{(n + 2t')T_d}{2} \left(1 - \sum_{i=1}^{R} 1/L_i\right) + \sum_{i=1}^{R} T_{si}/L_i \qquad (2.42)$$

where L_i is the conversion loss from sideband i to the output frequency, and T_{si} is the temperature at the port for sideband i (in many cases $T_{si}=T_s$ for i=1,...,R).

By reactively terminating more frequencies the noise from these frequencies can be ignored. In a typical situation, that of a broadband mixer, as a further simplification only the signal (at ω_1), image (ω_{-1}), and i.f. (ω_0) may be considered resistively terminated. The output noise per unit bandwidth is then:

$$N_o = k \{ [(n + 2t').T_d/2](1 - 1/L_1 - 1/L_{-1}) + T_s(1/L_1 + 1/L_{-1}) \} \qquad (2.43)$$

where L_1 is the conversion loss from signal to i.f., and L_{-1} is that from image to i.f.

The noise factor for the mixer, called a single sideband noise factor since the signal is in only one sideband, is then defined:

$$F_{SSB} = L_1 N_o / kT_O =$$

$$((n+2t')/2)(T_d/T_O)(L_1 - 1 - L_1/L_{-1}) + (1 + L_1/L_{-1}) \qquad (2.44)$$

The ratio in the first set of parentheses in the above equation can be defined as another effective noise-temperature ratio, t" (still not t_r), which relates the noise generated in the device to thermal noise at the reference temperature. It could also be derived from equation (2.41) by dividing it by the mean-square noise voltage from a source of resistance (R_b+r_s), where $R_b=1/G$, and at temperature 290K.

If $L_1=L_{-1}=L$, then

$$F_{SSB} = 2 + t''.(L - 2)$$

In the above case, the minimum loss in the absence of parametric effects is L=2; it can be seen that then $F_{SSB}=2$, a degradation in the SNR of 2, which must be intuitively correct since the noise from two sidebands is available, whereas the signal is only available in one. In the above equations for both the mixer noise factor and the output noise generally, it can be seen that the shot noise due to the photocurrent will directly increase the mixer noise.

2.3.6 Mixer noise-temperature ratio

In general, the noise factor of the mixer on its own is not that important a parameter due to the conversion loss of the mixer. This loss means that the noise factor of the following network, the i.f. amplifier, will be very significant in determining the overall noise factor of the receiver. The validity of the above statement comes directly from the cascade formulae for noise-temperatures and noise factors[73]. Assuming the i.f. amplifier has sufficient gain, subsequent receiver stages will have negligible effect on the noise performance.

Application of the cascade formula leads to the commonly-used expression for the single-sideband noise factor of a broadband receiver:

$$F_R = L_1 (t_r + F_{IF} - 1) \tag{2.45}$$

where t_r is the noise-temperature ratio of the mixer, given by:

$$t_r = T_n / T_0 = N_o / kT_0 \tag{2.46}$$

Using the terminology of eqn.(2.43) this may also be written:

$$t_r = [\ (n/2 + t').(T_d/T_0).(L_1 - 1 - L_1/L_{-1}) + (1 + L_1/L_{-1})\ ].\ (1/L_1) \qquad (2.47)$$

The dependence of t_r on the conversion at both signal and image frequencies can be seen; in a more general case t_r will be dependent on the terminations and the conversion at other sideband frequencies. Again, the optical current generation has a direct effect, increasing the noise-temperature ratio compared to a conventional mixer. According to eqn.(2.45), this will increase the noise factor, although the extent to which the performance of a receiver employing the device will be detrimentally affected will depend on how low the conversion loss is, and on the performance of the low-noise i.f. amplifier. Theoretical results for the performance of a tunnelling optically pumped mixer, using the above theory and conversion loss predictions from a frequency domain model, are described in Chapter 5.

2.4 Chapter summary

In this chapter the theory which will be used to examine the performance of optically pumped mixer devices has been outlined. The photocurrent generation occuring in such devices has been discussed and the effects of the contributions to this current from two main sources, carriers generated within the barrier region and those generated outside, examined. The frequency response of optically pumped mixer devices depends on three main

factors: the illumination wavelength, the barrier width, and (if the diffusion current contribution is significant) the minority-carrier diffusion length in the semiconductor.

A summary of analytic mixer theory has been given which is useful in demonstrating the relationship of parameters such as the conversion loss (obtained from a linear analysis) to the device nonlinear characteristics, which are used to calculate the equivalent network of the device under l.o. excitation. Extension of this simplified analysis to optically pumped mixing is straightforward.

Finally, the types of noise that occur in receiving systems have been discussed and the noise generated in nonlinear diodes investigated. An extension of mixer noise analysis to optically pumped mixers clearly shows the excess shot noise contribution of the photocurrent.

CHAPTER THREE

COMPUTER MODELLING OF OPTICALLY PUMPED MIXERS

3.1 Introduction 89

3.2 Overview of computer models 91

3.2.1 Microwave mixer models 91

3.2.2 Optically pumped mixer models 94

3.3 Nonlinear analysis in the frequency domain 95

3.3.1 Method and modifications implemented 95

3.3.2 Calculation sequence 97

3.4 Nonlinear analysis in the time domain 101

3.4.1 Basic theory and equations 101

3.4.2 Calculation sequence 104

3.4.3 Discussion of further modifications 107

3.5 Performance of frequency domain model 109

3.5.1 Required input data 109

3.5.2 Performance and output 111

3.6 Performance of time domain model 112

3.6.1 Required input data 112

3.6.2 Performance and output 115

3.7 Chapter summary 118

3.1 Introduction

In this chapter, the models of optically pumped mixers developed for use in computer programs will be described. These models enable more accurate predictions to be made than would be the case with the analytic models of section 2.4, and predict the mixer performance under different external bias and embedding network conditions. The basic problem for an optically pumped mixer model can be described by the circuit of Fig.3.1; the diode is connected to an external bias via some embedding network, with the diode itself being represented by a parallel combination of a nonlinear resistance, a nonlinear capacitance, and an illumination-dependent (and bias-independent) current generator - this model for the optically generated current has been described in sections 1.3 and 2.1.

In the analytic theory of section 2.2 it was shown how mixer analyses are usually divided into two parts, a large-signal analysis in which the current, voltage and admittance of the device over a l.o. cycle are found, and a small-signal analysis in which the Fourier components of these waveforms are used to derive parameters such as signal and i.f. port impedances and the conversion loss. Considerable simplifications are required in analytic models, the most important being the simple diode I-V relationship required and the assumption of a sinusoidal driving voltage (representing the local oscillator) across the diode. If the harmonics of the l.o. are not presented with a perfect short circuit, which will always be the case in reality, the harmonic currents generated in the nonlinear diode flowing through the embedding network will cause harmonic voltages to impinge on the diode, thus making the diode voltage non-sinusoidal. Saleh has shown

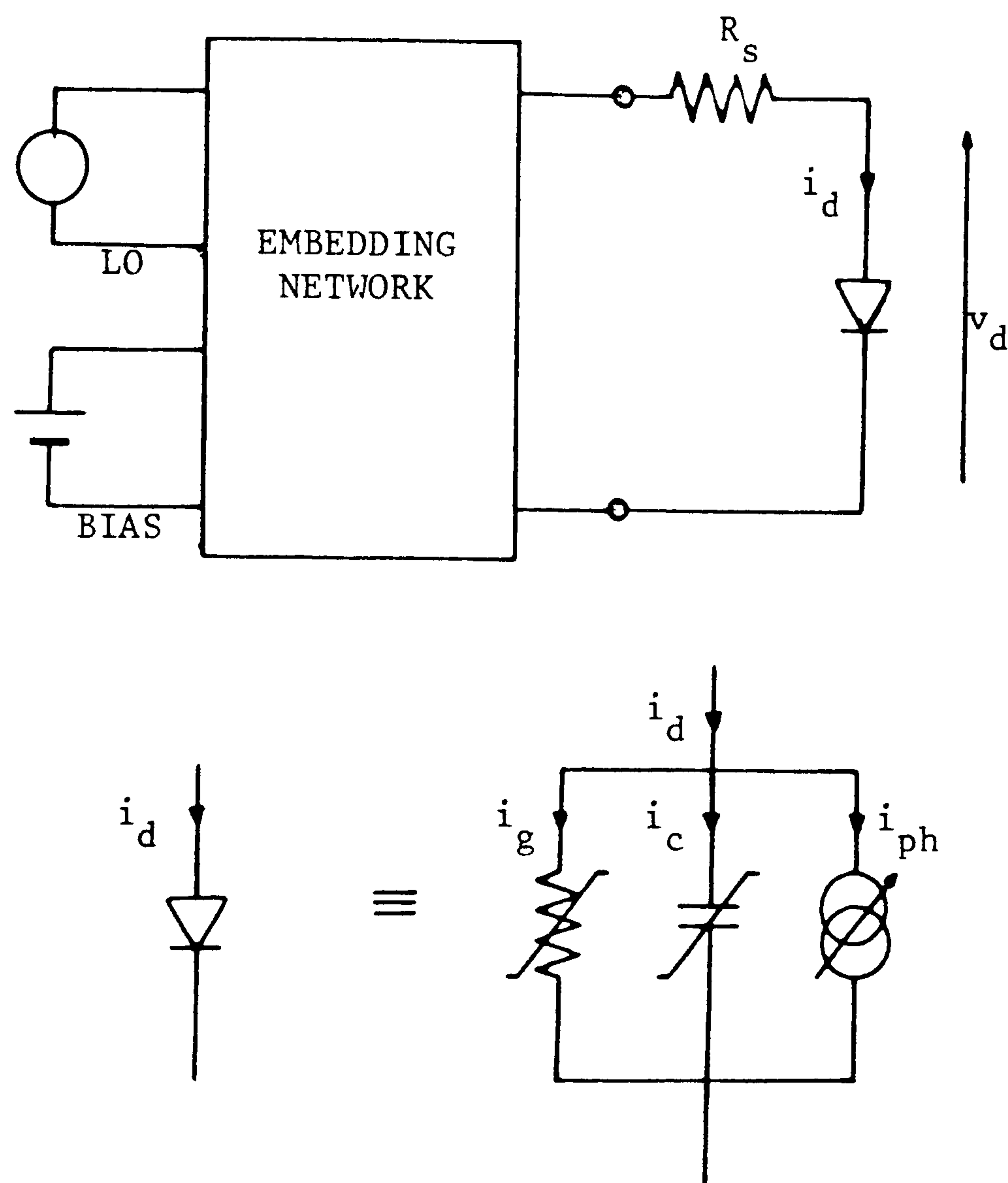

Fig.3.1 Basic circuit for large-signal analysis of optically pumped mixer problem

that even if the power in these harmonics is low, there can be no certainty that the voltage variation is not significant[71]; a significant voltage variation will affect the conductance and capacitance waveforms of the diode and so affect the admittance matrix used in the linear analysis. In order to take into account the effect of the harmonics of the l.o., computer solutions of the mixer problem have been found necessary.

3.2 Overview of computer models

3.2.1 Microwave mixer models

The nonlinear analysis of Egami[81] is performed in the frequency domain. The technique is to balance the amplitudes of the harmonics of the voltage and current at the diode with those at the embedding network, the solution being found by a Newton-Raphson iterative procedure. This will be explained in greater detail in section 3.3. Egami did not consider the diode nonlinear capacitance in his analysis; Gwarek has shown that severe convergence problems emerge if it is considered[82].

Gwarek has used a time domain analysis to determine the diode voltage and current waveforms[82]. The embedding network consists of a simple lumped-element network in series with a string of input voltage-dependent voltage sources, one at each harmonic of the l.o. frequency, see Fig.3.2. The embedding network is thus able to simulate any complex network as it appears at the l.o. frequency and its harmonics. The method is very economical of computer time. However, with randomly generated embedding impedances Schüppert found divergence in over 40% of cases[83]; the performance should be better than this with

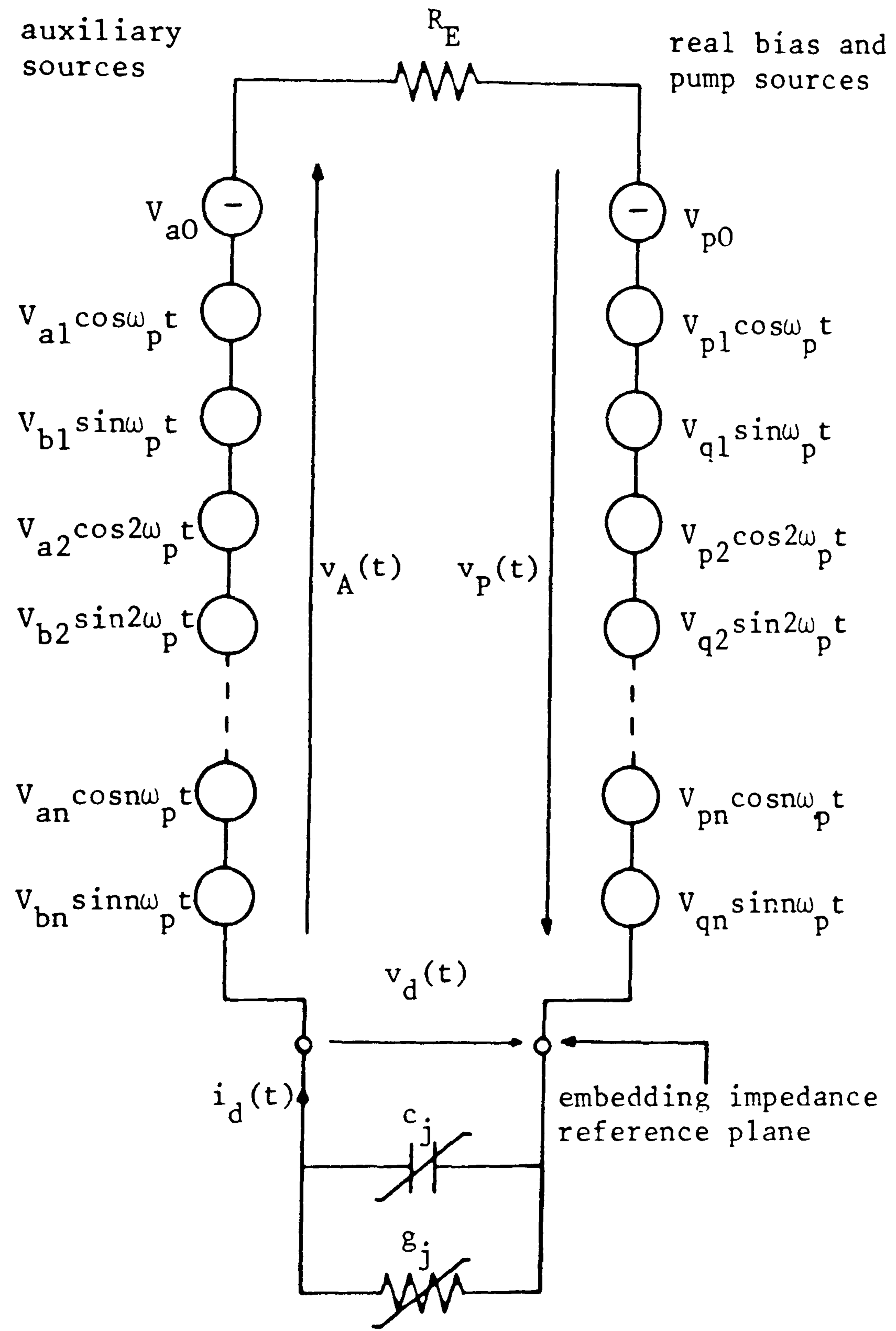

Fig.3.2 Formulation of the large-signal problem in Gwarek's analysis[82].

realistic impedances, but these results do suggest significant convergence problems.

The nonlinear analysis of Kerr[84] uses a multiple reflection technique, in which a transmission line of electrical length equal to an integer multiple of l.o. wavelengths (and thus l.o. harmonic wavelengths) is inserted between the nonlinear diode elements and the linear circuitry: the steady-state solution is thus unaffected. The technique allows the solution of the two less complicated problems on either side of the line (almost) independently - this is explained in greater detail in section 3.4.

Hicks and Khan[85] have proposed a voltage-update method which has a unit degree of memory in that the values from the iteration before the one currently being updated are brought into the calculation. The solution is achieved slightly faster than with Kerr's method, but it depends on a suitable degree of involvement of the previous iteration being specified. No analytic expression for this degree of involvement is given and it must be found by trial and error for individual problems; this is obviously not suitable for unknown mixer circuits.

Schüppert[83] has modified Gwarek's method and obtained convergence in 99% of cases with randomly generated embedding impedances, and in all cases with the realistic impedances he has used. The mean number of iterations required is also substantially reduced, and is now more than an order of magnitude less than that required in Kerr's analysis.

3.2.2 Optically pumped mixer models

The remainder of this chapter describes the optically pumped mixer models actually employed, and presents some predictions from them.

The nonlinear analyses described in the previous section, and such analyses generally, are concerned with electrically pumped microwave mixers using conventional diodes; modifications are required to model optically pumped mixers. The first and most important modification is the modelling of the optically generated current - this has been done by using the illumination-dependent and bias-independent current generator model described in section 2.1. A second modification is required in that the simple I-V relationship assumed for the diode in most mixer analyses, including those described above, will not necessarily apply for optoelectronic mixers - this is certainly the case for the tunnelling contacts described in Chapters 4 and 5. The diode I-V characteristic must be stored as a function in the mixer computer program.

Two nonlinear large-signal analyses have been developed. The first is a frequency domain model based on that of Egami[81]. Since such a model is very slow when a large number of l.o. harmonics are considered, and cannot be expected to give very accurate predictions because it ignores the nonlinear diode capacitance, the model implemented is a simple frequency-independent analysis in which all of the l.o. harmonics are assumed short-circuited and only the effect of the diode nonlinear resistance is taken into account.

The second large-signal analysis is a time domain model based on that of Kerr[84]. The computer program had been almost completed by the time a clear description of Schüppert's analysis[83] was published; writing and testing a completely new program would have been very time

consuming. However, it is likely that Schüppert's microwave mixer model could be easily adapted to the modelling of optically pumped mixers, and bring similarly improved performance. Kerr's method was preferred to those of Gwarek[82], and Hicks and Khan[85], due to the convergence problems of the former, and the trial and error procedures required in the latter. A number of modifications are required to the method and these are described in section 3.4.

The linear analysis used is the same in both the above computer programs, although it is in a much simplified form in the first case. It is due to the analysis of Held and Kerr[86]. Since the linear analysis even for an optically pumped mixer relates only electrical components, especially those of the input signal frequency and output intermediate frequency, no modifications are required to the linear analyses used for microwave mixers. A summary of the linear analysis used is presented in Appendix B.

3.3 Nonlinear analysis in the frequency domain

3.3.1 Method and modifications implemented

The frequency domain model used is based on the large-signal analysis of Egami[81]. The equivalent circuit for the problem to be solved is shown in Fig.3.3. The diode also has series resistance, junction capacitance and lead inductance, but assuming a constant junction capacitance and a simple load network, these can be modelled in the load admittances representing the embedding network in Fig.3.3. In less trivial cases the embedding network may have to be modelled by a set of admittances, one at each frequency considered, rather than the LCR circuit in Fig.3.3. The frequency domain model requires the diode

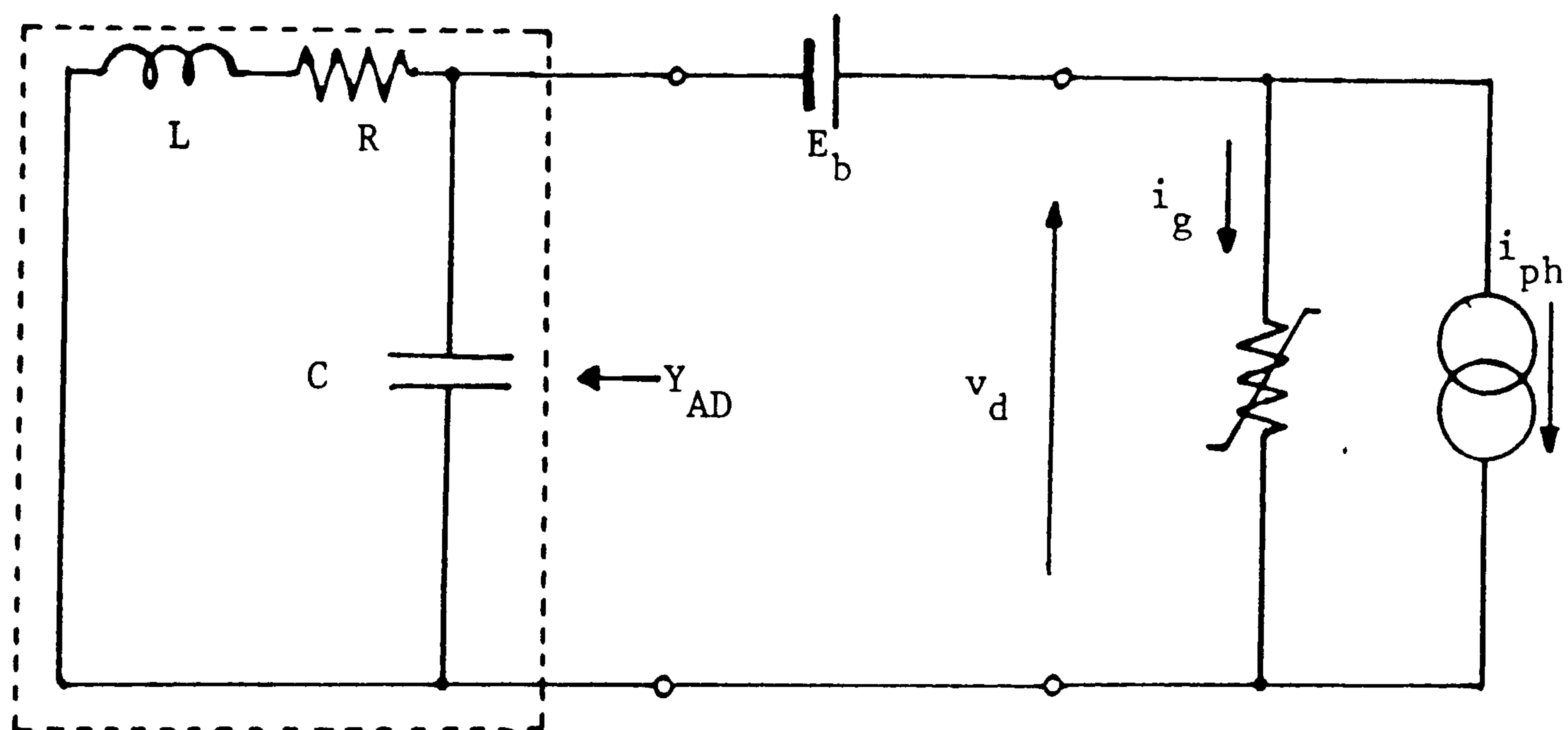

Fig.3.3 Equivalent circuit for frequency domain large-signal analysis.

capacitance to be approximated by a constant value. However, convergence is slow when reactive components and many local oscillator harmonics are modelled. As mentioned in section 3.2.2, an important modification has been used in the frequency domain model actually implemented: only the components at the d.c. and l.o. frequencies have been taken into account. Also, it has been used as a frequency-independent analysis with the admittance network replaced by a single conductance. The results, therefore, can only give a general idea of the mixer behaviour rather than precise simulations - however, since the nonlinear junction capacitance must be ignored this would have been very much the case anyway. The advantage of the frequency domain model has been that many runs have been performed very easily and quickly and from the results much information has been gained about the behaviour of optically pumped mixers - this will be discussed further in section 3.4 and Chapters 5 and 6. In the description of the frequency domain model that follows, generality has been preserved in the use of an admittance network and an unspecified number of l.o. harmonics.

3.3.2 Calculation sequence

Referring to Fig.3.3, at the diode junction, the diode voltage, v_d, and the current through the barrier conductance, i_g, are related by the diode I-V characteristic:

$$i_g = f (v_d) \tag{3.1}$$

The embedding network also specifies a condition which must be satisfied:

$$i_g + i_{ph} + Y_{AD} (v_d - E_b) = 0 \tag{3.2}$$

where i_{ph} is the optically generated current, Y_{AD} is the admittance of the embedding network seen by the diode, and E_b is the external bias.

The instantaneous values of voltage and current can be represented by Fourier series, where the Fourier components will be denoted by upper-case letters. For example, the diode voltage can be written:

$$v_d = \sum_{n=-\infty}^{\infty} V_{d,n} \exp (jn\omega_p t) \qquad V_{-n} = V_n^* \qquad (3.3)$$

where ω_p is the l.o. frequency. So, by using Fourier coefficients and balancing the harmonic voltages and currents, assuming the embedding network admittance at each frequency is known, (3.2) can be modified to:

$$I_{g,n} + I_{ph,n} + Y_{AD,n} (V_{d,n} - E_{b,n}) = 0 \qquad (3.4)$$

$$\text{where} \qquad E_{b,n} = E_b \quad , n = 0$$

$$= 0 \quad , n \neq 0$$

The nonlinear analysis is performed using a Newton-Raphson iterative procedure; basically this method solves for a value x of a function f(x)=0 by iteratively minimising the function - this is done according to[87]:

$$x \Rightarrow x + f(x)/f'(x)$$

In the nonlinear analysis used here, a function, F, at each harmonic is minimised:

$$F_n = I_{g,n} + I_{ph,n} + Y_{AD,n} (V_{d,n} - E_{b,n}) \qquad (3.5)$$

The differentials of the above are also required:

$$D_n = F'_n = d/dv_d(I_{g,n}) + Y_{AD,n} \qquad (3.6)$$

(The D values are thus calculated from the Fourier coefficients of the differential (slope) conductance and the embedding network admittance at each harmonic.)

Using the Newton-Raphson method, the diode voltage after each iteration becomes:

$$V_{d,n} \Rightarrow V_{d,n} - F_n / D_n \qquad (3.7)$$

The diode current and differential conductance are calculated for the next cycle and the solution is obtained when a convergence test is satisfied:

$$| F_n / D_n | \leqslant \varepsilon \qquad (3.8)$$

for all harmonics considered, where ε is an accuracy parameter.

A flow-chart summarising the calculation sequence is shown in Fig.3.4.

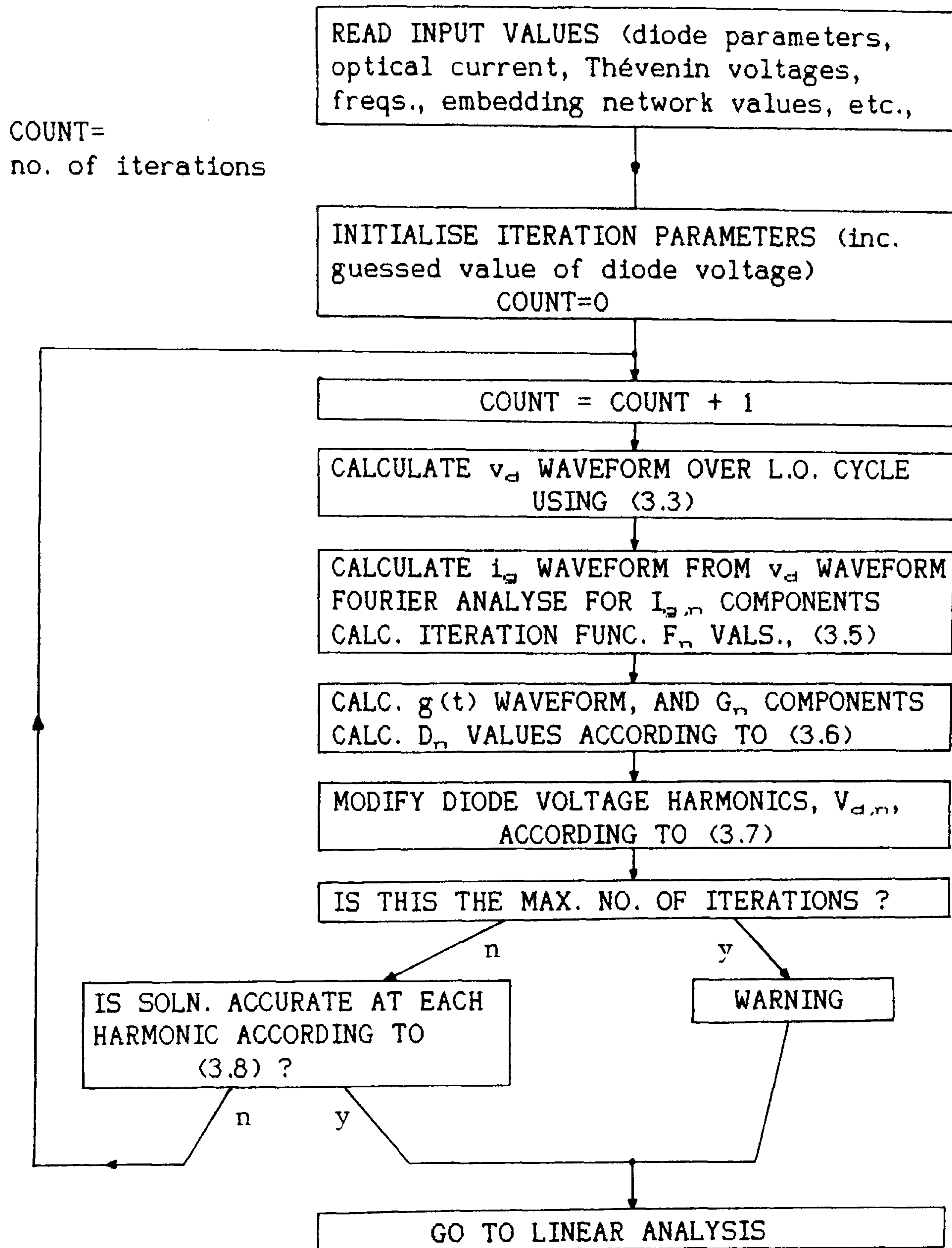

Fig.3.4 Flow-chart showing calculation sequence in frequency domain large-signal analysis. (See text for meaning of symbols and numbered equations.)

3.4 Nonlinear analysis in the time domain

3.4.1 Basic theory and equations

The time domain nonlinear analysis used is based on that of Kerr[84], as implemented by Siegel and Kerr[88]. With this method, the basic problem, the circuit of Fig.3.1, is modified by the insertion of a transmission line between the nonlinear diode barrier and the linear embedding network and series resistance, see Fig.3.5. If the transmission line (assumed lossless) is made an integral number of half-wavelengths long at the l.o. frequency, it will have no effect on the steady-state solution. Also, the networks on either side of the line can alternately reach equilibrium with it if the line is made long enough, that is, if it provides a sufficient time-delay. The actual length of the line, therefore, is not important and it is merely assumed that: 1) the line is long enough to provide a sufficient time delay and 2) it is an integral number of half-wavelengths long. With these assumptions, then, for each of the propagating waves $e_R(x,t)$ and $e_L(x,t)$ there is then no quantitative difference between their values at x=0 and x=L in Fig.3.5; i.e. $e_R(0,t)=e_R(L,t)$ and $e_L(0,t)=e_L(L,t)$. Just incident and reflected voltages may be specified and the problem reduced to solving the two circuits of Fig.3.6 - circuit (a) is solved in the frequency domain, (b) in the time domain.

The theory of the multiple reflection technique is given in ref[84]; here the relevant results will be stated together with their application to the optically pumped mixer problem. It should be noticed that in Figs.3.5 and 3.6 the bias and embedding network at d.c., and the electrical l.o. and embedding network at the l.o. frequency have been replaced by their Thévenin

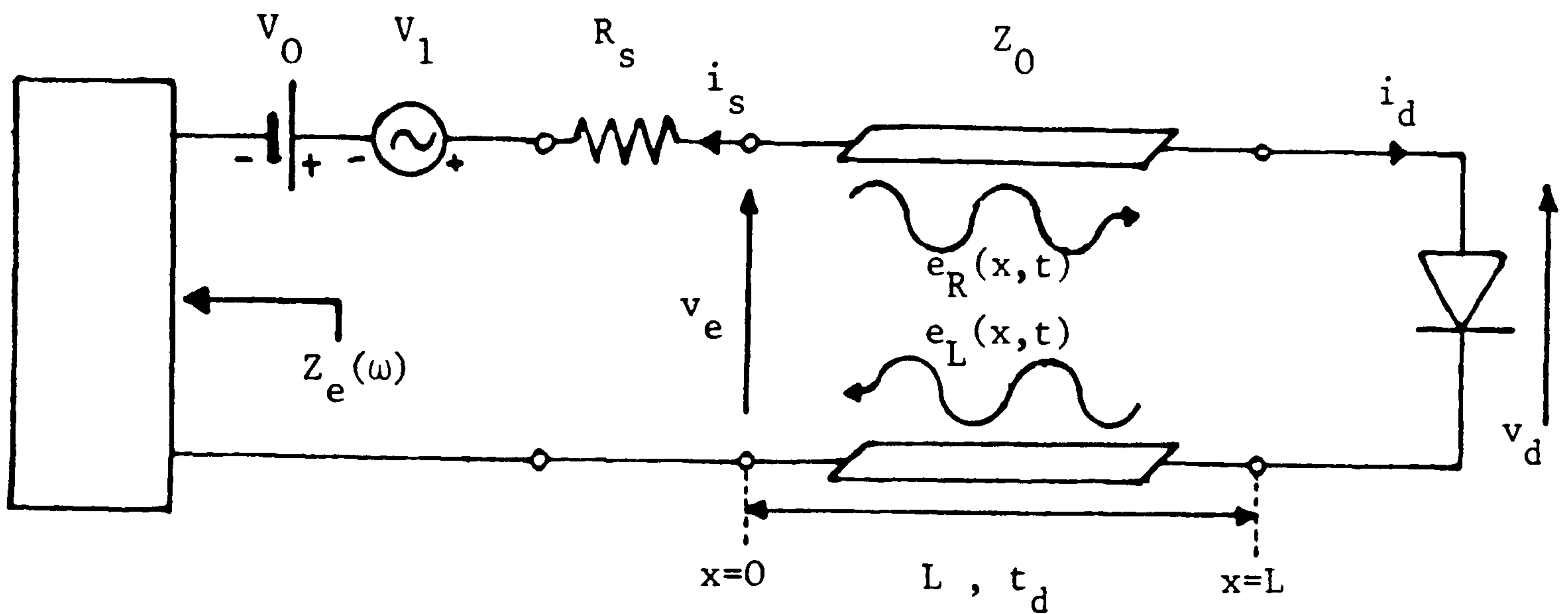

Fig. 3.5 Equivalent circuit for the multiple-reflection transmission line model used in the time-domain analysis. (After ref.[84])

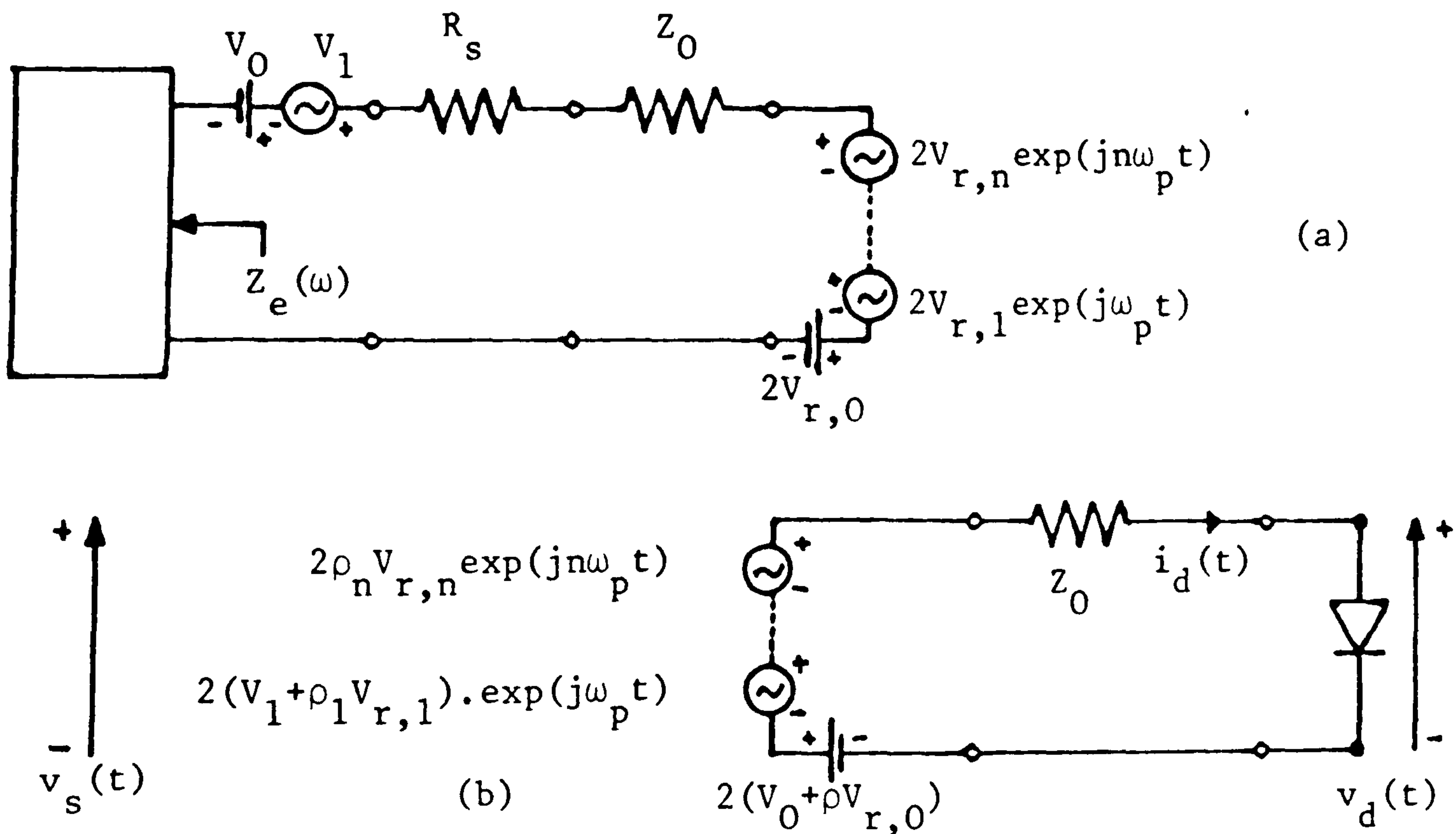

Fig. 3.6 Separate circuits formed in the time domain model analysis. Circuit (a) is solved in the frequency domain, (b) in the time domain (after ref.[84])

equivalents. Although not required, the voltage source at the l.o. frequency has been preserved to increase versatility; it can be simply turned off when not required. In Fig.3.5, the components of the Thévenin equivalent bias and l.o. voltages actually propagated down the line, V_0' and V_1', are given by:

$$V_0' = V_0 Z_0 / (Z_e(0) + R_s + Z_0) \tag{3.9a}$$

$$V_1' = V_1 Z_0 / (Z_e(\omega_p) + R_s + Z_0) \tag{3.9b}$$

and the reflection coefficients ρ_n, at each harmonic are:

$$\rho_n = \frac{Z_e(n\omega_p) + R_s - Z_0}{Z_e(n\omega_p) + R_s + Z_0} \tag{3.10}$$

where $Z_e(\omega)$ is the embedding impedance at angular frequency, ω; R_s is the diode series resistance; and Z_0 is the transmission line characteristic impedance.

The diode voltage and current can be represented by Fourier series:

$$v_d(t) = \sum_{n=-\infty}^{\infty} V_{d,n} \exp\,(jn\omega_p t) \qquad V_{d,-n} = V_{d,n}^*$$

$$(3.11)$$

$$i_d(t) = \sum_{n=-\infty}^{\infty} I_{d,n} \exp\,(jn\omega_p t) \qquad I_{d,-n} = I_{d,n}^*$$

If Fourier coefficients are similarly defined for the incident and reflected voltages at the diode, $V_{i,n}$ and $V_{r,n}$, the following equivalent equations can be written:

$$V_{i,n} + V_{r,n} = V_{d,n} \qquad (3.12a)$$

$$(V_{i,n} + V_{r,n}) / Z_0 = I_{d,n} \qquad (3.12b)$$

where the coefficients $V_{i,n}$ are also equivalent to the Fourier coefficients of the right-propagating wave $e_R(x,t)$ at x=0 and x=L as stated previously, and similarly for $V_{r,n}$ and $e_L(x,t)$.

With the above equations a summary of the solution cycle can be given; for clarity, this is also given in flow-chart form in Fig.3.7.

3.4.2 Calculation sequence

From the equivalent incident wave $v_s(t)$ in Fig.3.6(b) the diode voltage is calculated from the diode characteristic equations:

$$i_d = i_g + i_c + i_{ph} \qquad . (3.13)$$

where the currents through the barrier conductance and capacitance and the photocurrent, i_g, i_c, and i_{ph}, respectively, are given by:

$$i_g = f_1(v_d) \ , \quad i_c = c_j(dv_d/dt) \ , \quad c_j = f_2(v_d)$$

$$\text{and} \quad i_{ph} = -I_{ph,0} - I_{ph,1}\cos(\omega_p t)$$

where f_1 and f_2 are defined functions, c_j is the barrier capacitance, and $I_{ph,0}$ and $I_{ph,1}$, are the d.c. and a.c. components of the photocurrent. As it enters the analysis in the time domain the photocurrent can, in fact, be modelled using any function of time over an l.o. cycle. In the program, the function expressing the I-V

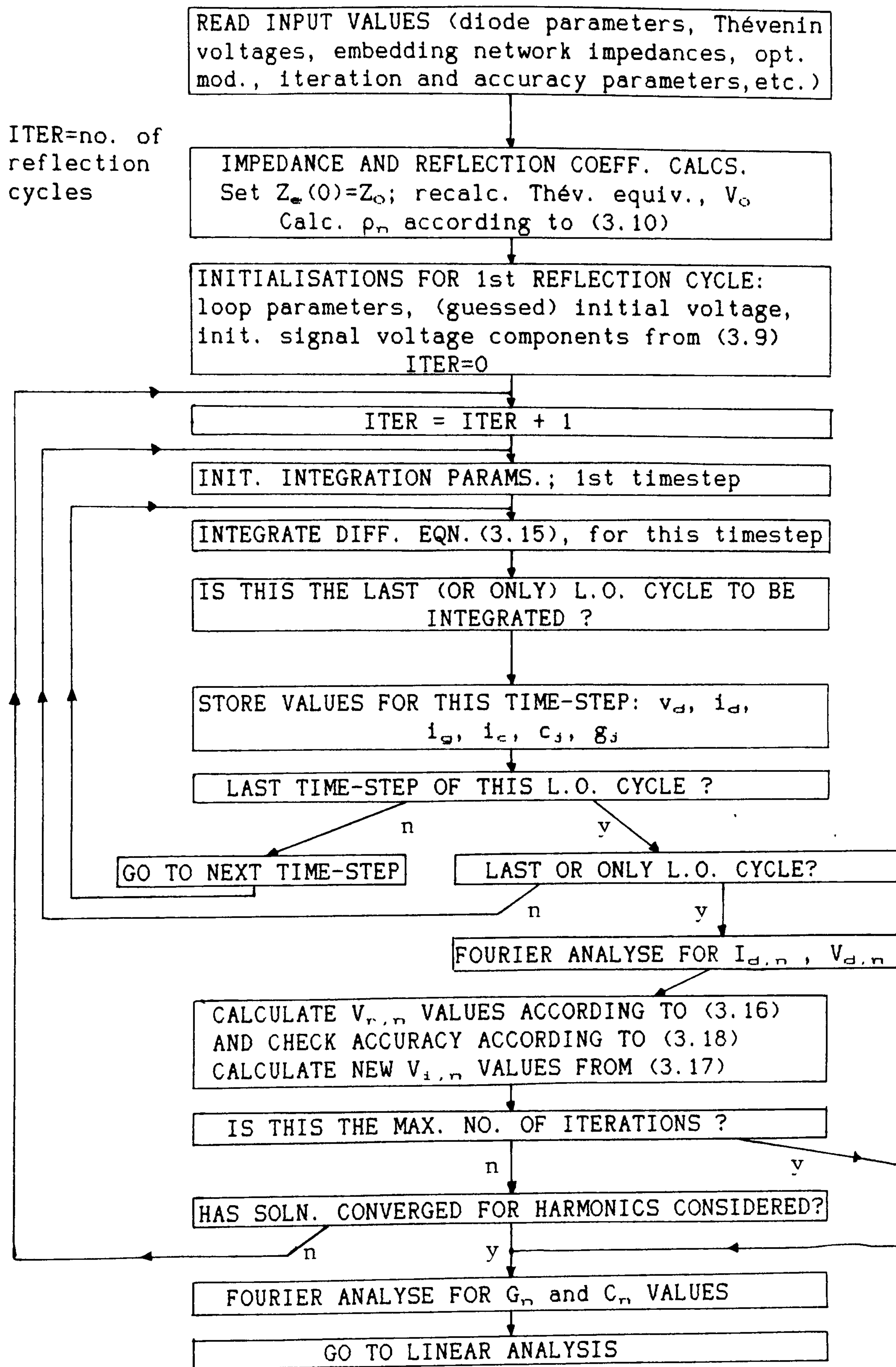

Fig.3.7 Flow-chart showing calculation sequence in time domain large-signal analysis.

characteristic also has as arguments normalised time (the point in the l.o. cycle for which the solution is required) and photocurrent parameters. It therefore gives the value of $i_g + i_{ph}$. In section 5.2.3 the parameters used to describe a pulsed waveform will be discussed.

From Fig.3.6(b) it can be seen that:

$$v_s(t) = v_d(t) + i_d(t).Z_0 \qquad (3.14)$$

and by substituting for $i_d(t)$ from eqn.(3.13) this gives the differential equation:

$$dv_d/dt = [(v_s(t)-v_d(t))/Z_0 - i_g(t) - i_{ph}(t)]/c_j(t) \qquad (3.15)$$

The above differential equation is solved in the time domain for $v_d(t)$ by integrating using a Runge-Kutta method. From $v_d(t)$, values of $i_g(t)$ and $c_j(t)$ over a l.o. cycle can be found. Reflected voltage components are calculated using the Fourier coefficients of the diode voltage and current (see eqn.(3.12)):

$$V_{r,n} = (V_{d,n} - I_{d,n}Z_0) / 2$$

$$\text{or} \qquad V_{r,n} = (V_{d,n} - V_{i,n}) \qquad (3.16)$$

After these waves are themselves reflected back by the embedding network, the new incident waves on the diode can be calculated according to:

$$V_{i,n} = V'_{i,n} + \sum_{n=-\infty}^{\infty} \rho_n \, \Delta V_{r,n} \exp(jn\omega_p t) \qquad (3.17)$$

where $V'_{i,n}$ are the Fourier components of the incident wave from the previous reflection cycle, and $\Delta V_{r,n}$ are the changes in the Fourier components of the reflected waves from the previous cycle.

The cycles continue until convergence is achieved; this is defined by a convergence parameter, δ, for each harmonic of the l.o., for n>1:

$$\delta(n) = \{ |V_{d,n}|/|I_{d,n}| \ / \ |Z_e(n\omega_p) + R_s| \} - 1 \qquad (3.18)$$

and convergence is considered achieved when $\delta(n) \leqslant \varepsilon$ for all n>1 considered, where ε is an accuracy parameter.

According to the above calculation the final solution for the waves set up on the transmission line can be given by:

$$v_i(t) = \frac{Z_0 \ V_0}{Z_e(0) + R_s + Z_0} + \frac{Z_0 \ V_1 \exp(j\omega_p t)}{Z_e(\omega_p) + R_s + Z_0} + \sum_{n=-\infty}^{\infty} \rho_n \ V_{r,n} \ \exp(jn\omega_p t) \qquad (3.19)$$

3.4.3 Discussion of further modifications

Apart from the important modifications concerning the photocurrent and the diode I-V characteristic already discussed, further modifications are required to the program as implemented by Siegel and Kerr[88], because of the assumptions used. In their program implementation, Siegel and Kerr[88] have made the embedding impedances at d.c. and the l.o. frequency, ω_p, equal to the transmission line impedance to speed up execution. The d.c. bias voltage across the diode is specified so that the solution is unaffected as long as the Thévenin equivalent of the embedding network at d.c. provides this bias at the diode.

The Thévenin equivalent of the l.o. is used to provide a specified rectified current through the diode. An initial guess of the l.o. voltage, V_1, is used and after a certain number of l.o. cycles V_1 is adjusted up or down, so as to give the desired rectified current. When this is achieved the reflection cycle iterations continue until convergence is achieved.

For the optoelectronic mixer model the nonlinear diode barrier consists of an optically controlled current generator as well as barrier conductance and capacitance, Fig.3.1. In its implementation some differences in defining the bias voltage, etc., are also required. In a discussion of optoelectronic mixer performance it is unlikely that the rectified current would be specified as an important parameter. Although finding the l.o. equivalent voltage, V_1, is not necessary for an optically pumped mixer (and the adjustment loops can therefore be simply omitted) the rectified current is required in Siegel and Kerr's analysis to define the equivalent d.c. bias:

$$V_0 = V_b + I_b Z_e(0)$$

where V_b is the diode bias voltage, I_b is the diode rectified current, and $Z_e(0)$ is the embedding network impedance at d.c. In the optoelectronic mixer program Thévenin equivalent voltages for the bias and l.o. must be supplied as input data; at d.c. the Thévenin equivalent impedance is made equal to the transmission line impedance in order to speed up execution; at the l.o. frequency it is not.

3.5 Performance of frequency domain model

3.5.1 Required input data

In the input data for the frequency domain model it is necessary to provide information describing the diode I-V characteristic. The nature of this information will depend on the model for the characteristic used. In the program the I-V characteristic is stored as a function which takes as an argument the diode voltage and gives the diode current as the result. The form of the function itself depends on the diode being modelled and is significantly different for the tunnelling contacts described in Chapter 4 and the rectifying Schottky barriers described in Chapter 6. The input parameters needed to describe the I-V characteristic will therefore be discussed in these chapters after the form of the characteristics themselves are described. It should be stated now, however, that the I-V characteristic expressed in the function must be analytic since its derivative is also required in the analysis; the derivative is stored in a separate function which, of course, will use the same input parameters as the I-V characteristic function.

The photocurrent is modelled by a d.c. component and a fundamental component, the amplitudes of which are read in as input data. The fundamental (l.o.) frequency must be specified, as must the intermediate frequency which is required in the linear analysis. The embedding network impedance at the l.o. frequency depends on the values input for the LCR circuit of Fig.3.2, while at d.c. the resistance will be R. Although this seems restrictive it is not unduly so if the bias voltage, E_b, read in by the program and the resistance, R, are considered to be the Thévenin equivalent of the d.c. supply. In the mode used by the program, the inductance and capacitance have been

ignored (i.e. L=C=0) and so the results are independent of frequency.

The final set of data required by the program is the iteration parameters; for the frequency domain model only an accuracy parameter and the maximum number of iterations need to be specified. The accuracy does not need to be very great as the solution will not be exact due to the simplifications involved in the model.

Some typical input data for the frequency domain analysis program are given in Table 3.1; for now, the diode details will be omitted until the characteristics for the devices used have been discussed (see Chapters 4, 5 and 6).

Embedding circuit parameters			
external bias	resistance	capacitance	inductance
-0.800 V	750 Ω	0 pF	0 nH
Photocurrent parameters			
d.c. value	a.c. value	l.o. freq.	i.f.
500 μA	500 μA	150 MHz	15MHz

Table 3.1 Input parameters example for frequency domain model

d.c. and fundamental components from large-signal analysis	V_0 -151 mV	V_1 174 mV
	I_0 -364 μA	I_1 -258 μA
	G_0 3.64 mS	G_1 -1.81 mS
results from small-signal analysis	$Z_{IF,opt}$ 421 Ω	
	L_c 10.3 dB	

Table 3.2 Typical output from frequency domain model (corresponds to input of Table 3.1 for tunnelling contact characteristic).

3.5.2 Performance and output

The nonlinear analysis produces output detailing the d.c. and fundamental components of the diode voltage, current, and conductance. It also writes values of the diode conductance over a l.o. cycle to a separate file to enable plotting. Although this conductance waveform is not itself restricted to the first harmonic, the voltage waveform from which it is derived is, and, therefore, both the voltage and conductance waveforms are only of limited value in analysing the actual mixer behaviour.

After the linear analysis has been performed, the optimum i.f. impedance for the mixer under the specified operating conditions is given together with the conversion loss for this i.f. impedance. Typical output data, corresponding to the input data given previously for a tunnelling contact mixer, are given in Table 3.2.

When used in the frequency-independent mode the frequency domain model is useful in performing a number of runs quickly. Operation is fast (typical compile and run times are less than 20 seconds on an ICL2988 at Queen Mary

College, London) and the program can be used interactively. By selecting information from a number of runs, the variation of parameters such as the conversion loss with parameters such as bias and source resistance (at the l.o. frequency), can be very quickly and easily found; such variations are described in Chapter 5 (Figs.5.1 to 5.3).

3.6 Performance of time domain model

3.6.1 Required input data

As for the frequency domain model, the parameters describing the diode I-V and dI/dV characteristics will depend on the analytic functions used to model these characteristics. The functions used in both models are thus very similar, with the exception that, as mentioned in section 3.4.2, the photocurrent is also calculated within the I-V function. Hence, in the time domain model this function requires further arguments, which are the normalised time (over a l.o. cycle) and the amplitudes of the d.c. and a.c. components of the photocurrent (assuming sinusoidal modulation). Non-sinusoidal modulation can be modelled by modifying this function. However, generally, some parameters describing the photocurrent need to be specified as input data. (The time normalisation is carried out within the program.)

Data for the C-V characteristic are also required for the time domain model; typically these will include the zero bias value, C_0, and the contact potential, Φ, according to:

$$c_j = C_0 \,/\, [\, 1 - (v_d/\Phi)]^{1/2}$$

although, again, this will depend on the characteristic used.

The value for the Thévenin equivalent voltage at d.c. must also be specified, as must the transmission line characteristic impedance. The value of the resistance of the embedding network at d.c. is made equal to the characteristic impedance; this can take any value without affecting the steady-state solution assuming the voltage source at d.c. is changed to provide the same bias across the diode. However, the impedance value chosen does affect the speed at which the solution is found; a value of 200Ω has been found to give efficient operation. As has been stated, the time domain model can also analyse the effect of an electrical l.o., if a value is assigned to a Thévenin equivalent source at the l.o. frequency.

As with the frequency domain model, the maximum number of iterations to be performed and the required accuracy need to be specified. However, it should be remembered that in this case the accuracy is calculated using eqn.(3.18) up to the eighth harmonic of the l.o.. A further iteration parameter is the number of l.o. cycles over which the integration is to be carried out. The integration can be carried out over several l.o. cycles but only the values for the last cycle are used in the remainder of the reflection cycle iteration, the advantage being that a more stable solution is obtained after several l.o. cycles have been integrated. The greater computing time involved usually outweighs this advantage and one l.o. cycle is usually specified.

Table 3.3 shows typical input data for the time domain model. Again, the parameters specifying the diode characteristics have been omitted here, but are covered in Chapter 4 for the tunnelling structures and Chapter 6 for the rectifying Schottky-type structures.

equiv. d.c. bias	-0.230V	series resistance	0Ω
zero bias capacitance	0pF	contact potential	1.1V
average photocurrent	500μA	a.c. photocurrent	500μA
iteration parameters			
max. no. of iterations	200	accuracy	7.5%
transmiss. line impedance	200Ω	points in l.o. cycle	51

embedding impedances	
harmonic no.	impedance (Ω)
0	750
1	750 + j10
2	64.48 + j99.15
3	29.02 + j166.0
4	59.18 + j232.4
5	43.50 + j299.2
6	68.31 + j367.8
7	61.45 + j438.5
8	81.49 + j511.4

Table 3.3 Typical input parameter set for time domain large-signal analysis (diode I-V parameters not included).

The embedding impedances for the higher l.o. harmonics given in Table 3.3 are arbitrary, since with the relatively high loss obtained with the tunnelling structure they do not have a significant effect on the performance; this is discussed in more detail in Chapter

5. If accurate predictions were required for a real, relatively low loss mixer, the embedding circuit would have to be accurately characterised, perhaps involving measurement at each of the relevant frequencies.

3.6.2 Performance and output

The nonlinear analysis predicts the Fourier components of the diode voltage, current, conductance, and capacitance up to the eighth harmonic of the l.o.; values for each over a l.o. cycle are also written to a separate file to enable the waveforms to be plotted. These waveforms are obviously much more useful in observing the mixer behaviour than the corresponding waveforms from the frequency domain model. Examples of the waveforms for a tunnelling contact optically pumped mixer are shown in Fig.3.8.

After the linear analysis has been performed the optimum i.f. impedance for the mixer under the specified operating conditions is written to the main output file, together with the input impedances at the upper- and lower-sideband frequencies, and the conversion loss for both upper- and lower-sideband down-conversion. Part of a typical output file from the time domain model is shown in Fig.3.9; this corresponds to the results for a tunnelling contact structure (to be described more fully in Chapters 4 and 5) with the input parameters of Table 3.3.

The run time of the program is very much dependent on the number of iterations required, each iteration taking perhaps as much as half as long as the whole of the rest of the program. On an ICL2988 machine at Queen Mary College, London approximately 2.3 seconds are required per iteration. For the problem described above with 7.5%

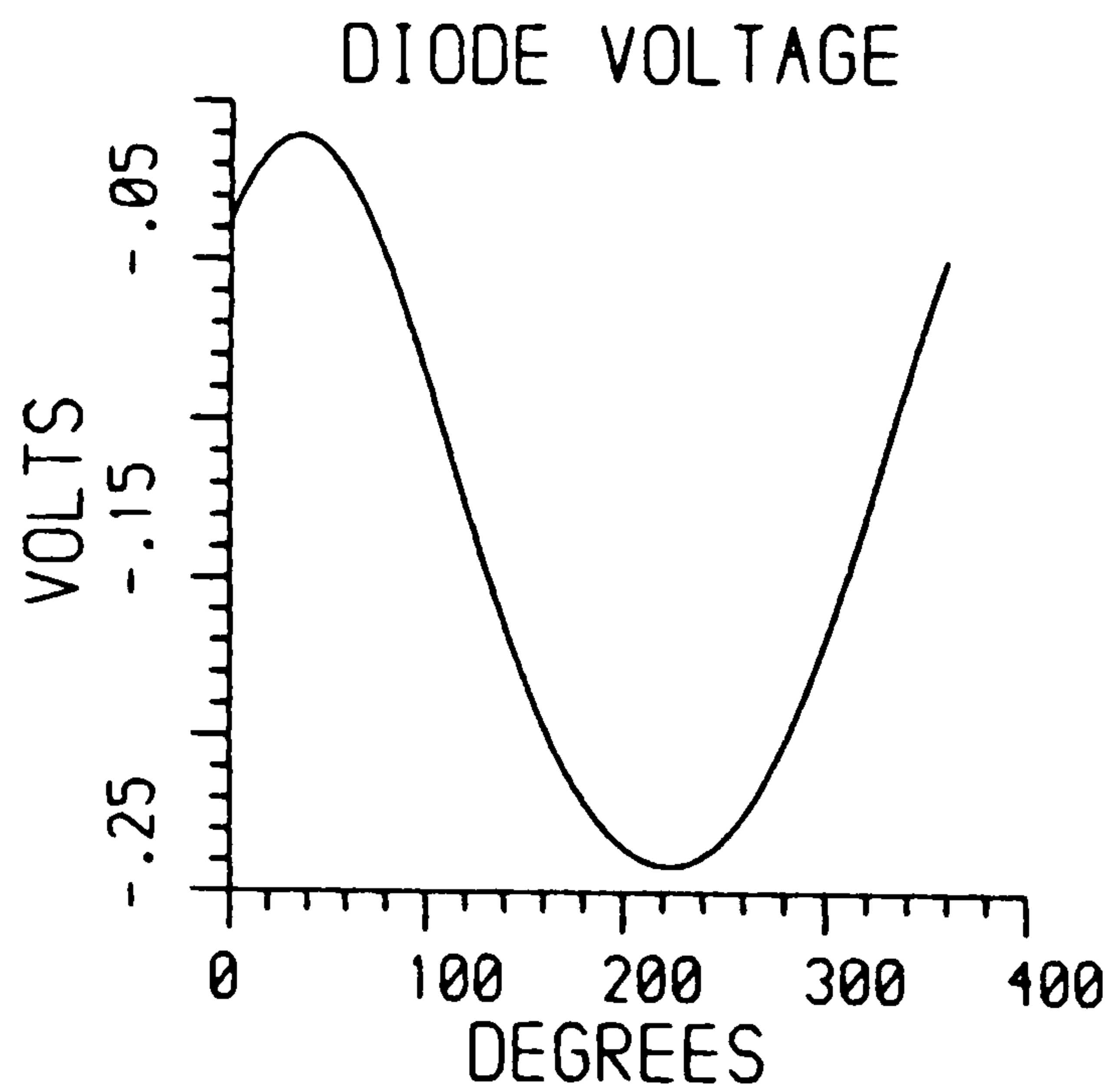

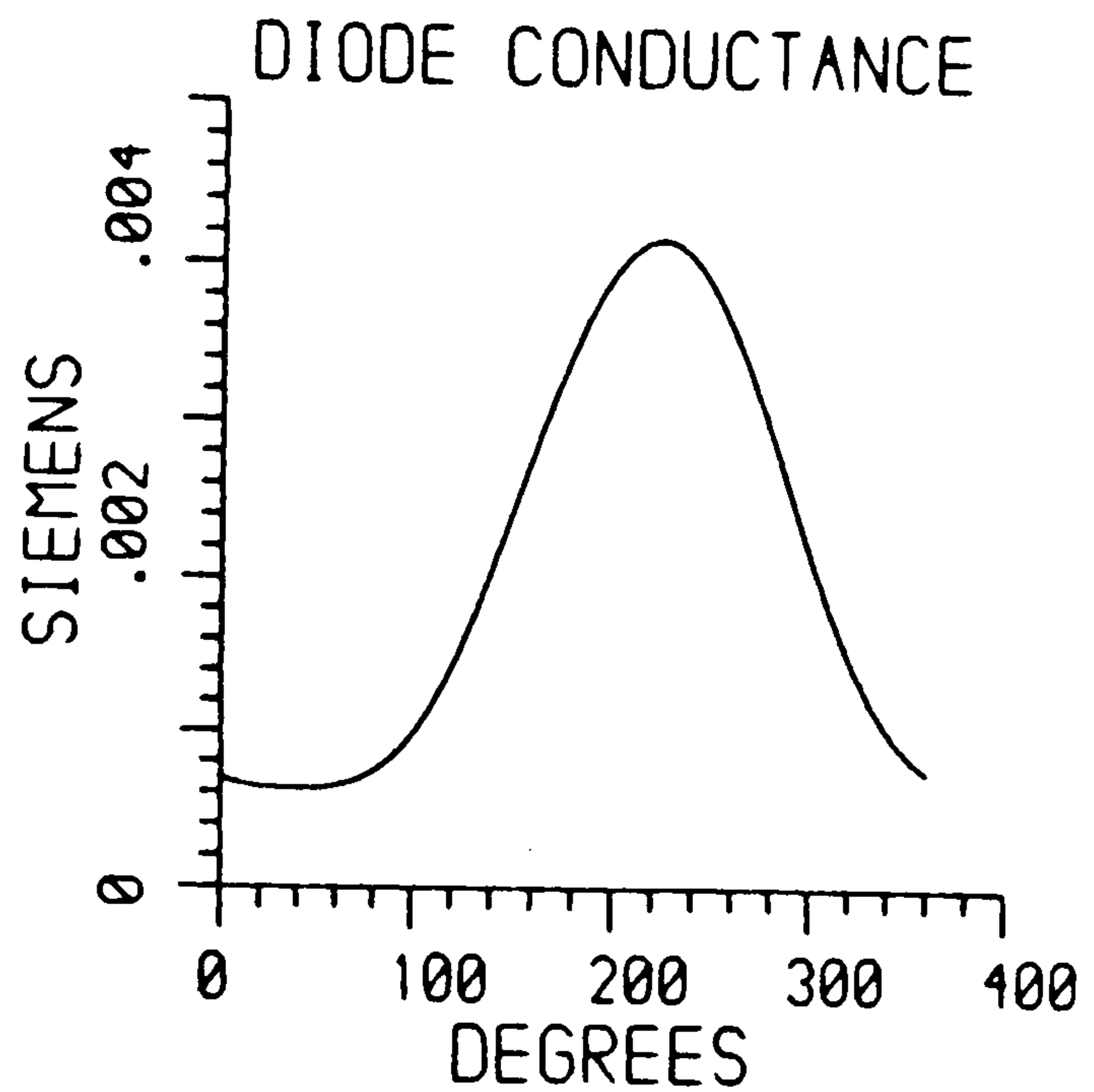

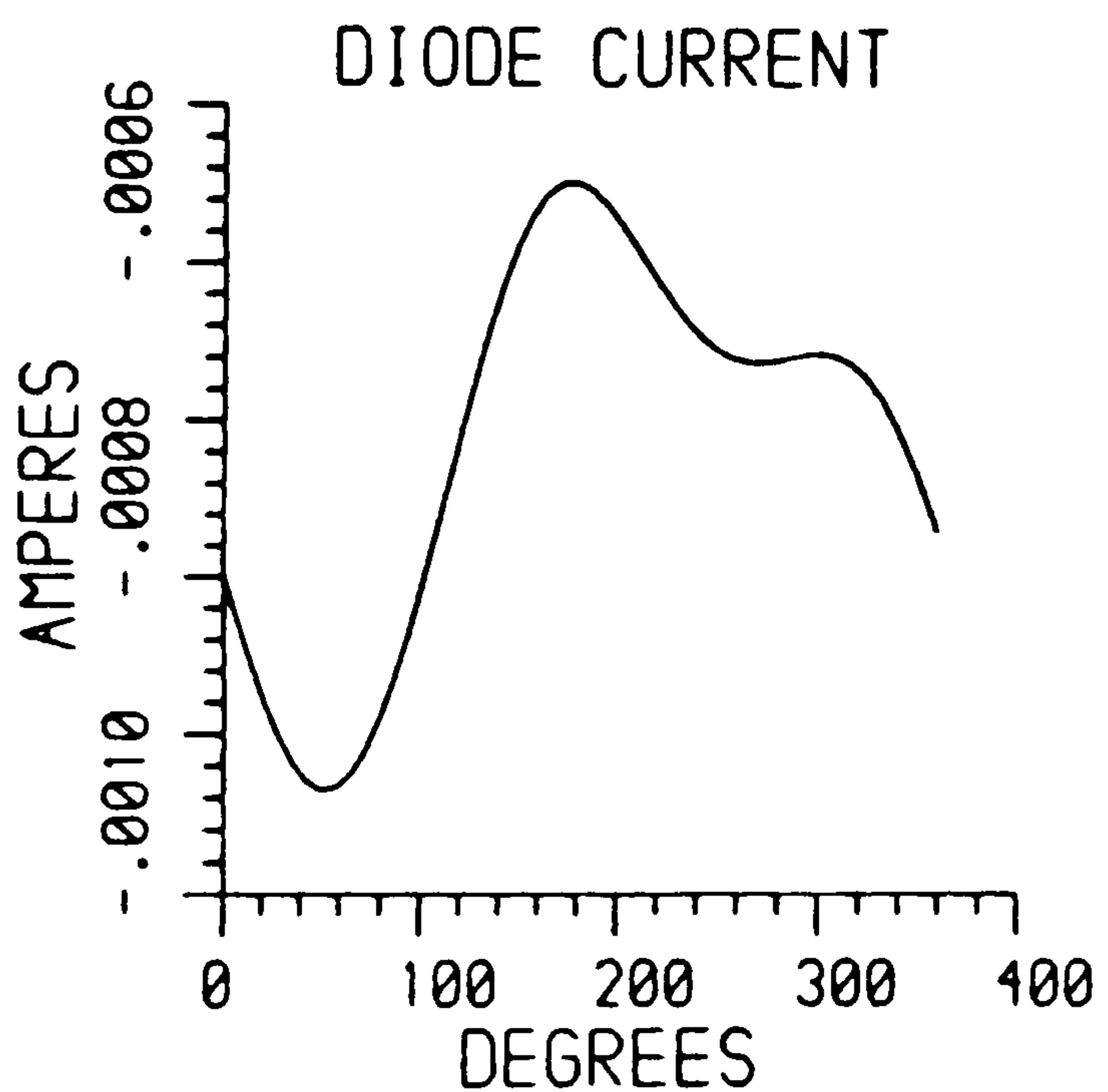

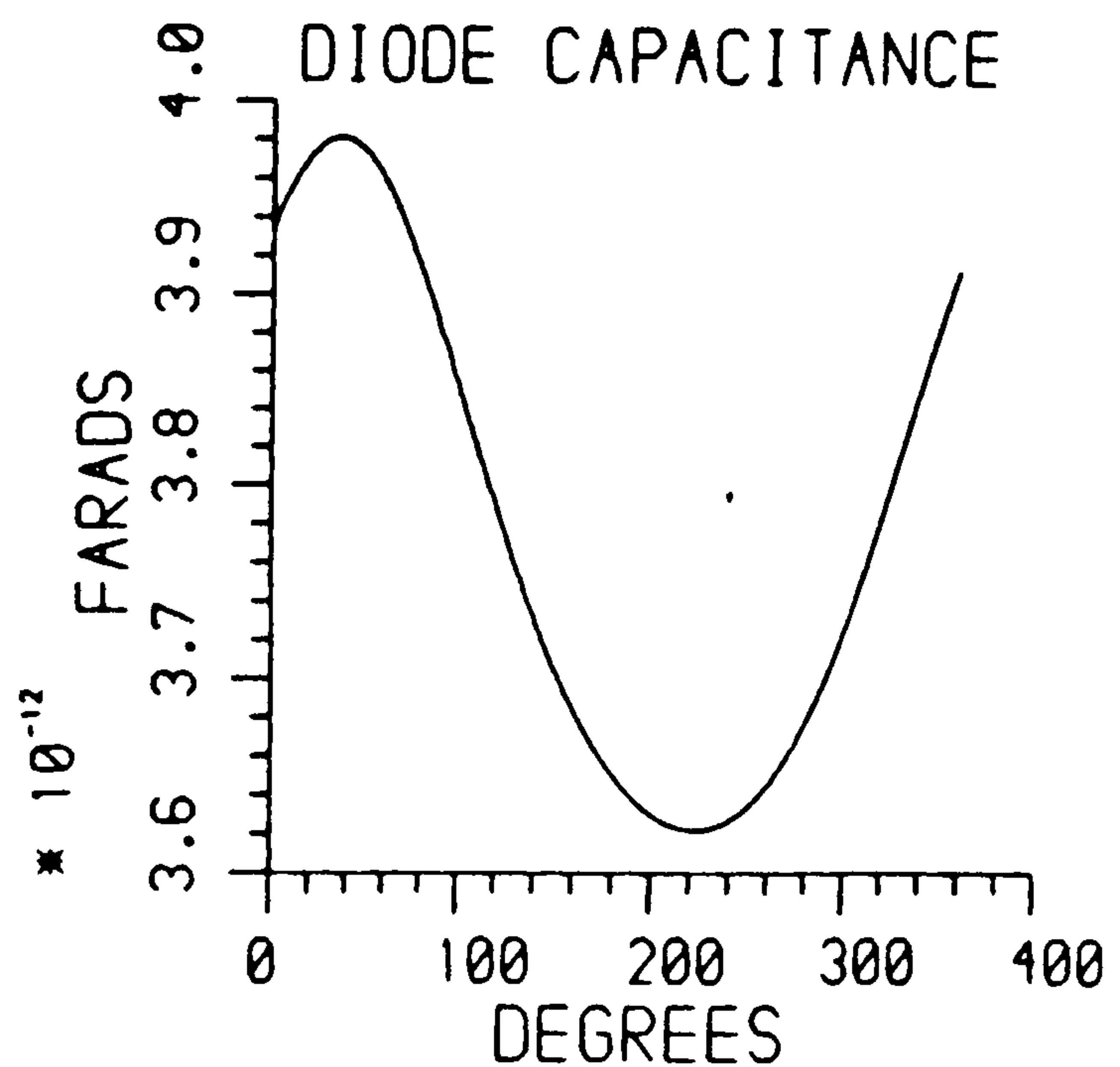

Fig.3.8 Diode waveforms over a local oscillator cycle predicted by the time domain model - 500μA average photocurrent generated in a tunnelling contact optically pumped mixer, the operation of which is described in Chapter 5.

```
***RESULTS OF NONLINEAR ANALYSIS***
    AFTER   57 ITERATIONS:

 ZQFLAG =    0

            DIODE VOLTAGE                 DIODE CURRENT
HARM.        REAL        IMAG              REAL        IMAG
    0    -0.164E+00                    -0.792E-03
    1     0.101E+00-0.466E-01          -0.134E-03  0.640E-04
    2     0.816E-02-0.467E-02          -0.451E-05  0.794E-04
    3     0.816E-03 0.104E-03          -0.143E-05  0.465E-05
    4     0.192E-03 0.774E-04          -0.510E-06  0.696E-06
    5     0.128E-04-0.617E-05           0.141E-07  0.449E-07
    6    -0.155E-05 0.385E-05          -0.935E-08-0.594E-08
    7     0.585E-06 0.280E-06          -0.852E-09  0.118E-08
    8    -0.598E-07-0.703E-07           0.175E-09-0.133E-10
             CONDUCTANCE                   CAPACITANCE
HARM.        REAL        IMAG              REAL        IMAG
    0     0.260E-02                     0.280E-11
    1    -0.101E-02 0.485E-03           0.565E-13-0.259E-13
    2     0.879E-04-0.152E-03           0.590E-14-0.414E-14
    3     0.105E-04-0.111E-04           0.683E-15-0.292E-15
    4     0.107E-05 0.724E-06           0.147E-15-0.301E-18
    5     0.452E-06 0.897E-07           0.182E-16-0.846E-17
    6    -0.581E-07-0.112E-06           0.774E-18 0.102E-17
    7    -0.178E-07 0.354E-08           0.505E-18 0.165E-18
    8     0.159E-08-0.545E-08           0.183E-19-0.327E-19

*** RESULTS OF LINEAR ANALYSIS ***

UPPER SIDEBAND INPUT IMPEDANCE =  0.247E+03 +J-0.219E+03
LOWER SIDEBAND INPUT IMPEDANCE =  0.237E+03 +J-0.214E+03

  I.F. OUTPUT IMPEDANCE =  0.472E+03 +J-0.854E+01

UPPER SIDEBAND CONVERSION LOSS :  0.150E+02 DB
LOWER SIDEBAND CONVERSION LOSS :  0.151E+02 DB
```

Fig.3.9 Part of a typical output file from the time domain computer program (corresponds to input of Table 3.3)

accuracy up to the eighth l.o. harmonic, 54 iterations are required; the run time is approximately 135 seconds. Many runs take longer than this; for complex problems in which greater accuracy is required, 500 or more iterations may be needed, corresponding to run times of well over 1000 seconds. The execution time is too long for the program to be run from the terminal; however, it is not too long to prevent frequent and quick running by submitting batch jobs.

The time domain model not only offers a significant improvement in accuracy but can also handle the diode nonlinear capacitance, which is essential if criteria such as the frequency response of the mixer are to be analysed. By extracting information from a number of runs, curves such as those described in Chapter 5, see Fig.5.5, can be plotted, which are directly comparable to the conversion loss versus diode bias curve produced from runs of the frequency domain, e.g. Fig.5.3. Both curves have used similar input data, the reasons for the difference between the two are the effect of the power loss to other frequencies, not taken into account in the simple frequency domain model, and RC limitations, which are only modelled in the time domain model. If attempts are made to tune out the barrier capacitance the predicted conversion loss from the time domain model can be reduced towards that predicted by the frequency domain one. This is discussed in further detail in Chapter 5.

3.7 Chapter summary

The theory behind the modelling of microwave mixers has been modified in order to model optically pumped mixing. Two approaches to the problem have been described: one in which the large-signal analysis of the mixer is carried

out in the frequency domain, the other in which this is done in the time domain. The frequency domain approach can give only approximate solutions, but by making a few simplifying approximations and using it as a quasi-static (frequency-independent) analysis, it can operate very quickly, making it very useful if many runs need to be made. This will be the case if the dependence of certain parameters on others, for example conversion loss on diode bias, is required. The time domain approach takes into account a number of l.o. harmonics and the nonlinear diode capacitance, giving very accurate predictions; in many cases its accuracy will be restricted mainly by the accuracy to which the diode characteristics and embedding network impedances can be specified.

CHAPTER FOUR

TUNNELLING METAL-SEMICONDUCTOR CONTACT: DEVICE CHARACTERISATION

4.1 Device physics 121

4.1.1 Structure 121

4.1.2 Current transport mechanisms 123

4.2 Modelling the I-V characteristics 125

4.2.1 Theoretical I-V characteristic expressions 127

4.2.2 Expressions used for actual characteristics 131

4.3 Equivalent circuit 135

4.4 Effect of illumination 146

4.4.1 Optical current generation 146

4.4.2 Frequency response limitations 152

4.5 Chapter summary 155

In Chapter 1 it was explained how a reverse-biased tunnelling junction could be used as an optically pumped mixer. In this chapter a detailed characterisation of a particular type of tunnelling junction, a heavily doped metal-semiconductor contact, is presented. The performance of this device as an optically pumped mixer will be described in Chapter 5.

4.1 Device physics

4.1.1 Structure[45]

The structure of the tunnelling metal-semiconductor contact is shown in Fig.4.1. RSRE, Malvern were already making high-speed photodiodes using Schottky contacts to lightly doped N^- GaAs material, and so it was a relatively simple step to modify the fabrication process and replace the N^- epitaxial layer with a heavily doped N^+ layer. After some preliminary measurements of the I-V characteristics of the contacts, a nominal doping density of $2x10^{18}cm^{-3}$ was selected for the optoelectronic mixer device.

The devices were fabricated at RSRE. The epitaxial layer was grown by MOCVD on an N^+ GaAs substrate using Si as the dopant. The barrier is formed at the interface of the semitransparent metallisation, consisting of 10nm of evaporated gold, and the epitaxial semiconductor layer. Contact fingers and bond pads are also of evaporated gold, with the bond pads being separated from the semiconductor by a 3μm layer of polyimide.

Devices of several different areas were fabricated, although all of the optically pumped mixing experiments to be described in the following chapter were performed with devices of contact area $25x25\mu m^2$. Most of the measurements

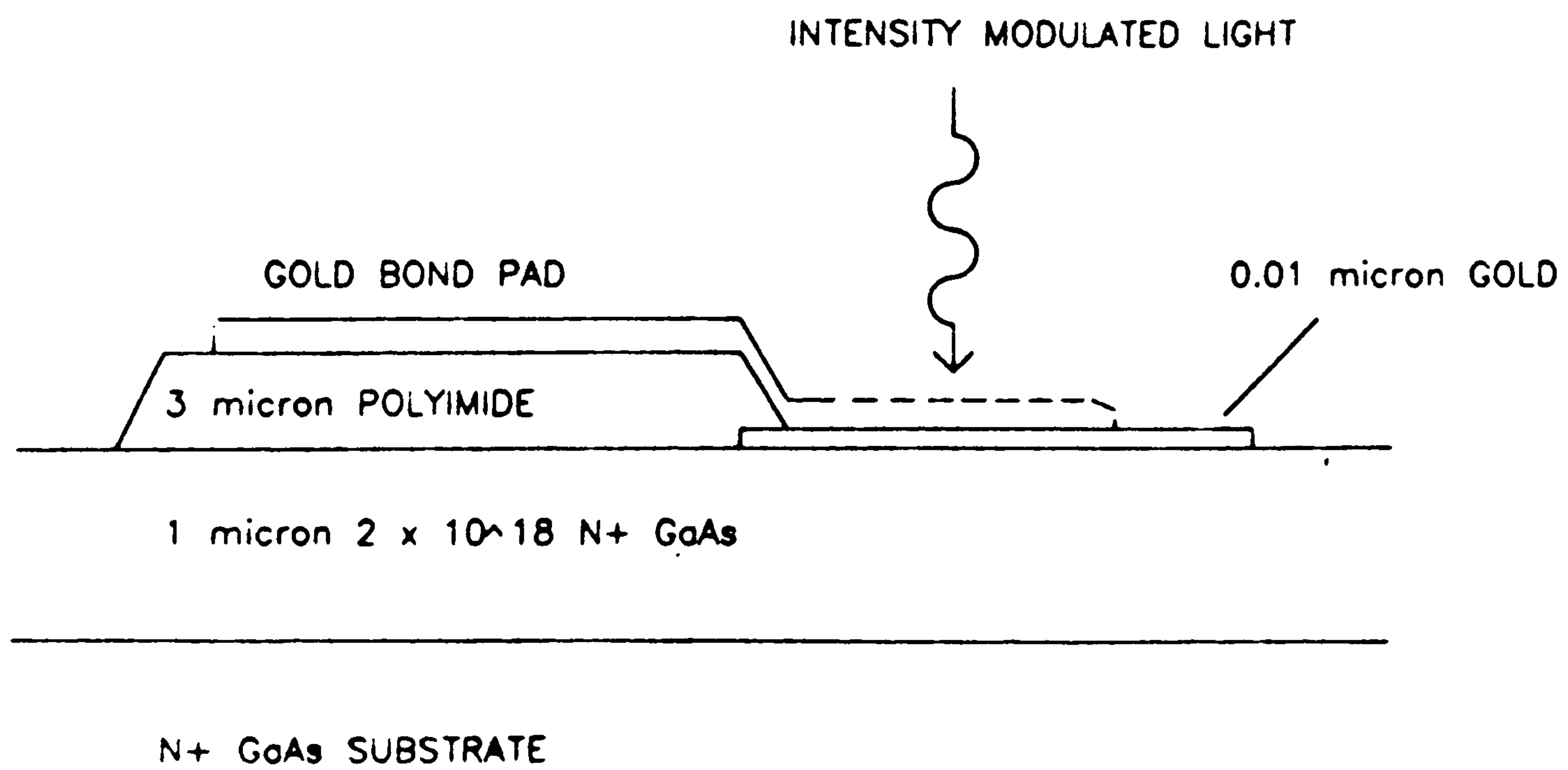

Fig. 4.1 Structure of a tunnelling metal-semiconductor contact of the type investigated in this thesis.

described in this chapter, therefore, also correspond to devices of area $25x25\mu m^2$, although some vector voltmeter impedance measurements on larger area devices ($50x50\mu m^2$) are described too. Since the fabrication processes for the devices are identical, it can be assumed that the electrical characteristics will be similar, and that, discounting edge effects, the characteristics of devices of different areas may be simply scaled.

4.1.2 Current transport mechanisms

The current transport mechanisms in moderately and heavily doped metal-semiconductor contacts are shown diagrammatically in Fig.4.2. There are two basic current transport mechanisms in such a contact - thermionic emission over the top of the barrier, and tunnelling through the barrier. The tunnelling mechanism may be further subdivided into two types, since tunnelling can be considered to occur at the Fermi-level (this is termed field emission), or, if the electrons have considerable thermal energy, at a higher energy (termed thermionic-field emission) where the barrier may be significantly narrower, and therefore more penetrable. The height and width of the barrier, then, are of fundamental importance in determining the significance of each of these transport mechanisms.

At sufficiently high temperatures the electrons have enough thermal energy to flow over the top of the barrier, and so thermionic emission would be the dominant transport mechanism. At low temperatures thermionic emission is negligible and tunnelling would dominate, with field emission becoming more important at lower temperatures, and thermionic-field emission less so.

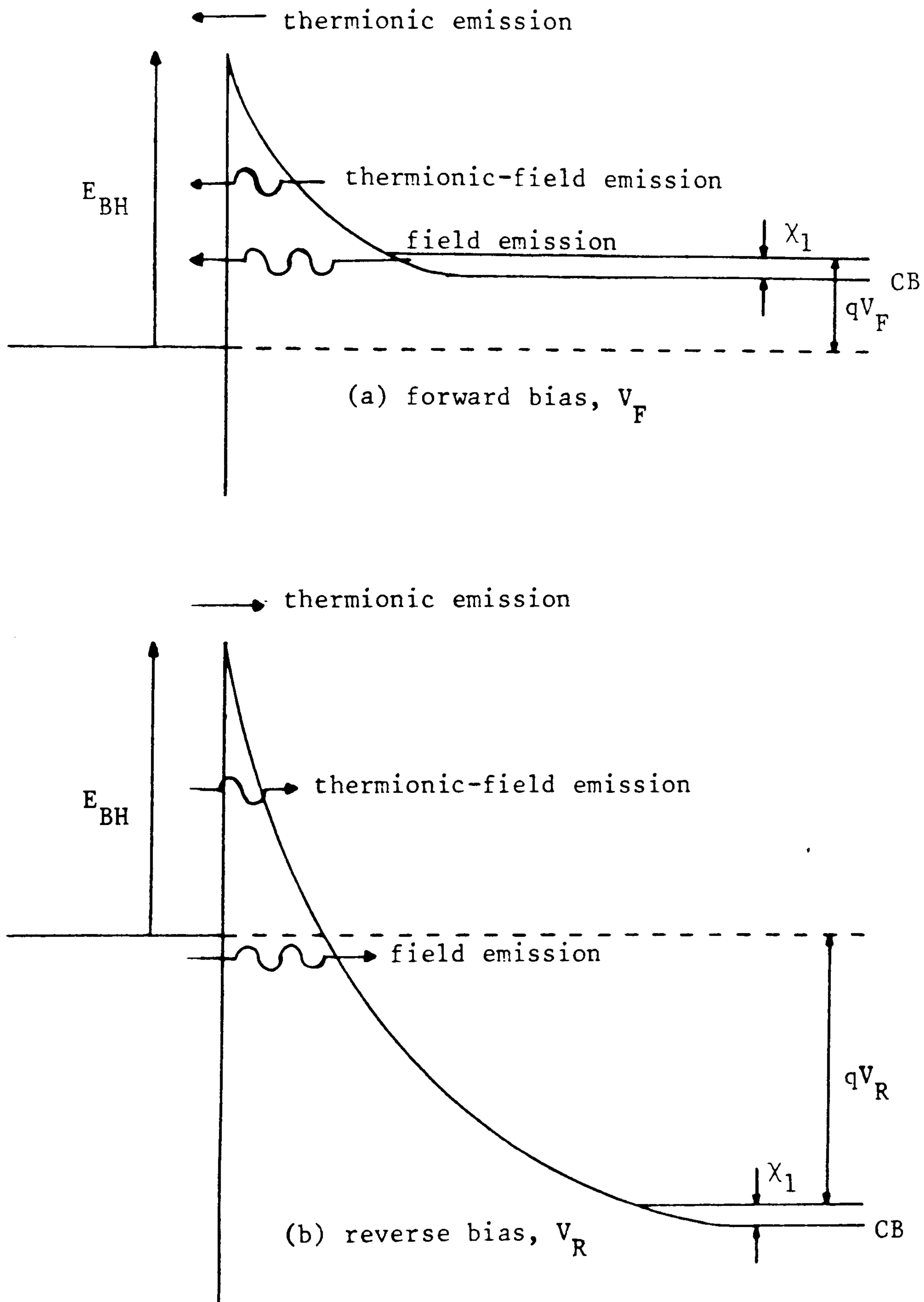

Fig.4.2 Current transport mechanisms in metal-semiconductor contact for moderate to heavy doping levels, and n-type material. Thermionic-field and field emission are tunnelling mechanisms. χ_1 is the Fermi level penetration into the conduction band (degenerate material shown).

The barrier the electrons have to penetrate is the space-charge layer or depletion region of the junction. The width of this region is proportional to $1/\surd N$, where N is the semiconductor doping level, and so increased doping produces a narrower barrier and enhances the tunnelling probability. For contacts to GaAs with n-type doping $>10^{18}cm^{-3}$ field emission can be the dominant transport mechanism even at room temperature.

A qualitative assessment of the effect of the applied bias can also be gained from Fig.4.2. From Fig.4.2(a) it can be seen that if the bias is increased towards a value equal to the barrier height, the electrons will require very little thermal energy to flow over the top; so, in a system which may be dominated by tunnelling at low bias, thermionic emission will tend to dominate at increasing forward bias.

In reverse bias (Fig.4.2(b)) the thermionic emission current is not enhanced by increasing bias since the electrons have to surmount the same barrier. However, although the total depletion width increases with increasing reverse bias, the barrier which the tunnelling electrons have to penetrate, either at the metal Fermi-level in the case of field emission or at a higher energy for thermionic-field emission, is decreased. In contacts in which thermionic-field emission or even thermionic emission dominate in forward bias, field emission may dominate at increasing reverse bias.

4.2 Modelling the I-V characteristics

In describing the mixer programs in Chapter 3, it was explained that they require an analytic expression of the diode I-V characteristic. So, if a theoretical study (and/or predictions) of the performance of the tunnelling

contacts as optically pumped mixers is required, an analytic expression for the I-V characteristic is necessary. For a tunnelling contact conducting in the reverse bias regime as well as the forward, it is obvious that the usual exponential expression will not suffice, although a modified form of this expression is often proposed for such devices. The typical diode equation[78,89]:

$$I = I_s\{\exp(qV/nkT) - 1\} \qquad (4.1)$$

may be modified to[78]:

$$I = I_s\{ \exp(qV/nkT) - \exp[(n^{-1}-1)qV/kT] \} \qquad (4.2)$$

where I_s is a saturation current, usually treated as a constant, and n the ideality factor $\geqslant 1$. Such a characteristic would suggest that under significant forward or reverse bias, a plot of $\log(|I|)-|V|$ would give a straight line of slope q/nkT in forward bias, and $(n^{-1}-1)q/kT$ in reverse. Since the characteristic is a summation of the forward and reverse currents, under low forward (reverse) bias the still significant reverse (forward) current will cause departures from this straight line relationship. Experimentally measured characteristics for an actual device are shown in a log-lin plot in Fig.4.3. It can be seen that although under forward bias the exponential dependence is obvious, under reverse bias such a dependence cannot be deduced. For this reason an accurate model for the I-V characteristics of devices dependent on field- and thermionic-field emission is required.

The model used is due to the theory of Padovani and Stratton[90], as modified by Padovani[91]. Padovani's model uses the WKB (Wentzel-Kramers-Brillouin) approximation for

tunnelling across a parabolic barrier[91,92]; it therefore ignores the image force modification to the barrier profile, which causes a rounding of the top of the barrier. The image force is due to the moving electron inducing an opposite and, hence, attractive charge on the opposite side of the barrier, thus reducing the effective barrier it has to surmount; its main effect, therefore, will be to shift the bias points at which the different transport mechanisms become dominant. This effect can be largely negated, as in most analyses for the current-voltage characteristics, by using the image-force lowered barrier height rather than the intrinsic one in the calculations. Conversely, predictions of the barrier height from I-V measurements give the lowered barrier height (while C-V measurements give the intrinsic barrier height)[89]. Although the image-force also causes a narrowing of the barrier which would affect the tunnelling probability, and therefore Padovani's model, this narrowing is negligible[93], and so neglecting the image-force is not a serious limitation. In section 4.2.1 the I-V characteristics resulting from Padovani's analysis are presented; for their derivation the reader is referred to the original text. The expressions actually used for modelling the tunnelling contacts are discussed in section 4.2.2.

4.2.1 Theoretical I-V characteristic expressions

Padovani[91] derives a set of analytic expressions for the I-V characteristics of metal-semiconductor contacts under forward and reverse bias in the three regimes: field emission (F-E), thermionic-field emission (T-F-E), and thermionic emission (T-E), as described above.

As a result of the WKB approximation used to calculate the tunnelling probability, an important energy

characteristic, E_{00}, of the particular semiconductor material is defined[91]:

$$E_{00} = (qh/4\pi).(N/\varepsilon m^{*})^{1/2} \qquad (4.3)$$

where q is the electronic charge, h is Planck's constant, N is the semiconductor doping level, ε the permittivity, and m^{*} the effective tunnelling mass of the electrons. The greater this energy characteristic is, the higher the tunnelling probability.

At higher temperatures (i.e. for T-F-E), modified versions of this energy characteristic are required[91]:

$$E_0 = E_{00}\coth(E_{00}/kT) \quad \textit{used in forward bias} \qquad (4.4a)$$

$$E' = E_{00}/[(E_{00}/kT) - \tanh(E_{00}/kT)] \qquad (4.4b)$$

Under reverse bias in the F-E regime the predicted current, I, for an applied voltage, V, is given by[91]:

$$I = \frac{SA'\pi E_{00}\exp[-2E_{BH}^{3/2}/3E_{00}(E_{BH}-V+\chi_1)^{1/2}]}{kT[E_{BH}/(E_{BH}-V+\chi_1)]^{1/2}\sin\{\pi kT[E_{BH}/(E_{BH}-V+\chi_1)]^{1/2}/E_{00}\}} \qquad (4.5)$$

where E_{BH} is the barrier height, χ_1 is the Fermi-level penetration into the conduction band or degeneracy (see Fig.4.2), A' is a modified Richardson constant, and S is the contact area. In cases when $E_{00} \gg kT$ the above equation can be simplified to[91]:

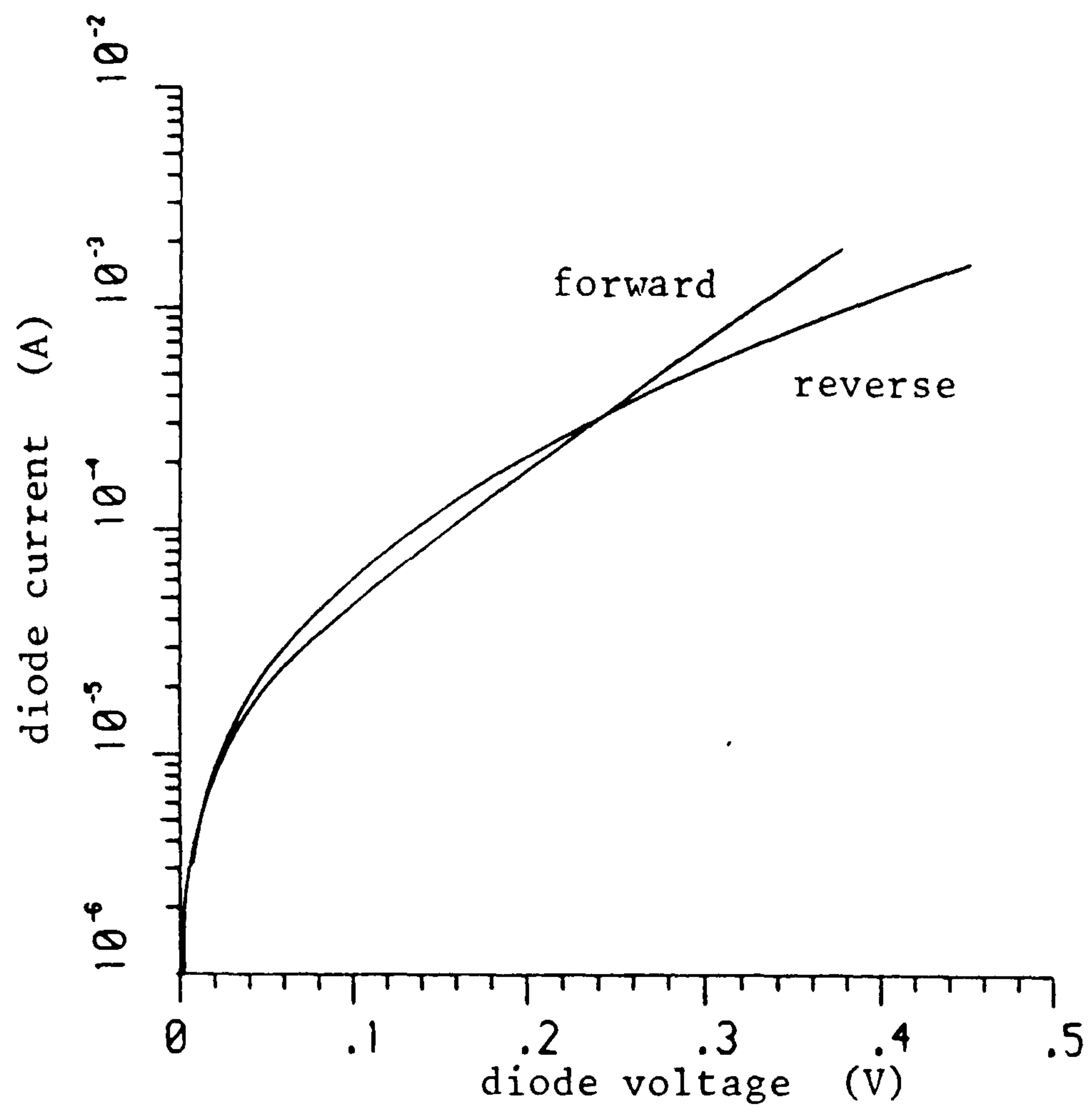

Fig. 4.3 Experimentally measured I-V characteristic of a tunnelling metal-semiconductor contact.

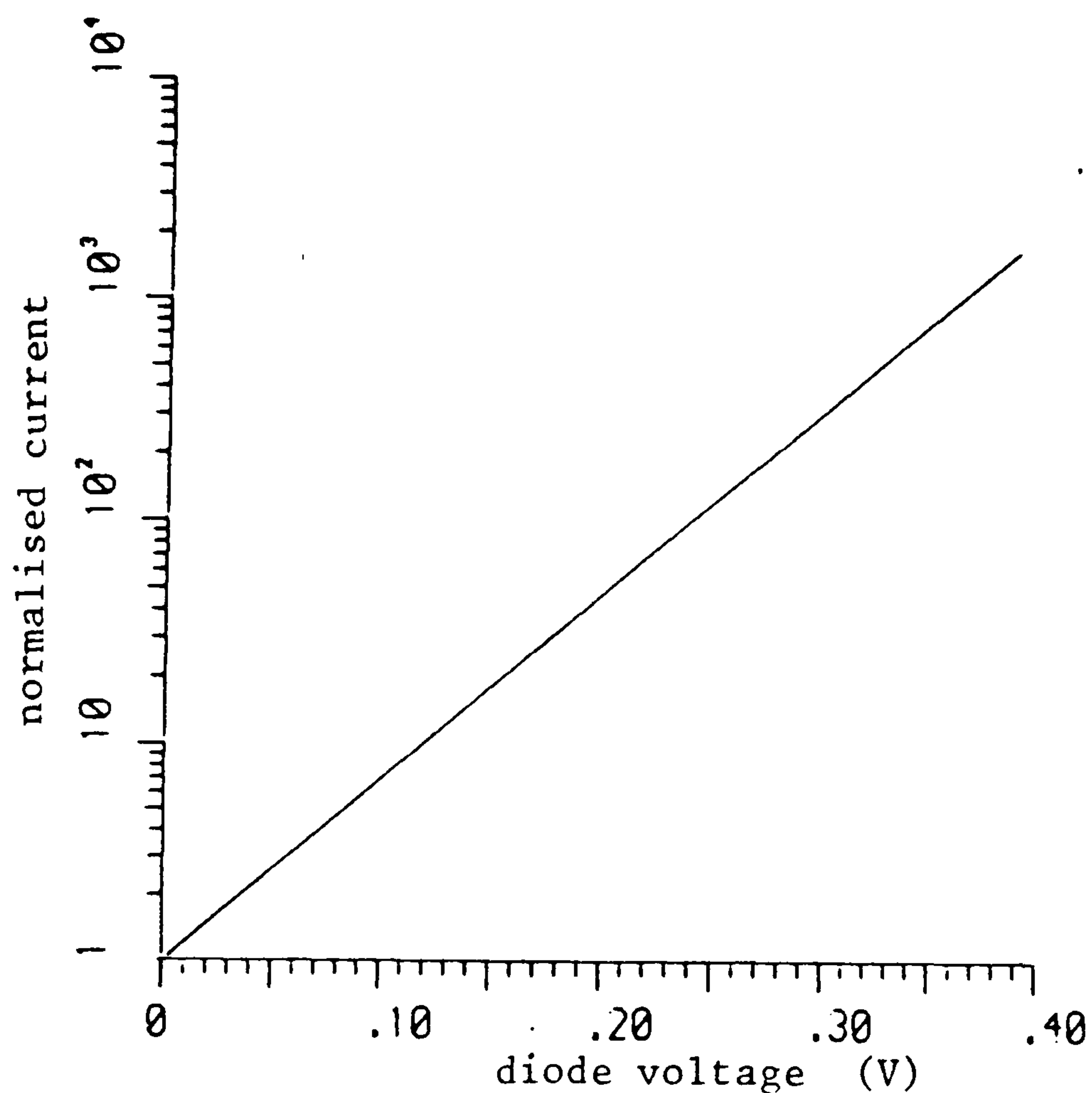

Fig. 4.4 I-V plot of exact form of forward bias thermionic-field emission relationship , equation (4.8)

$$I = SA' (E_{00}/kT)^2 [(E_{BH}-V + \chi_1)/E_{BH}]$$

$$\times \exp[-2E_{BH}^{3/2}/3E_{00}(E_{BH}-V + \chi_1)^{1/2}] \qquad (4.6)$$

In the T-F-E regime for reverse bias[91]:

$$I = I_{r1} \exp(-V/E') \qquad (4.7)$$

where

$$I_{r1} = SA'[\surd(\pi E_{00})/kT].\{-V + \chi_1 + [E_{BH}/\cosh(E_{00}/kT)]\}^{1/2}$$

$$\times \exp(-E_{BH}/E_0)$$

is a slowly varying function of bias.

It is unlikely that for forward bias field emission will dominate at room temperature in the contacts being used here. In the T-F-E regime for forward bias[91]:

$$I = I_{f1} \exp(V/E_0) \qquad (4.8)$$

where

$$I_{f1} = \frac{SA'\{\pi E_{00}(E_{BH}-V + \chi_1)\}^{1/2}}{kT \cosh(E_{00}/kT)}.\exp[(\chi_1/kT) - ((E_{BH}+\chi_1)/E_0)]$$

is, again, only slowly varying with bias; as a result I_{f1} is often approximated by a constant. The validity of this approximation can be seen from Fig.4.4 where a plot of current (normalised at zero bias) against voltage for an exact form of eqn.(4.8) with values of $E_{BH}+\chi_1$=0.8eV and E_0=50meV is shown to have near linear semi-log dependence over more than three decades of current. Generally, however, the value of 'E_0' necessary to obtain the fit

using the approximate, constant I_{f1} form of eqn.(4.8) will be slightly different to the 'actual' E_0 which would be used in the more exact form of eqn.(4.8).

The above expressions give separate values for the forward and reverse currents under the two different tunnelling regimes. For thermionic emission the forward and reverse currents may be simply combined to represent the whole characteristic with the expression:

$$I = I_s\{ \exp(qV/kT) - 1 \} \tag{4.9}$$

When compared to the typical diode equation (4.1) the above expression obviously relates to the case of an ideality factor n=1. If the approximation following eqn.(4.8) is assumed, then the expression for thermionic-field emission in forward bias can also be compared to the typical diode equation with $n \equiv E_0/kT$. Padovani and Stratton have shown the dependence of E_0 on temperature, but it is also useful to know the dependence of E_0 on E_{00} at constant temperature. Fig.4.5 shows the dependence of both E_0 and n on E_{00} at kT=25.9meV (corresponding to T=300K).

4.2.2 Expressions used for actual characteristics

If $\log\{ I/\left((E_{BH}-V+\chi_1)/E_{BH}\right) \}$ is plotted against $\surd(E_{BH}-V+\chi_1)$ then according to equation (4.6) a straight line should be obtained if field emission is dominant. This type of plot is shown in Fig.4.6 for a measured device characteristic assuming values of E_{BH}=0.75eV and χ_1=0.05eV. It can be seen (Fig.4.6) that a very good straight line fit to Padovani's model is obtained compared with the poor fit of the usual semi-log plot of Fig.4.3; Fig.4.6 can be directly compared to similar plots given in Padovani's monograph [ref.91, Figs. 19 and 34]. The values above were found to fit the measured characteristics quite

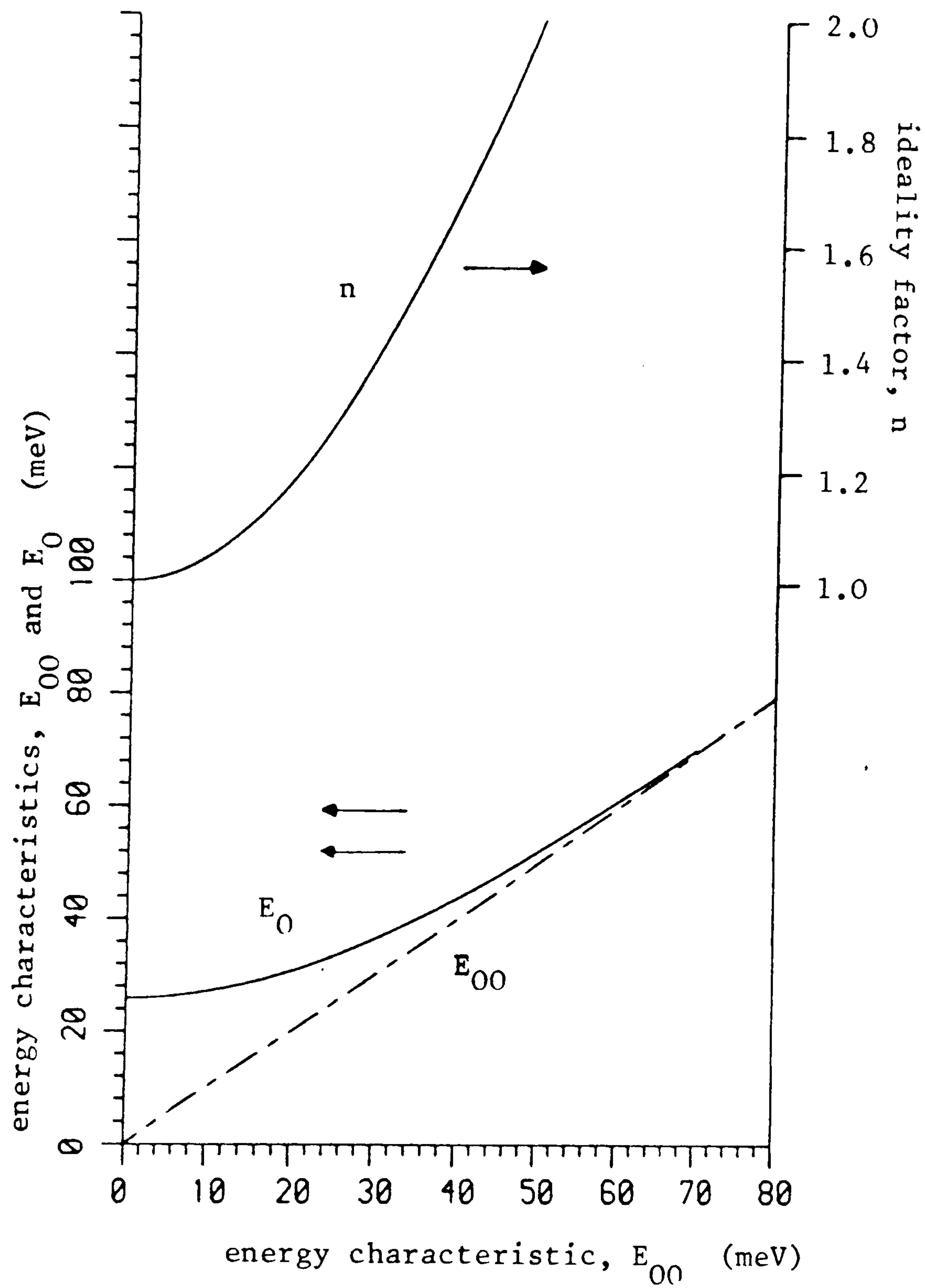

Fig. 4.5 Dependence of E_0 and n (ideality factor) on E_{00} at 300K. (E_0 and E_{00} are characteristic energy parameters of the barrier defined in the text.)

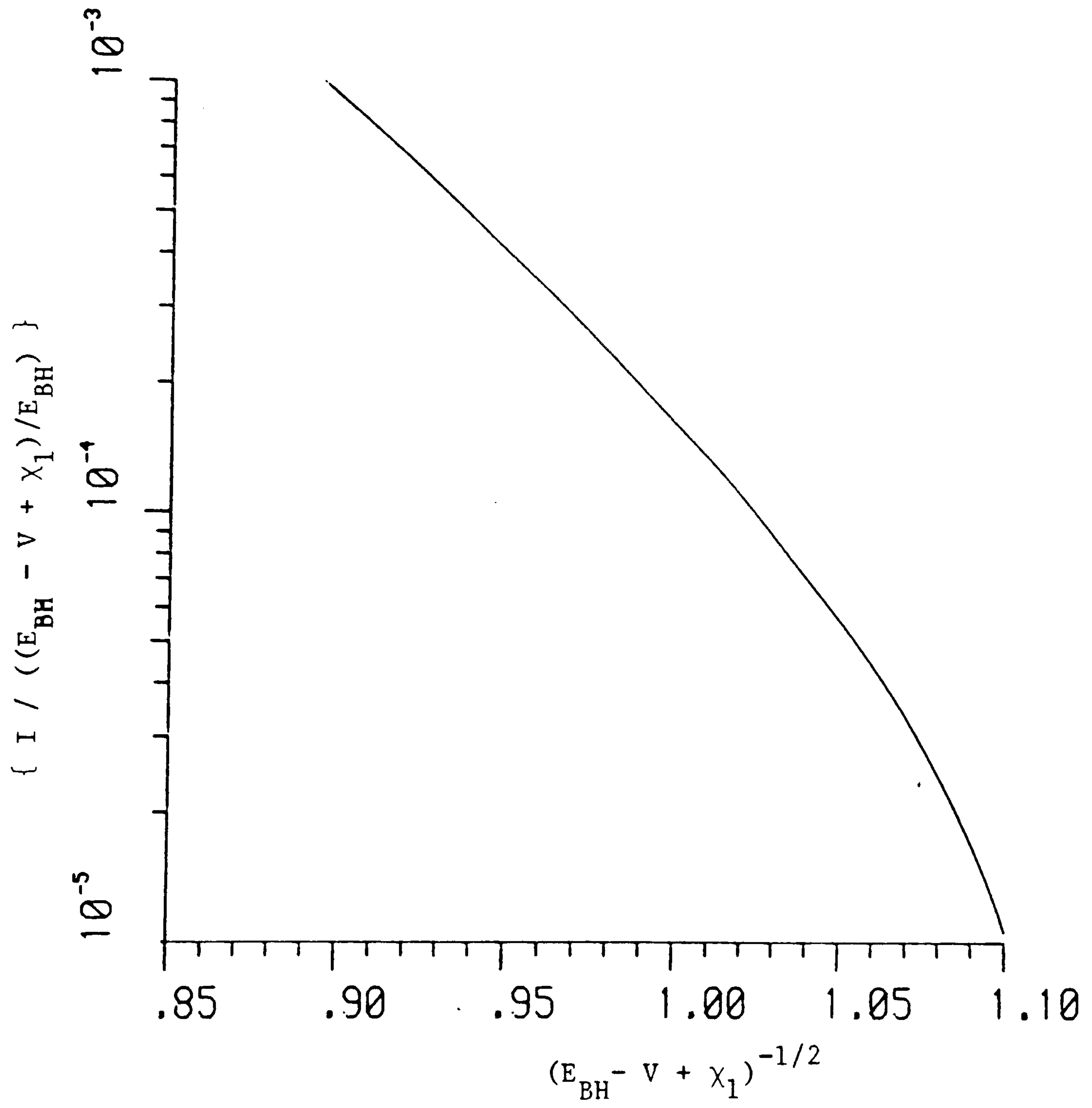

Fig.4.6 Fit of reverse characteristic to field emission equation of Padovani's theory (c.f. ref. [79], Figures. 19 & 34)

well. Generally, the reverse characteristics of the tunnelling contacts may be modelled by an equation of the form:

$$I_R = -I_{S,R}[(k_1-V)/k_2].\exp[k_3/\surd(k_1-V)] \qquad (4.10)$$

which is directly comparable to eqn.(4.6).

The forward characteristic is of the form of the T-E or approximated T-F-E equations:

$$I_F = I_{S,F}\exp(V/E_m) \qquad (4.11)$$

with the saturation current assumed constant. All of the parameter values in equations (4.10) and (4.11) are chosen to fit the measured characteristics, although they are not assigned unreasonable values. For example, it is known that surface states tend to pin the barrier height in metal-GaAs systems at around 0.7⇒0.85eV, and that for n-type doping $>10^{18}cm^{-3}$ GaAs starts to become degenerate; therefore, with the formalism used $0.7eV<k_2<0.85eV$ and $k_1 \geqslant k_2$. The parameter E_m, however, assumes much higher values than can be expected from calculations of the energy characteristics of the semiconductor material. With $E_m \equiv nkT/q$ the measured characteristics suggest $n \simeq 2.2$ when values of $n \simeq 1.2$ are expected according to equations (4.3) and (4.4). In material with very short carrier lifetimes such as GaAs, recombination-generation current can be significant and will dominate at low bias; this current mechanism shows a characteristic $n=2$ dependence on bias[89]. At higher bias the thermionic (or thermionic-field) emission current should dominate and the ideality factor should tend towards a value nearer unity. That such a low n value region cannot be seen to occur at all in the forward characteristics (see Fig.4.3) is probably due to diode series resistance which, if it has a value of 20Ω

(see the next section) will start to have a significant effect as the current approaches the milliampere level, or as the voltage exceeds 0.2V. Although the n values are even greater than 2 they are not, however, unexpected; in their research on the metallisation of n-type GaAs contacts, Sinha and Poate[94] have found that surface states and alloying behaviour can produce such 'poor' ideality factors. It needs to be mentioned that the degree of reproducibility of the contacts seemed to be such that, with devices of nominally similar doping, the current at a certain bias in one device could be twice that at the same bias in the other.

With suitably chosen values for the forward and reverse characteristics, the two equations, (4.10) and (4.11), are summed to model the whole I-V characteristic. Fig.4.7 shows a plot of the modelled and measured I-V characteristic of a tunnelling contact; very good agreement over the bias range of interest is obtained.

4.3 Equivalent circuit

A typical equivalent circuit for a semiconductor diode is shown in Fig.4.8. It consists of a parallel combination of the two nonlinear, voltage-dependent barrier elements, R_b and C_b, in series with a resistance, r_s, and inductance, L_s. The series resistance is caused by the ohmic resistance of the bulk and undepleted semiconductor material, by the resistance of the opposite, 'ohmic', contact and by any ohmic resistance in the metallisation; the inductance is due to the contacting leads. There may also be some parasitic capacitances, C_p, due to the diode package. All of the elements in Fig.4.8 are assumed frequency-independent, but in reality the series resistance, for example, will be frequency dependent due

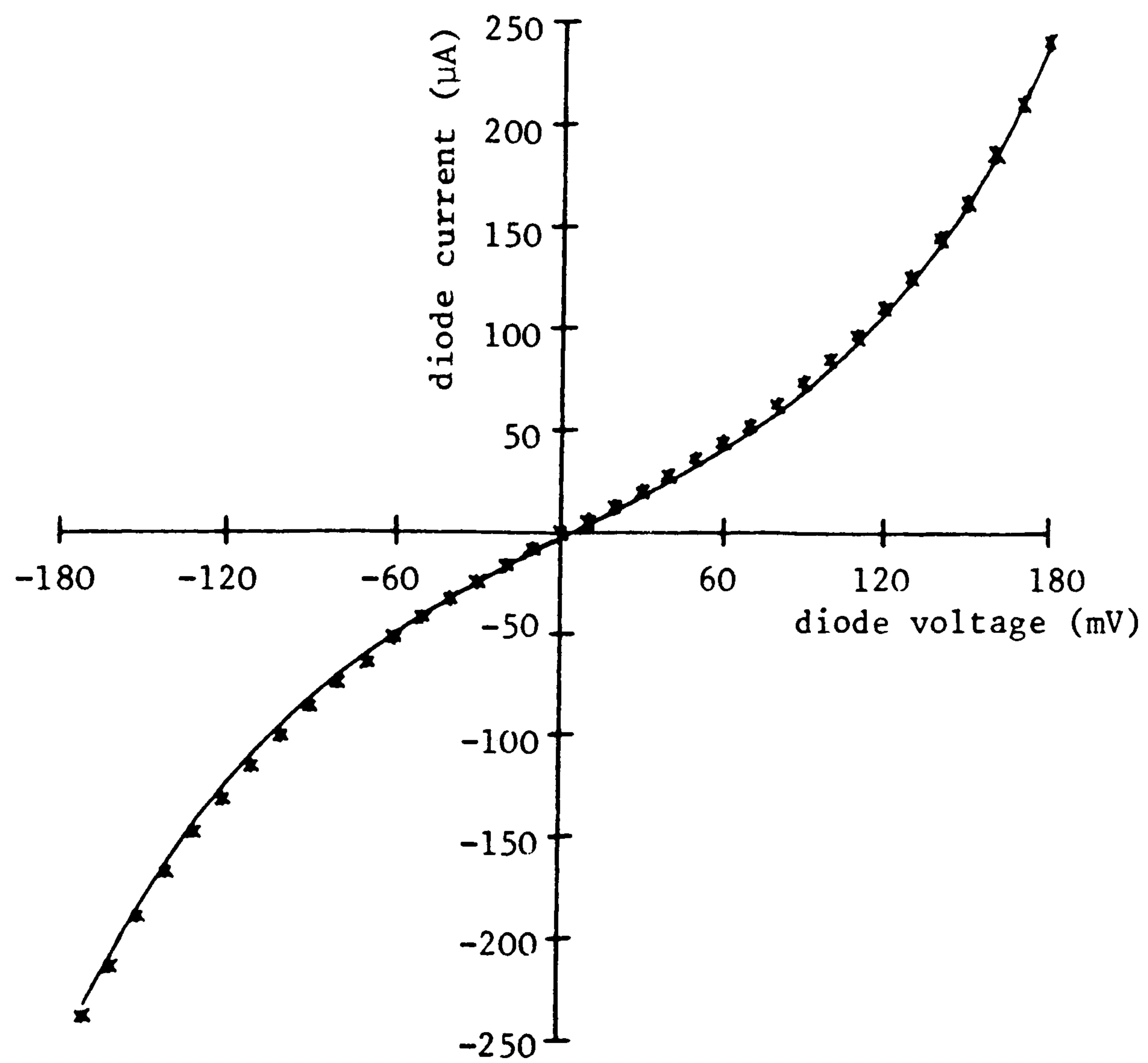

Fig. 4.7 Tunnelling metal-semiconductor contact: comparison of modelled (———) and experimentally measured (*) I-V characteristics.

to the skin-effect. The equivalent circuit is therefore a simplification, but any equivalent circuit can only approximate the actual behaviour of the device and a balance must be struck between the complexity of the equivalent circuit and its accuracy.

The expected barrier width of the devices at zero bias if they are doped at approximately 2×10^{18} donors/cm^{-3} is $\simeq$ 24nm (assuming a barrier height $\simeq$ 0.8eV). For a device of the 'minimum' area considered in this thesis ($10\times10\mu m^2$, as described in Chapter 2), this would result in a zero bias capacitance of 0.5pF; however, the tunnelling contacts investigated, and to be characterised in this chapter, had areas $25\times25\mu m^2$ which suggests a capacitance of 3pF. Operation frequencies for these devices would typically be restricted to under one gigahertz, so the lead inductance, which should have a value of $\leqslant$1nH, will be insignificant. For simplicity the package capacitance, C_p, will also be ignored for now. The resulting equivalent circuit then consists of a parallel combination of barrier resistance (R_b) and capacitance (C_b), in series with r_s. The values of these components of the equivalent circuit can be found by using a Cole-Cole plot[95].

A Cole-Cole plot is a plot of the imaginary part of the diode impedance versus the real part over a wide frequency range[95]. If the three element equivalent circuit is a realistic approximation of the device, the Cole-Cole plot will result in a semicircle. The intercept (projected or actual) of this semicircle with the real axis at very low frequencies, when the reactance of the diode capacitance will be large, will give the value of R_b+r_s; the intercept at very high frequencies will give the value of r_s. The barrier capacitance can then be calculated according to:

$$1/\omega C_M = \omega C_b R_b^2/(1 + \omega^2 C_b^2 R_b^2) \qquad \textit{see Fig. 4.9} \qquad (4.12)$$

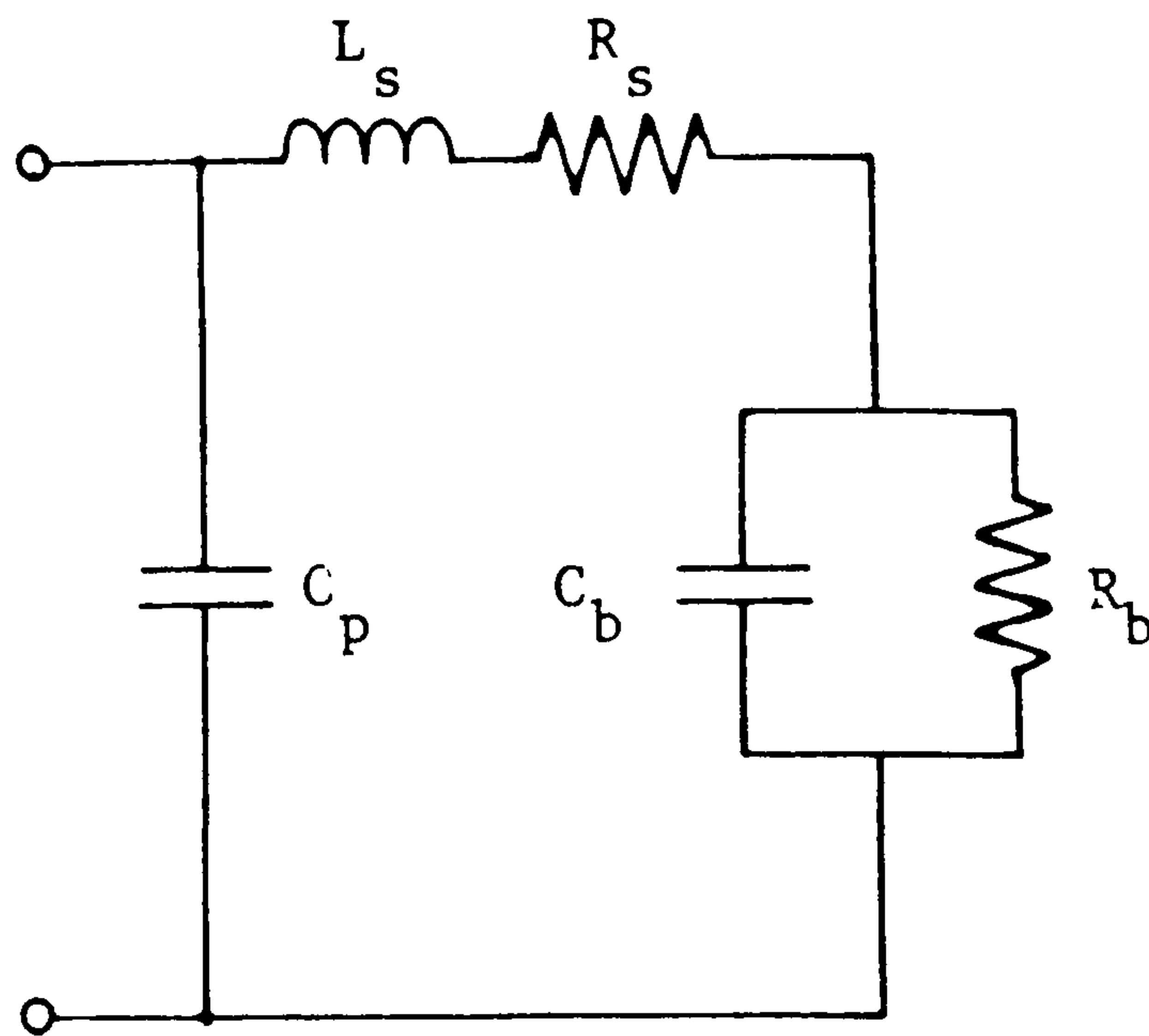

Fig. 4.8 Equivalent circuit for a semiconductor diode

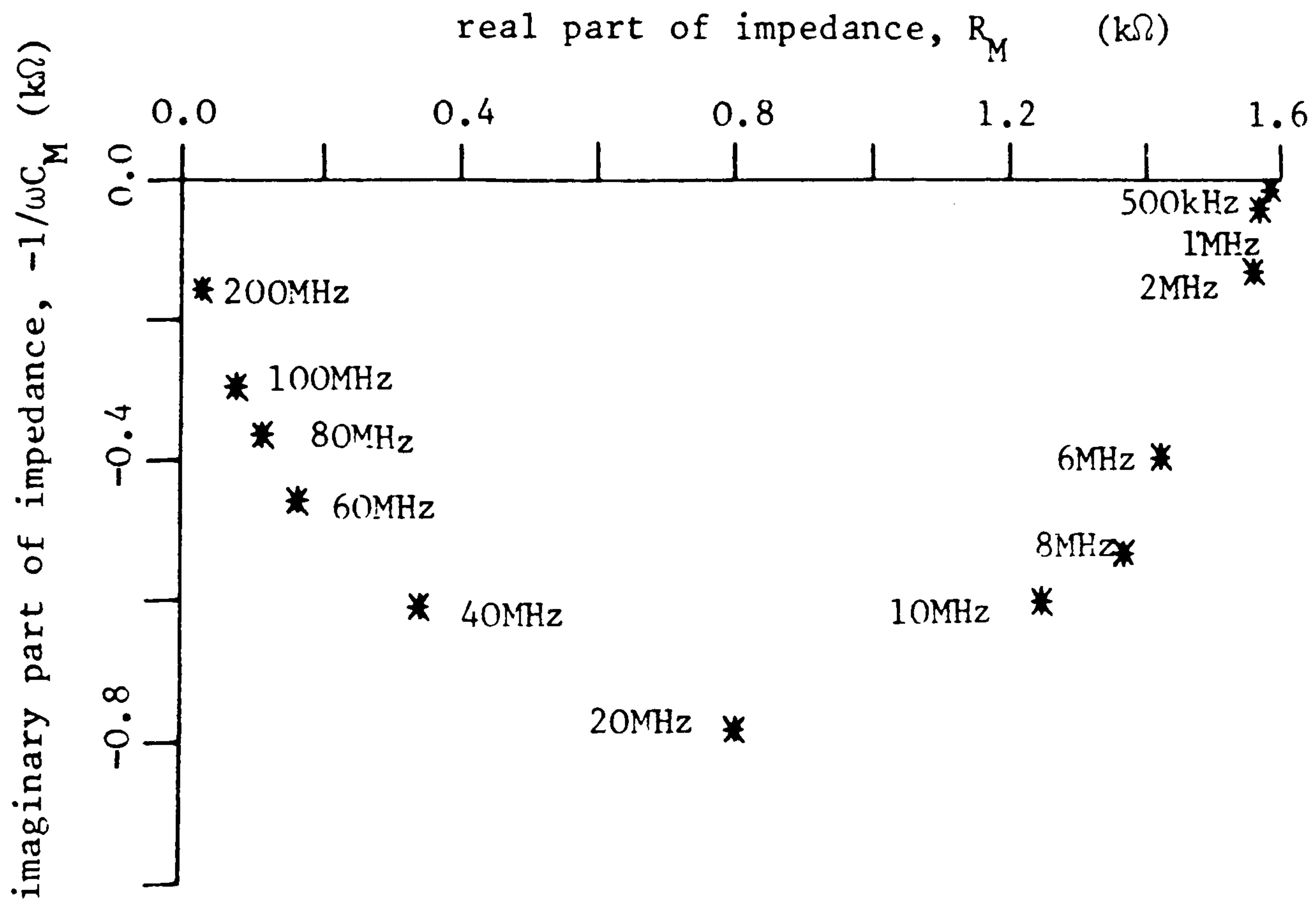

Fig. 4.9 Cole-Cole plot of impedance (taken from network analyser admittance measurements) of tunnelling contact.

Measurements of the diode impedance taken at RSRE using a network analyser were found by the author to give a very good Cole-Cole plot fit, as shown in Fig.4.9. From the Cole-Cole plot of Fig.4.9 values of $r_s \approx 20\Omega$, $R_b + r_s \approx 1.58k\Omega$, and therefore $R_b \approx 1.56k\Omega$, and $C_b \approx 5.1pF$ have been deduced.

Separate measurements at RSRE suggested a package capacitance, mainly due to the two 50Ω lines to which the diode was connected, of 1.7pF or 0.85pF per line. The measurements used for the Cole-Cole plot of Fig.4.9 were taken with the diode connected to only one 50Ω line; a package capacitance of 0.85pF must therefore be taken into account. This may be done quite easily: because the series resistance is small compared to the barrier resistance, and compared to the reactance of the barrier capacitance at the measurement frequencies, the package capacitance may be subtracted from the total capacitance deduced from the Cole-Cole plot. The measured barrier capacitance is therefore, $C_b \approx 4.25pF$ (which compares favourably with the value predicted above, especially as there is likely to be some extra fringing capacitance), with a package capacitance of $C_p \approx 0.85pF$ or 1.7pF depending on whether the diode is connected to one or both 50Ω lines.

The value of the series resistance deduced from Fig.4.9 is very much an estimate. Assuming the three element Cole-Cole plot model used, higher frequency measurements would be necessary to deduce the series resistance accurately; however, at higher frequencies the effects of parasitics that have been neglected, such as the lead inductance, will become significant. For the low resistivity semiconductor material used in the devices a value of 20Ω is too high to be due to the resistance of the bulk or to that of the 'ohmic' contact. The very thin layer of metallisation forming the Schottky contact is probably the main cause of the series resistance.

The actual dependence of the nonlinear resistance and capacitance on bias needs to be known. Since it is a.c. signals which are of concern, the barrier resistance of interest is the differential or slope resistance of the diode. Being a nonlinear device, the resistance 'shown' to an a.c. signal by a tunnelling contact will depend on the signal level; however, for small signals the resistance will tend to the value of the reciprocal of the dI/dV relationship at the bias point. The dynamic resistance of a tunnelling contact calculated in this way, corresponding to the I-V characteristic shown in Fig.4.7, is shown in Fig.4.10; the diode resistance decreases with both positive and negative applied bias. Due to the increasing barrier width with reverse bias the barrier capacitance should decrease according to the 'parallel-plate' depletion capacitance model[53]. In forward bias the depletion width shrinks and the barrier capacitance should increase. For a barrier to a uniformly doped semiconductor this dependence is usually given by the expression[89]:

$$C_b = C_0/[1 - (V/\Phi)]^{1/2} \qquad (4.13)$$

where Φ is the contact potential, equivalent to the barrier height with the image-force lowering neglected, and C_0 is the zero bias barrier capacitance. Diffusion capacitance, due to minority-carrier charge storage, dominates the forward bias capacitance of p-n diodes, but Schottky barriers are majority-carrier controlled devices in which such charge-storage can be neglected.

At RSRE, measurements of the admittance of a tunnelling contact at a frequency of 1MHz over a range of applied bias were made using a network analyser. The conductive part of the admittance was assumed to be due to the barrier conductance, while the reactive part was assumed

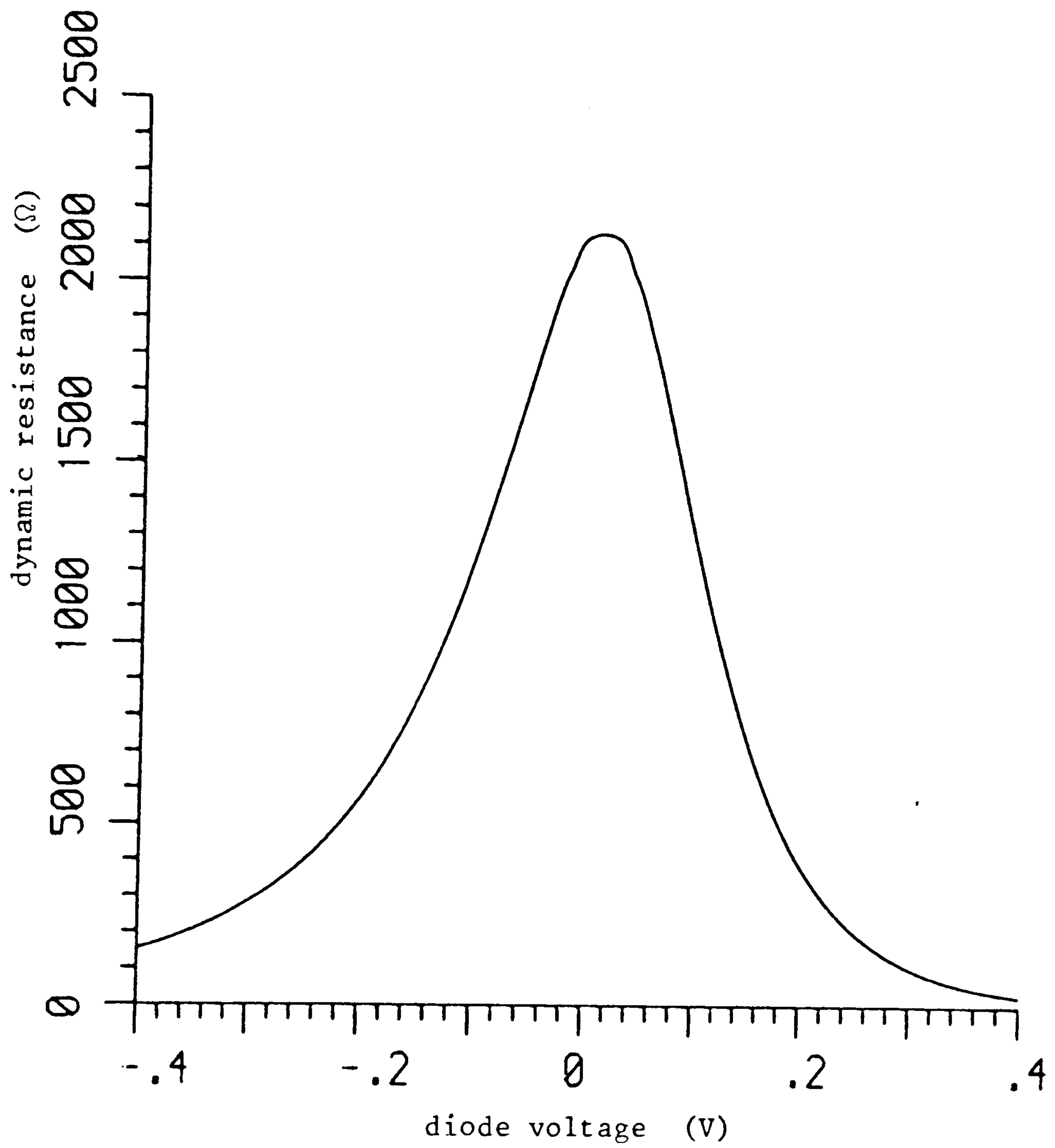

Fig. 4.10 Typical variation of the dynamic resistance of a tunnelling contact with diode voltage bias.

to be due to the barrier capacitance plus the package capacitance; these assumptions rely on the fact that the series resistance is small. The value estimated for the package capacitance may therefore be subtracted from the total capacitance, calculated from the reactive part of the admittance, to give the barrier capacitance. This method is more accurate at low bias for the tunnelling contacts where the barrier resistance is high. The results of calculations for the barrier capacitance are illustrated in Fig.4.11. It can be seen that the barrier capacitance increases with decreasing reverse bias, but has a maximum in very low forward bias after which it decreases with increasing forward bias.

In Fig.4.12 the results of further measurements on a larger area device ($50x50\mu m^2$) using a vector voltmeter to measure the complex reflection coefficient are presented. It can be seen that the capacitance of the barrier is increased by a factor of approximately four compared to the data of Fig.4.11, as would be expected with a device of four times the area. Fig.4.13 shows a plot of C_b^{-2} against V; linear dependence as predicted by eqn.(4.13) occurs around zero and at low reverse bias. However, the capacitance again seems to decrease in forward bias.

Macdonald[96] has proposed the concept of a geometrical capacitance between the two contacts of a device. At high enough fields in the device, the field between the two contacts will become uniform and so (even in forward bias) the capacitance will tend towards this very small geometrical capacitance. In real situations (non-uniform fields) the effect of this capacitance is hard to predict, but it is one possible explanation for the behaviour of the C-V characteristic of the tunnelling contacts.

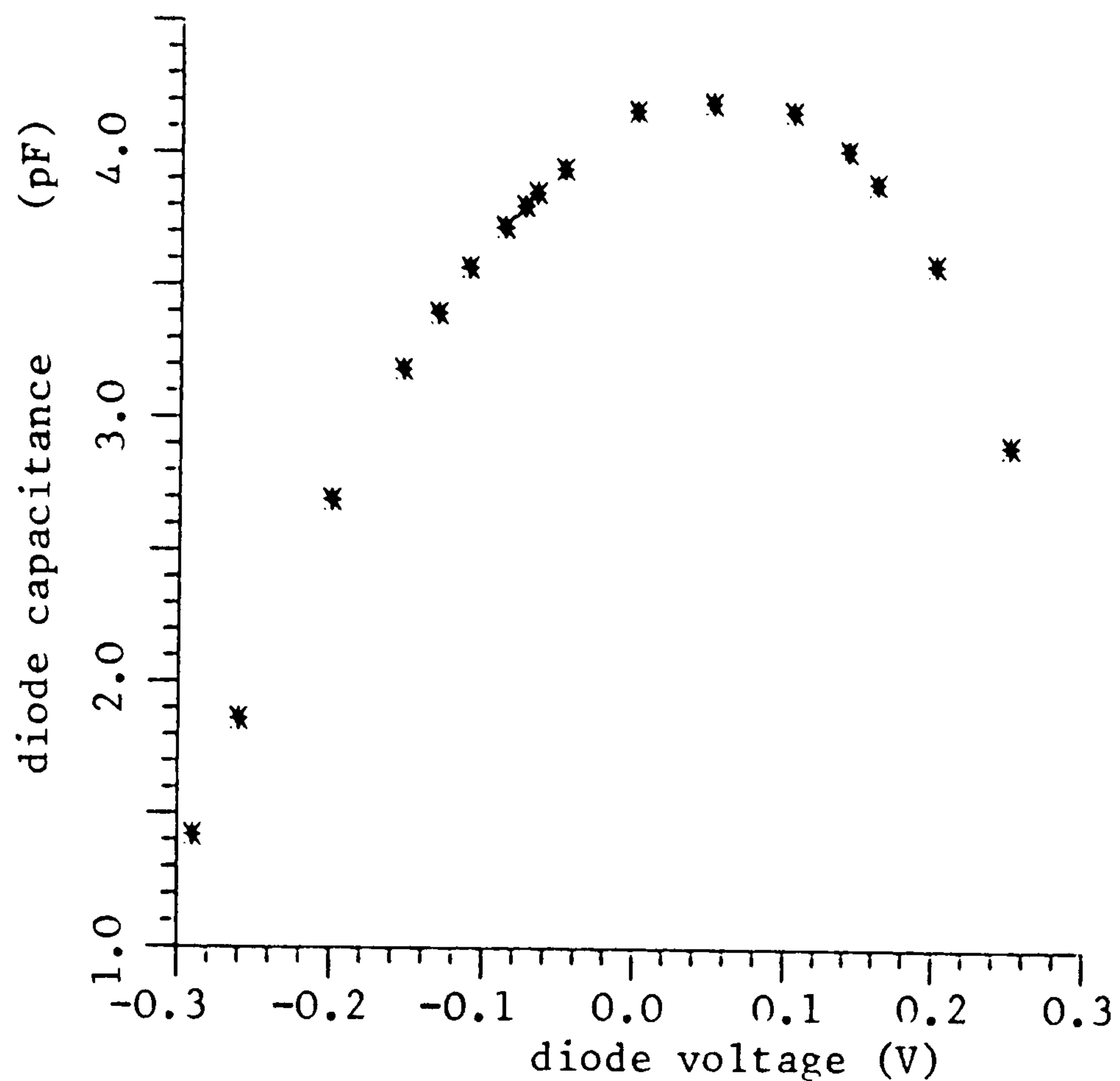

Fig.4.11 Barrier capacitance of a 25 x 25 μm^2 contact calculated from network analyser measurements.

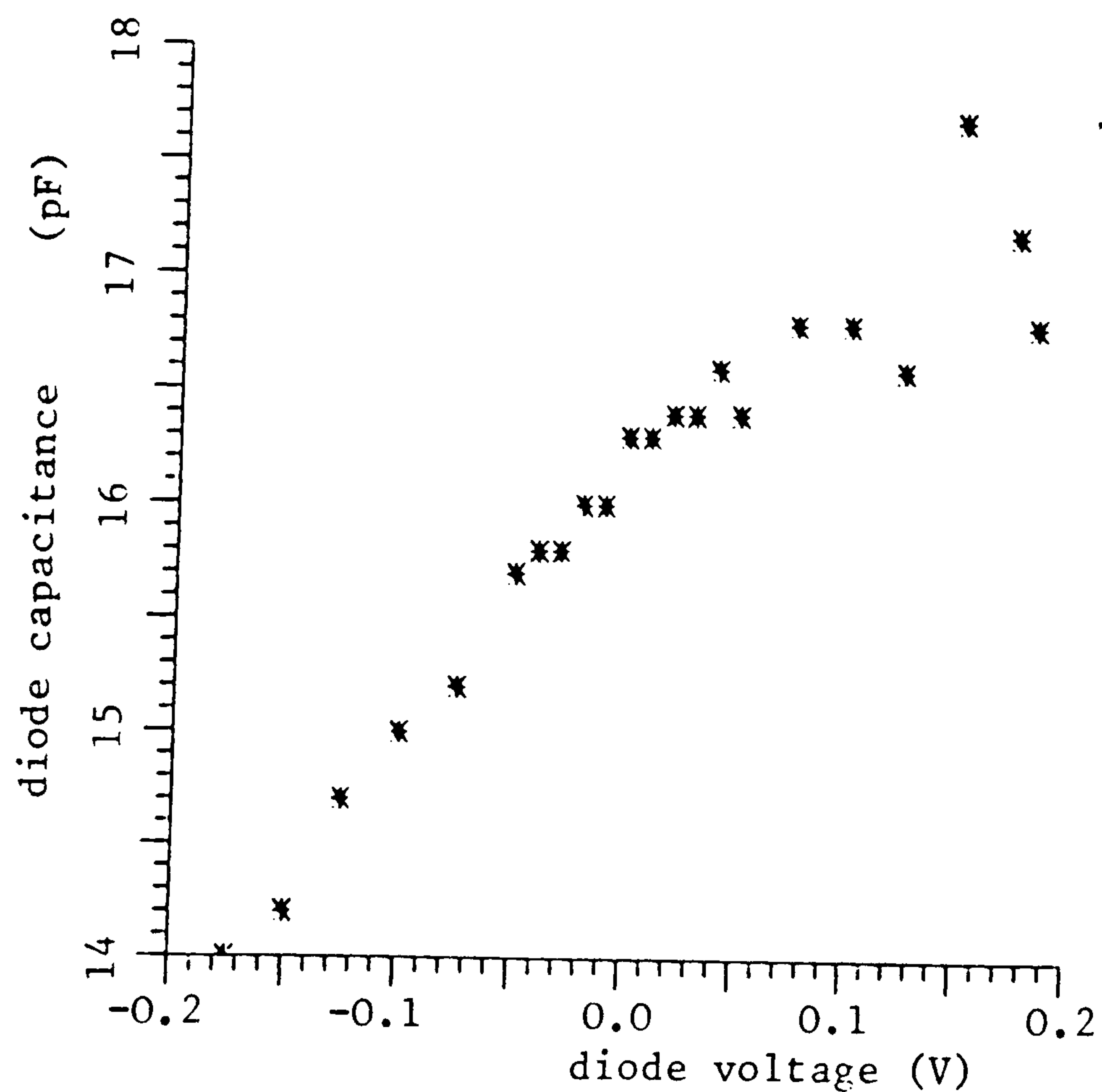

Fig.4.12 Barrier capacitance of a 50 x 50 μm^2 contact calculated from vector voltmeter measurements.

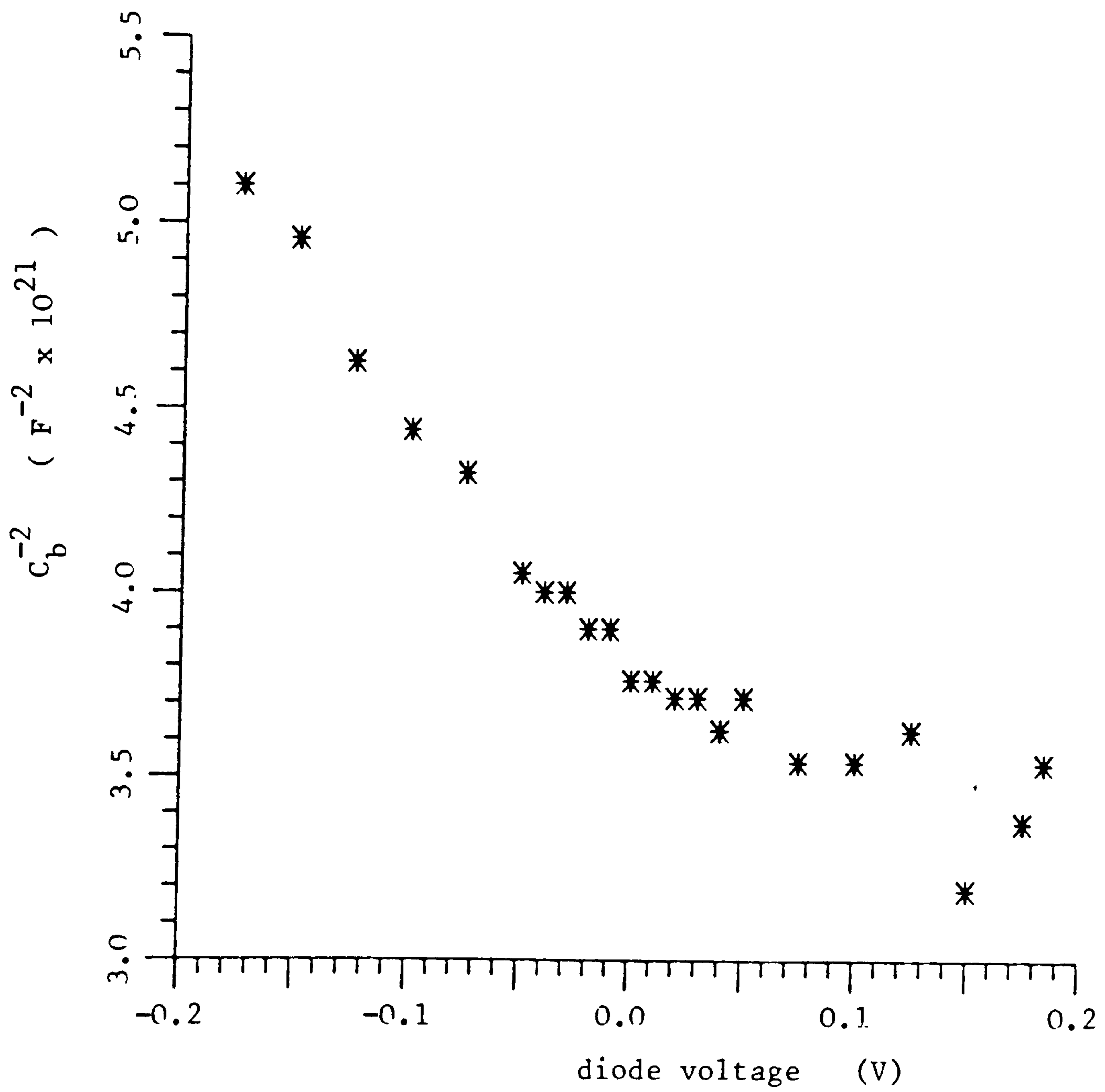

Fig. 4.13 Plot of C_b^{-2} (C_b is the barrier capacitance) against diode bias voltage, from the vector voltmeter measurements.

A more fundamental limitation to the forward bias barrier capacitance can be considered if the 'flat-band' situation is imagined; in this case the applied voltage is such that the barrier, which is the space-charge layer, effectively disappears - this means there is no charge storage and therefore no capacitance[89]. So, in fact, the barrier capacitance should theoretically tend to zero as the forward bias is increased indefinitely, rather than infinity as predicted by eqn. (4.13). The reason for the discrepancy is that the Schottky model, as represented by eqn. (4.13), takes into account only the width of the depletion region and not the charge storage in the region which actually causes the capacitance.

The maximum RC cutoff frequency will be that caused by the series resistance and barrier capacitance; with the values calculated above, the maximum -3dB cutoff frequency is $\approx$1.9GHz, using the zero bias value of capacitance. There will be some bias dependence in the RC cutoff, but this will not be very significant for the contacts investigated as the capacitance increases by a factor of only 1.2 between -150mV and +100mV. In many systems the device will 'see' a 50Ω load; then with the values of capacitance calculated above, assuming wide-band operation, the RC cutoff will be reduced to $\approx$750MHz; higher impedance systems will reduce the RC cutoff frequency further.

However, the above maximum RC cutoff frequency represents that for the prototype devices investigated in this thesis and not for smaller area devices which could be fabricated. For a $10\times10\mu m^2$ device the resultant reduction in capacitance would give an RC cutoff frequency of 11.7GHz, assuming the same series resistance. Although in many devices a reduction in area can cause an increase in series resistance resulting in some degradation of the RC cutoff, with the tunnelling contacts the reverse may be

true as the major part of the series resistance is probably caused by the thin semitransparent metallisation.

4.4 Effect of illumination

4.4.1 Optical current generation

Table 4.1 shows the optical current generation in a tunnelling contact under illumination from different lasers, and the absorption coefficients expected (from an analysis by Casey et al.[97]) in the GaAs material at the lasing wavelengths. Three semiconductor lasers have been used, all Hitachi devices, one of type HL7801E and two of type HLP1400, as well as a frequency-doubled neodymium:YAG laser. The Nd:YAG laser must be mode-locked for frequency doubling, and the sharp mode-locked pulses in conjunction with the nonlinear barrier make it difficult to ascertain directly the average photocurrent; the value in Table 4.1 has been estimated by comparing experimental conversion loss versus bias results with those from a computer modelling study - this will be described in Chapter 5.

In section 2.1 it was shown that the optically generated current consists of two distinguishable components: that due to carriers generated in the depleted (barrier) region, and that due to carriers generated outside this region which manage to diffuse into it. Equations for the magnitudes of these current components showing their dependence on device and material parameters were stated (eqns. (2.1) - (2.3)). These equations will now be applied to the analysis of the photocurrent generation in the tunnelling metal-semiconductor contacts.

For a doping concentration of about $2 x 10^{18} cm^{-3}$, the barrier width around zero bias will be approximately 25nm;

by assuming a set of α values for a certain doping concentration (close to $2\times10^{18}cm^{-3}$ since this value is used to estimate the depletion width) and a certain diffusion length, L_p, then from eqn. (2.3) the quantity

$$\lambda\{ 1 - [\exp(-\alpha w)/(1+\alpha L_p)] \}$$

at each wavelength, λ, should be proportional to the responsivities at the corresponding wavelengths, given in Table 4.1. The best fit to the experimental measurements has been found by using absorption coefficient values corresponding to a doping level of $2.5\Rightarrow3.0\times10^{18}cm^{-3}$, and a diffusion length of just under $0.4\mu m$. The doping level agrees fairly well with the value that has been assumed in estimating the depletion width. Hwang[98,99] has shown that the hole diffusion length in GaAs decreases rapidly at doping levels above $N_D\simeq10^{18}cm^{-3}$ (at $2\times10^{18}cm^{-3}$, $L_p\simeq1\mu m$, while it is less than $0.1\mu m$ when N_D is just $>5\times10^{18}cm^{-3}$). Other deep level impurities may reduce the diffusion length even further. The estimated diffusion length of $0.4\mu m$ agrees quite well with Hwang's measurements if the doping level in the devices is indeed over $2\times10^{18}cm^{-3}$.

At the shorter semiconductor laser wavelengths (797nm) it is estimated that the device responsivity is 33.3mA/W, while at the Nd:YAG laser wavelength the estimate is 58.5mA/W; these are both only approximately 15% of the expected responsivities, i.e. if it is assumed that the metallisation has negligible reflectance and that all of the available laser light is coupled into the devices, and if the loss of photo-generated carriers recombining near the interface is neglected - see the discussion at the beginning of section 5.1.

{laser} wavelength (nm)	measured optical power (mW)	measured photo-current (μA)	measured respon-sivity (mA/W)	expected $\alpha \div 10^4$ (cm^{-1}) at doping level:			
				high purity	2×10^{18} (cm^{-3})	3.3×10^{18} (cm^{-3})	6.7×10^{18} (cm^{-3})
{1} 797	2.7	90	33.3	1.5→1.4	1.4	1.25	0.87
{2a} 830	8.0	90	11.3	1.06	0.65	0.41	0.14
{2b} 857	10.0	37	3.7	0.85	0.23	0.061	0.019
{3} 532	3.42	200	58.5	≃10.0	≃10.0	≃10.0	≃10.0

Table. 4.1. Optical current generation in tunnelling contacts using lasers of different emission wavelengths, and expected optical absorption coefficients at these wavelengths.

The applied bias on the diode will affect the depletion width and so the contributions of the carriers generated within the barrier and outside it to the total current. Table 4.2 shows, for different values of diode bias, the expected depletion width and, for two wavelengths (λ=797nm and λ=532nm), the predicted total current normalised to the total current at zero bias at the corresponding wavelength. Absorption length values of 0.1μm at 532nm and 0.75μm at 797nm, as determined by Casey et al., and a diffusion length of 0.4μm, have been assumed. The total current has been calculated according to eqn.(2.3). The percentage contribution of the carriers generated in the depletion region to the total current has also been estimated.

It can be seen from Table 4.2 that the contribution of the carriers generated in the barrier is much more significant at shorter wavelengths, but that even at 532nm it is small compared to the diffusion current component. At the bias levels of interest for optically pumped mixing, -200 ⇒ +100 mV (see Chapter 5), the variation in the contribution of the carriers generated in the depletion region with bias is small, and the variation in the total current even less significant. This agrees with the measured results as shown in the illuminated and unilluminated I-V characteristics of Fig.4.14, in which the photocurrent generated in the device can be seen to be approximately independent of bias; the current generator model of the photocurrent described in section 1.3.1 is, therefore, applicable in the modelling of the tunnelling contact optically pumped mixer.

bias (mV)	expected depletion width (nm)	wavelength: 797nm		wavelength: 532nm	
		$I_{tot}/I_{tot,0}$	I_{drift}/I_{tot}	$I_{tot}/I_{tot,0}$	I_{drift}/I_{tot}
+300	19.0	0.988	6.87%	0.990	20.73%
+100	22.5	0.996	8.06%	0.997	23.98%
0	24.0	1.000	8.55%	1.000	25.32%
-100	25.5	1.003	9.04%	1.003	26.64%
-200	26.9	1.007	9.49%	1.005	27.84%
-400	29.5	1.012	10.35%	1.010	30.02%

Table. 4.2. Optical current generation dependence on bias.

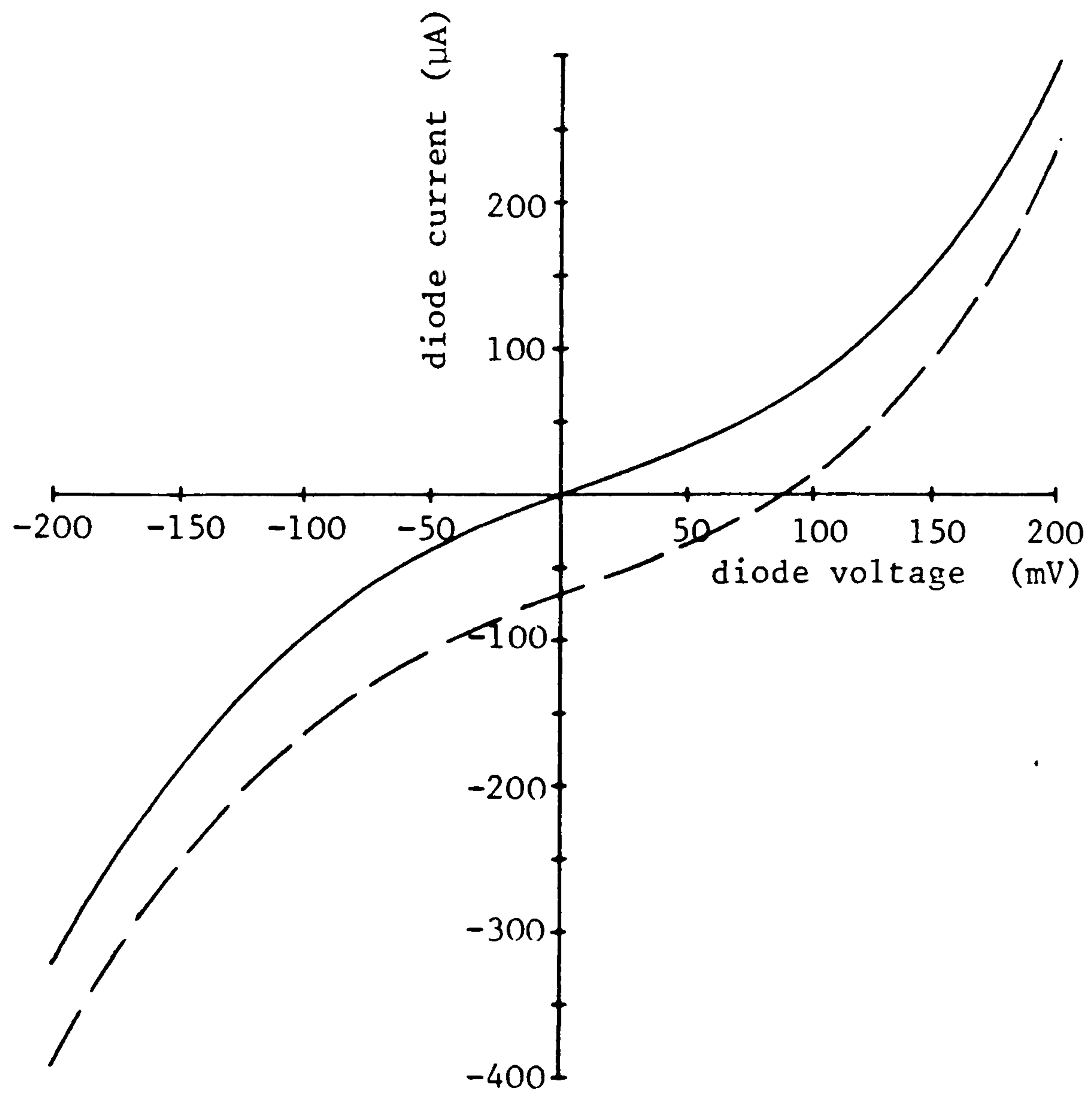

Fig.4.14 Measured I-V characteristics of tunnelling contact under illumination (broken line) and in the dark (solid line). Optically generated current is ≃ 70μA.

4.4.2 Frequency response limitations

From Table 4.2 it can be seen that the larger contribution to the total current is made by the carriers generated outside the depletion region. The transit-time limitations can then be considered to be mainly due to the minority-carrier diffusion process, and these limitations were described in section 2.1.3.

Fig.4.15 shows the relative (power) response to modulated incident light versus the modulation frequency for the tunnelling contacts assuming the frequency response is limited by transit-times due to minority-carrier diffusion only. The response is shown for five different values of optical absorption length ($1/\alpha$ = 0.1, 0.25, 0.5, 0.75, 2.5μm) for a device in which the hole (minority-carrier) diffusion length is 0.4μm, and the hole diffusion constant has a typical value of $9cm^2/s$. It can be seen that for illumination at a wavelength, λ=797nm, with $1/\alpha$=0.75μm, the transit-time-limited -3dB cutoff frequency ≈ 2.4GHz. For illumination at the frequency-doubled Nd:YAG laser wavelength, λ=532nm, with $1/\alpha$=0.1μm, the transit-time-limited cutoff frequency is just under 24GHz. The curves shown in Fig.4.15 for the frequency response at each illumination wavelength are normalised to the d.c. response at that wavelength. As has already been discussed, the d.c. response itself depends on the illumination wavelength; from the discussion in 2.1.1 it is obvious that the response at longer wavelengths, in terms of the magnitude of the signal detected, will deteriorate due to fewer carriers contributing to the total current as well as due to transit-time limitations.

There will be a small component in the photocurrent due to drift only, and this will enhance the frequency response. For example at the semiconductor laser wavelengths, it can be assumed that at -150mV bias 9.25% of the photocurrent is due to drift only. If the drift

time is assumed negligible, then according to the analysis of section 2.1.3, only 61.45% of the diffusion current would have to contribute effectively, instead of 70.7%; the transit-time-limited cutoff is increased to 4.6GHz. At +100mV, due to the smaller drift component (8%), the transit-time-limited cutoff is increased to slightly less than this, 4.0GHz. At frequency-doubled Nd:YAG laser wavelengths, the contribution of carriers generated in the depletion region is likely to be even more significant.

Of course, for the actual device cutoff frequency, the RC limitations as discussed in section 4.3 must also be considered. For the optically pumped mixer devices characterised in this chapter, with RC cutoff frequencies of 1.9GHz, the effect of transit-time limitations will be very significant at semiconductor laser illumination wavelengths, since the cutoff frequencies due to the two effects are similar; with shorter wavelength illumination the actual cutoff frequency will tend to that limited by RC considerations. Using the diffusion limitations only, it can be stated that with $1/\alpha=0.1\mu m$, the actual -3dB cutoff frequency will be at least 1.6GHz, whereas for $1/\alpha=0.75\mu m$ it will be at least 800MHz. For smaller area devices, of area $10x10\mu m^2$, and with an RC cutoff frequency of 11.7GHz, the effect of transit-time limitations will be much more significant at longer wavelengths. Assuming a full transit-time-limited cutoff of over 4GHz at 797nm illumination wavelength, the actual cutoff frequency will be approximately 3GHz. For a 532nm illumination wavelength the actual cutoff frequency will probably approach 10GHz.

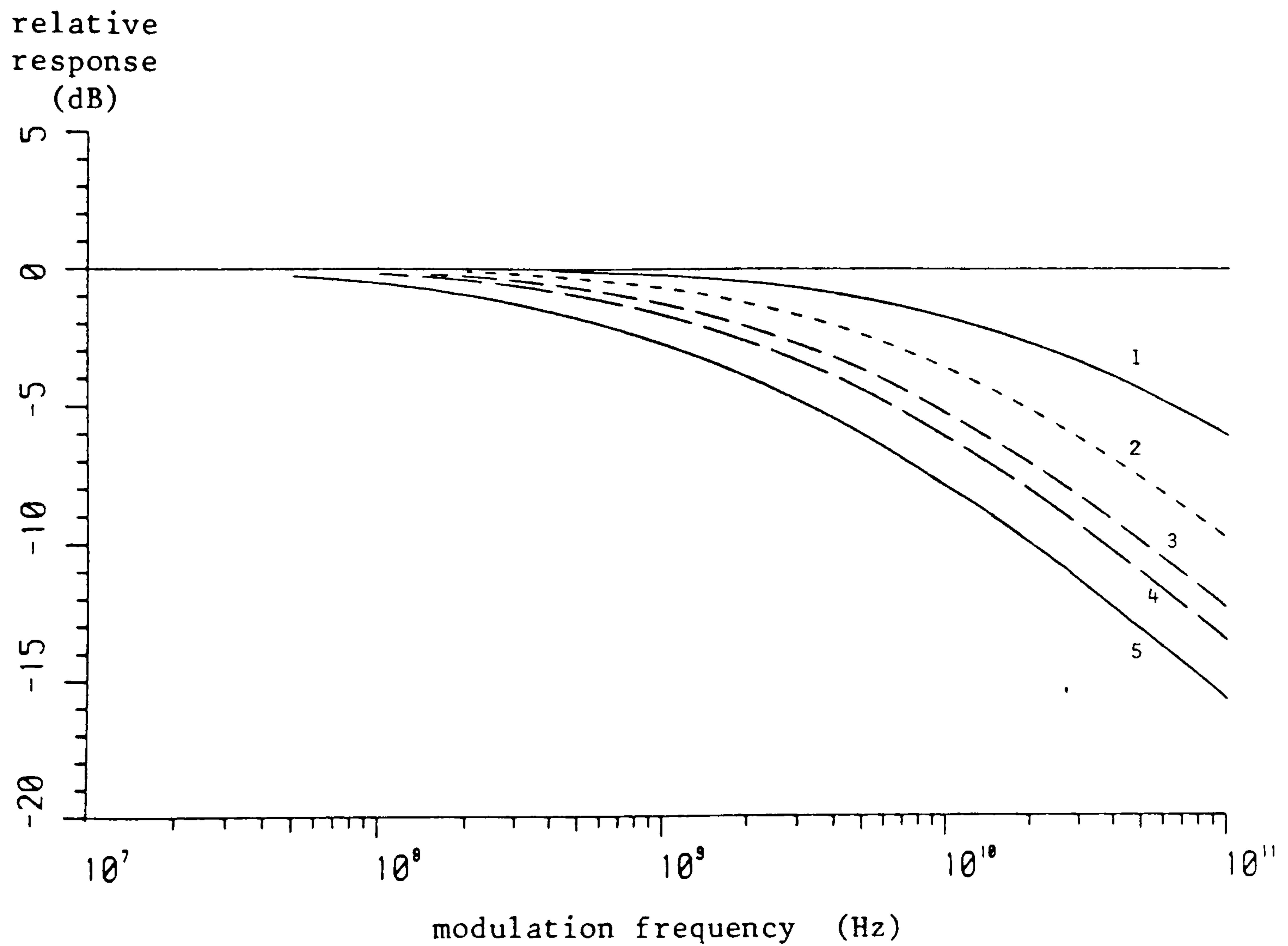

Fig.4.15 Predicted response (normalised to dc level) of tunnelling contact to modulated incident light versus the modulation frequency, taking into consideration transit-time limitations only. (Parameter: absorption length, $1/\alpha$)

1: 0.1μm; 2: 0.25μm; 3: 0.5μm; 4: 0.75μm; 5: 2.5μm.

4.5 Chapter Summary

Tunnelling metal-semiconductor contacts fabricated at RSRE by modifying a photodiode process have been characterised. The modification consisted of forming a semitransparent Schottky contact to heavily doped (2 x $10^{18}cm^{-3}$) rather than lightly doped n-type GaAs material.

Measurements of the I-V characteristics of the metal-semiconductor contacts have shown poor fit to typical exponential diode equations, especially in reverse bias. However, the shape of the characteristics do follow closely a theory for field and thermionic-field emission due to Padovani and Stratton[90]. This theory has been used to form analytic expressions for the I-V characteristics of the tunnelling contacts, which, with the correct selection of parameters, show good agreement with the measured characteristics over a useful bias range.

Further measurements on a $25x25\mu m^2$ device, which was the contact area of the devices used in the mixing experiments to be described in Chapter 5, indicated a barrier capacitance of just over 4pF. The series resistance was perhaps as high as 20Ω, suggesting that the devices have a maximum RC -3dB cutoff frequency ≃1.9GHz.

By measuring the responsivity of the contacts at different wavelengths the minority-carrier (hole) diffusion length has been estimated. Over reasonable bias ranges, and with the illumination at wavelengths between 532nm and 860nm, the photocurrent is mainly due to the diffusion of carriers generated in undepleted material. At GaAs laser wavelengths ≤800nm the response to modulated light will have a corner frequency due to carrier diffusion limitations ≃ 2.4GHz. However, the short absorption length (≃0.1μm) at 532nm (frequency-doubled Nd:YAG laser wavelength) results in a large number of

carriers being generated very near the barrier; carrier diffusion limitations are now estimated to set in only at frequencies ≃24GHz. The small proportion of carriers generated in the depletion region will enhance the high-frequency cutoff. Effectively, the bandwidth in the short wavelength case will be limited by RC considerations - the actual cutoff frequency is estimated to be at least 1.6GHz - while with illumination near 800nm wavelength the cutoff frequency is reduced towards 800MHz. For small area devices ($10 \times 10 \mu m^2$), however, cutoff frequencies in X-band may be possible at short wavelengths.

CHAPTER FIVE

TUNNELLING METAL-SEMICONDUCTOR CONTACT: DEVICE PERFORMANCE

5.1 Preliminary predictions 158

5.1.1 Conversion loss dependence on embedding impedance 160

5.1.2 Conversion loss dependence on bias 160

5.2 Conversion loss measurements using semiconductor lasers 166

5.2.1 Provision of the optical l.o. 166

5.2.2 Experimental circuit arrangement 170

5.2.3 Results 174

5.3 Conversion loss measurements using Nd:YAG laser 177

5.3.1 Experimental arrangement and results 177

5.3.2 Discussion using time domain model predictions 178

5.4 Other parameters 185

5.4.1 Noise performance 185

5.4.2 Diode impedance 192

5.4.3 Dynamic range 195

5.4.4 Operation frequencies 197

5.5 Comparison with photodetector-mixer combination 201

5.5.1 Conversion efficiency considerations 201

5.5.2 Noise performance considerations 206

5.6 Chapter summary 211

In this chapter the performance of tunnelling metal-semiconductor contacts as optically pumped mixers is described. In section 5.1 predictions for the conversion loss assuming high (but not unreasonable) values of optically generated current from the computer models described in Chapter 3 are discussed; these predictions can be considered to be near the optimum performance that can be expected. Experimental measurements of the conversion loss using semiconductor laser (sec.5.2) and neodymium : yttrium aluminium garnate (Nd:YAG) laser (sec.5.3) illumination as the optical l.o. are then described. The other performance parameters pertaining to mixer operation, including the noise ratio, are discussed in section 5.4. A comparison of the performance of the tunnelling contact in particular, and optically pumped mixers generally, with conventional photodetector-mixer combinations is given in section 5.5.

5.1 Preliminary predictions

The predictions presented in this section assume up to 500µA average photocurrent with 100% (sinusoidal) modulation. The photocurrent generated in the device is related to the optical power incident on the contact by:

$$I_{ph} = qP_{opt}(1-R)\frac{\lambda}{hc}\left(1 - \frac{\exp(-\alpha w)}{1+\alpha L_p}\right) \qquad (5.1)$$

using equation (2.3), and the terminology used there. Assuming the metallisation has negligible reflectance, the above equation suggests that at an illumination wavelength of 532nm ($1/\alpha \simeq 0.1\mu m$) an average incident optical power $\geq$1.4mW would be required to generate the 500µA average

photocurrent - this is with L_p=0.4μm and w=25.5nm (corresponding to approximately 100mV reverse bias). At just under 800nm, with $1/\alpha \simeq 0.75\mu m$, an average incident optical power of ≥2.2mW would be required to generate this current. These are average values - for 100% modulation twice these power levels should be available from the optical local oscillator sources.

From the above calculations, 500μA average photocurrent is regarded as a theoretically attainable value in tunnelling contacts with high laser power levels. However, it is interesting to note that with the responsivities measured for the tunnelling contacts investigated in this thesis, the required optical power levels would be even higher - over 8.5mW average power at 532nm and over 15mW at 797nm. One reason why the required power levels are so much higher (or, conversely, why the measured responsivities are so poor) is that not all of the available laser power can be effectively focussed onto the contacts. This difficulty has arisen for $25x25\mu m^2$ contacts; with smaller area devices the focussing will be even more problematical. Apart from focussing, other reasons for the reduced responsivity are the reflectance of the metallisation, and, probably, the recombination of carriers generated very near the metal-semiconductor interface which do not contribute to the current, and, indeed, may be extracted as an opposing current as discussed in section 2.1.2. The latter effect is especially important at short wavelengths, but should not be unduly restrictive in the relatively high fields (tens of kV/cm) present in the heavily doped contacts.

5.1.1 Conversion loss dependence on embedding impedance

Fig.5.1 shows the conversion loss dependence on the embedding impedance at the l.o./signal frequencies, termed the 'source' impedance, with a constant external bias using frequency domain model predictions. The source impedance in the case of the frequency domain model is in fact a resistance, since the diode capacitance and other reactive elements are ignored in the mode in which the program is used in this thesis. Keeping the external bias constant and changing the source impedance also alters the quiescent diode voltage; the peak in the curve is due to this variation of the operating point - the mechanism behind it is described in sec.5.1.2. It is useful, therefore, to consider the conversion loss variation with source impedance at a constant diode voltage.

Fig.5.2 shows this variation for a tunnelling contact at a diode voltage, V_d=-150mV, and for two photocurrent levels of average values 500μA and 250μA (with 100% modulation in both cases). The importance of having a sufficiently high impedance to convert the photocurrent variation to a large voltage and hence conductance variation is clearly demonstrated.

5.1.2 Conversion loss dependence on bias

Fig.5.3 shows the conversion loss dependence on bias predicted by the frequency domain model. A minimum of $L_c \simeq 10$dB can be seen at $V_d \simeq -145$mV. The peak in the conversion loss curve is due to the near asymmetry of the I-V characteristic around zero bias which causes a cancellation of the fundamental component of the diode (dynamic) conductance. It is useful to consider the variation of dynamic conductance with diode voltage, which can be deduced from the dynamic resistance plot of

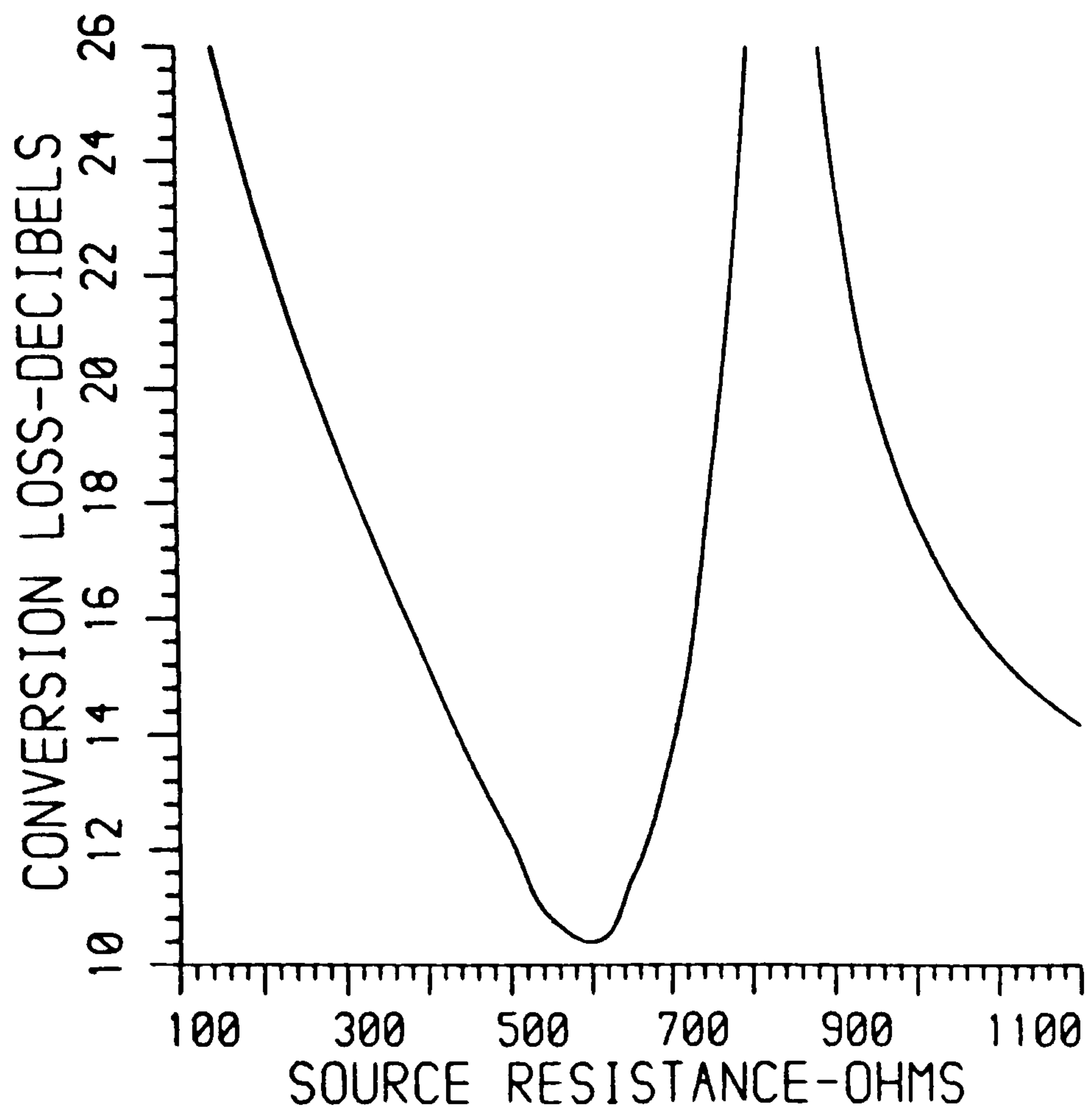

Fig.5.1 Conversion loss variation with source resistance predicted by frequency domain model. Average photocurrent of 500μA, 100% modulation, constant external bias.

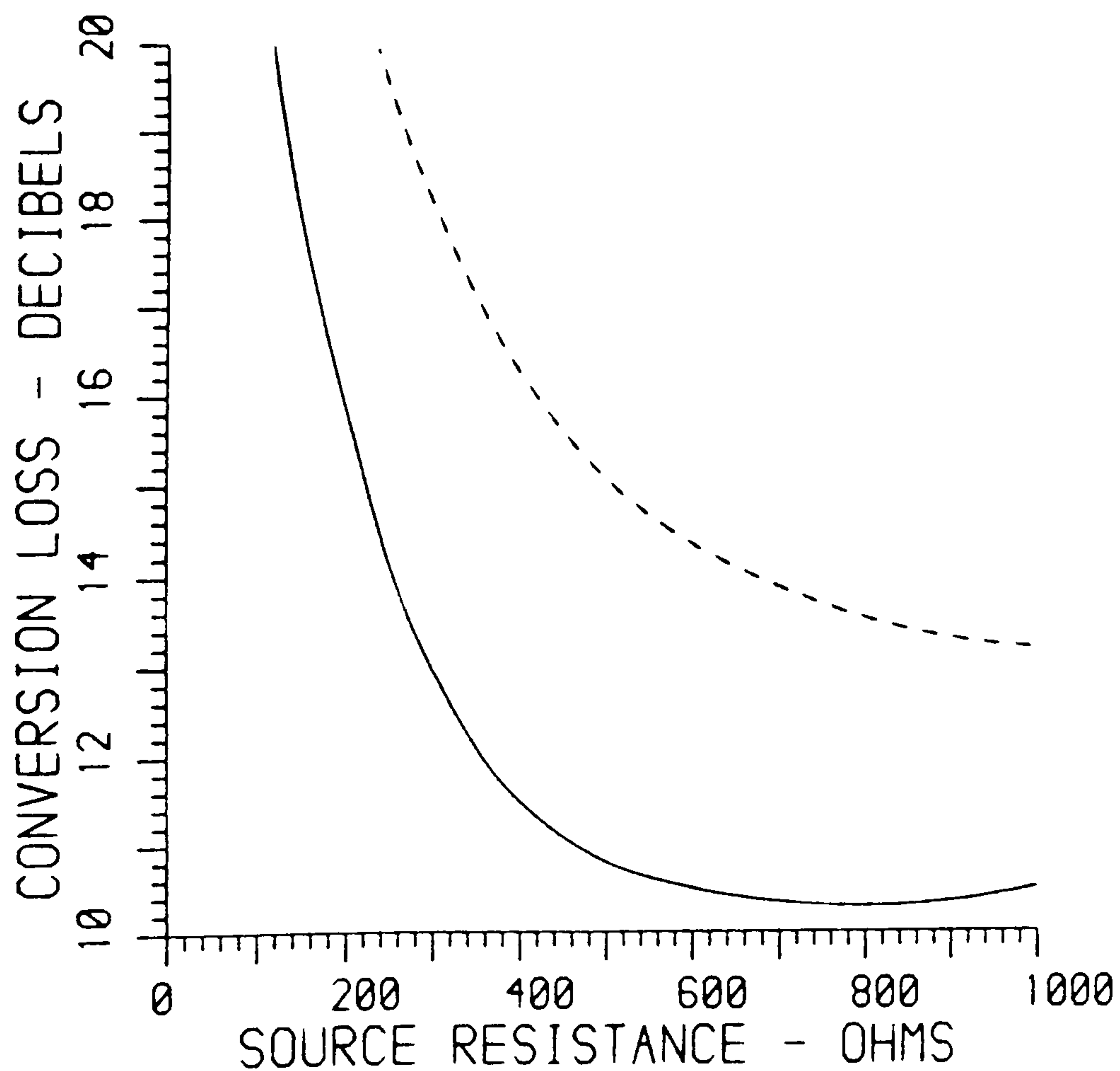

Fig.5.2 Conversion loss variation with source resistance predicted by frequency domain model. Constant (-150mV) diode voltage, ——— 500μA, - - - - 250μA av. photocurrent.

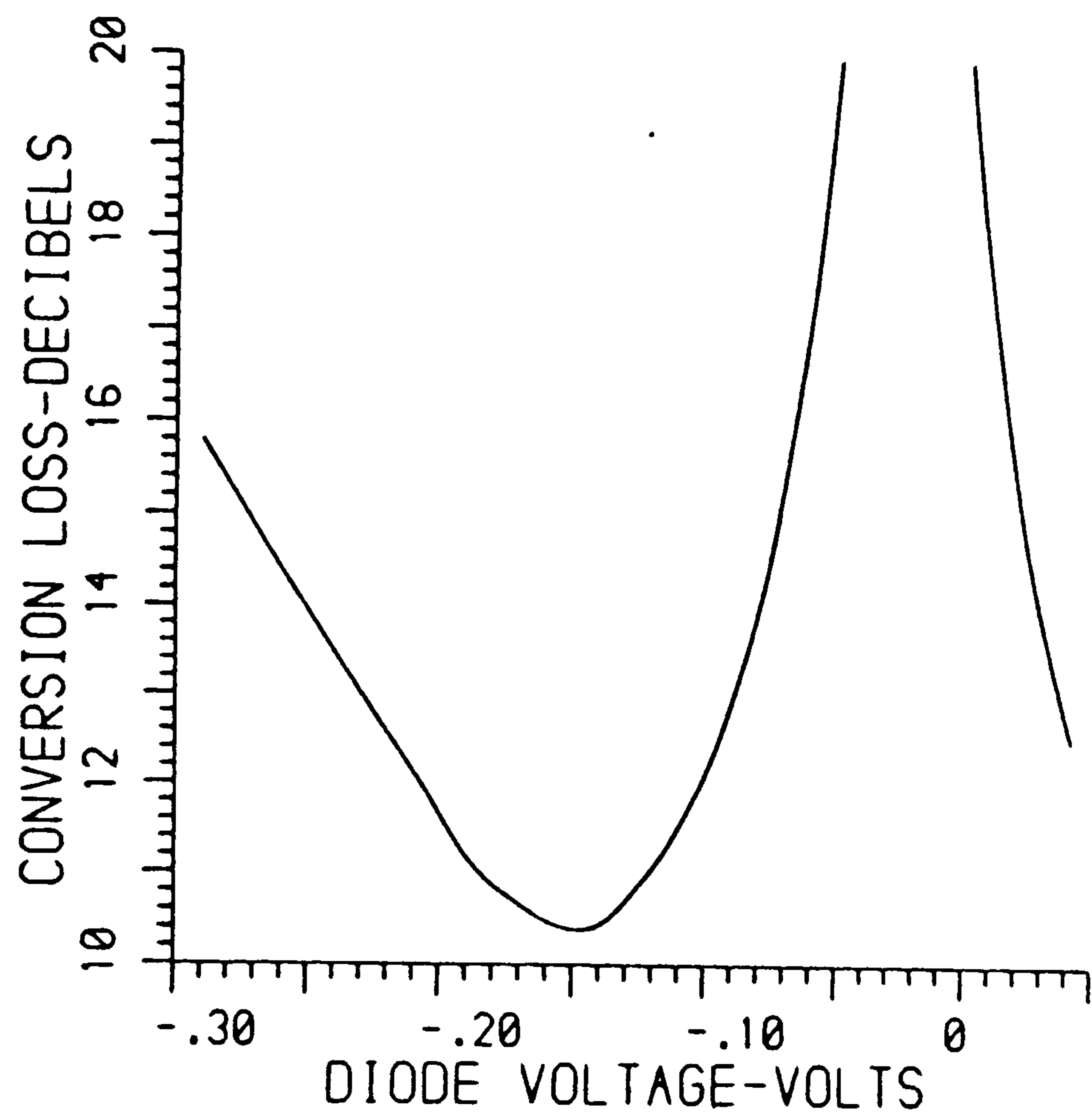

Fig.5.3 Conversion loss dependence on diode bias predicted by frequency domain model. Source resistance 750Ω, average photocurrent 500μA, 100% sinusoidal modulation.

Fig.4.10. In operation the mixer diode will have some quiescent value of dynamic conductance, with a variation around this point due to the local oscillator modulation. Although such a limit should never be reached because, by definition, the local oscillator is a large signal, it can be imagined that for a small l.o. signal the fundamental component of conductance will be proportional to the slope of the dynamic conductance curve (which would be the d^2I/dV^2 curve, or the diode nonlinearity). At the conductance minimum (resistance maximum) the fundamental component will be zero. For a real l.o. signal, there will always be variation about the minimum, but the positive and negative slopes may cancel and in this case the second harmonic component of the dynamic conductance will be of significant magnitude.

Fig.5.4 shows the variation in the fundamental component of the diode dynamic conductance with bias voltage (in this case predicted by the time domain model).

The conversion loss variation as predicted by the time domain model is shown in Fig.5.5, in this case for reverse bias only. The parameters are equivalent to those used in the frequency domain model - same diode characteristics and photocurrent level - although the operation frequencies, l.o. at 110MHz and i.f. of 10MHz with upper-sideband down-conversion, and the diode capacitance, 4pF at zero bias, are now also relevant. The embedding impedances at the l.o., signal and image frequencies are again fairly high and mainly resistive (750Ω). The effect on the conversion loss of varying the embedding impedances at the other harmonic and sideband frequencies is not very great (less than 1dB), which is acceptable if only a general idea of the behaviour of the device is required, and is due to the fact that the predicted conversion is still relatively inefficient, $L_c \simeq 15$dB. The loss predicted by the time domain model is higher than that predicted by the

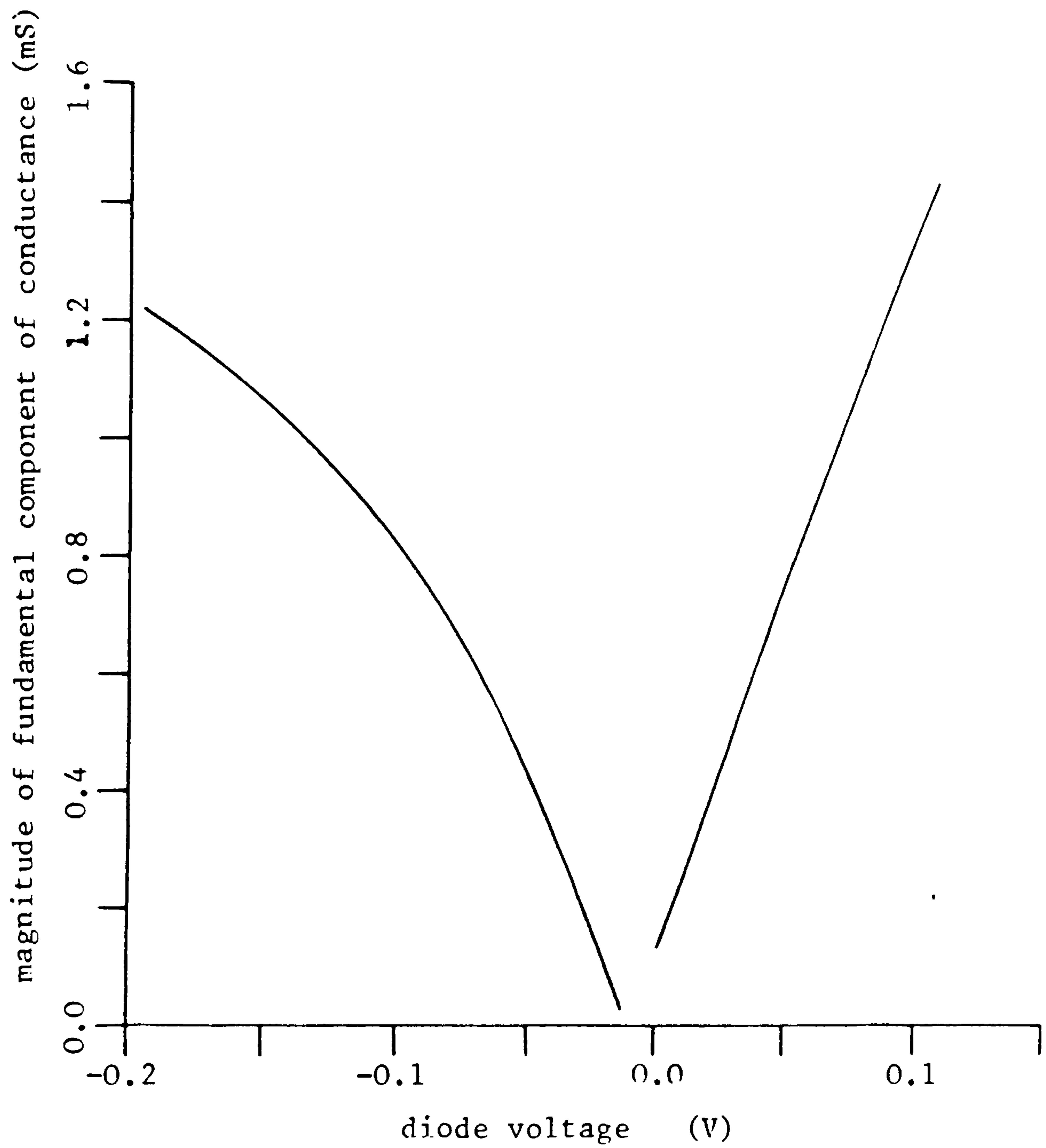

Fig.5.4 Variation of fundamental component of diode (dynamic) conductance with bias as predicted by results from the time domain model. Source resistance 750Ω, average photocurrent 500μA, 100% sinusoidal modulation.

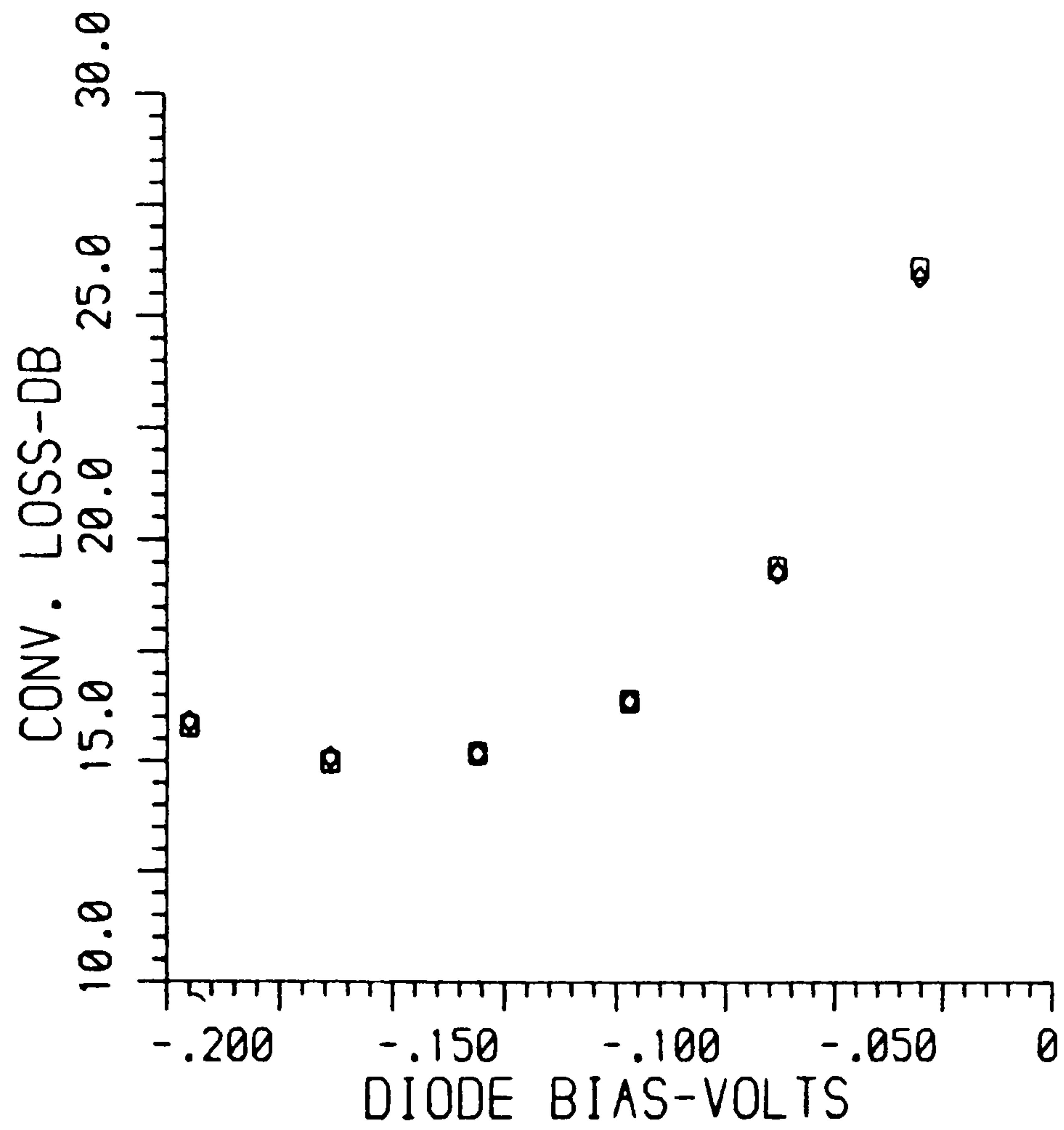

Fig. 5.5 Conversion loss dependence on diode bias predicted by time domain model. Source resistance 750Ω, average photocurrent 500μA, 100% sinusoidal modulation.

(Squares represent upper-sideband down-conversion; diamonds lower-sideband down-conversion.)

frequency domain model, so the diode capacitance must be having a detrimental effect on performance. No attempt has been made to optimise the embedding impedances at the l.o., signal and image frequencies; if this is done the conversion loss can be reduced towards the 10dB predicted in the frequency domain model (see the discussion at the end of section 5.4.4).

5.2 Conversion loss measurements using semiconductor lasers

The basic test arrangement required to perform conversion loss measurements on the optically pumped tunnelling mixer is shown in Fig.5.6. Both the tunnelling contact (the mixer device) and the laser will have d.c. bias arrangements, which, for simplicity, are assumed within the respective device blocks in Fig.5.6.

5.2.1 Provision of the optical local oscillator

The l.o. signal provided by a semiconductor laser in the test arrangement of Fig.5.6 is due to the modulation of its bias current. This modulation is provided by a signal generator via an a.c. bias path containing a resistor of nominal value 47Ω; together with the laser diode 'on' resistance (≃2→3Ω) the laser circuit is then approximately matched to the signal generator output impedance of 50Ω. For any known signal generator output power level the laser bias current variation can then be calculated.

Two types of semiconductor laser have been used: Hitachi types HL7801 and HLP1400. The results described in this section, however, are from measurements using the former, with which better performance was achieved despite

the fact that the HLP1400 lasers are higher power devices. There are two reasons for the superior performance with the HL7801 devices:

(a) the absorption coefficient in the heavily doped GaAs falls rapidly at wavelengths above 800nm; the HLP1400 devices emit at around 850nm where the responsivity is low, whereas the HL7801 devices emit at 780→800nm. This was described in section 4.4.1.

(b) due to (a), high optical power is required from the HLP1400 devices to generate a significant photocurrent. Even in the case of the shorter wavelength HLP1400 device emitting at 830nm (see section 4.4.1), where an optically generated current of similar magnitude to that generated using a HL7801 device can be generated, the quiescent laser bias current required to do this is so far above the lasing threshold current that, with the signal generators used, the laser is not 'switched off' during the l.o. cycle. The modulation depth is thus less than 100%, and it is, of course, the modulated photocurrent which provides the l.o. pumping. The maximum power available from the signal generators used was 13dBm (20mW), which should give a peak laser bias current variation of ±28mA. A typical operating point for a HL7801 device is 55mA, which is (typically) just over 12mA above threshold; in the case of the 830nm HLP1400 laser, the operating point to generate similar photocurrent is ≃95mA - approximately 35mA above the lasing threshold in this device.

The above arguments also show that the assumption of pure sinusoidal modulation used in the analyses of section 5.1 is a simplification. For the HL7801 device at an operating bias of 55mA, and with a.c. modulation of 13dBm, giving a bias current modulation of ±28mA, the laser will obviously be 'off' for a significant part of the l.o.

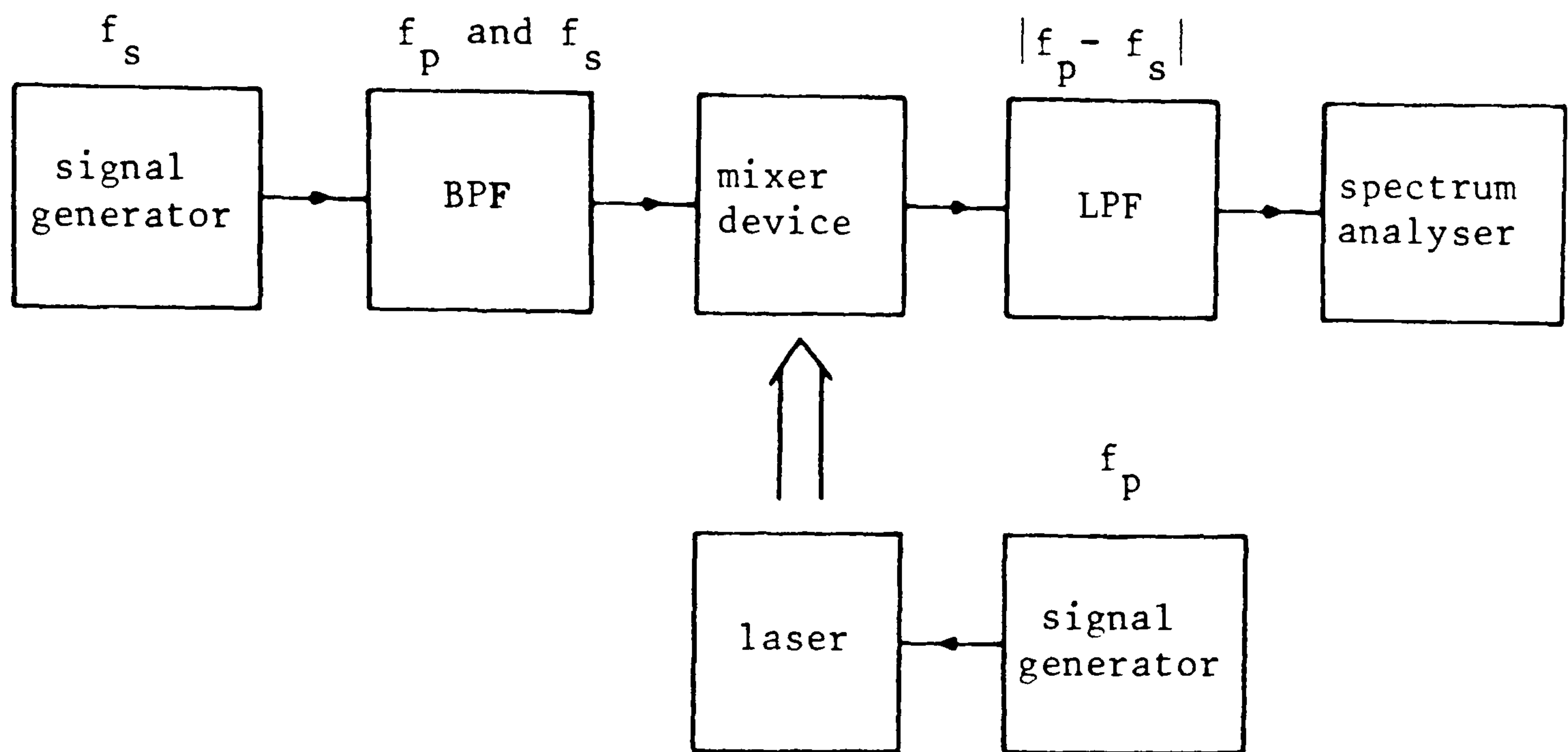

Fig.5.6 Basic test arrangement for measurement of conversion loss of optically pumped mixer.

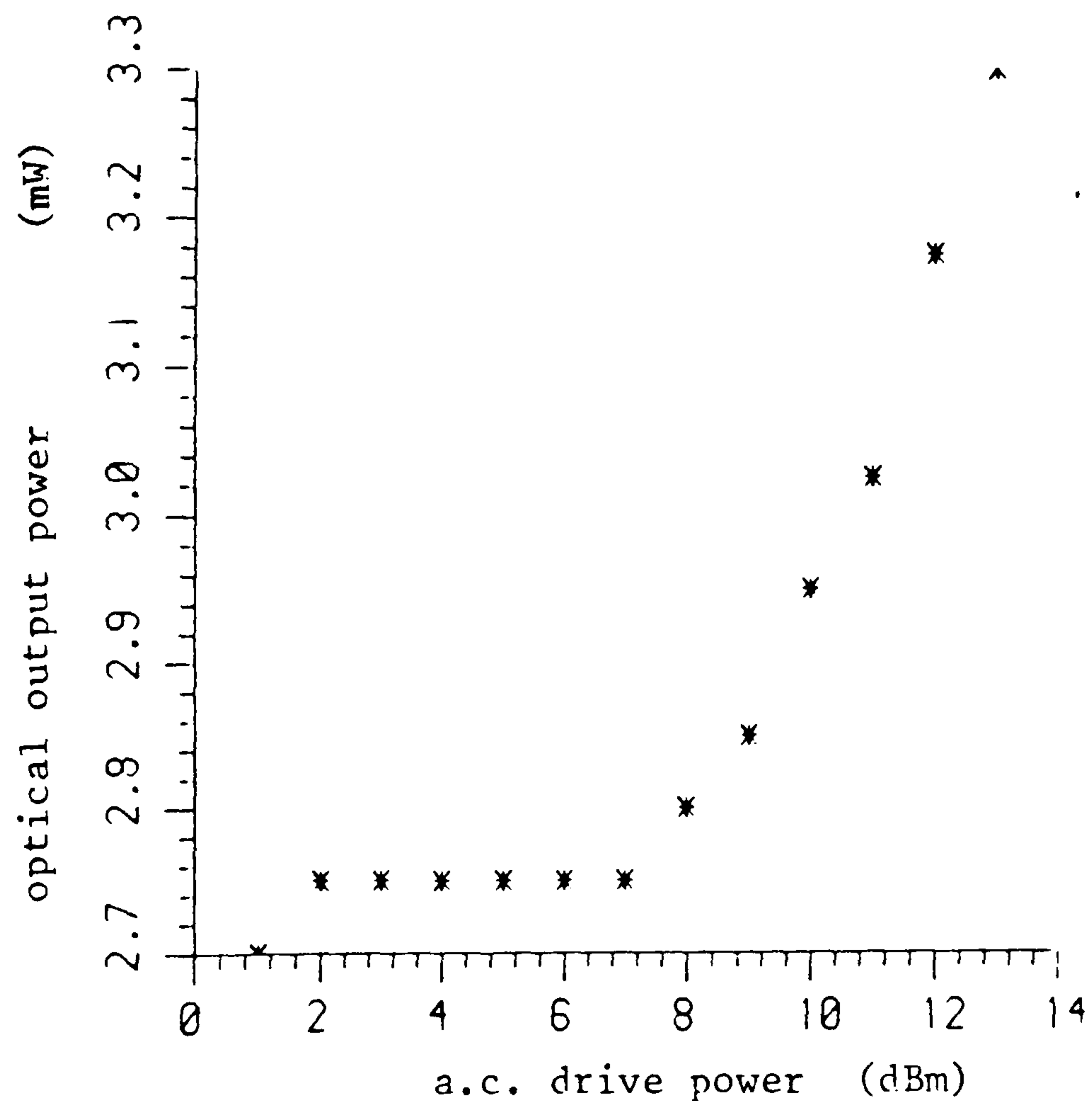

Fig.5.7 Optical output power of HL7801E laser versus the a.c. drive power with constant laser bias current of 55mA.

cycle. Performance should still be improved with higher a.c. drive on the laser as the peak and average optical power levels are increased above their levels when the laser is unmodulated. At a d.c. bias point of 55mA the average optical power output should be approximately constant for a.c. drive levels of up to 5.5→6.0dBm, which would give the necessary current variation to switch the laser 'off' or '100% modulation'. Above this level the average optical power should be affected. The results of measurements of the optical power output at different a.c. drive levels for a bias current of 55mA are shown in Fig.5.7; it can be seen that the output is indeed flat up to a signal generator output of 7dBm. The relatively small discrepancy could be explained by less than optimum coupling between the signal generator and the laser.

There are further reasons why the assumption of sinusoidal modulation is a simplification: for large signal variations the power output versus bias current curve cannot be considered exactly linear, this becoming especially true for high current levels where the curvature due to the diode series resistance is more noticeable, and for variations around the threshold where there is significant deviation from linearity.

From the discussion in section 4.4.1 the optical illumination can be considered to produce a directly proportional photocurrent. For laser a.c. drive levels greater than or equal to that necessary to produce 100% modulation, the photocurrent can be considered to consist of a d.c. component and a fundamental a.c. component of equal amplitude, plus some higher order components giving the non-sinusoidal waveform as described above - the actual photocurrent waveform is different to that in the modelling described earlier. In the frequency domain model only the fundamental components of voltage, current, and conductance are considered, so the higher order components

could not be modelled anyway. However, since the higher order components should be of a much lower level than the fundamental component and will be further attenuated by transit-time limitations, the modelling of such components in the time domain model is considered to be a somewhat unnecessary complexity.

In the test arrangement, the mixer and its embedding circuit were mounted on a block attached to a three-axis translation stage with micrometer screw adjustments; this stage could be mounted onto either an optical table or an optical bench. The focussing of the semiconductor laser light beam onto the small area contact was performed using a x20/0.54 N.A. microscope objective.

5.2.2 Experimental circuit arrangement

As has been explained, for efficient performance it is necessary for the tunnelling contact to be embedded in a circuit of sufficiently high impedance at the l.o. frequency. This was borne out by initial conversion loss experiments on a tunnelling contact optically pumped mixer in a 50Ω system[45]; very high conversion loss was obtained, as can be seen from Fig.5.8. Therefore, in line with the initial predictions already described, the tunnelling contact was embedded in a higher impedance system.

The experimental circuit arrangement for the mixer experiments is shown in Fig.5.9. The necessary impedance at the l.o. frequency was obtained using a tuned r.f. transformer circuit (L_1 and C_1 in the circuit diagram); the circuit transforms the impedance of the signal generator (50Ω) to an effective embedding impedance ≃750Ω and it also provides matching for the input signal. C_2 and L_2 are resonant at the l.o./signal frequencies, presenting

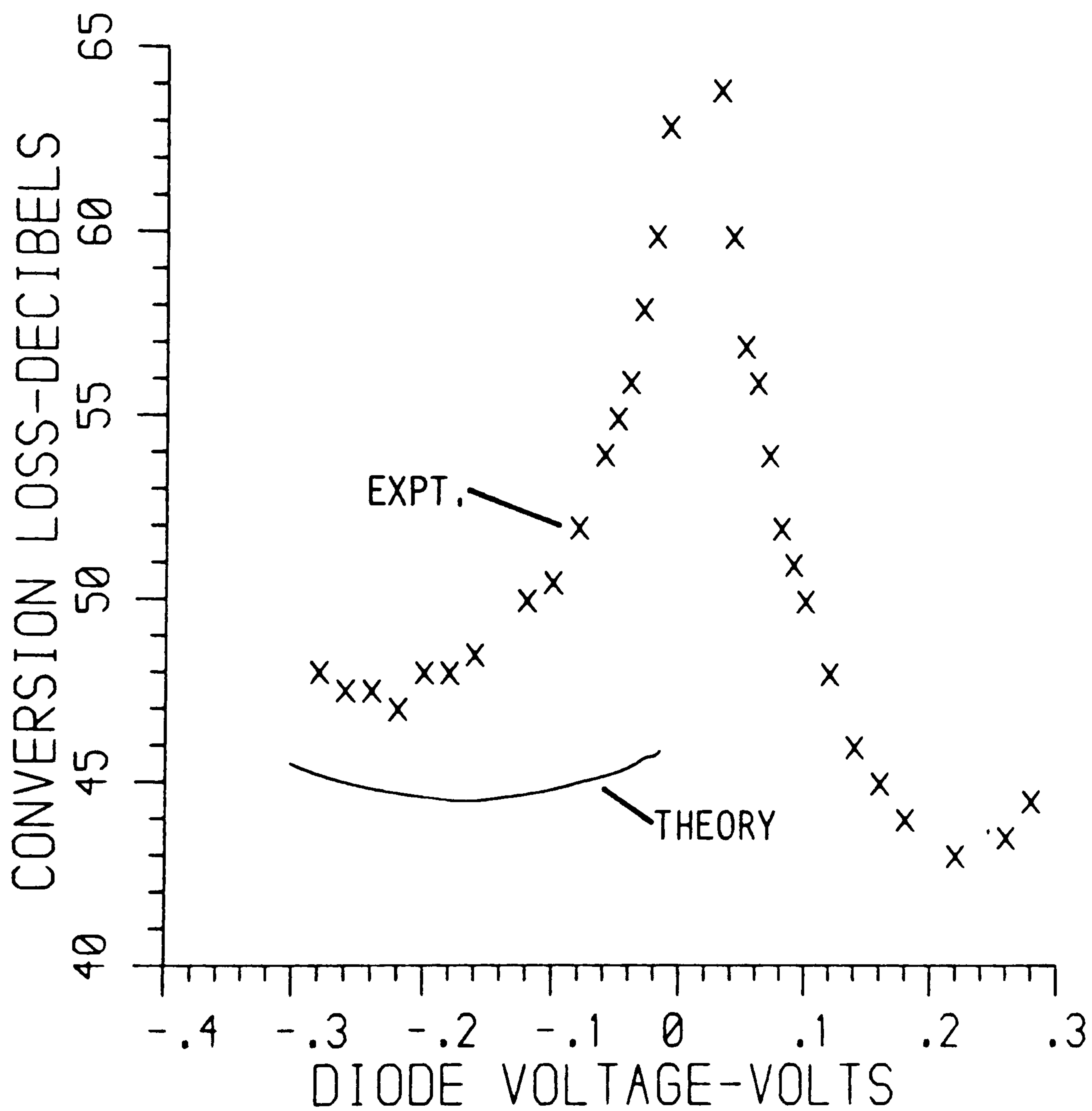

Fig.5.8 Measured conversion loss variation with diode bias voltage in unmatched 50Ω system. The photocurrent generated was approximately 50μA. Also shown are predictions for the tunnelling contact mixer in a 50Ω system for this level of photocurrent from the frequency domain model.

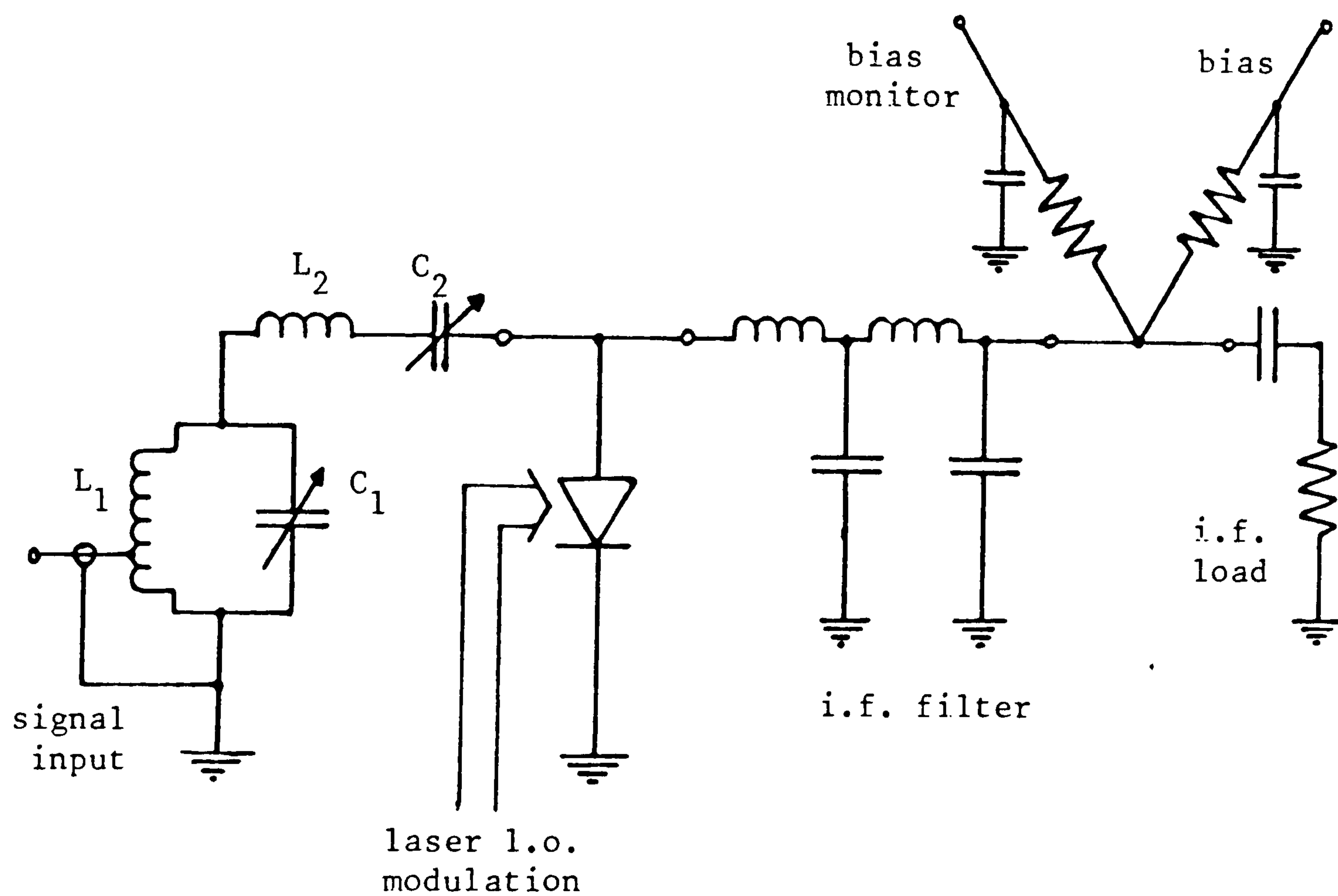

Fig.5.9 Experimental circuit arrangement for the tunnelling contact optically pumped mixer. The high input impedance for the signal and l.o. frequencies was provided by transformer-coupling the signal source.

a high impedance to out-of-band frequencies. In reality, of course, there will be some interaction between all four of the aforementioned elements and the quiescent barrier capacitance as well. The i.f. output was obtained, and the d.c. bias applied via a low-pass filter in parallel with the input network - the i.f. filter was matched in the pass-band to its terminating load resistance of about 500Ω. Again, at the higher, out-of-band frequencies the input to the i.f. network will look like a very high impedance.

Due to the relatively high impedances used in the mixer circuit, a spectrum analyser input impedance of 50Ω could not be used to realise the required output impedance. This, however, could be done in one of two ways:

(a) by using a high impedance probe, which would actually be measuring the voltage across a 470Ω load resistor; the probe can be calibrated by noting the displayed levels obtained for known powers in known resistances.

(b) by connecting the spectrum analyser in series with the 470Ω load resistor. The total load resistance is now 520Ω, and the i.f. power is calculated as being approximately 10dB higher than the power delivered to the spectrum analyser.

Both methods have been used. The conversion loss (in dB) was then determined as being the difference between the input power available from the signal generator (in dBm) and the output power calculated from the spectrum analyser level (in dBm).

The choice of optimum intermediate frequency is very much circuit dependent; frequencies in the range 1→10MHz have been used, but optimum conversion has been achieved with an i.f. of 2MHz.

Similarly, the exact choice of the l.o. and signal frequencies will depend on the tuning of the input circuitry. Initially, experiments with l.o./signal frequencies of between 100 and 120MHz were performed; good performance was obtained with an l.o. frequency of 106MHz and a signal frequency of 108MHz. Later, the input circuit was substantially retuned for operation with a 76MHz l.o. - this was done specifically for operation with a Nd:YAG laser system (see section 5.3), but measurements using semiconductor laser illumination were also performed at this frequency.

5.2.3 Results

Conversion loss measurements were taken with l.o. frequencies in the range 100→120MHz and at 76MHz. With the l.o. frequency at 106MHz and the signal at 108MHz, giving an i.f. of 2MHz, a reverse bias conversion loss minimum of just over 25dB was recorded (at V_d=-110mV). At these frequencies the conversion loss under forward bias could be reduced even further due to the greater diode nonlinearity. The diode capacitance does not continue increasing under forward bias as predicted by the depletion approximation, as was discussed in section 4.3, and so RC effects do not negate the improved conversion efficiency from the greater diode nonlinearity. However, it was shown in sec.4.4.1 that although the total photocurrent shows little dependence on bias, the proportion generated in the depletion region does vary. Transit-time limitations on device performance are likely to set in at lower frequencies under forward bias, and so more consideration is given to the reverse bias performance of the devices.

The measured conversion loss variation with bias with an l.o. frequency of 76MHz and an i.f. of 2MHz for upper-

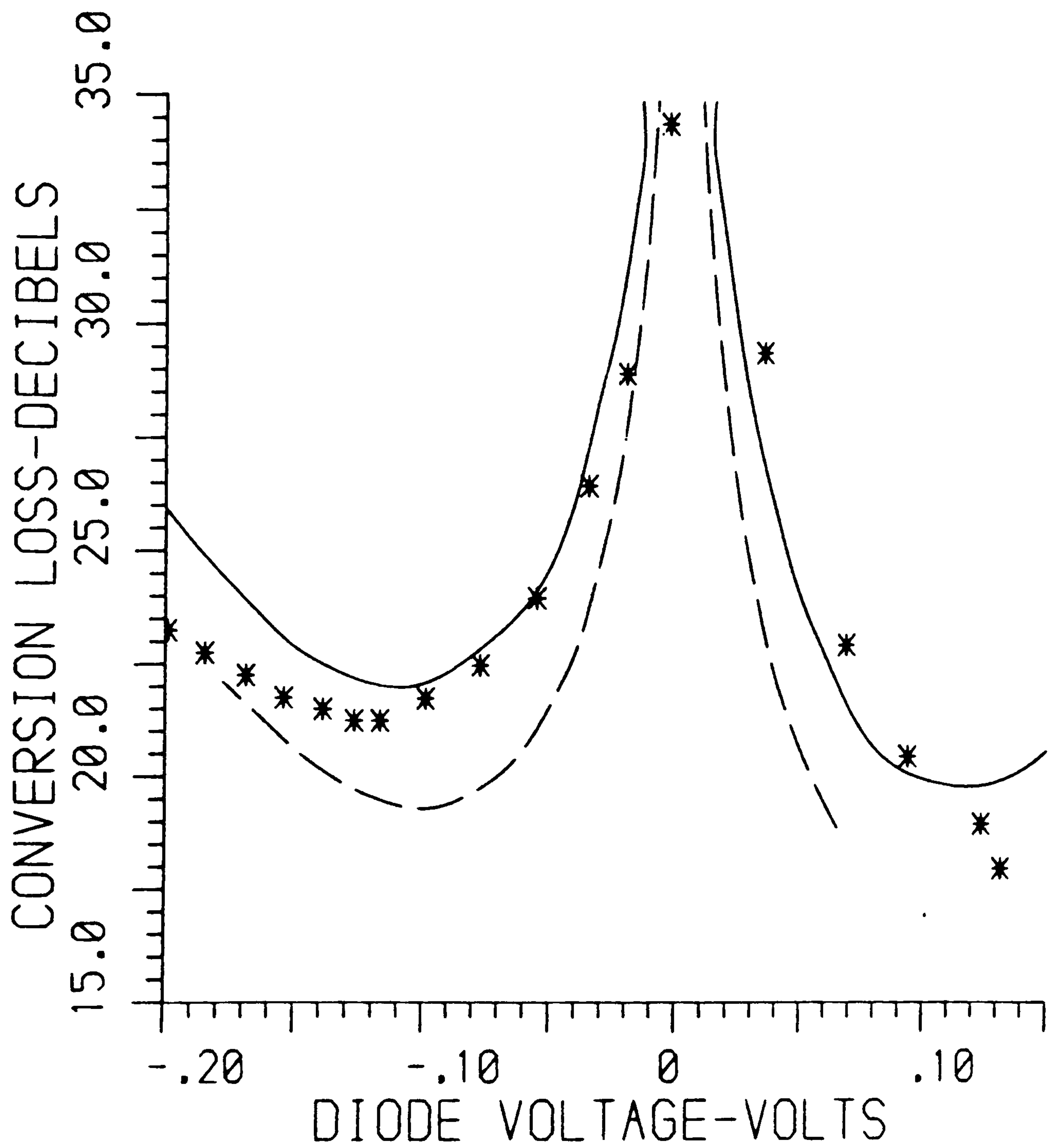

Fig.5.10 Experimental conversion loss variation with intensity modulated semiconductor laser illumination, and predictions for experimental arrangement from time (———) and frequency (— —) domain models.

sideband down-conversion is shown in Fig.5.10. The reverse bias minimum, at $V_d \simeq -120mV$, is 21.5dB while under forward bias a conversion loss as low as 18dB has been measured. The improved conversion compared to the performance at 106MHz, may be due to the lower frequencies, but will also be due to the increased photocurrent generated; this is because improved translation stages were used after the circuit was retuned. Also shown in Fig.5.10 are predictions obtained from the computer models for the experimental arrangement, assuming the levels of photocurrent actually generated (120μA average). Since the embedding impedance at the l.o./signal frequencies in the experimental arrangement was obtained by tuning the input circuit to minimise the conversion loss at $V_d \simeq -110mV$, the embedding impedance used in the time domain analysis was 'broad-band matched' at $V_d \simeq -110mV$ (which also gave approximately minimum conversion loss in this case). The agreement between the measured results and the time domain predictions, especially, can be seen to be very good. A discrepancy occurs in the position of the peak of the conversion loss curve, perhaps due to a slight inaccuracy in the modelled I-V characteristic; otherwise the agreement between -100mV and +100mV, the region over which the diode characteristics are best fitted, is excellent. At higher reverse bias the time domain model under-estimates the actual performance, which tends towards the predictions of the frequency domain model. This is probably due to a combination of under-estimating the nonlinearity of the I-V characteristic and not accurately modelling the embedding impedances at the l.o., signal and image frequencies, which may be well matched to the diode impedance with its reduced capacitive element. The C-V characteristic used is a square-law relationship which holds well for the tunnelling contact in reverse and up to low forward bias - at higher forward bias it does not model the measured C-V characteristic accurately,

predicting a much higher capacitance, so the under-estimate of performance at higher forward bias by the time domain model is easily explained.

A further, more general reason for discrepancies between the measured and predicted conversion loss is that the optically generated current is assumed to be purely sinusoidal in the computer models. In reality this is not the case. Even if the optical intensity were sinusoidally modulated, the different transport processes and especially the finite diffusion times of the photo-generated carriers would affect the shape of the current waveform. Also, as discussed in sec.5.2.1, the optical intensity modulation is unlikely to be purely sinusoidal even if the laser bias current is modulated by a pure sinusoid.

5.3 Conversion loss measurements using a Nd:YAG laser

5.3.1 Experimental arrangement and results

The measured conversion loss of the tunnelling contacts is much greater than the predictions presented and discussed in section 5.1 because of the low levels of photocurrent generated. This current can be increased by using higher optical power levels and/or using shorter wavelength illumination, for which the absorption length is less than the minority-carrier diffusion length, so that a larger proportion of the photo-generated carriers contribute to the current. These features can be obtained by using solid-state, gas and dye lasers, the problem then being modulating them. External modulators generally show low power handling capabilities, and fast modulators are expensive. To overcome this a frequency-doubled mode-locked Nd:YAG laser was used; the mode-locking produces pulses of FWHM $\leqslant$ 70ps, at a repetition rate of 76MHz; the

frequency-doubling gives an emission wavelength of 532nm (the main emission wavelength of Nd:YAG lasers being 1064nm).

The arrangement for the mixing using the frequency-doubled mode-locked Nd:YAG laser as the l.o. source was similar to that used for the semiconductor lasers, but the beam was attenuated before focussing onto the device due to the high power available from the laser. The measured conversion loss dependence on bias for two illumination levels (average optical power = 1.8 and 3.42 mW) is shown in Fig.5.11. The most obvious difference compared with the variation using semiconductor lasers is the position of the peak - this can be explained by the shape of the illumination intensity waveform. The time domain model can be used to analyse the behaviour of the mixer with pulsed excitation as a number of l.o. harmonics can be taken into account (therefore enabling non-sinusoidal waveforms to be modelled). Thus, an explanation of the effects of the pulse waveform is aided by predictions from the time domain model in which the waveform shape is varied.

5.3.2 Discussion using time domain model predictions

The waveform for the optically generated current enters the analysis in the I-V characteristic function as described in section 3.3.2; it will represent the photocurrent at the barrier after transit-time limitations have had their effect. The exact shape of the current pulses, or indeed the laser pulses producing them, is not known; Gaussian and $sech^2$ pulse shapes are commonly used and a comparison of the two is shown in Fig.5.12. The latter have been used in this analysis.

The waveform over one l.o. cycle has been modelled by the function:

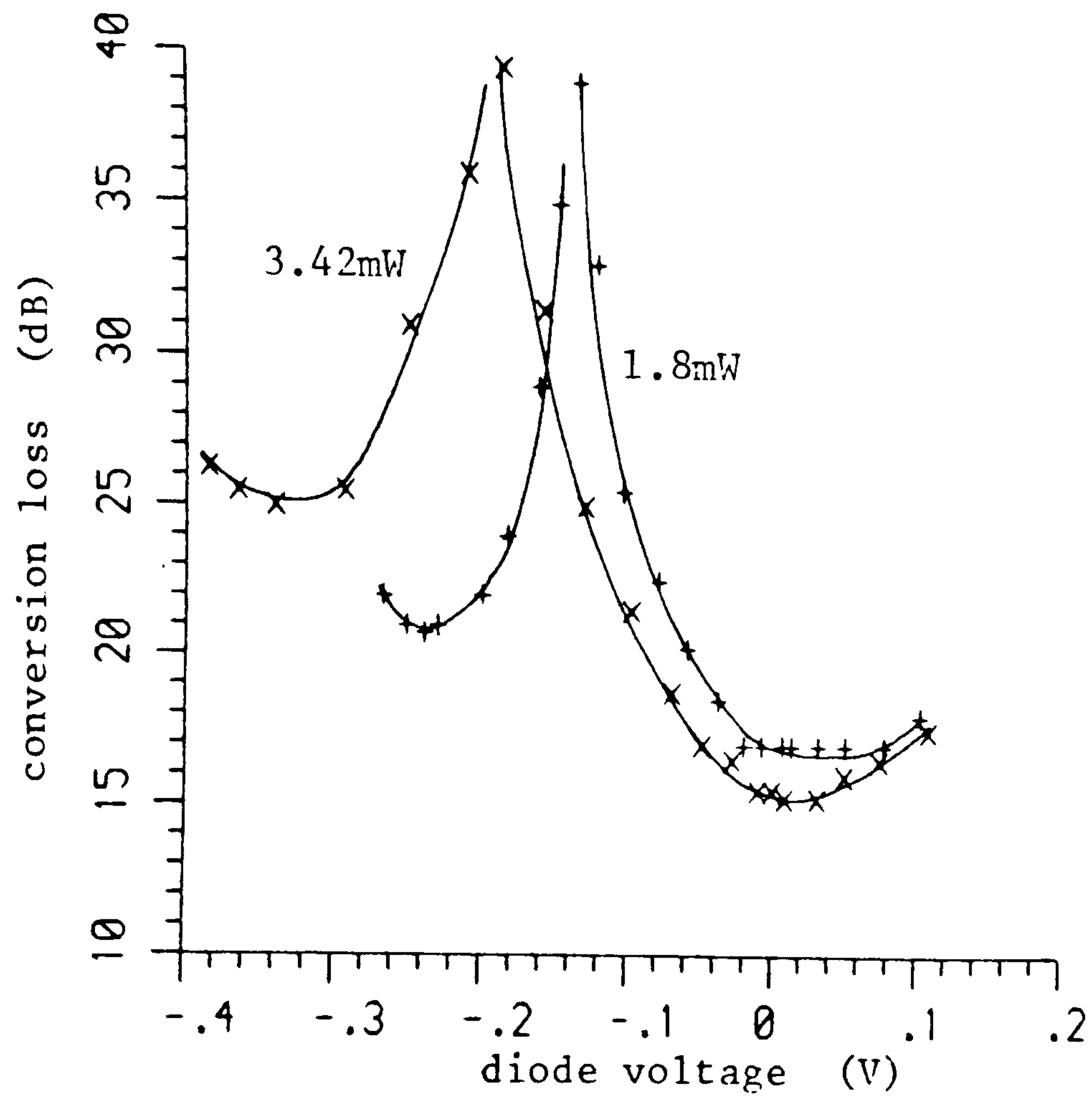

Fig.5.11 Experimental conversion loss variation with mode-locked frequency-doubled Nd:YAG laser.

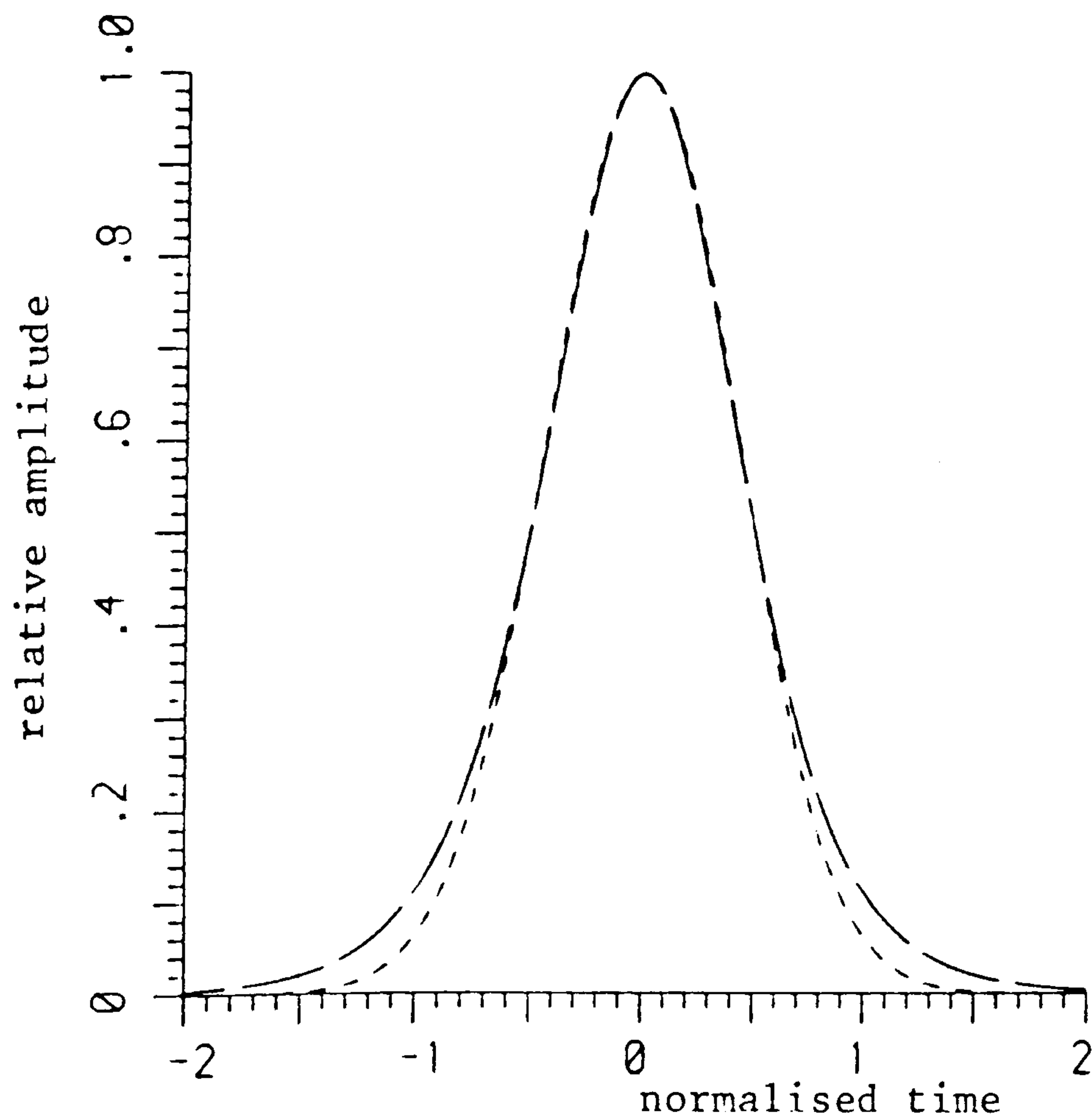

Fig.5.12 Comparison of Gaussian (- - - - -) and $sech^2$ (— —) pulse shapes of same (unity) pulse width.

$$i_{ph}(\theta) = I_{pk}\mathrm{sech}^2[A(\theta-\pi)/\pi] \qquad (5.2)$$

for $-\pi \leqslant \theta \leqslant \pi$ and $\theta \equiv \omega_p t$. I_{pk} is the peak amplitude of the photocurrent pulse, and A defines its sharpness (the pulse becoming narrower as A increases). For $A \geqslant 3$, the average photocurrent can be expressed as I_{pk}/A.

Figs.5.13(a) and (b) show predicted conversion loss variations from the time domain model with sech^2 pulses, and with the embedding impedance at the l.o./signal frequencies constant and the same as that in the sinusoidal illumination predictions for 76MHz, since for the experiments the input circuit was not adjusted. The shape of the variations is consistent with the experimental measurements. Precise agreement is difficult because the pulse shape is not known exactly and the modelled diode characteristics should be accurate over a much wider range of bias than is the case for sinusoidal photocurrents of the same average level.

Fig.5.13(a) shows the effect on the conversion loss versus bias characteristic of varying the pulse amplitude while keeping its half-width or shape constant. This is equivalent to increasing the photocurrent and, therefore, the optical intensity. The peak in the conversion loss is due to the cancellation of the fundamental component of the dynamic conductance; since the photocurrent pulse causes a sharp pulse into (or toward) forward bias, the cancellation will occur as the quiescent point is moved further into reverse bias for increasing optical power. It can be seen that in forward bias the conversion loss is reduced by increasing the l.o. power, but that in reverse bias it may be increased as the minimum is pushed further into reverse bias. This effect is visible in the experimental results of Fig.5.11.

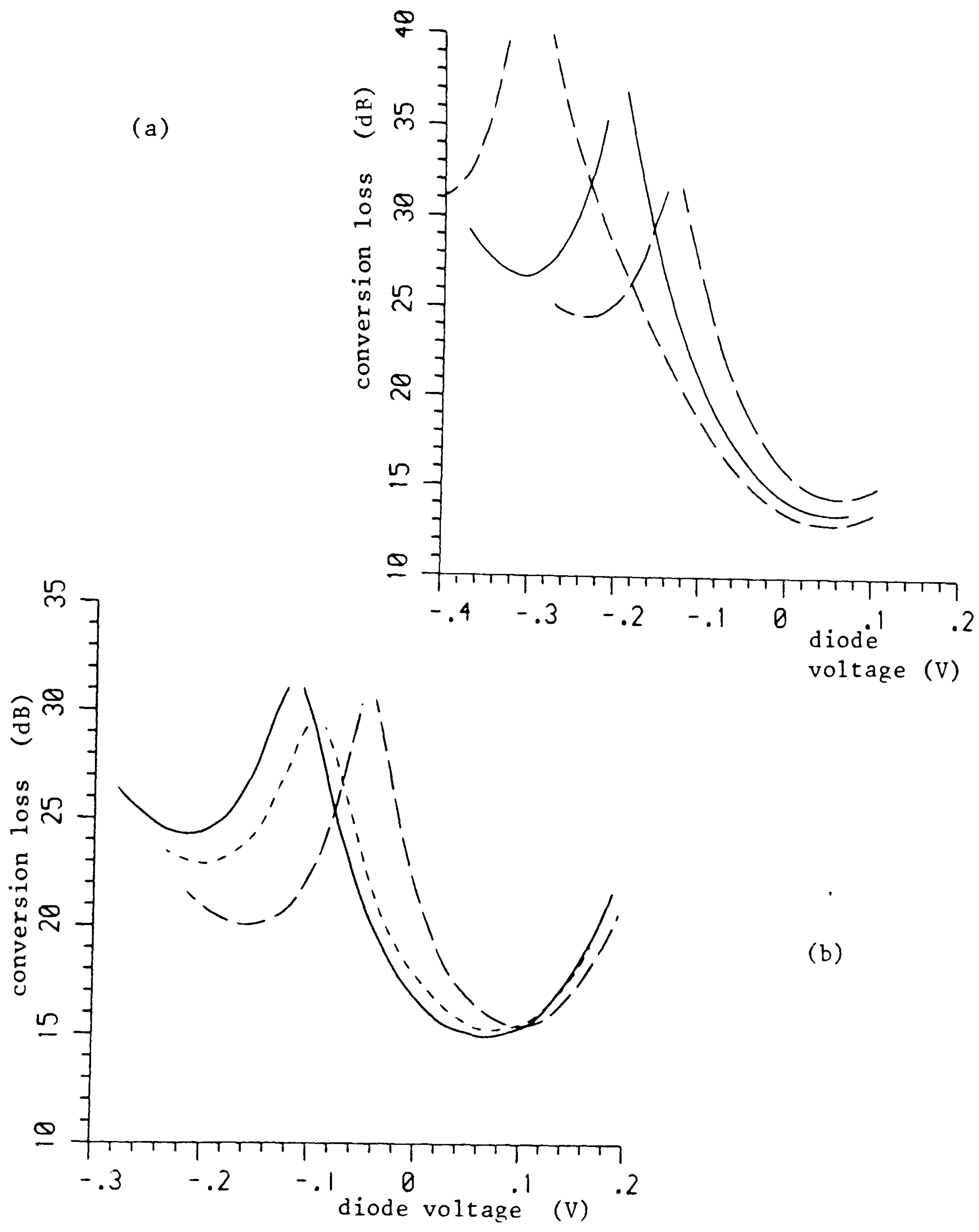

Fig.5.13 Predicted conversion loss variation with $sech^2$ photocurrent pulses, effect of change in peak current.
(a) half-width constant: peak current = 15mA (— — — —), 10mA (————), 7mA (—— ——), A = 50.
(b) av. photocurrent constant (120μA):
———— I_{pk}=7.2mA, A=60 - - - - I_{pk}=3.6mA, A=30
— — I_{pk}=1.2mA, A=10

Fig.5.13(b) shows the effect of the pulse waveform on conversion loss; the variation with bias is plotted for three different values of peak power while the average power is kept constant - the waveform shape is therefore being modified. Narrower pulses of higher peak amplitude are seen to reduce conversion loss in forward bias, but the minimum in reverse bias is increased, again as its position moves further into reverse bias.

The explanation as to why the conversion efficiency is improved in forward bias with narrow pulse excitation, but not in reverse bias, is aided by referring to typical voltage, current, conductance and capacitance waveforms in a device over an l.o. cycle. Predicted waveforms at the conversion loss minimum in forward bias and at the minimum in reverse bias are shown in Figs. 5.14 (a) and (b), respectively. At the forward bias minimum the diode voltage hovers around zero bias and peaks sharply in the forward direction to quite high forward bias (>0.4V); this produces a conductance variation with a very high peak. At the reverse bias minimum, however, the conductance variation is not so large; the voltage variation is a pulse from reverse bias into much lower forward bias than in the previous case. If the diode is assumed to be a resistive mixer (which, in the main, it is) its capacitance will tend to short out higher frequencies. Thus, despite the fact that the actual embedding impedances are high, the mixer behaviour will tend towards that of Saleh's Y-mixer[71]. The effects of the pulse waveform described above are in good agreement with Saleh's theory, which defines the optimum conductance waveform for a mixer approaching the ideal Y-mixer case as approaching an impulse train[71]. A conductance waveform of sharp pulses is one which can only be produced by light pulses in forward bias operation. For the tunnelling contact, to produce an optimum waveform for reverse

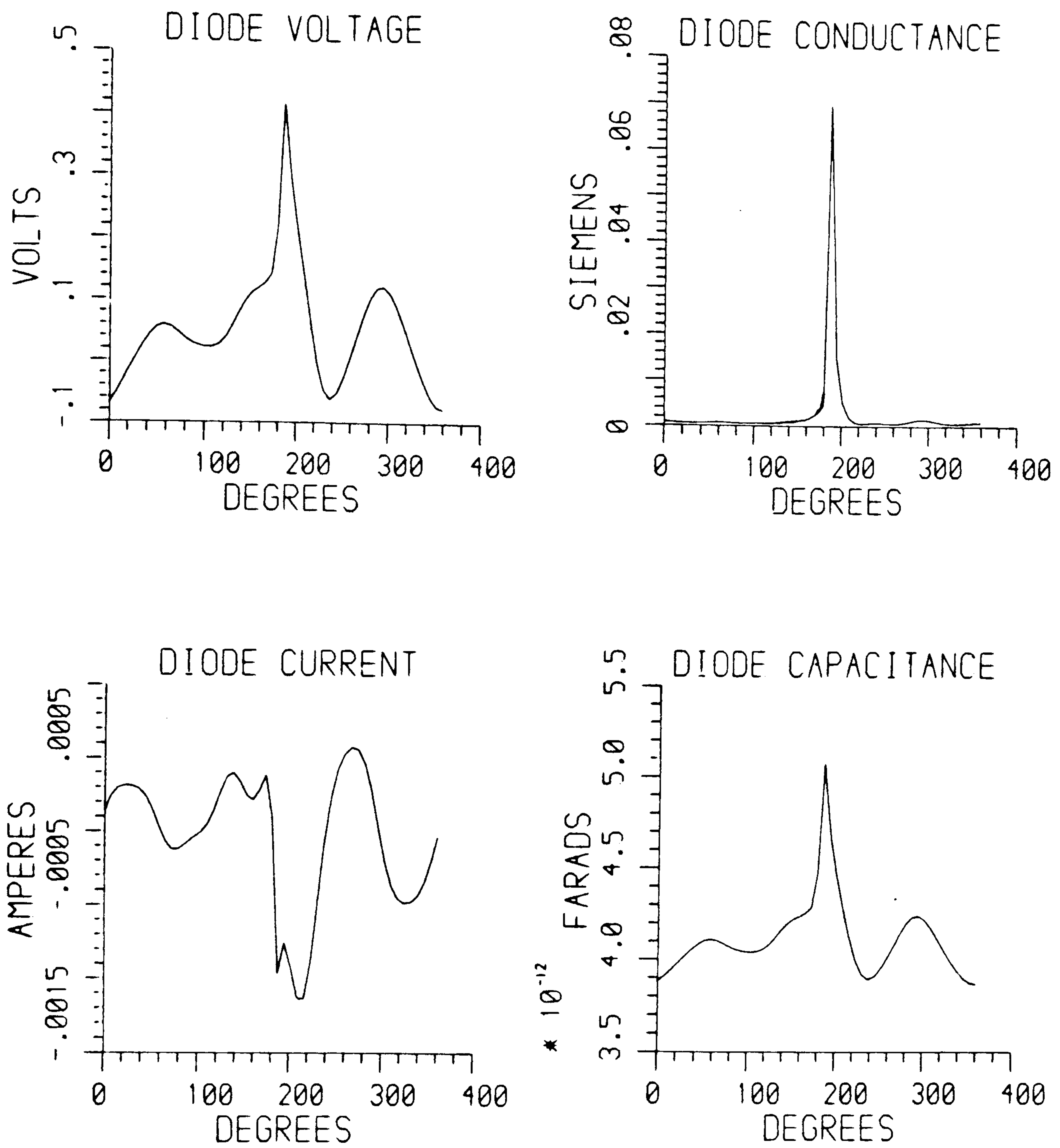

Fig.5.14(a) Example of predicted diode waveforms with pulse excitation at forward bias conversion loss minimum.

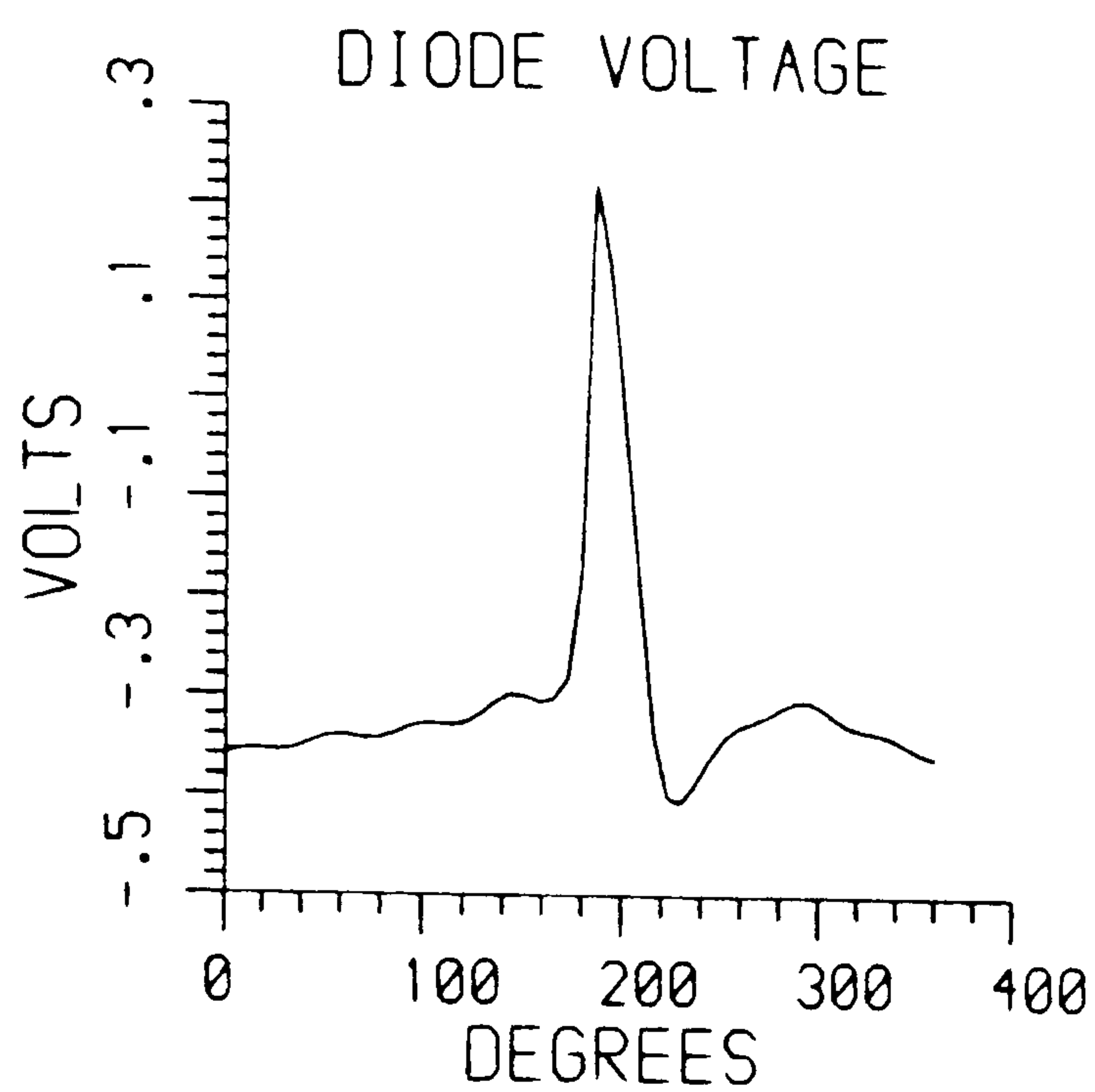

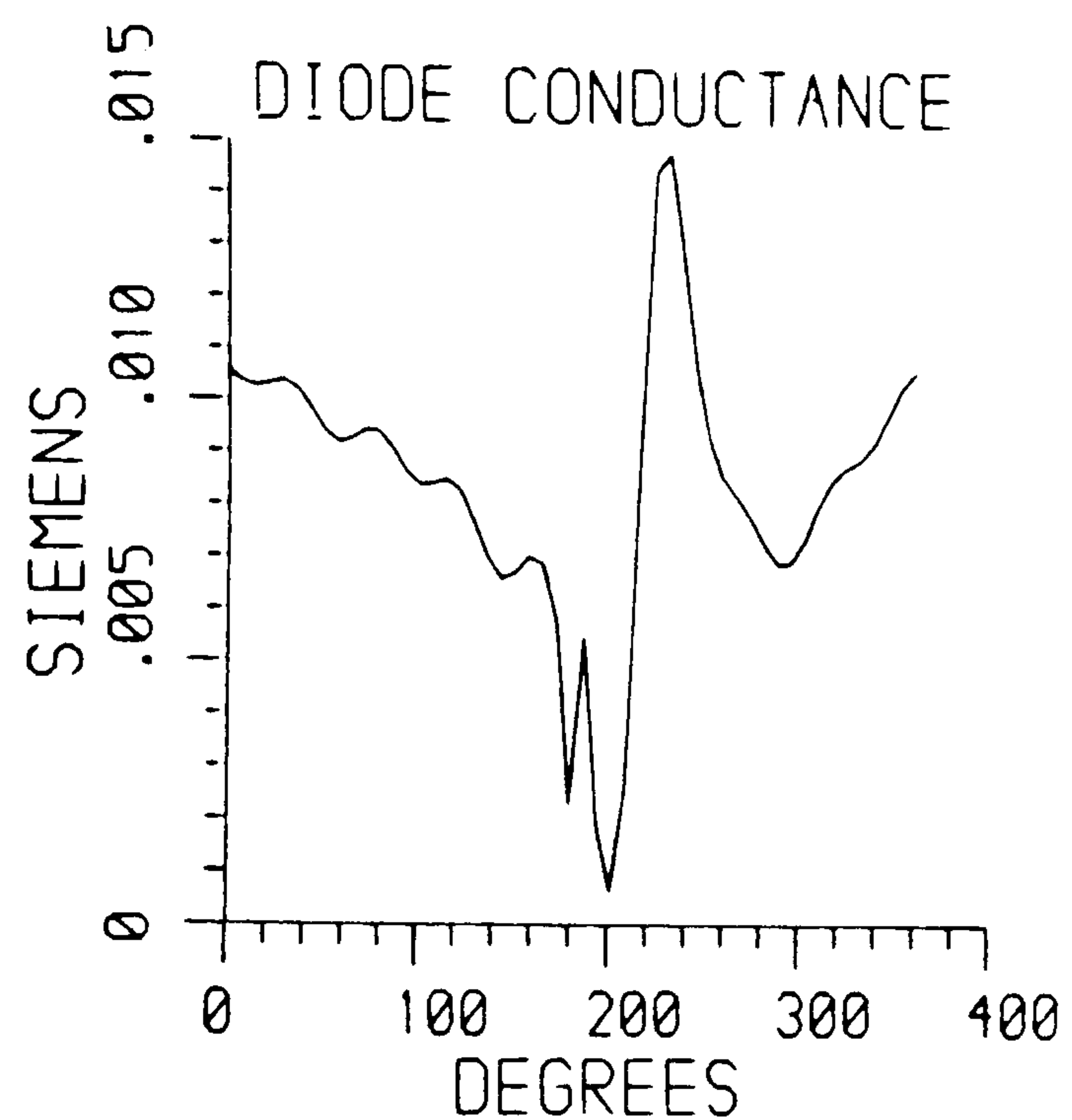

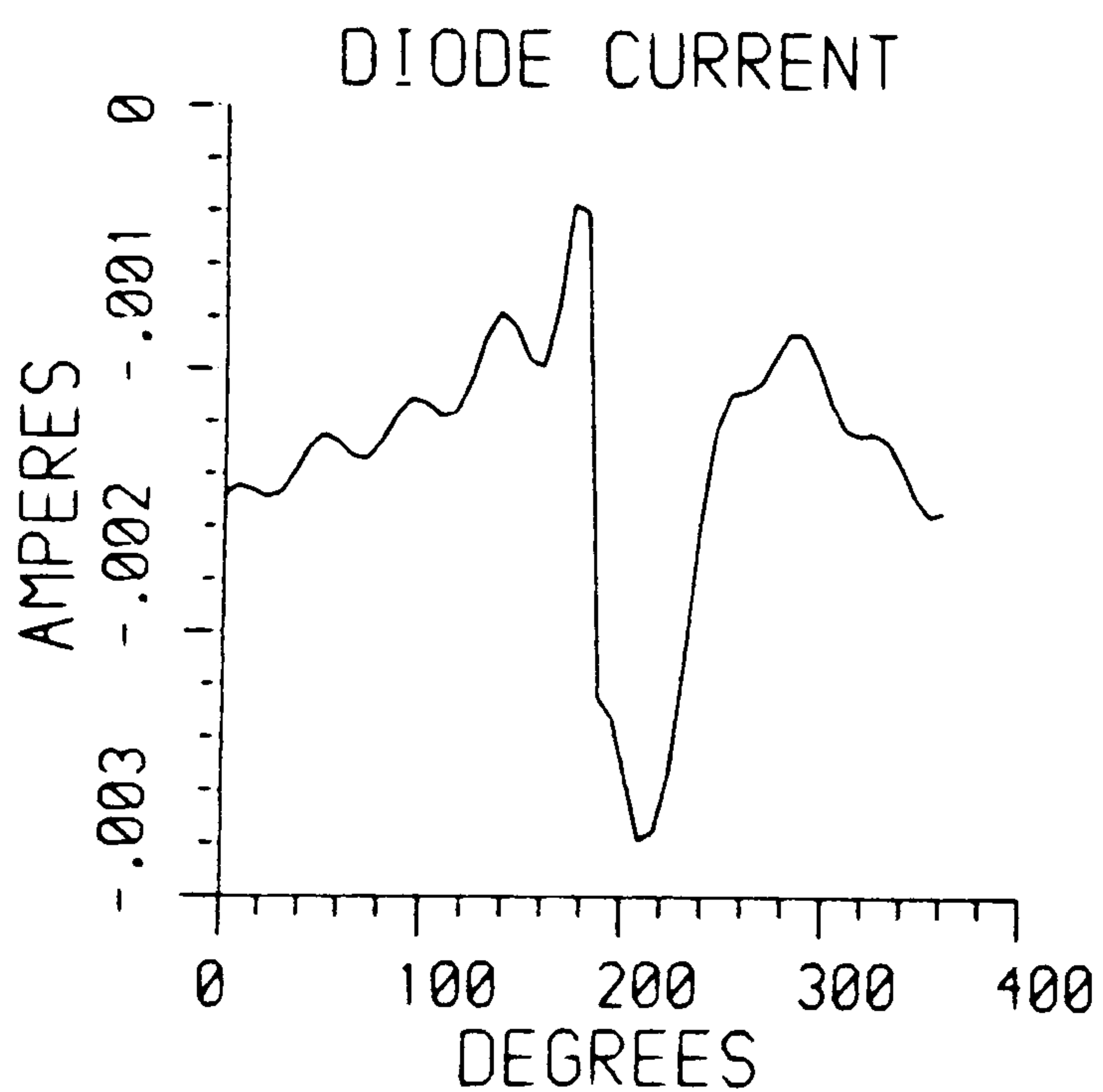

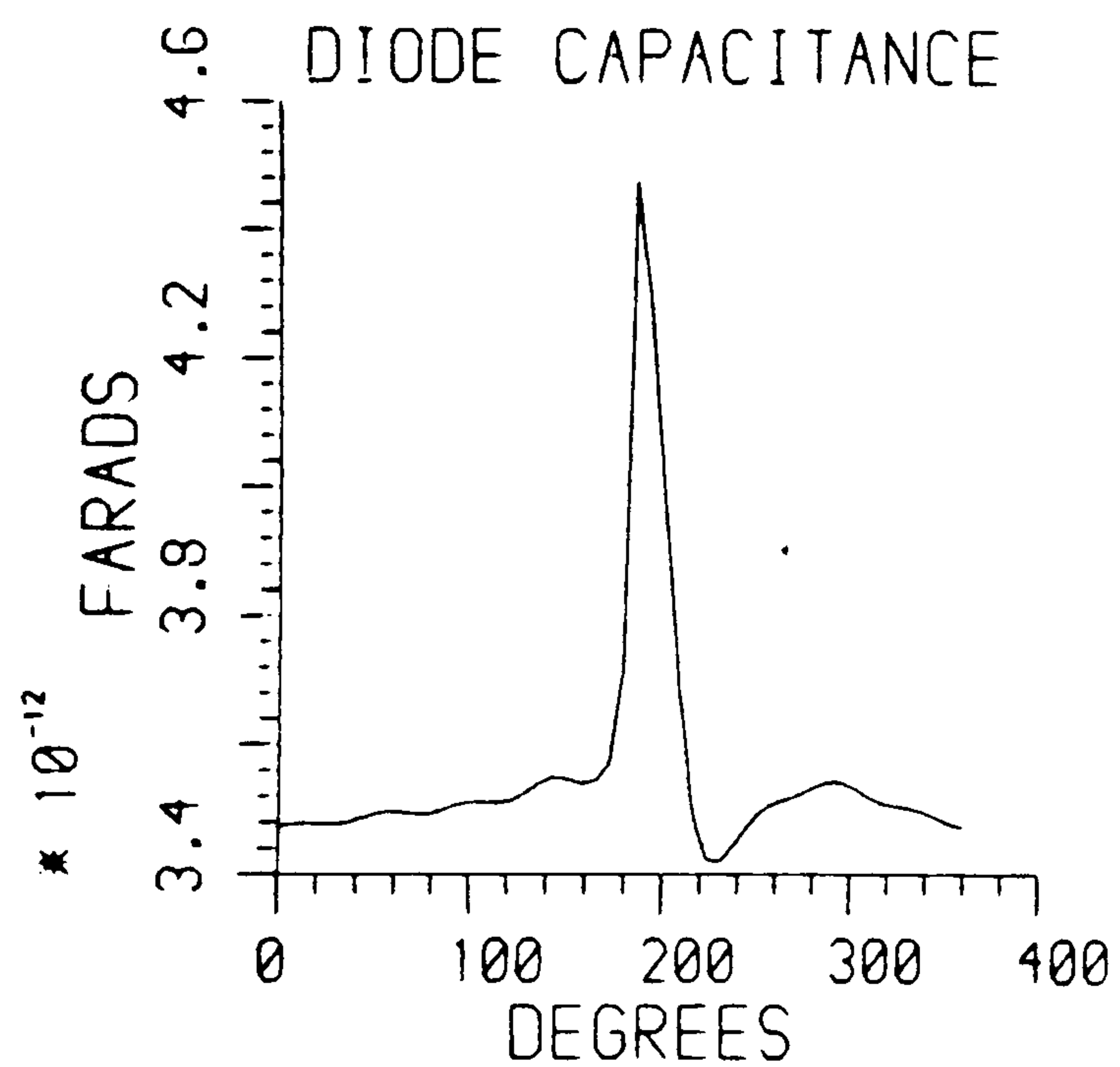

Fig.5.14(b) Example of predicted diode waveforms with pulse excitation at reverse bias conversion loss minimum.

bias operation, a constant illumination level periodically switched off for a short space of time would be required.

The best fit for the experimental results at the higher power level (3.42mW) is probably with values I_{pk}=10mA and A=50, which suggests an average photocurrent of 200μA, Fig.5.15. (This is how the value of photocurrent used to characterise the device in sec.4.4.1 was derived - it cannot be derived directly from experimental measurements because of the diode nonlinearity and the large voltage excursion across the diode that the photocurrent pulse produces.) The main discrepancy - the under-estimate of the performance of the diode under reverse bias - is consistent with a similar feature in the predictions for sinusoidally-varying illumination, and again, may be due to an under-estimate of the diode nonlinearity in this region.

5.4 Other parameters

5.4.1 Noise performance

The noise performance of the tunnelling contacts has been characterised using the simplified analysis described in section 2.3. Broadband reception has been assumed (equal conversion losses from signal to i.f. and image to i.f.), and only the four frequencies, l.o., signal, image, and i.f., have been assumed to be resistively terminated (all other frequency components are reactively terminated). Further, correlation between shot noise components has been neglected. Shot noise has been characterised as due to barrier forward current, barrier reverse current and photocurrent; thermal noise due to the diode series resistance is also modelled.

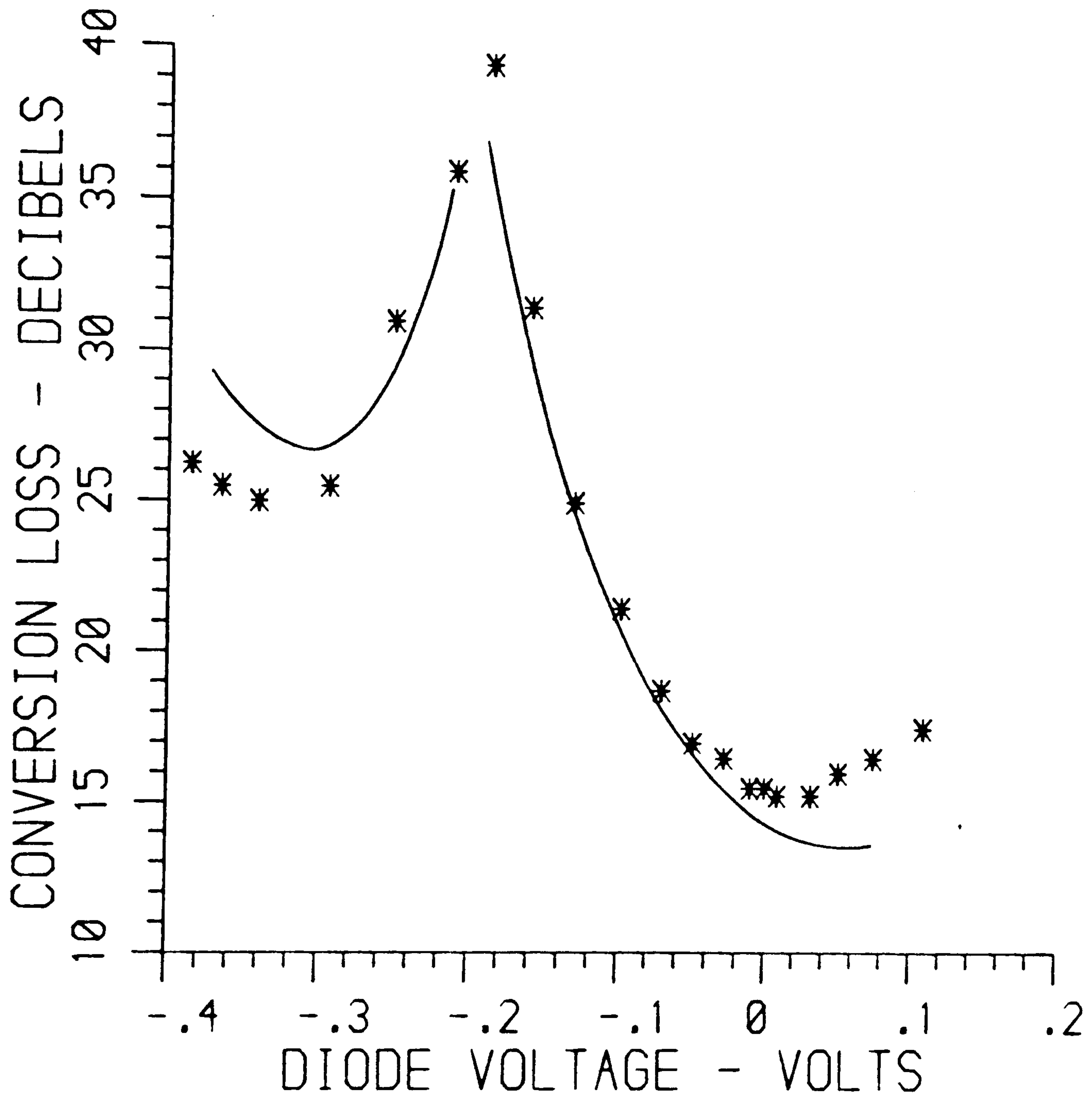

Fig.5.15 Conversion loss variation with diode bias using Nd:YAG laser:

* experimental points (average optical power = 3.42mW)

——— time domain model predictions (peak photocurrent of 10mA and A=50, which results in an estimated average photocurrent of 200μA).

With the above assumptions the output noise-temperature of a tunnelling contact has been calculated using equation (2.43) for average photocurrents of 120μA (which corresponds to many of the experimental results) and 500μA (which has been used for many performance projections). The variation of the output noise-temperature with bias for these photocurrent levels is shown in Fig.5.16. At typical reverse bias operating voltages of between -90mV and -150mV, the output noise-temperature is seen to vary between approximately 1200K and 950K for 120μA average photocurrent, and 2900K and 1780K for 500μA average photocurrent; this corresponds to noise-temperature ratios (t_r) of $4.2>t_r>3.2$ and $10>t_r>6.1$ for 120μA and 500μA average photocurrents respectively.

A single-sideband noise factor for the mixer could be derived using eqn.(2.44). However, as discussed in sec. 2.3.6, the noise factor of the receiver is a much more important parameter. Using the output noise-temperatures calculated above (from which the noise-temperature ratios can be found) and the conversion loss predictions from the frequency domain model (for which very similar assumptions have been made), and by assuming a noise factor for the following i.f. amplifier, the receiver single-sideband noise factor can be calculated according to eqn.(2.45). Fig.5.17(a) shows the receiver noise figure variation with bias predicted in the above way for 120μA average photocurrent and three values of i.f. amplifier noise figure, F_{IF}=1.5dB, 3dB, 5dB. Fig.5.17(b) shows the receiver noise figure variation for the same i.f. amplifier noise figure values, but with 500μA average photocurrent. It is important to note that the above analysis assumes that suitable i.f. amplifiers with input impedances equal to the conjugate of the i.f. output impedance of the mixer diode can be found. If this is not so, then in the general case, the bias for the contact may

have to be varied in order to match the output impedance to the i.f. amplifier, despite the fact that this may not give optimum conversion efficiency. This is especially significant for the tunnelling contacts, since their output impedances under typical operating conditions are higher than those of most mixer diodes under typical operating conditions.

Figures 5.17(a) and (b) compare the noise figure variation with bias with the conversion loss variation, since the latter has a dominant effect on the former. With 120μA average photocurrent, which corresponds to the experimental arrangement, the frequency domain model under-estimates the conversion loss and so, if the assumptions used hold, the noise figure minimum (25.5→27dB) will be an under-estimate as well. It can be seen that with higher photocurrent (500μA average compared to 120μA) although the conversion loss minimum is reduced by approximately 9dB, the noise figure reduction is somewhat less, approximately 7dB. With 500μA average photocurrent the conversion loss reverse bias minimum is ≃10dB, but the minimum noise figure is 18.5→19.5dB.

The effect on the noise figure of the excess diode noise caused by the photocurrent generation can be seen from Fig.5.18. Here the noise figure and the conversion loss for the optically pumped mixer with 500μA average photocurrent are compared to the noise figure of the equivalent voltage-pumped mixer - that is, with the voltage pumping giving the same voltage modulation of the barrier as the photocurrent generation does in the optically pumped case. (An i.f. amplifier noise figure of 3dB is assumed in obtaining the curves of Fig.5.18.) The noise figure is now seen to be less than 5dB greater than the conversion loss and over 4dB better than the noise figure with the photocurrent generation.

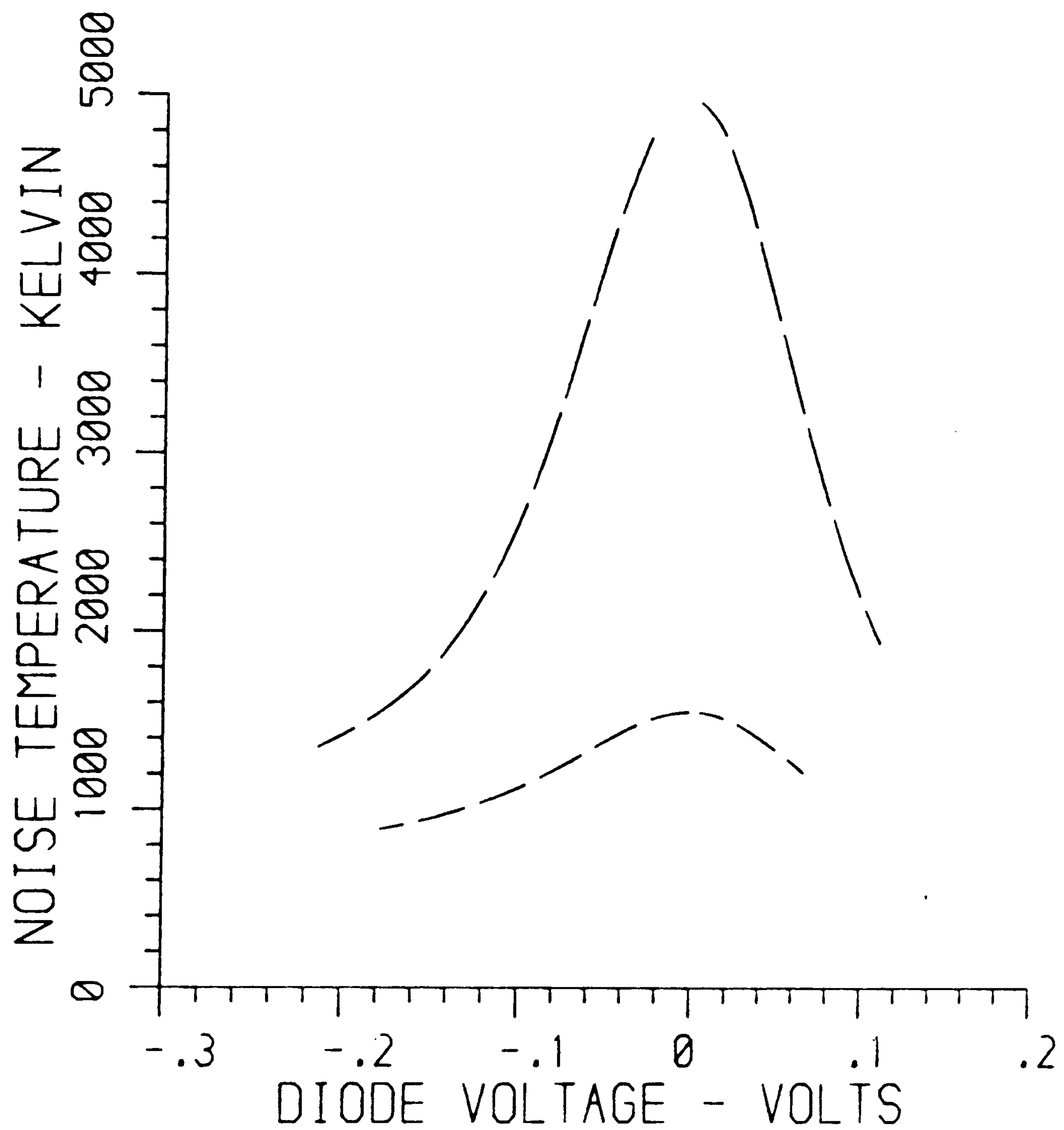

Fig.5.16 Output noise-temperature (T_n) of an optically pumped tunnelling contact mixer:

— — — — 120μA average photocurrent

—— —— —— 500μA average photocurrent

(100% modulation assumed)

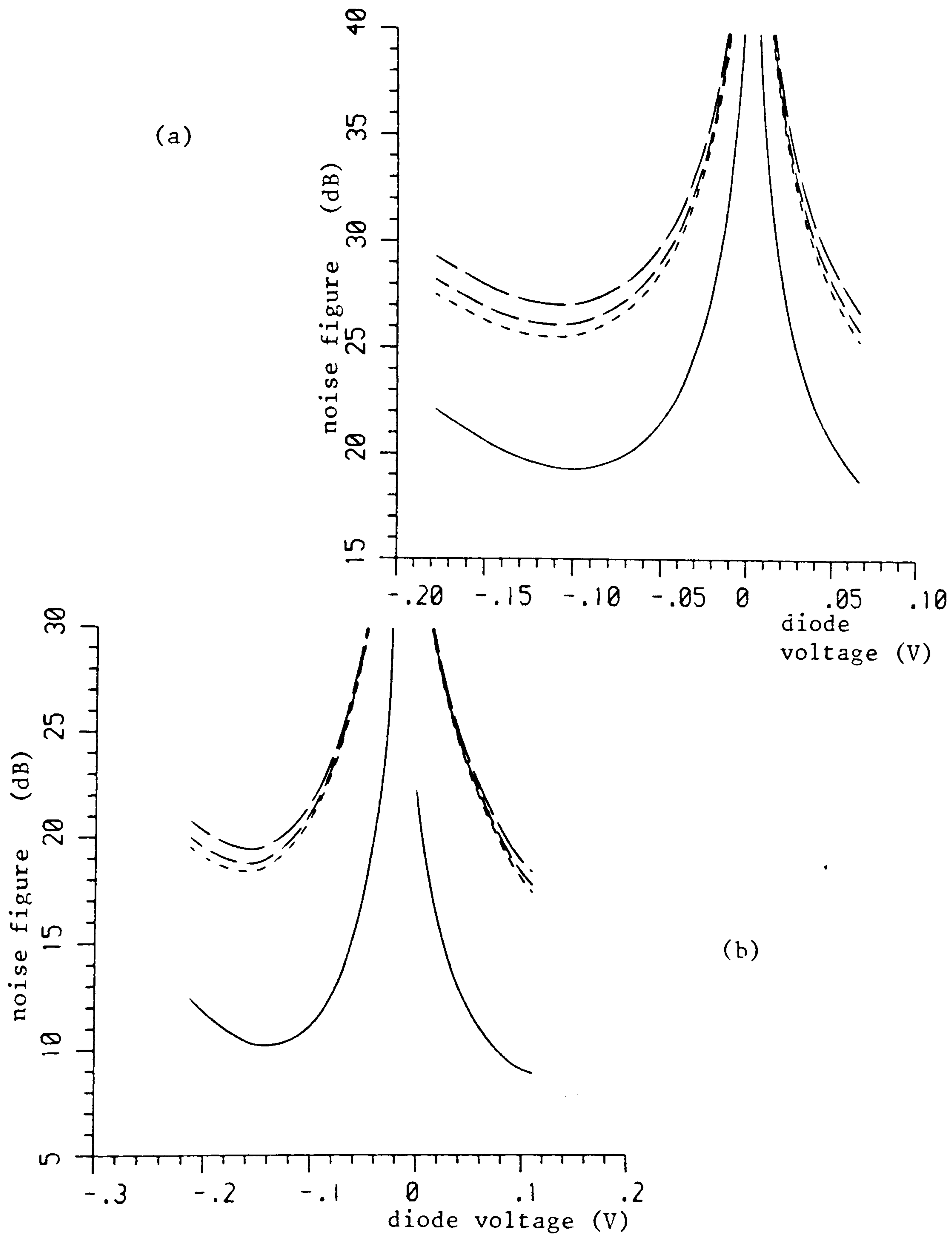

Fig.5.17 Noise figure of receiver employing tunnelling contact optically pumped mixer using frequency domain model predictions. IF amplifier noise figure, F_{IF}

---- F_{IF} = 1.5dB — — — F_{IF} = 3.0dB

— — F_{IF} = 5.0dB (——— predicted conv. loss)

(a) 120μA and (b) 500μA average photocurrent (100% mod.)

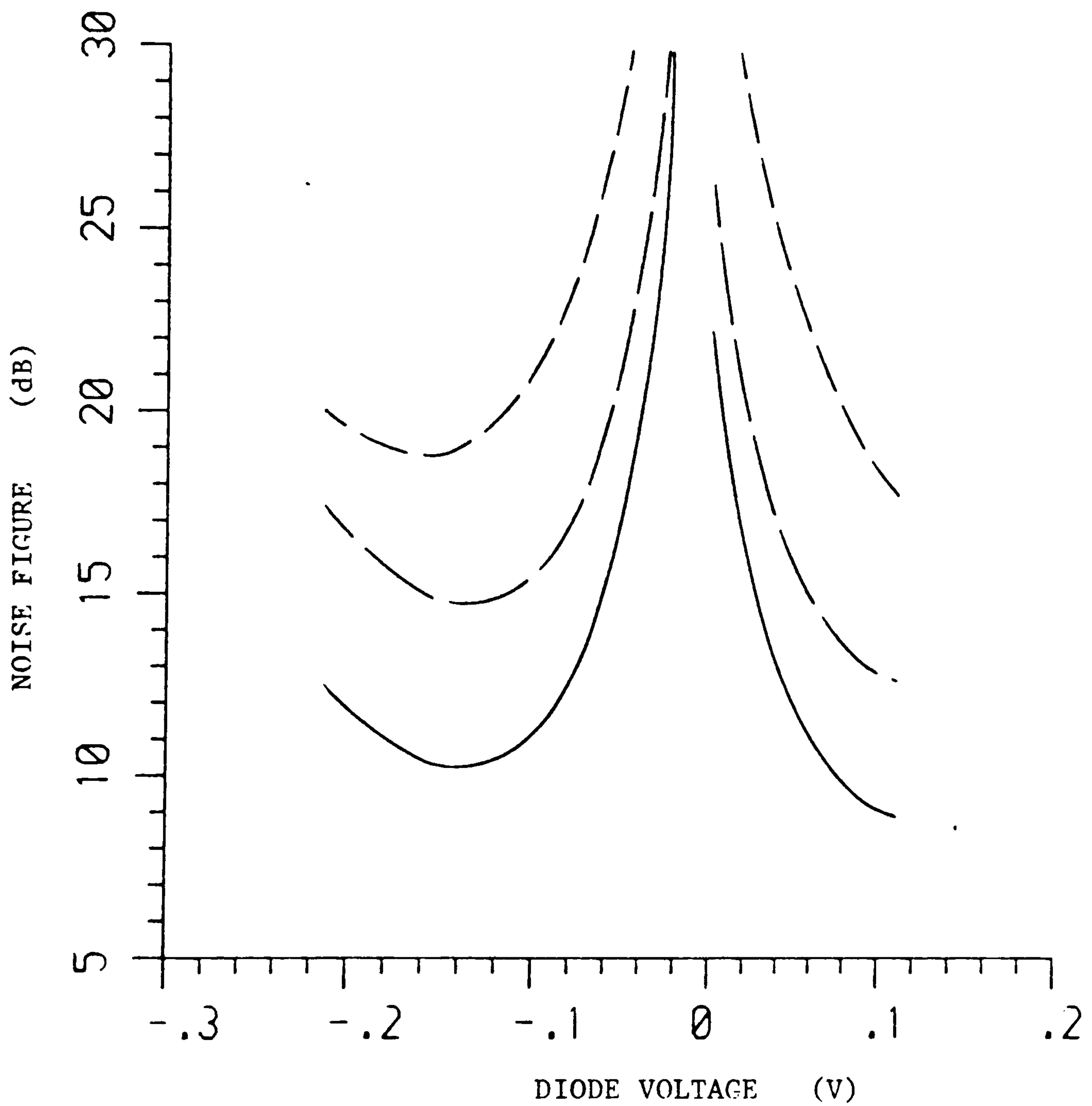

Fig. 5.18 Comparison of noise factors of receivers employing optically pumped and equivalent (same conversion loss, bias, etc.) electrically pumped tunnelling contact mixers. IF amplifier noise figure = 3dB.

— — — optically pumped mixer, 500μA average photocurrent

—— —— equivalent electrically pumped mixer.

(Also shown: ———— conversion loss.)

The above noise figures, calculated for theoretical receivers employing the tunnelling contacts as optically pumped mixers, suggest that severe problems could be encountered due to the poor noise performance of the devices. However, it is possible that some of the assumptions used to predict the noise performance, especially that of no correlation, may be leading to significantly pessimistic results. There will be correlated shot noise not only due to the shot noise components at the various sideband frequencies being modulated by the local oscillator, as was discussed in sec.2.3.3, but more fundamentally, because the photocurrent modulates the barrier current. There must, therefore, be some correlation between the shot noise of the photocurrent and that of the barrier current. The reason why this effect can be neglected for photodiodes is that the barrier current, the reverse dark current in operation, is almost constant in reverse bias, and so largely unaffected by the photocurrent. In order to study the effect of correlated shot noise a more detailed noise analysis is required; a modification of the microwave mixer noise analysis of Held and Kerr[86] may be of significant benefit (see Appendix C).

5.4.2 Diode impedance

The impedance of the mixer at both signal input and i.f. output ports is important since mismatch will increase loss. The linear mixer analyses used (see sec.2.2.3 and Appendix B) have assumed that the i.f. load is conjugate-matched to the mixer, since this is usually relatively easy to do as the i.f. is very different to the other frequencies involved. The signal frequency, on the other hand, is very close to both the l.o. and image frequencies; generally, a broadband match is the simplest arrangement, but it is not one which will give minimum

conversion loss. An exact match at the signal frequency may result in a less than optimum impedance at the l.o. frequency, causing a deterioration in the conversion efficiency. Returning again to the output impedance, in most receiver configurations the mixer will be followed by an i.f. amplifier, the noise performance of which is specified for a certain input impedance. It is necessary to ensure that the output impedance of the mixer provides the amplifier with this impedance if the overall noise factor of the receiver is to be controlled; the provision of this impedance will depend not only on the bias and pumping of the diode but, for stronger pumping levels, on the embedding network at the l.o., signal, and image frequencies.

Obviously, some indications of the diode impedance can be gained from the equivalent circuit measurements described in sec.4.3. However, the barrier resistance and capacitance are strongly dependent on bias and are both nonlinear; with strong pumping the nonlinear variations will make the impedance of the diode at any particular frequency very difficult to predict from a knowledge of the equivalent circuit parameters alone. Since the input and output impedances of the mixer depend strongly on the mixer's operating conditions, impedance measurements are not a straightforward task. However, useful predictions can be gained from the time domain model, which gives very accurate results if the diode characteristics and embedding impedances are known. The predicted input and output impedance variation with diode bias for the experimental arrangement conditions are shown in Fig.5.19.

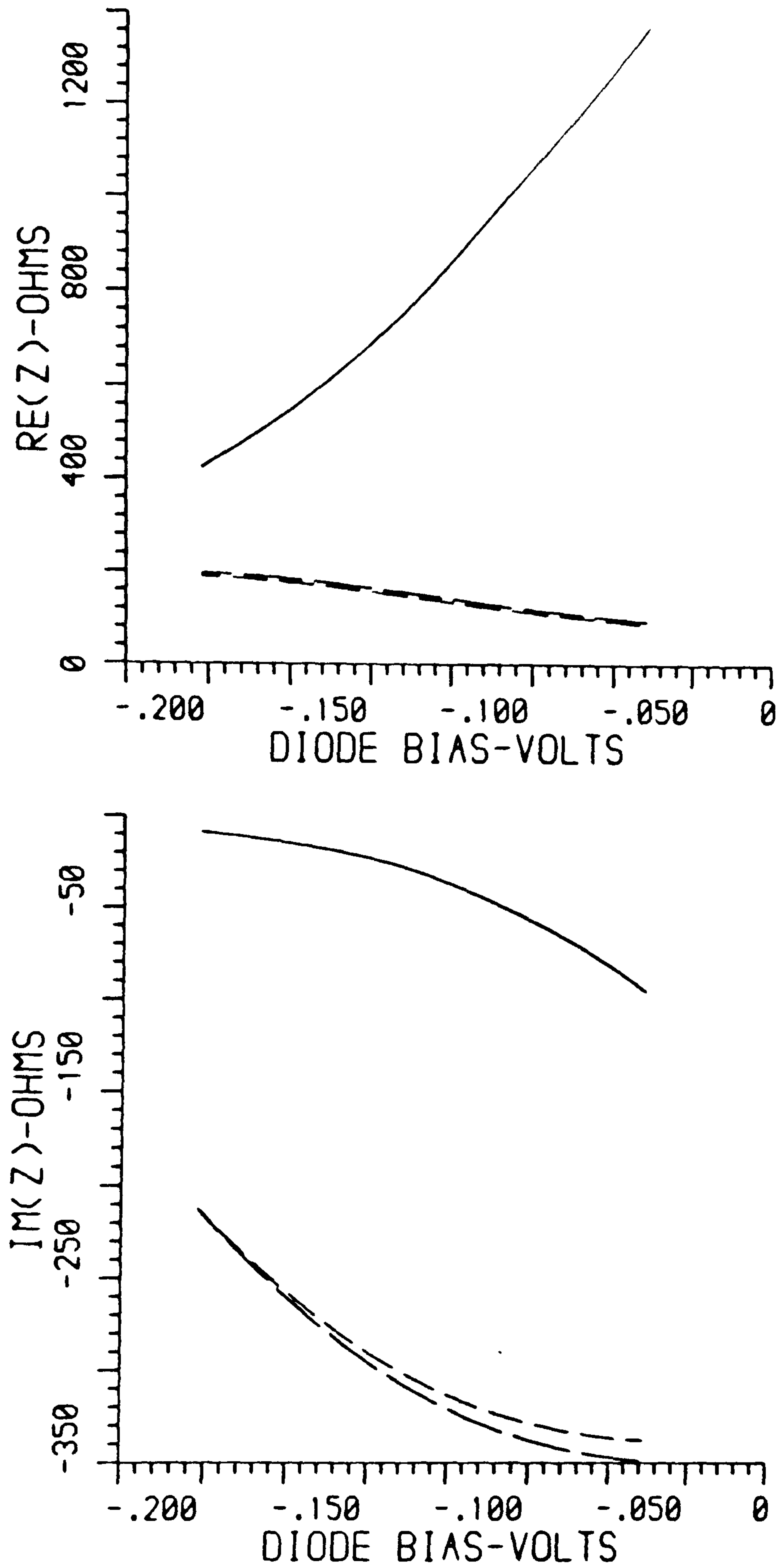

Fig.5.19 Diode impedance predictions from time domain model for test arrangement conditions. Input impedances: (— — — —) upper- and (—— —— ——) lower-sideband. Output (i.f.) impedance: ————————

5.4.3 Dynamic range

The dynamic range of a network is the input signal range over which a linear relationship exists between the input and discernible output signal levels.

It has been shown that the mixer can be modelled using linear relationships between the various sideband frequencies (most importantly the signal, image, and i.f.) under the assumption that these signals are of much lower level than the l.o. If the signal level is increased sufficiently these relationships will obviously break down and the output will tend to saturate; the signal itself will also cause significant variations across the nonlinear diode resulting in distortion. There are, therefore, two common definitions for the upper limit to the dynamic range:

(a) the compression point, defined as that input signal level at which the output signal level deviates by 1dB from the extrapolation of the linear relationship between the two.

(b) the third-order intercept point, which is that input signal level at which the slope of the 3rd-order intermodulation products variation with input signal level intercepts the slope of the fundamental output variation with signal level; as output saturation generally occurs before this point it is necessary to project these variations to find the intercept of the slopes.

Since the third-order intercept point usually occurs after saturation, although it may be used to define an upper limit for the dynamic range, it will not in itself be a realistic value for it. For conventional mixers the third-order intercept is typically about 10dB above the compression point. As the characteristics for the diodes used in this analysis are unlike those of typical mixer diodes, the relationship between the third-order intercept

and the compression point becomes less clear. For the purposes of this analysis the compression point will be used as the upper limit of the dynamic range.

For a receiver, the lower limit of the dynamic range is the input signal level at which the output signal is just discernible above the noise. This is called the minimum detectable signal (MDS) and may be assumed to be the signal level which is twice the noise level in the receiver, or:

$$MDS = 2 \, (kT_O F_R B) \qquad (5.3)$$

although it is also sometimes defined to be the signal level equal to the noise level in the receiver.

Both limits to the dynamic range are strongly dependent on the operating conditions of the mixer. This is especially true with regard to the pump conditions, since the relative amplitudes of the pump and signal will affect the compression point - the linear mixer analysis, for example, is derived specifically for the condition that the signal amplitude is much smaller than the pump. Higher pump power will also reduce the conversion loss and hence reduce the receiver noise factor, as long as any accompanying increase in diode noise is less significant; from eqn. (5.3) a lower noise factor will give a lower MDS.

The receiver noise factors calculated in sec. 5.4.1 have used the conversion loss predicted by the frequency domain model, which gives slightly optimistic predictions. Unlike the upper limit to the dynamic range, which is absolute, the lower limit (the MDS) depends on the i.f. bandwidth. Assuming a reasonable i.f. bandwidth of 1MHz, for a noise factor ≃30dB the MDS will be ≃-81dBm.

Fig.5.20(a) shows a measured compression point for the tunnelling contact optically pumped mixers for laser a.c.

drive level sufficient to give approximately 100% modulation. The results correspond to measurements taken with an average optically generated current ≃ 90μA, hence the conversion loss is approximately 28dB. The compression point can be seen to be at approximately -20dBm, but will increase with higher photocurrent. This can be seen from Fig.5.20(b) which shows a lower compression point for a lower laser a.c. drive level.

It can be stated from the above arguments that the dynamic range of a receiver employing the tunnelling contact as an optically pumped mixer would be approximately 60dB for the photocurrent levels generated experimentally, assuming a 1MHz bandwidth. With increased responsivity there would certainly be an extension to the upper limit of the dynamic range, i.e. the compression point; however, an extension to the lower limit - the minimum detectable signal - would depend on the improvement in the conversion efficiency being more significant than the extra shot noise that would result from the higher photocurrent, and be very much dependent on the noise considerations (such as the shot noise correlation) discussed at the end of sec. 5.4.1.

5.4.4 Operation frequencies

The device cutoff frequencies for the tunnelling metal-semiconductor contact have been analysed in section 4.4.2. For a typical optically pumped mixer structure it was found that with illumination of 780→800nm, transit-time and RC limitations to the optical modulation response were similar and the actual device cutoff frequency would probably be ≥800MHz. For shorter wavelength illumination, the cutoff frequency is mainly due to the RC limitations; for example, at the frequency-doubled Nd:YAG laser wavelength the cutoff frequency is ≥1.6GHz.

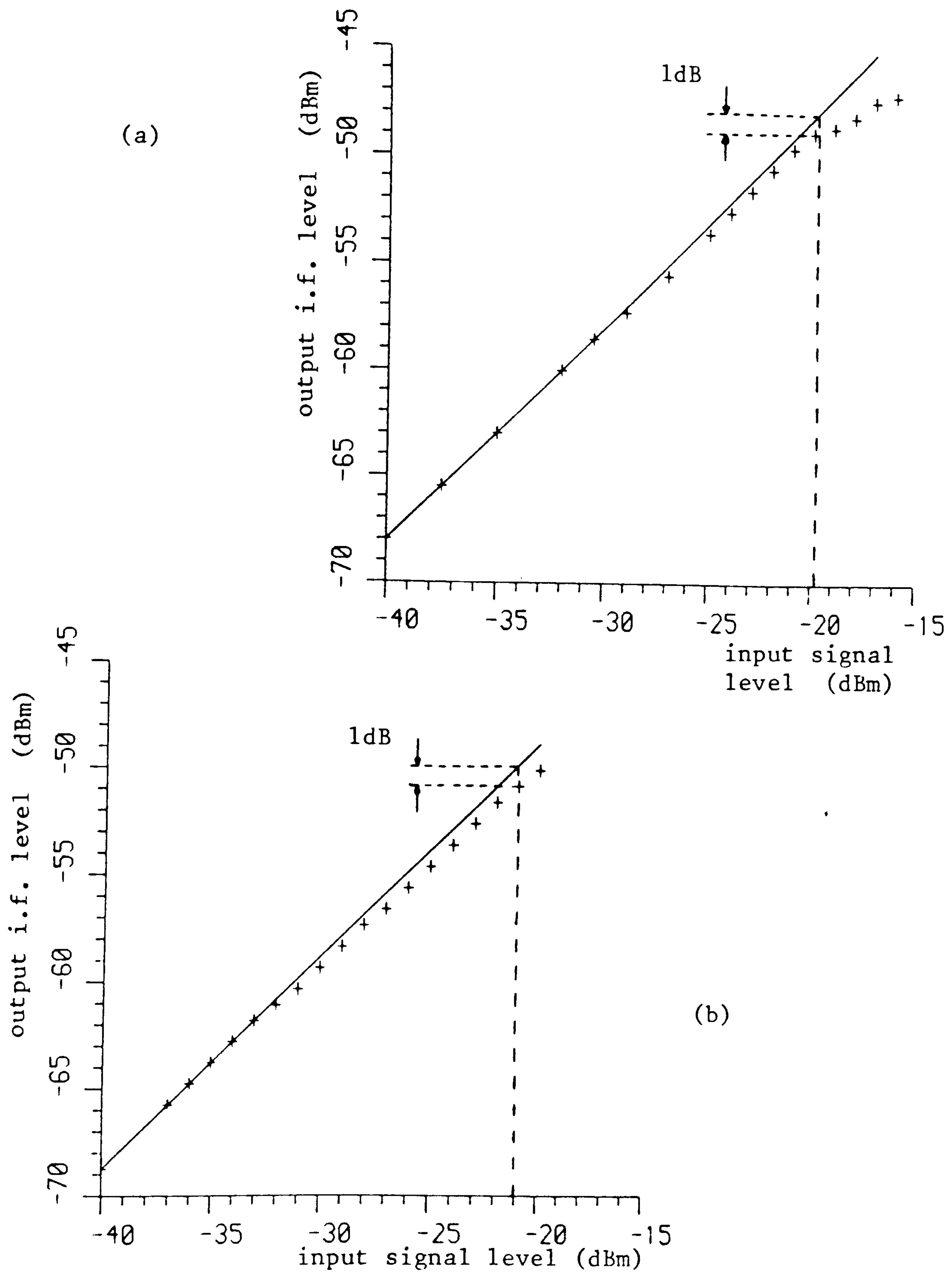

Fig.5.20 Measured compression points for tunnelling contact optically pumped mixers: (a) laser drive level at 13dBm, and (b) at 10dBm

The mixing efficiency, however, cannot be expected to have a linear relationship with the optical modulation response of the device since the photocurrent is the large signal l.o. drive on a nonlinear device. At higher frequencies, as well as the effective modulation depth of the photocurrent being reduced, the diode impedance will be reduced and there will be a trade-off between the high port impedances needed for the photocurrent to modulate the diode voltage and conductance, as illustrated by the simple load-line model of Chapter 1 (Fig.1.3), and the matching of the diode to its embedding network.

Fig.5.21 shows the predicted conversion loss variation of a tunnelling contact optically pumped mixer, assuming approximate broadband matching at the signal/l.o./image frequencies and 500μA average photocurrent. The predictions are from the time domain model for a mixer under -115mV bias and with an intensity-modulated optical l.o. at an illumination wavelength of 797nm. The a.c. photocurrent used at each frequency corresponds to that which can be expected after diffusion transit-time limitations have been taken into account - 100% sinusoidal modulation of the incident light is assumed. It can be seen that at 600MHz the mixing efficiency is more than 13dB down on its lower frequency (10MHz) value; this is despite the fact that 600MHz is below the -3dB frequency of the diode photo-modulation response. If the 12dB loss of the 10MHz l.o. operating frequency is taken as the low frequency value, then the -3dB frequency for mixer operation is about 125MHz; by scaling, it can be imagined that for a $10\times10\mu m^2$ device (<1/6th of the area, and, approximately, capacitance), a -3dB frequency of near 1GHz should be obtainable.

Finally, Fig.5.21 allows a further comparison to be made between the predictions of the frequency domain model (used as a frequency-independent analysis) and those of

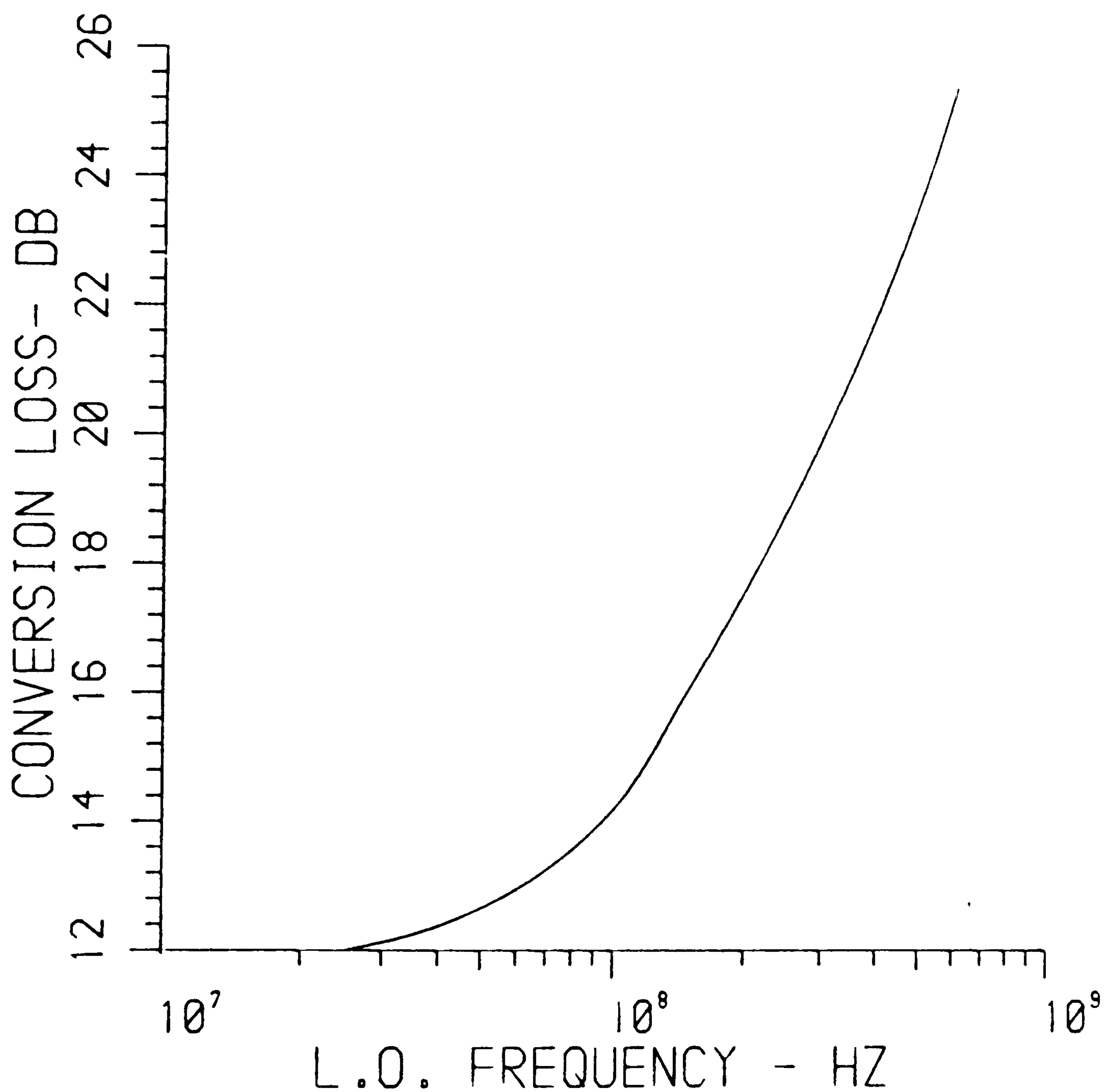

Fig.5.21 Conversion loss variation with l.o. frequency predicted by time domain model taking into account the decrease in the a.c. photocurrent. The embedding circuit is approximately broad-band-matched at the l.o., signal and image frequencies. The i.f. is 1/25th of the l.o. frequency and upper-sideband down-conversion is assumed.

the time domain model. It can be seen that as the frequency is reduced the predictions do tend towards the 10.6dB predicted by the frequency domain model for this diode bias (-115mV). For a complete verification it would be necessary either to make the diode capacitance almost zero, or to work at very low frequencies. Due to the formulation of the differential equation integrated in the analysis, which contains the capacitance - frequency-normalised in the program - in the denominator (see eqn.(3.15)), both routes cause the program to fail.

5.5 Comparison with photodetector-mixer combination

5.5.1 Conversion efficiency considerations

In the previous sections of this chapter, the performance of the tunnelling contact optically pumped mixer has been characterised using the performance parameters applied to conventional mixers. However, since the optically pumped mixer would be used in a situation where optical distribution of the l.o. offered some distinct attraction, the performance of such a device should really be compared not with a conventional mixer on its own, but with a photodetector-mixer combination. For the sake of the comparison it will be assumed that a photodiode, consisting of a parallel combination of illumination-dependent current generator and diode capacitance, may be a.c. coupled to the microwave mixer so that the modulated photocurrent provides an l.o. current drive (see Fig.5.22).

Mixer conversion losses are dependent on the l.o. drive power (among other factors). Generally, increasing the drive power will improve the conversion efficiency, although beyond a certain point the improvement will become insignificant, whereas the noise will continue to

increase. With current drive the power supplied to the mixer can be calculated if its input impedance is known. However, the impedance of a mixer diode will depend on bias and drive level, and hence, there will be a relationship between the conversion efficiency and impedance, too. Further, this relationship will be device- and circuit-dependent. In the following discussion it is assumed that obtaining efficient conversion depends on supplying the mixer with a certain, minimum drive power.

Assuming a photodiode responsivity R, and 100% modulation for the illumination (and photocurrent), then the power delivered to the mixer in Fig.5.22 will be:

$$P_m = (R^2 P_{opt}^2 / 2) R_{IN} \tag{5.4}$$

The power requirements for mixer devices are usually in the range 0→20dBm, although 7→10dBm is more typical for Schottky mixers[100]. For the application being considered here low drive power is of interest; low-level Schottky mixers[101] (Schottky diodes of low barrier height ≃ 0.3eV) and backward diode mixers[50] can operate with drive powers down towards 0.1mW (-10dBm)[100-102]. Minimum conversion losses with these devices tend to be slightly higher than with ordinary Schottky mixers, typically 6→8dB rather than 5dB. These conversion losses, however, are still considerably lower than the 10dB minimum predicted earlier for the tunnelling contact.

For high-speed photodiodes there is a trade-off between the responsivity and bandwidth (due to transit-time limitations) as they have opposing requirements on the depletion widths of devices. Millimetre-wave photodiodes have been fabricated[103,104], but the responsivities of these structures are typically ≃0.2A/W at GaAs/GaAlAs laser wavelengths. Parker, however, has

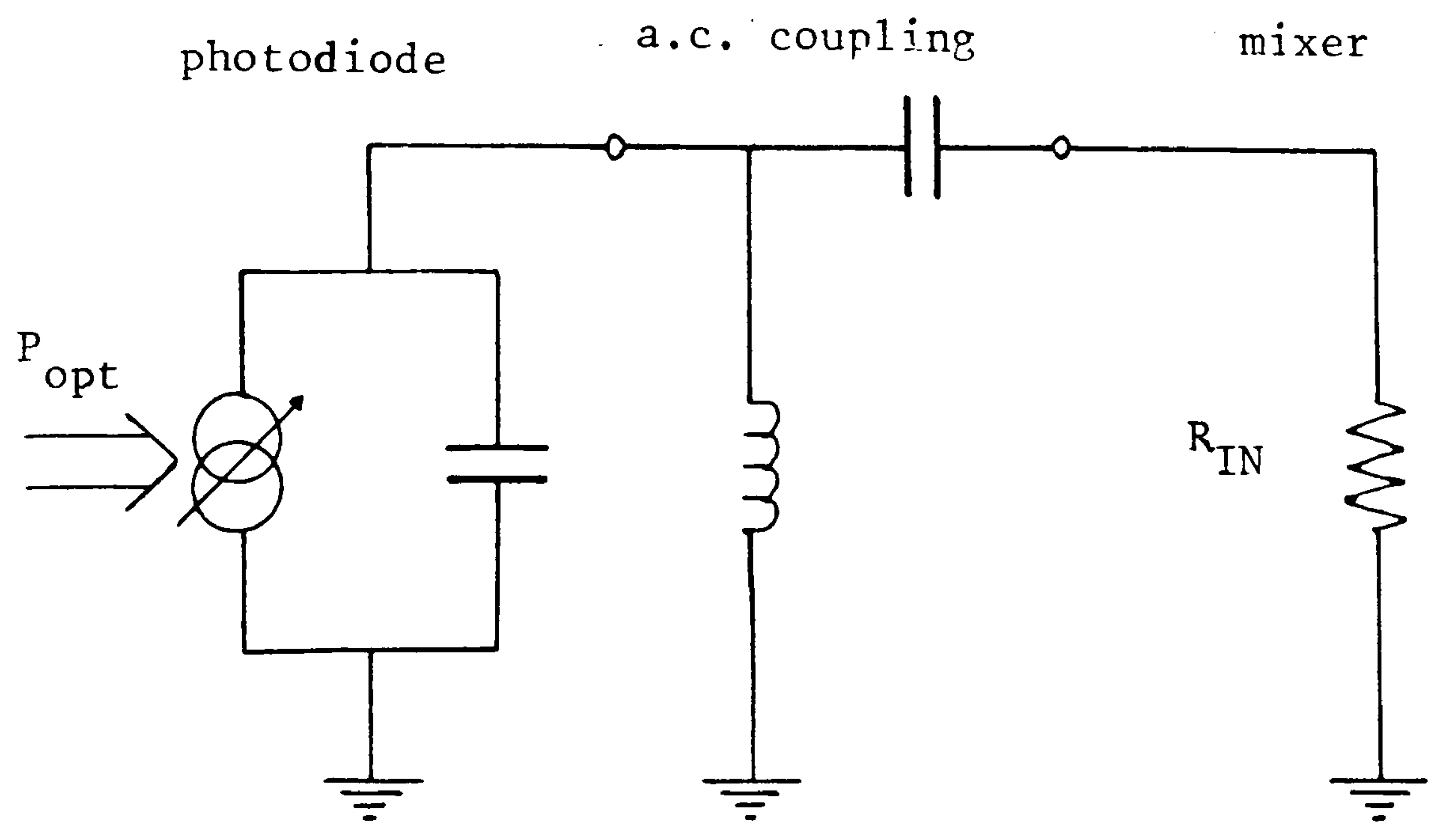

Fig.5.22 Circuit for the analysis of the optical power requirements of a photodiode-mixer combination.

demonstrated a 20GHz bandwidth photodiode with a responsivity ≃0.4A/W in the 800→850nm wavelength range[105]. Commercially available high-power laser diodes, such as the HLP1400's, with approximately 10mW output power would then generate up to 4mA photocurrent.

At low enough frequencies the diode capacitance can be neglected, and it can be assumed that all of the modulated photocurrent is coupled into the mixer. Using eqn. (5.4) the optical power requirements for a combination consisting of an 0.4A/W responsivity photodiode and a low-level mixer would be ≥1.8mW, assuming a 750Ω input impedance, and ≥7.1mW assuming a 50Ω input impedance. The above predictions do not take into account either the fact that l.o. power may be lost in the embedding network, or any requirements for isolation of the signal and l.o. ports (which through the use of directional couplers or balanced configurations will require higher l.o. power[100]).

At higher frequencies, the effect of the photodiode capacitance will severely degrade performance. The photodiode cutoff frequencies mentioned previously were measured with 50Ω loads. With a 750Ω input impedance mixer the l.o. power requirements would double at ≃2.3GHz (equivalent to a quadrupling of the required optical power) if driven by the 20GHz photodiode of Parker, assuming a barrier capacitance of less than 0.1pF[106]. Lower impedance configurations requiring higher photocurrent will therefore be preferable. The significant reactance of the photodiode will also affect the embedding impedances of the mixer arrangement.

It is apparent that, theoretically, a photodiode-mixer combination could be found that would give more efficient conversion (≥7dB rather than ≥10dB), at higher frequencies (up to perhaps 20GHz rather than 1GHz) than the smaller area tunnelling contact described in section 5.4.4. The optical power requirements may also be less, even assuming that the responsivity of the tunnelling contacts more closely approached their expected rather than their measured values. The inferior performance of the tunnelling contact optically pumped mixers is due to device limitations: poorer frequency response, lower levels of photocurrent, and a less nonlinear characteristic. It is conceivable that these limitations could be removed by employing alternative, improved structures - the quest for one such structure is described in Chapter 6. Practically, problems with the isolation of the l.o. and signal ports, with the loading effect of the finite photodiode reactance may occur with a photodiode-mixer combination; the use of a single, efficient, optically pumped mixer may then be of considerable benefit.

As far as conversion efficiency is concerned, optimum performance should be obtainable with the amplification of the detected photocurrent. The photodiode and mixer impedances could then be separately matched to the input and output impedances of the amplifier, respectively; such an arrangement will also give the greatest flexibility as far as the optical power and mixer drive requirements are concerned. The arrangement may, however, suffer from serious noise limitations, especially with high-gain amplifiers, and this will be discussed towards the end of the next section.

5.5.2 Noise performance considerations

The noise performance of a receiver is most affected by the mixer conversion loss. The reduced conversion loss that should be obtainable with a photodetector-mixer combination compared to a tunnelling contact optically pumped mixer should result in improved noise performance. However, it has already been stated that the performance of the tunnelling contact suffers from device limitations, and that improved structures for optically pumped mixers may exist. Of central interest, therefore, is an investigation of any fundamental limitation to the noise performance of optically pumped mixers due to the generation of the photocurrent within the device. Although the tunnelling structure is not itself an efficient optically pumped mixer, as it has been extensively studied and many results and predictions have been obtained, it is useful to employ some of these predictions in the investigation.

The investigation can be made by comparing the performance of a tunnelling contact optically pumped mixer, in which a certain photocurrent is generated, with that of a tunnelling contact employed as a conventional mixer driven by the same level of modulated photocurrent from a photodiode. Although, as discussed in secs.2.3.6 and 5.4.1, the most important measure of performance is the overall noise factor of the receiver employing the mixer, for the sake of comparison it is simpler to use the mixer noise factors.

The mixer noise factor can be calculated from the output noise-temperature, T_n, and the conversion loss, L_c, according to:

$$F = L_c t_r \qquad (5.5)$$

where t_r is the noise-temperature ratio given by:

$$t_r = T_n/T_0$$

from eqns.(2.24) and (2.45). Output noise-temperatures for optically pumped tunnelling contact mixers and their electrically pumped equivalents have been calculated in sec. 5.4.1. The noise-temperatures of the optically pumped mixers are significantly higher than those of the electrically pumped mixers, which, according to eqn.(5.5) would lead to significantly higher noise factors. However, in the electrically pumped case the noise-temperatures do not take into account the effect of photocurrent shot noise applied to the mixer via the l.o. port; since this noise is of low level compared with the l.o., that portion within the mixer bandwidth can be assumed to be linearly converted to the output; it may substantially degrade the performance of a photodetector-mixer combination.

The above arguments are best illustrated with the aid of an example. Operation with 500μA average photocurrent at the reverse bias minimum of V_d=-133mV is assumed for the comparison between an optically pumped tunnelling contact and one used as a conventional mixer driven by a photodiode (see Fig.5.23). For the optically pumped mixer with V_d=-133mV, L_c=10.3dB and $T_n \simeq$2000K; this gives a noise factor of 18.7dB. For the conventional mixer (L_c=10.3dB, $T_n \simeq$525K) the noise factor, similarly calculated, is 12.9dB. A bandwidth of 1MHz is chosen, but this is not of real significance since it has the same effect on both the optically pumped mixer and photodetector-mixer configurations. Initially, the intensity noise of the illumination will be neglected; that is, the optical l.o. will be assumed noiseless.

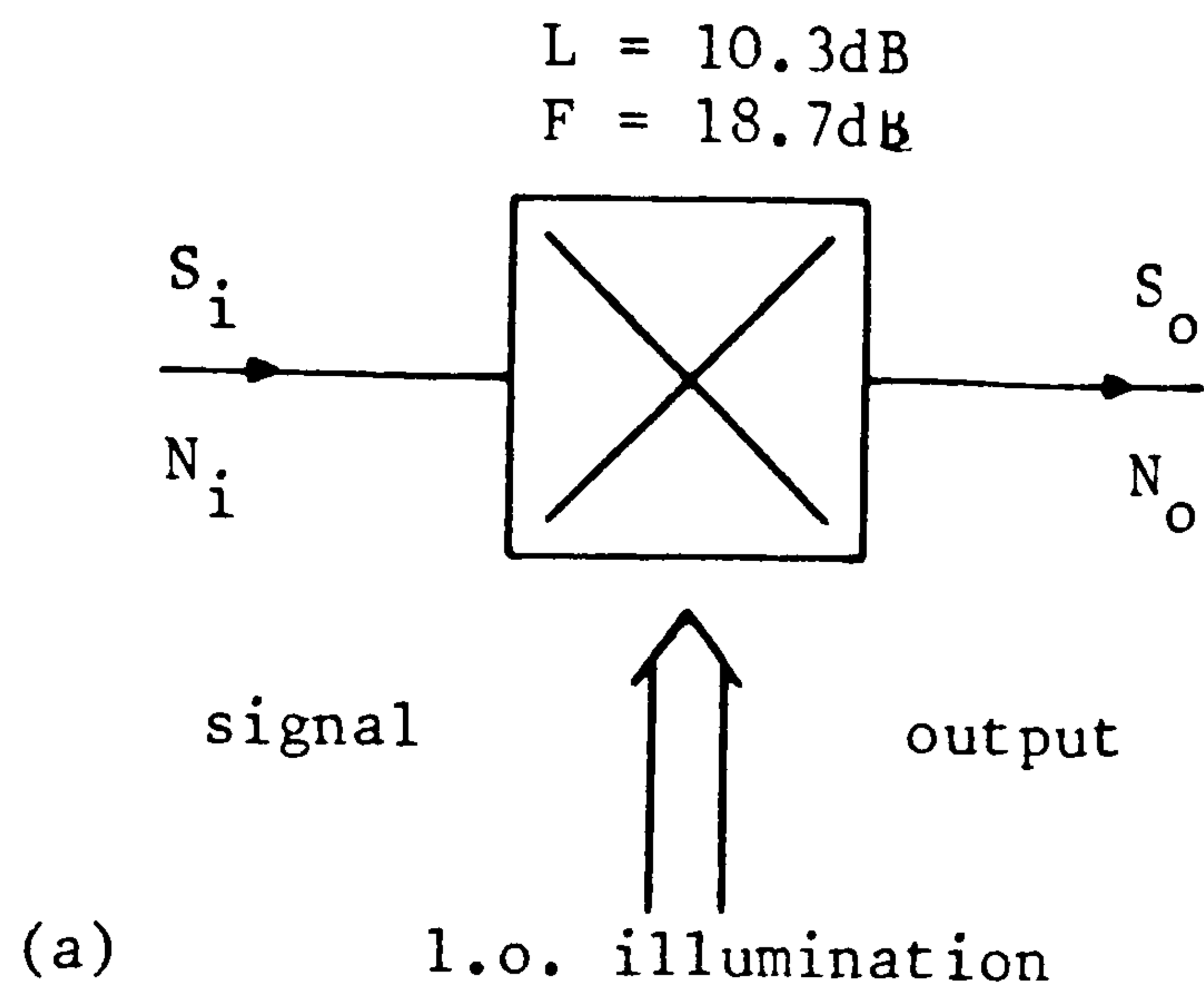

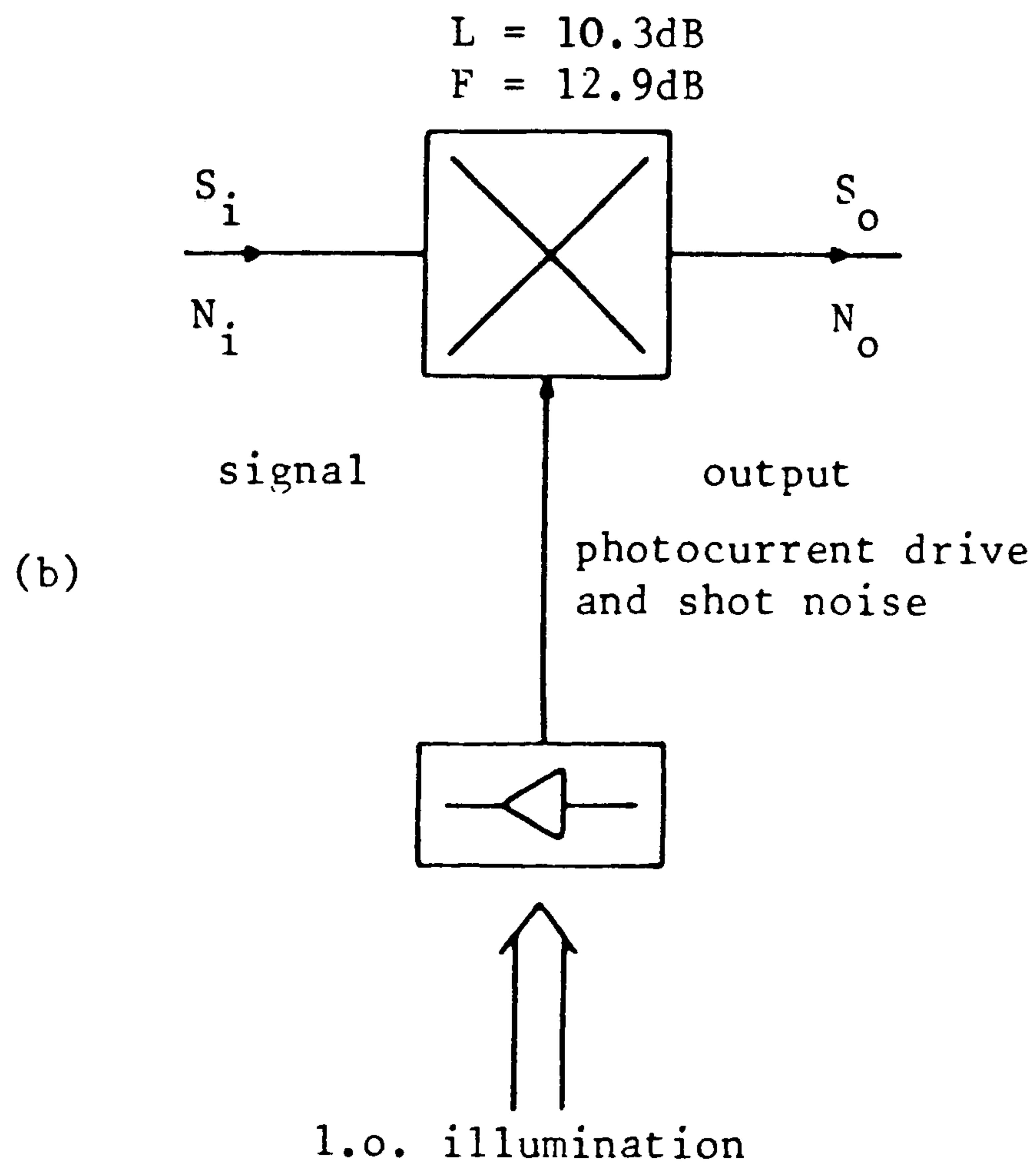

Fig.5.23 Comparison between performance of (a) optically pumped mixer and (b) photodetector-mixer combination.

Assuming a signal level, S_i=-30dBm, and input noise of kTB=-114dBm, then for the optically pumped mixer the output signal, S_o, will be:

$$S_o = S_i/L = -30 - 10.3 = -40.3\text{dBm}$$

and the output noise level will be:

$$N_o = kTBF/L = -105.6\text{dBm}$$

As expected, this represents a degradation in the SNR by the noise factor, F=18.7dB.

For the conventional mixer with the same S_i and N_i, while S_o will still be -40.3dBm, N_o as calculated above will now be -111.4dBm, since the noise factor is now 12.9dB. However, there will also be noise due to the photocurrent. In a 750Ω system the photocurrent shot noise power (2qIBR) will be -99.2dBm; the noise power converted to the output will thus be of level -109.5dBm, and together with the previously mentioned output noise due to the input port (with which it is uncorrelated) the total output noise power will be -107.3dBm. The equivalent noise factor of the combination is thus 17dB which is now only a relatively small improvement on the optically pumped mixer. Further, the contribution of converted l.o. noise in the case of the photodiode-mixer combination will become more significant as the conversion loss is reduced. For the photodetector-mixer combination, optimum coupling has been assumed between the photodetector and mixer circuits - in practice even if this is achievable it may prove difficult. The simplicity of using a single device may more than outweigh the slightly inferior noise performance.

So far the optical l.o. signal itself has been assumed to be noiseless. If laser intensity noise is much more significant than the shot noise in the photodetection process, then the performance of both configurations discussed will be substantially altered. This is likely to be the case with semiconductor lasers, which show levels of intensity noise 10→20dB above the shot noise limits[107]. The level of intensity noise compared to the laser output is dependent on the laser current compared to its threshold current, and varies with frequency. It is also device-dependent. As was the case for the photocurrent shot noise above, the intensity noise will cause a direct increase in the noise factor of the optically pumped mixer, whereas for the photodetector-mixer combination the equivalent noise factor will be increased due to the conversion of the intensity noise to the output port; again, the performance of the latter configuration will tend towards that of the former as the conversion loss is reduced, and more noise is converted to the output.

Finally, a comparison can be made with a receiver employing an amplifier between the photodetector and mixer, since amplification of the photocurrent will give a higher power l.o. and result in reduced conversion loss. With a 0dBm l.o. the conversion loss of the tunnelling contacts can be reduced towards ≃ 6.5dB (the 500μA peak photocurrent into a 750Ω load represents ≃ -10dBm); the noise factor can be expected to be ≃ 7.5dB. In the discussion that follows, the exact values are not important since it will be seen that the photocurrent noise can dominate the SNR of the system.

Assuming the values of input signal and noise used above, the output signal level will be -36.5dBm, and the noise contribution from the input and the mixer noise will be -113dBm. If the l.o. frequency is required to be

adjustable within the 1MHz bandwidth of the system, then with an amplifier of 750Ω input impedance, and of the necessary gain of 10dB, the photocurrent noise will also be amplified by 10dB, giving a l.o. noise level of -89.2dBm at the input, and of -95.7dBm at the output. Effectively, the noise figure of the system will then be 24.8dB. Employing a low input impedance amplifier may be useful in obtaining a higher frequency response, but the noise performance would not be significantly changed. The circumstances in which the photodetector-amplifier-mixer system could give better performance than optically pumped mixers are when the l.o. frequency is fixed and filtering is used between the photodetector and amplifier. In the above system, with filters of bandwidth ≤ 100kHz the performance would be improved compared to that of an optically pumped mixer. However, it can be seen that the system has become quite complex; the very reason why optically pumped mixers have been investigated is to reduce system complexity.

5.6 Chapter summary

Using the computer models of Chapter 3, preliminary predictions of the conversion loss performance of tunnelling contact optically pumped mixers with high, but not unrealistic values of photocurrent have been obtained. The predictions have shown the importance of having a sufficiently high embedding impedance if significant conductance modulation and hence efficient frequency conversion is required. With 500μA average photocurrent (and 100% modulation) a conversion loss of about 10dB is predicted for reverse bias operation.

Experimental measurements of the conversion loss at low frequencies (≃100MHz) have been taken using several

different lasers as optical l.o. sources. With semiconductor lasers, due to the lower levels of photocurrent generated, the measured conversion loss is much higher than that of the preliminary predictions. However, it is shown that short wavelength illumination (as well as higher optical power) can be used to generate substantially higher current. Frequency-doubled mode-locked Nd:YAG lasers provide such short wavelength illumination - the mode-locking also providing a form of modulation. Unfortunately, the pulse waveform is not conducive to efficient mixing in reverse bias, which is the situation of most interest in the tunnelling contacts. In forward bias, however, with the devices used, the conversion loss was reduced to about 15dB. Conversion loss performance predictions from the computer models for the tunnelling contacts in the above experimental arrangements, and with the values of photocurrent generated experimentally, have shown very good agreement with the measured results; this is especially true for the time domain model predictions.

The noise performance of the tunnelling contact optically pumped mixer has been investigated using the simple noise analysis of section 2.3. The noise-temperature ratio minimum for the device is between 6 and 10 (with 500μA average photocurrent) due mainly to the shot noise contribution of the photocurrent. A high noise-temperature ratio means that the noise factor of a receiver employing the device would be much higher than that of a typical microwave receiver.

Accurate predictions of the diode impedance under l.o. excitation can be found using the time domain computer model. The dynamic range at the low level end - the minimum detectable signal - has been found to be restricted mainly by the high conversion loss, although with lower loss the high device noise will become more

significant; at the high signal level end - the compression point - the restriction comes about due to the low level of l.o. power available. The -3dB operating frequency of the tunnelling contacts investigated is restricted to about 125MHz, although with a smaller area device this could be increased to perhaps 1GHz.

The tunnelling contacts investigated experimentally will not compare favourably with good photodetector-mixer combinations. However, this is due to device limitations; it has been shown that the fundamental aspect of the optically pumped mixer, that the photocurrent generation and the mixing occur in the same device, does not lead to significant limitations, while the simplicity of the arrangement may be of considerable benefit. Neglecting device limitations, that is if the generated photocurrent is similar to that in a fast photodetector, and the I-V nonlinearity similar to that of a microwave mixer, the noise factor of a photodiode-mixer combination will be only 1→2dB better than that of the optically pumped mixer.

With the optically pumped mixer and photodetector-mixer systems it is assumed that conditions for broad-band matching of the l.o./signal/image frequencies exist. The l.o. noise converted to the output will be the photocurrent shot noise and laser intensity noise in the i.f. bandwidth. With an amplifier between the photodetector and mixer the noise performance would not be improved unless a narrow-band filter was also placed between the photodetector and amplifier to reduce the noise bandwidth of the l.o. noise.

CHAPTER SIX

RECTIFYING SCHOTTKY STRUCTURES

6.1 Proposed device structure 215

6.2 Current transport in Schottky/Mott diodes 218

6.2.1 Diffusion and thermionic emission theories 219

6.2.2 Current-voltage characteristics 221

6.2.3 Equations used for current-voltage characteristic 224

6.2.4 Calculation sequence and results 229

6.3 Frequency response limitations 234

6.3.1 Preliminary predictions 234

6.3.2 Transit-time limitations using combined theory 237

6.4 Predicted performance 245

6.4.1 Conversion loss 245

6.4.2 Other parameters 252

6.5 Chapter summary 256

In Chapter 1 (sec.1.3.1) it was described how a rectifying Schottky-type device could be used in forward bias as an optically pumped mixer. The device would remain 'punched through' even in forward bias, where the I-V characteristic is highly nonlinear, and hence retain efficient photodetection and low capacitance properties. In this chapter a structure for such a Mott diode optically pumped mixer is proposed in section 6.1, and the physics and predicted operation of the structure presented in sections 6.2 to 6.4. In section 6.2 the current transport theory for barriers on lightly to moderately doped semiconductors is reviewed and applied to the contacts of interest in this work. In section 6.3 the frequency limitations of the Mott diodes are investigated. The performance of Mott diodes as optically pumped mixers is predicted in section 6.4.

6.1 Proposed device structure[47]

The proposed structure of an optically pumped mixer device is shown in Fig.6.1. A thin, semitransparent metallisation forms a rectifying contact to a lightly doped epilayer grown on a heavily doped substrate to minimise parasitic series resistance. The lightly doped layer is fully depleted even in forward bias, where the I-V characteristic is very nonlinear. Apart from the semi-transparency of the metallisation, the structure is very similar to that of Mott diodes which have been employed as microwave mixers[108]. The presence of the depletion region, however, suggests the use of the device as an optically pumped mixer. In the proposed structure, the barrier width, defined by the thickness of the epilayer, would be tailored to the optical absorption length at the desired

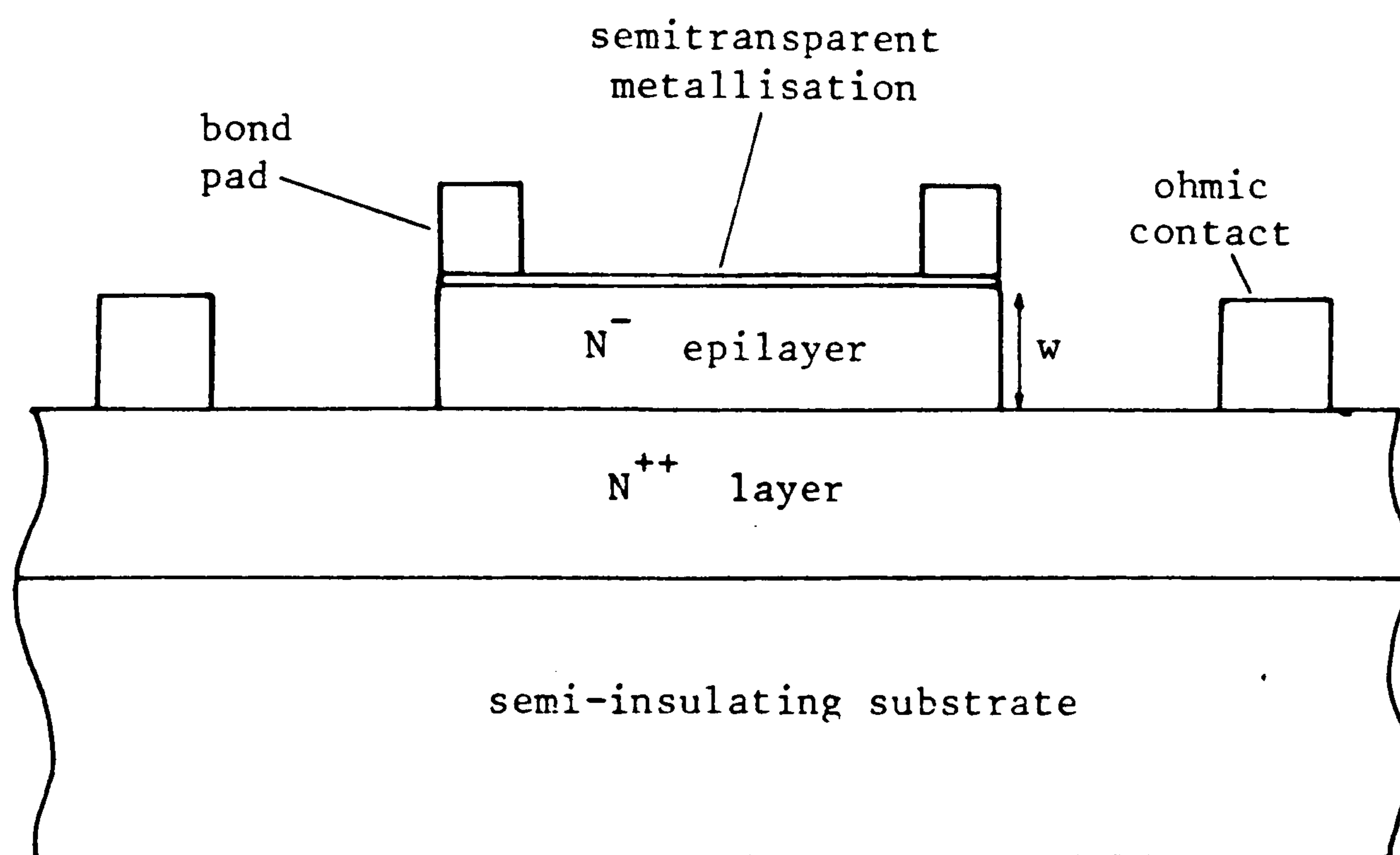

Fig.6.1 Proposed structure of an optically pumped Mott mixer diode. The lightly doped epilayer, which determines the barrier width, remains punched through even with the diode under forward bias, and is tailored to the optical absorption length at the desired operating wavelength.

operating wavelength. Gallium arsenide would be a suitable device material as its short absorption lengths (0.1μm to 1.4μm for illumination wavelengths between λ=500nm and λ=850nm) could enable the fabrication of narrow barriers which would retain efficient photodetection properties. Together with the high carrier mobility in GaAs, these narrow barriers should result in short transit times. As Mott diodes are dependent on majority-carrier diffusion, and the electron mobility is higher in GaAs, n-type material should be used. Thin epilayers, and high definition between the heavily and lightly doped layers, can be achieved using processes such as molecular-beam-epitaxy[109].

In operation the epilayer must remain punched through; that is, the depletion width must exceed or at least equal the epilayer width. For a contact to a uniformly doped semiconductor, the depletion width, w, according to the depletion approximation[89], is given by:

$$w = \sqrt{[2\varepsilon(V_{bi}-V)/qN_D]} \quad (6.1)$$

where N_D is the doping level (donor concentration), V_{bi} is the built-in voltage of the barrier, and V is the applied voltage. For the Mott type structures, when the device is punched through, the expression for the depletion width would have to take into account the different doping levels of the epilayer and the substrate. When the device is not punched through, the expression in eqn.(6.1) can be used with N_D being the epilayer donor concentration. Therefore, eqn.(6.1) can be used at the limit of punch-through by putting $w=w_{epi}$, where w_{epi} is the epilayer width, and rearranging to find the maximum applied voltage, or minimum $(V_{bi}-V)$, which will retain punch-through operation.

From eqn. (6.1), it is obvious that low doping and low forward bias are desirable to obtain wide punched through regions. However, the forward bias on the device is necessary to provide the barrier current, and for sufficient forward current and reasonably low diode impedance, high forward bias may be required. The current levels which can be obtained with the proposed structure for different epilayer doping levels and thicknesses are therefore important; these will be investigated in the next section.

6.2 Current transport in Schottky/Mott diodes

The I-V characteristic of a metal-semiconductor contact is usually expressed as:

$$I = I_s[\exp(qV/nkT) - 1] \qquad (6.2)$$

where the ideality factor, n, and the saturation current, I_s, are often assumed constant. From a non-physical view-point either n or I_s would have to be bias dependent in order to model actual characteristics. In a physical model both n and I_s may be bias dependent, the extent of this dependence being governed by the physical model applicable to the situation and hence used to derive the above relationship. In Chapter 4, for example, it was seen how the tunnelling mechanism caused n to deviate from its ideal value of unity in contacts to highly doped semiconductors. For contacts to lightly or moderately doped semiconductors, tunnelling should be insignificant at room temperature and under forward bias.

6.2.1 Diffusion and thermionic emission theories

The carrier transport in contacts to lightly and moderately doped semiconductors is due to a combination of diffusion and drift in the barrier region with thermionic emission at the top of the barrier. Both processes must occur and are in series, but depending on which is the greater impediment to current flow, either one of two models can be used to derive the current-voltage relationship. According to the diffusion theory of Schottky[110], it is the transport across the barrier region or depletion layer which restricts the current flow, whereas in Bethe's thermionic emission theory[111] the current flow is restricted by the actual emission process.

Fig.6.2 shows the band profiles and electron quasi-Fermi level for a forward biased metal-semiconductor contact. As n-type material is assumed the following discussion concentrates on electron current. The quasi-Fermi level variations predicted by the diffusion theory and the thermionic emission theory illustrate their differences. According to the diffusion theory the Fermi levels in the metal and the semiconductor align at the interface; the quasi-Fermi level droops across the depletion layer providing the necessary 'driving force' for the electron diffusion. The alignment of the Fermi-levels at the interface, however, makes it impossible to inject 'hot' carriers into the metal. According to the thermionic emission theory, the electron quasi-Fermi level is constant throughout the depletion region and the current flow is restricted by the communication between electron states in the metal and the semiconductor. Electrons which are emitted into the metal are 'hot' or energetic, but they lose this energy due to collisions with conduction electrons and the lattice and hence rapidly come into equilibrium with the conduction electrons in the metal. This causes the relatively abrupt

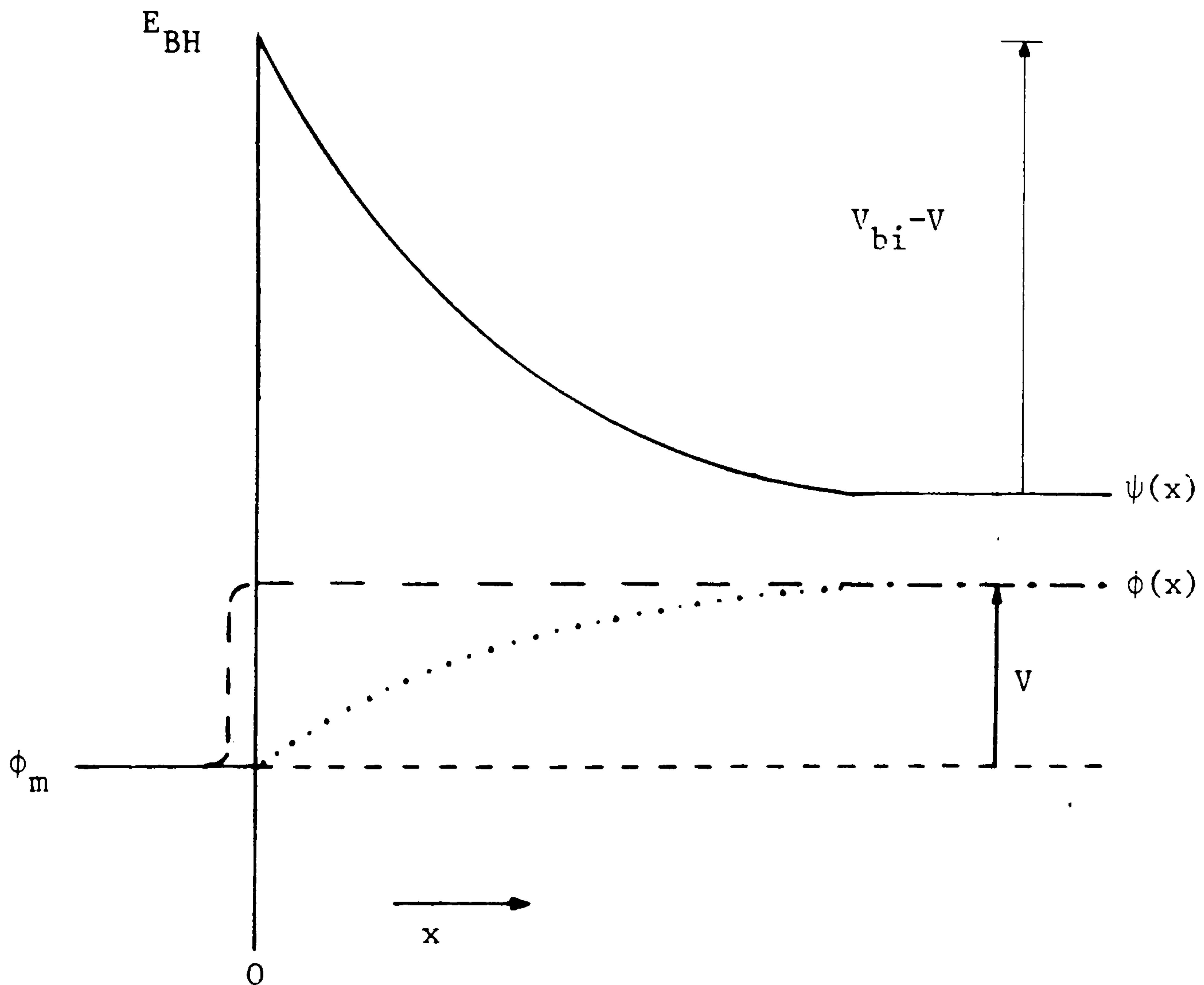

Fig. 6.2 Conduction band profile and electron quasi-Fermi level for a contact to n-type semiconductor under forward bias. The quasi-Fermi level variations according to the two extreme ideal situations of the thermionic emission theory (— — —) and the diffusion theory (··········) are shown.

drop in the quasi-Fermi level just on the metal side of the interface. The behaviour of real contacts will lie somewhere between the two extremes of the diffusion and thermionic emission theories.

6.2.2 Current-voltage characteristics

The current-voltage characteristic of a metal-semiconductor contact can be derived for either of the above theories. According to the diffusion theory it is derived from the equation for current continuity in the depletion layer:

$$J_n = qn_e\mu_e E + qD_e\frac{dn_e}{dx} \qquad (6.3)$$

which can be written:

$$J_n = q\mu_e n_e\frac{d\varphi}{dx} \qquad (6.4)$$

where φ is the electron quasi-Fermi level, using the Einstein relationship $\mu_e/D_e = q/kT$. In the above equations J_n is the electron current density (which is approximately the total current density), μ_e is the electron mobility, E is the electric field, D_e is the electron diffusion constant, and n_e is the electron concentration (x is the distance along the depletion layer from the metal-semiconductor interface and q is the electronic charge, k, Boltzmann's constant and T the absolute temperature). Equation (6.4) shows that the gradient of φ, the electron quasi-Fermi level, supplies the driving force for electron motion.

In the diffusion theory eqn.(6.4) is solved with $\varphi(0)=0$, where the zero level is taken as the Fermi level

in the metal. The current-voltage relationship obtained can be given by[53]:

$$J \simeq q^2 N_C D_e [2q(V_{bi}-V)N_D/\varepsilon]^{1/2} \exp(-E_{BH}/kT)\{\exp(qV/kT) - 1\} \tag{6.5}$$

where the expression in the first set of brackets shows the electric field dependence of the carrier transport. It can be seen that the diffusion theory predicts a bias dependent 'saturation' current, although the current variation with bias will still be dominated by the exponential voltage-dependent term. In eqn.(6.5), N_C is the density of states in the conduction band, N_D is the donor concentration, V_{bi} is the built-in voltage (see Fig.6.2), E_{BH} is the barrier height, and ε is the semiconductor permittivity.

With the thermionic emission theory, the electron thermal velocity is used to calculate the emission of electrons into the metal. The resultant expression for the characteristic is given by[53]:

$$J = qN_C v_{th} \exp(-qE_{BH}/kT)\{\exp(qV/kT) - 1\} \tag{6.6}$$

where $v_{th}=\surd(kT/2m^*\pi)$, or, equivalently, by:

$$J = A^* T^2 \exp(-qE_{BH}/kT)\{\exp(qV/kT) - 1\} \tag{6.7}$$

where the effective Richardson constant, $A^*= 4\pi m^* qk^2/h^3$, and where m^* is the electron effective mass. In GaAs, m^* is approximately $0.07m_0$, where m_0 is the free electron mass, and the thermal velocity ,v_{th}, is approximately 1.0×10^7cm/s.

Crowell and Sze[112] have combined the diffusion and thermionic emission theories by considering the two mechanisms to be in series and hence finding the quasi-Fermi level position which equalises the current flow in both processes. The result is an equation of the form:

$$J = \frac{qN_C v_c}{1 + v_c/v_d} \exp(-qE_{BH}/kT)\{\exp(qV/kT) - 1\} \qquad (6.8)$$

where the effective recombination velocity, v_c, can take into account the effects of electron-optical-phonon scattering[113] and quantum-mechanical reflection and tunnelling[114] which reduce the velocity from the thermal velocity by factors f_p and f_q, respectively. Confident estimates of f_p and f_q are difficult to obtain, but in practice their combined effect (which is bias dependent) is unlikely to reduce the recombination velocity by more than a factor of two[89]; this will therefore have little effect on the current-voltage relationship compared to the exponential dependence in eqns.(6.5), (6.6), (6.7), and (6.8). The effective diffusion velocity, v_d, is given by[53]:

$$v_d = \frac{\mu_e kT}{q} \left\{ \int_0^w \exp[q(\psi(0)-\psi(x))/kT]\, dx \right\}^{-1} \qquad (6.9)$$

where the term in the square brackets is a measure of the band bending, $\psi(x)$ being the conduction band potential at distance x.

If $v_c \gg v_d$, then diffusion dominates the relationship. For example, if the mobility were independent of the electric field, then $v_d=\mu_e E$, and eqn(6.8) would reduce to the standard diffusion result:

$$J = qN_C\mu_e E \exp(-qE_{BH}/kT)\{\exp(qV/kT) - 1\} \qquad (6.10)$$

which is directly comparable to eqn.(6.5) if use is made of the Einstein relationship described after eqn.(6.4).

On the other hand, if $v_d \gg v_c$ then the thermionic emission process would be the main restriction to current flow and eqn.(6.8) would reduce to eqn.(6.6).

6.2.3 Equations used for current-voltage characteristic

An accurate analysis of the current flow in a metal-semiconductor contact using the combined thermionic emission-diffusion theory as presented by Crowell and Beguwala[115] will be used to derive the current-voltage characteristics of contacts to uniformly doped semiconductor material. The contacts modelled are not the structures proposed in sec.6.1 since the lightly doped material is not assumed to be an epilayer which is punched through under normal operation. An analysis which takes into account a heavily doped substrate and punch-through operation would be a useful further step; however, careful consideration would have to be given to carrier mobility variation as well as the differences in band profile and depletion width variation for the non-uniformly doped structure.

In the analysis and results to be presented in the next section it is assumed that the simple uniformly doped barrier can adequately model the Mott structure. The thermionic emission process depends on the communication between electron states in the metal and the semiconductor - for reasonably wide epilayers ($\geq$ 50nm) for which tunnelling will be negligible, on the semiconductor side, the thermionic emission will depend only on the states in

the lightly doped epilayer. The diffusion process depends on the carrier concentration gradient, set up largely by the band bending in the semiconductor. Between the metal-semiconductor and epilayer-substrate interfaces the electric field and energy band profiles will be the same as those in a contact to uniformly doped material of the same doping level as the epilayer. Further, under relatively high forward bias, which is likely to be the mode of operation for the optically pumped mixer, most of the potential drop and hence band bending will occur within the epilayer, and so the band profiles will look very similar to those of the contact to the uniformly doped material.

The most obvious comments on these assumptions are that the thinner barrier which will occur due to the more heavily doped substrate if the epilayer is punched through, will provide less resistance to carrier flow, and that the increased carrier density at the edge of the barrier due to the higher donor concentration should provide a greater carrier concentration gradient, which is important for the forward diffusion current. These comments suggest that more ideal characteristics may be obtainable at higher currents for the punch-through diodes than will be predicted by the combined thermionic emission-diffusion theory for the simple 'full' barriers . Near ideal characteristics and high currents (over 500μA) have been obtained with microwave Mott diodes[109] but these devices have been fabricated with higher epilayer doping, and it is not clear that during operation they would remain punched through for the whole of a local oscillator cycle. Whereas for microwave mixers this may not be of great importance (increasing slightly the barrier capacitance and series resistance), for an optically pumped mixer it could have a serious effect since the presence of the depletion region provides the means by

which the local oscillator signal is coupled into the device.

Using the assumption that the characteristics of the Mott devices will be dependent almost exclusively on the metal - lightly doped epilayer interface and the carrier transport within the epilayer, the characteristics can be predicted from those calculated for contacts to uniformly doped material. The calculation of these characteristics is now presented. In the following analysis, the electron potentials shown in Fig.6.3 should be referred to; the positive direction of the x-axis is reversed as this simplifies the analysis. To calculate the current, the general expression,

$$J = q\mu_e n_e \frac{d\varphi}{dx} \tag{6.3}$$

is used, as outlined in sec.6.2.1. However, the boundary condition for the diffusion theory, that the Fermi levels in the metal and semiconductor coincide at the interface, is not used, and the combined theory is used to derive the electron quasi-Fermi level in the barrier.

In eqn.(6.3) the electron concentration is given by:

$$n_e(x) = N_C \exp[-q(\psi(x)-\varphi(x))/kT] \tag{6.11}$$

where $\psi(x)$ is the conduction band energy given by:

$$\psi(x) = E_{BH} + (qN_D(x^2-w^2))/2\varepsilon \tag{6.12}$$

The quasi-Fermi level potential is derived by Crowell and Beguwala and is given by[115]:

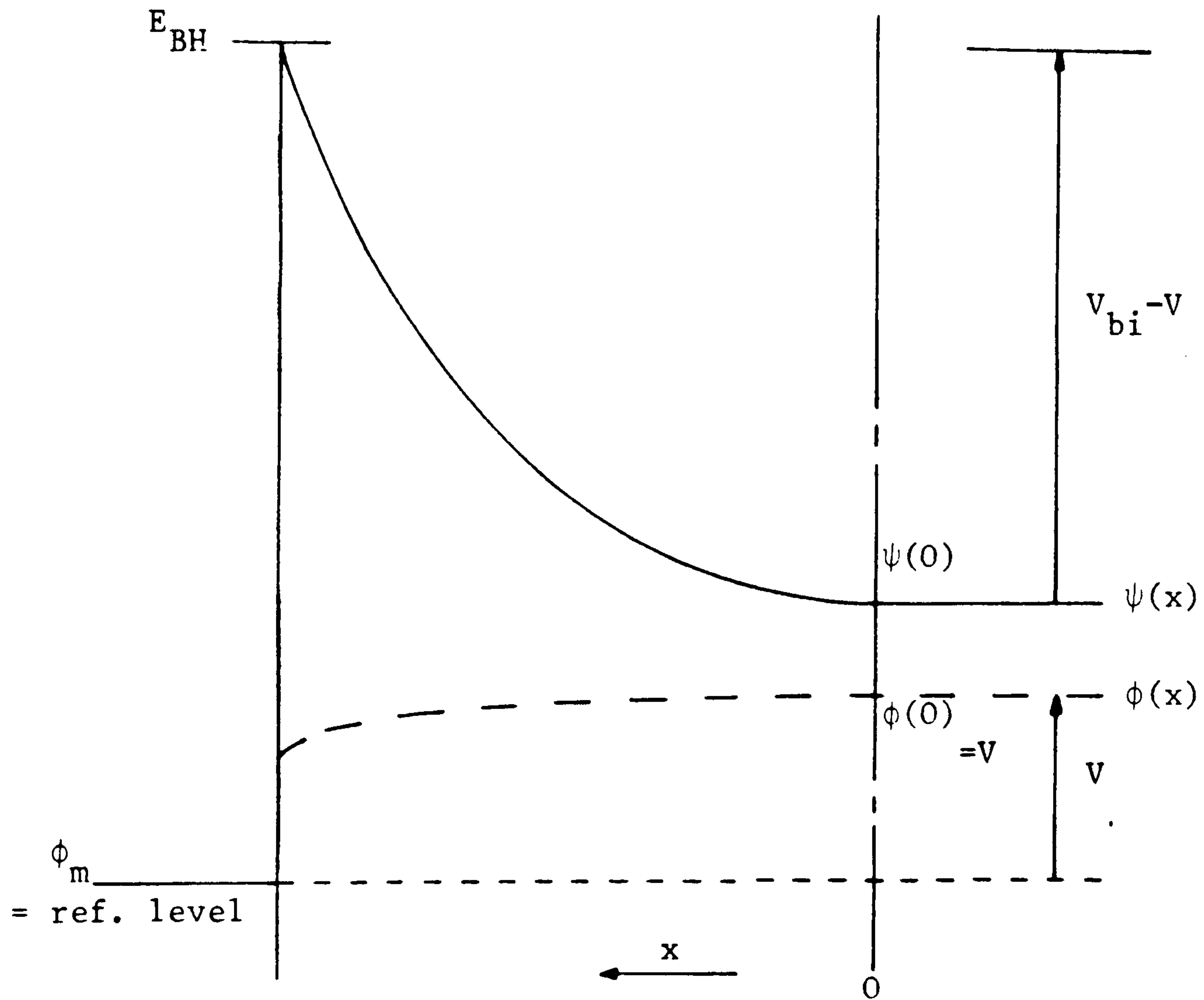

Fig.6.3 Electron energy levels in contact to n-type semiconductor used to determine the current flow under forward bias from the combined thermionic emission-diffusion theory. Note the reversal in the positive direction of the x-axis compared to Fig.6.2.

$$\varphi(x) = (kT/q).\ \ln\{1 - [\exp(-\beta).(1-\exp(-qV/kT)).\exp(x^2/w^2\beta) \times D_2/(\delta_v + D_1)]\} + V \quad (6.13)$$

where the parameter β is a measure of the band bending, given by:

$$\beta = q^2 w^2 N_D / 2\varepsilon kT \quad (6.14)$$

$\delta_v = v_D/v_c$ is the ratio of a Debye diffusion velocity to the recombination velocity, and v_D is given by:

$$v_D = \mu_e . \surd(kT/2qL_D) \quad (6.15)$$

where L_D is the Debye length,

$$L_D = \surd(\varepsilon kT/q^2 N_D) \quad (6.16)$$

and where D_1 and D_2 are Dawson functions[116], $f_d(y)$, which can be expressed:

$$D_1 = f_d(\surd\beta) \quad (6.17)$$

and

$$D_2 = f_d((x\surd\beta)/w) \quad (6.18)$$

The Dawson function is given by:

$$f_d(y) = \exp(-y^2) \int_0^y \exp t^2 \, dt$$

6.2.4 Calculation sequence and results

By employing the equations of sec.6.2.3 in a computer analysis, the I-V characteristics of contacts to semiconductors of different doping have been calculated. Physical constants such as ε_0, q, and k are held within the program. The input parameters are then the 'material' constants, N_C, ε_r, v_{th}, and f_p and f_q, and the particular 'barrier' constants, μ_e (which is doping dependent), N_D, E_{BH}, V and T. The calculation of w, β and δ_v is straightforward using the equations presented in the last section, eqns.(6.1), (6.14), (6.15). Only the two Dawson functions are required to define the electron quasi-Fermi level; these are found by the numerical integration of eqns.(6.17) and (6.18).

The electron quasi-Fermi level is numerically differentiated in order to find the electron current from eqn.(6.3) - hole current in these devices will be negligible. The above calculation sequence is repeated for a range of x values throughout the barrier region. The current remains constant throughout the barrier, of course, but this does serve as a check that the program is performing correctly.

Fig.6.4 shows the current (density) versus bias characteristics for contacts to n-type GaAs with donor densities of 1×10^{14}, 2×10^{14}, 5×10^{14}, and 1×10^{15} cm^{-3}, assuming a barrier height of 0.8eV. It can be seen that with lower doping the forward current is much lower at a particular bias level. At high forward bias, when the 'flat-band' situation is approached, the model becomes inaccurate because of the depletion approximation. 'Flat-band', the situation where the depletion region disappears, never actually occurs because of other limiting factors such as finite series resistance. The increased slope at higher forward bias, especially apparent for the lower doping cases, should be ignored due

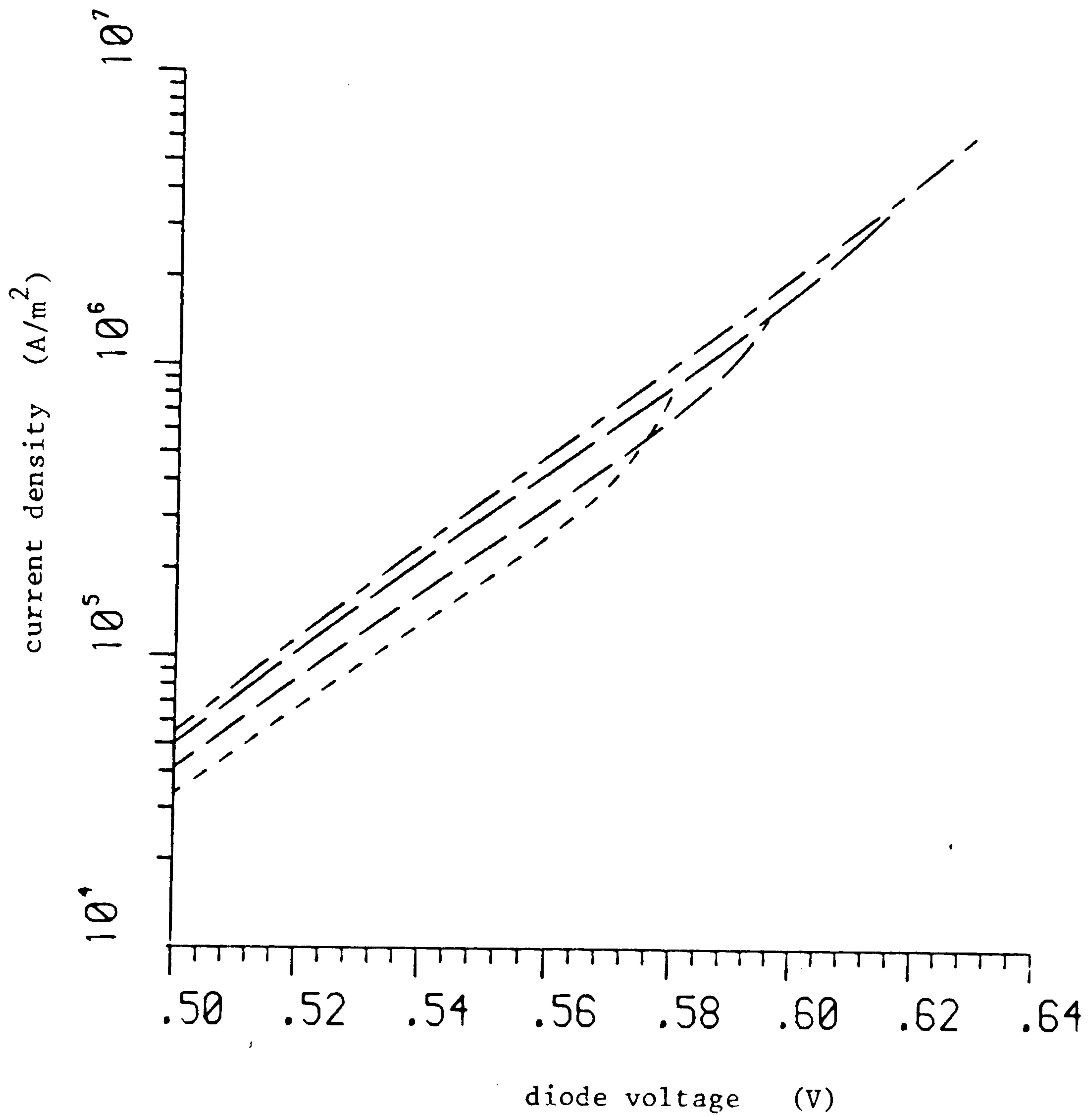

Fig.6.4 Current-voltage characteristics for contacts of barrier height 0.8eV to GaAs of the following donor concentrations:

----- $N_D = 1 \times 10^{14}$ cm^{-3} — — — $N_D = 2 \times 10^{14}$ cm^{-3}

—— —— $N_D = 5 \times 10^{14}$ cm^{-3} — - - — $N_D = 1 \times 10^{15}$ cm^{-3}

to the depletion approximation inaccuracy. The situation is approached at lower bias voltages with lower doped material because the built-in voltage is decreased due to the greater difference in the conduction band and electron Fermi energies. This is apparent in Fig.6.5 which shows computed conduction band and quasi-Fermi level variations for four situations: (a) doping of $10^{14}cm^{-3}$ and forward bias of 0.53V (forward current of 9.4μA), (b) same doping and forward current = 90μA (bias of 0.58V), (c) doping of $10^{15}cm^{-3}$ and forward bias of 0.53V (current of 16.9μA), (d) same doping as (c) and similar current to (b), 88μA (bias of 0.575V). It can be seen that even in the contacts to the lightly doped GaAs, the droop in the quasi-Fermi level is very small.

The results shown in Fig.6.4 are probably more informative if the current density is plotted against the difference between the applied voltage and the built-in voltage ($V-V_{bi}$) - this is done in Fig.6.6. Again, the points close to flat-band, or the built-in voltage, where the slope increases under high forward bias, should be ignored. As the depletion region shrinks when the forward voltage is increased, the length of undepleted, high-resistivity low doped material will increase. The series resistance will limit the current-voltage characteristics of the contacts at high forward bias; the slope of the log(J) vs. V characteristic will be reduced, giving high apparent ideality factors and reduced nonlinearity. From Fig.6.6, therefore, it is obvious that it may be difficult to obtain good ideality factors at reasonable forward current from the small area contacts desirable for optically pumped mixers (although at low bias before series resistance effects become significant, the curves in Figs.6.4 and 6.6 predict good values of ideality). For example, for a 10x10 μm^2 contact, a current density of $1x10^5 A.m^{-2}$ represents a current of only 10μA.

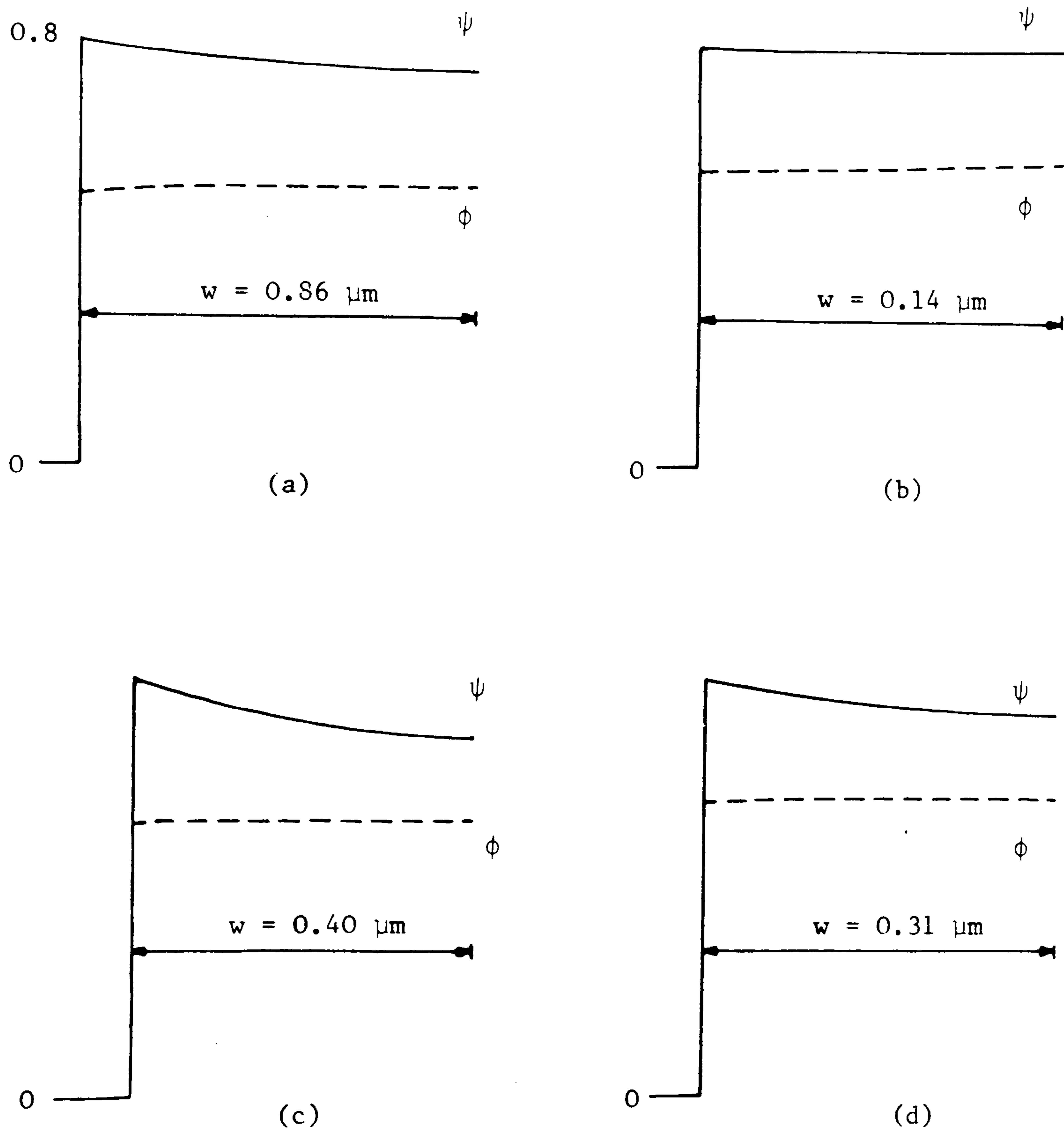

Fig.6.5 Computed conduction band and quasi-Fermi level variations for contacts of barrier height 0.8eV and

(a) $N_D = 10^{14}$ cm^{-3}, V = 0.53 V, I = 9.4 μA
(b) $N_D = 10^{14}$ cm^{-3}, V = 0.58 V, I = 90 μA
(c) $N_D = 10^{15}$ cm^{-3}, V = 0.53 V, I = 16.9 μA
(d) $N_D = 10^{15}$ cm^{-3}, V = 0.575 V, I = 88 μA

Current corresponds to that in a 10 x 10 μm^2 contact.

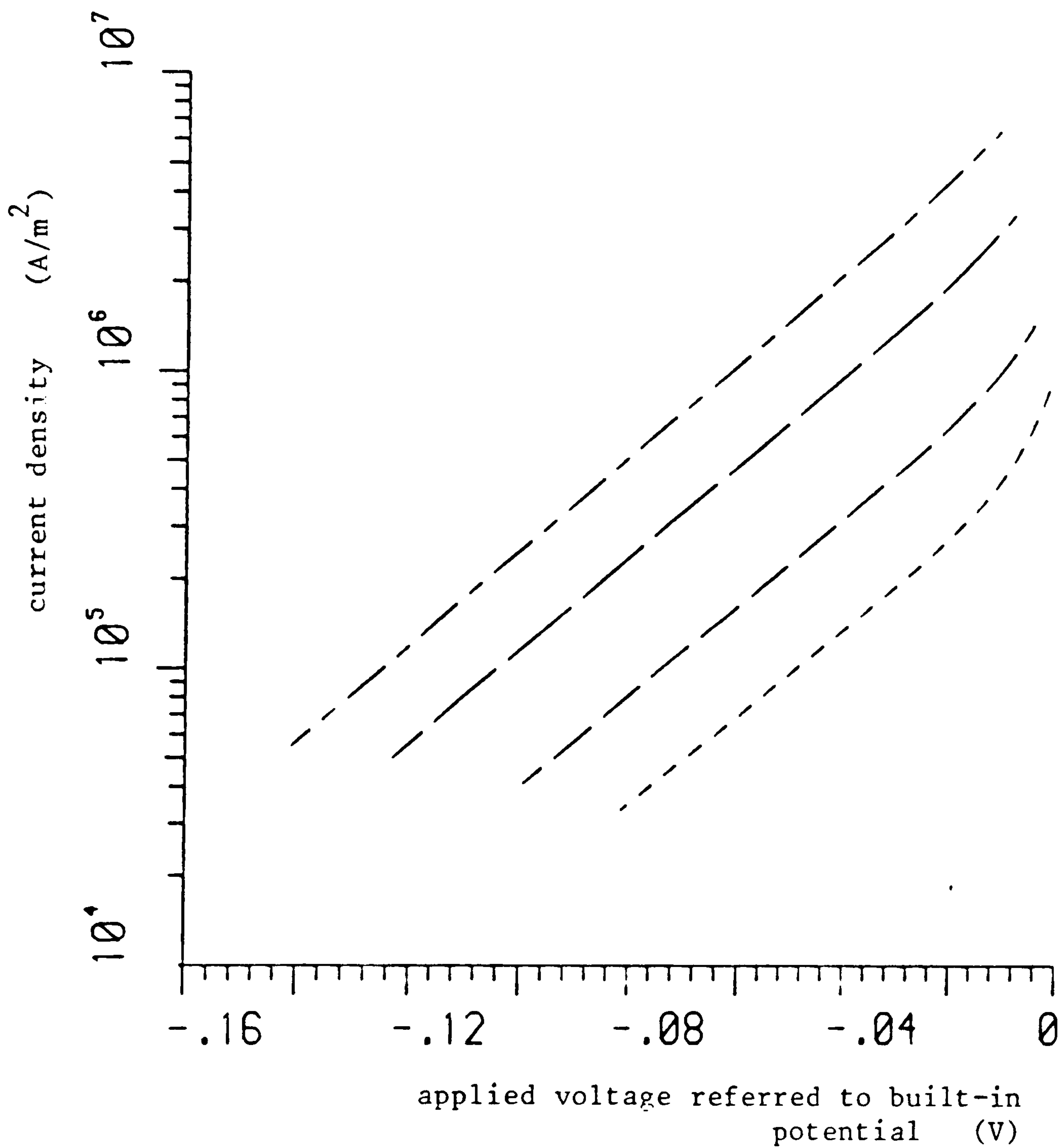

Fig.6.6 Current-voltage characteristics of contacts to n-type GaAs as given in Fig.6.4 but with the current density plotted against the difference between the applied voltage and the built-in potential. The zero on the x-axis, therefore, corresponds to the 'flat-band' potential. Parameters are as for Fig.6.4.

6.3 Frequency response limitations

6.3.1 Preliminary predictions

Carrier motion within barriers such as those described in the previous sections is dependent on a combination of diffusion and drift. The drift of electrons, for example, in the metal-n-type semiconductor barriers, is in the reverse current direction. The forward conduction in such devices can therefore be attributed to the situation when the electric field is low enough for the drift component to become much less significant than the diffusion. Since the forward current in Mott-type structures is dependent on diffusion, the transit-time limitations to the frequency response of such structures can be defined in a similar way to that in which the transit-time limitations for minority-carrier diffusion in p-n junctions are derived[68]. In this case, however, a majority-carrier diffusion constant, D (= D_e, for n-type barriers) must be used[108]:

$$f_t < D/\pi w^2 \qquad (6.19)$$

where w is the depletion width.

Fig.6.7 shows theoretical maximum cutoff frequencies for devices with epilayer widths made equal to the absorption length at the corresponding illumination wavelength. It can be seen that the short absorption length of GaAs at shorter wavelengths could mean very high-frequency operation. The transit-time-limited cutoff frequency, according to the inequality expressed in (6.19), can also be maximised by making the epilayer doping as low as possible and thus increasing the diffusion constant. For efficient operation the device

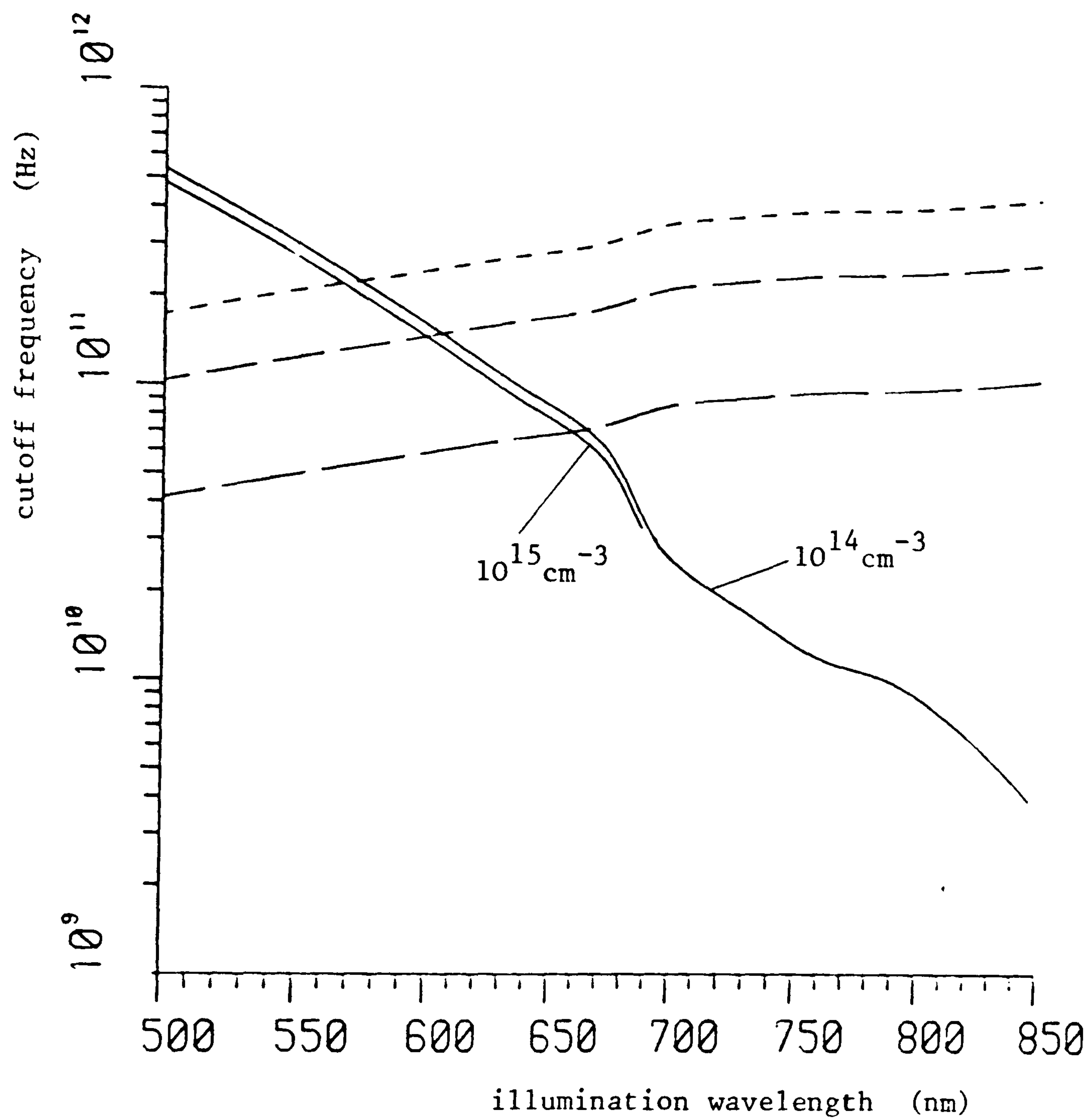

Fig.6.7 Theoretical maximum cutoff frequencies with the transit-time limitation calculated according to the inequality expressed in (6.19).

———— transit-time limitation. RC limitations:

- - - - - r = 6Ω, — — — r = 10Ω, —— —— r = 25Ω

r is the series resistance, and the total capacitance is made up of barrier capacitance and a constant 50fF parasitic capacitance.

would have to remain punched through for practically the whole of a local oscillator cycle. This is why the cutoff frequency curve for the $10^{15}cm^{-3}$ doped structures stops abruptly; epilayer widths greater than the absorption length at $\lambda \approx 670nm$ ($w > 0.55\mu m$) will not remain punched through with forward barrier currents of greater than $500\mu A$, according to a simple analysis of the voltage drop in the epilayer using the depletion approximation. The simple analysis, however, used an ideality factor, n=1, and a constant, bias-independent 'saturation' current. In the theory of section 6.2.4 it was seen that obtaining this level of current with wide punched through epilayers may be difficult. Therefore, in the next section the combined thermionic emission-diffusion theory will be used to calculate the transit-time limitations.

The RC cutoff frequencies shown in Fig.6.7 have been calculated according to:

$$f_c = 1/2\pi rC_t = 1/2\pi r(C_b+C_p) \tag{6.20}$$

where r is the diode series resistance, and the total capacitance C_t is made up of the barrier capacitance, C_b, and a parasitic capacitance, C_p. The barrier capacitance is calculated according to the depletion approximation from the epilayer width, the device area, and the semiconductor permittivity. An area of $10x10\mu m^2$ has been assumed. The parasitic capacitance has been assigned a typical constant value of 50fF[109].

6.3.2 Transit-time limitations using combined theory

The inequality expressed in eqn. (6.19) does not give a definite value for the transit-time-limited cutoff frequency. Also, in general, as the average velocity of carriers at any point in the barrier is due to a combination of drift and diffusion, and as drift velocity is field-dependent, the carrier velocity and hence transit-time will show bias dependence. Equations of the form of the inequality in (6.19) are derived in the context of minority-carrier diffusion in p-n junctions, and are usually applied to find the base transit-times in microwave transistors[68]. The band and quasi-Fermi level profiles in metal-semiconductor contacts will be very different to those in p-n junctions.

Using the current and carrier concentration calculated in the combined thermionic emission-diffusion theory, an effective velocity, v, can be defined for the electrons at a point, x, in the barrier from the general relation for current, $J_n = qn_e v$ (c.f. eqn. (2.9)). Hence the transit-time across a distance z can be defined as:

$$\tau_d = \int_0^z qn_e/J_n \, dx \qquad (6.21)$$

In the results which will be presented it is assumed that the conduction band profile and quasi-Fermi level within the epilayer of a punch-through device are similar to those that would exist within this depth of the 'full' barrier formed if the heavily doped substrate were not present. This is a reasonable assumption for the band profile up to very near the epilayer—substrate boundary; however, a fuller analysis would be necessary to determine the effect on the quasi-Fermi level. The assumption allows the electron concentration found in the analysis for a 'full' barrier to be used for the punch-through structure

for x between 0 and z, where 0 is the metal-semiconductor interface and z is the epilayer width. The current calculated in the previously described thermionic emission-diffusion analysis is also used, although the assumptions made in the analysis, stated at the beginning of section 6.2.3, should be borne in mind.

Fig.6.8 shows the predicted transit-time-limited -3dB frequencies for four contacts with epilayer widths equal to the absorption length at the corresponding illumination wavelength. The four contacts are of the same barrier height (0.8eV), but have different semiconductor doping levels: (a) $1 \times 10^{14} cm^{-3}$, (b) $2 \times 10^{14} cm^{-3}$, (c) $5 \times 10^{14} cm^{-3}$, (d) $1 \times 10^{15} cm^{-3}$. The different curves for each contact illustrate the variation in cutoff frequency with barrier current and applied voltage referred to the 'flat-band' or built-in potential $(V-V_{bi})$. The values of current correspond to contacts of area $10 \times 10 \mu m^2$. As in Fig.6.7, the curves are not continued when the applied voltage (or, equivalently, the barrier current) is such that the epilayer would not be fully depleted.

From Fig.6.8 it is again apparent that with the lightly doped devices especially, obtaining a substantial barrier current while retaining a wide depletion layer may prove difficult. However, it can also be seen that the RC cutoff frequencies, shown in Fig.6.7, for the longer wavelengths are much higher than the transit-time-limited cutoff frequencies for the corresponding wavelengths shown in Fig.6.8. Therefore, the device area could be increased, thereby reducing the current density required for a given barrier current. This would have the added benefit of easing the effective coupling of the illumination into the optically pumped mixer structure.

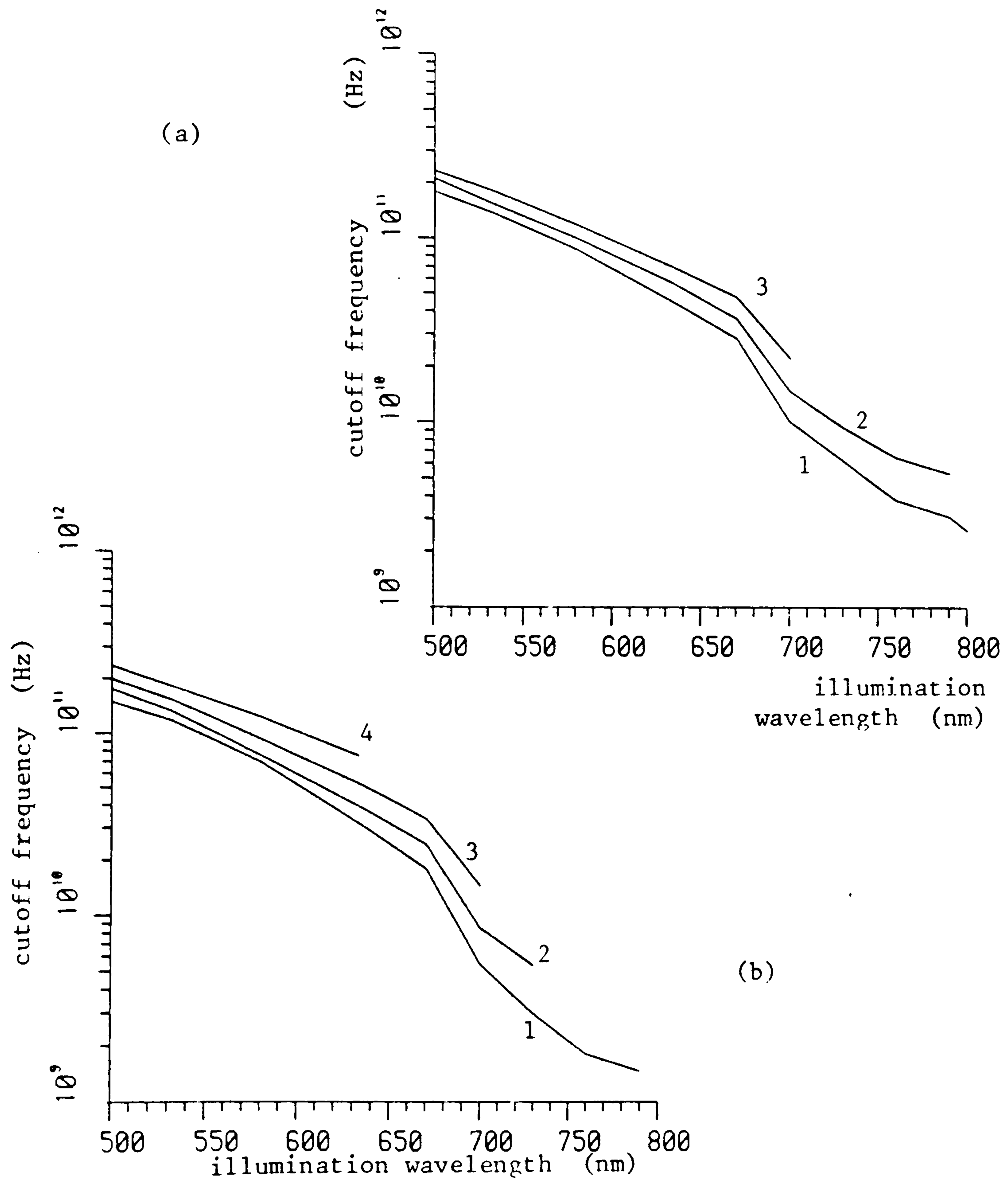

Fig.6.8 Predicted transit-time-limited cutoff frequencies for contacts of barrier height 0.8eV and with epilayer widths made equal to the absorption length at the corresponding illumination wavelength.

(a) $N_D=1 \times 10^{14}cm^{-3}$: 1. $V - V_{bi} = -0.0814V$, $I = 3.36\mu A$
2. $V - V_{bi} = -0.0514V$, $I=9.36\mu A$ 3. $V - V_{bi} = -0.0214V$, $I=26.9\mu A$

(b) $N_D=2 \times 10^{14}cm^{-3}$:
1. $V - V_{bi} = -0.0993V$, $I=4.13\mu A$ 2. $V - V_{bi} = -0.0693V$, $I=11.9\mu A$
3. $V - V_{bi} = -0.0393V$, $I=33.8\mu A$ 4. $V - V_{bi} = -0.0093V$, $I=111\mu A$

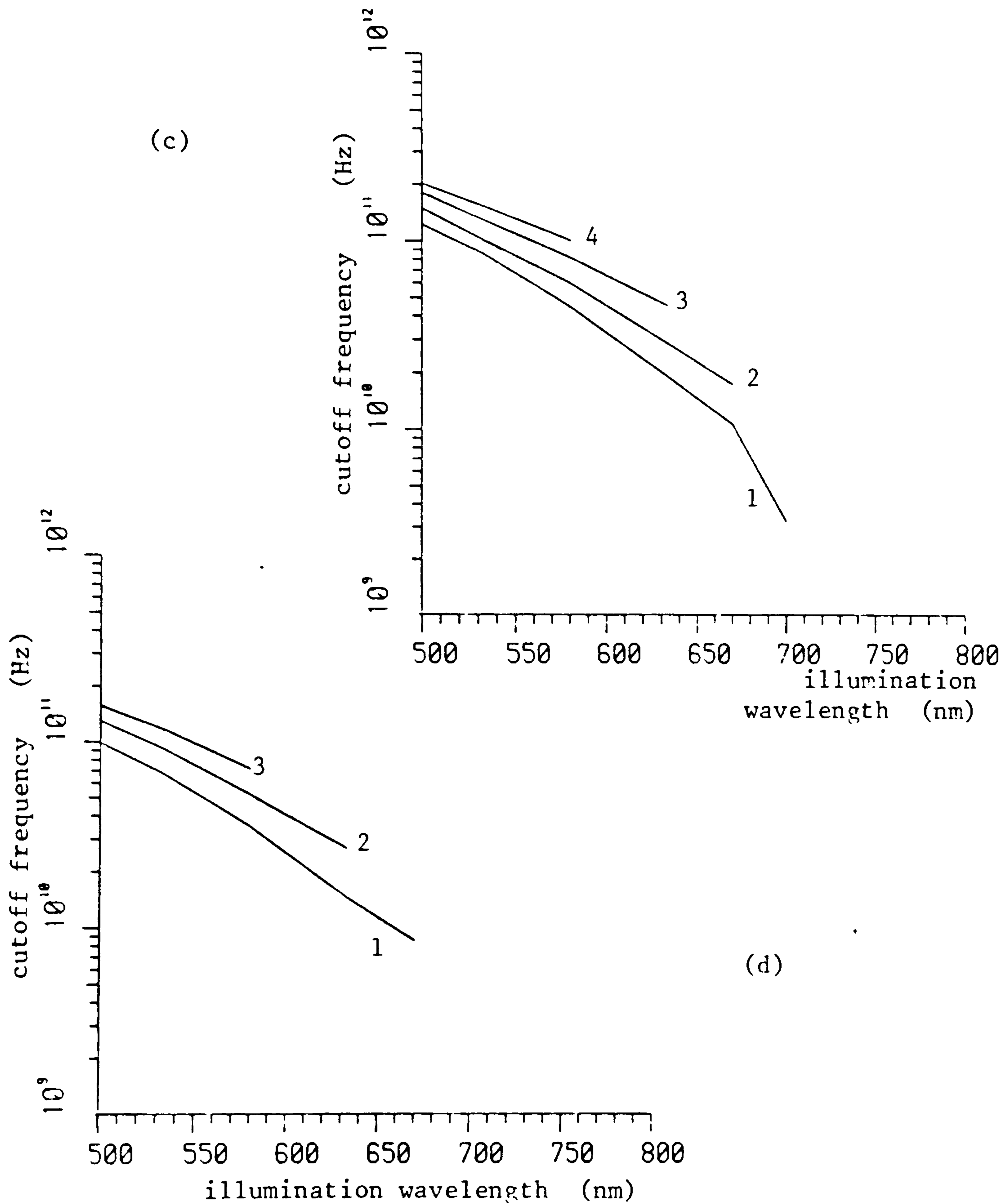

Fig.6.8 Predicted transit-time-limited cutoff frequencies for contacts of barrier height 0.8eV and with epilayer widths made equal to the absorption length at the corresponding illumination wavelength.

(c) $N_D = 5 \times 10^{14} cm^{-3}$:

1. $V - V_{bi} = -0.093V$, $I = 15.1\mu A$ 2. $V - V_{bi} = -0.063V$, $I = 44.4\mu A$

3. $V - V_{bi} = -0.033V$, $I = 129\mu A$ 4. $V - V_{bi} = -0.018V$, $I = 228\mu A$

(d) $N_D = 1 \times 10^{15} cm^{-3}$: 1. $V - V_{bi} = -0.0809V$, $I = 51.1\mu A$

2. $V - V_{bi} = -0.0509V$, $I = 152\mu A$ 3. $V - V_{bi} = -0.0309V$, $I = 313\mu A$

In Fig.6.9 it is assumed that the epilayer should remain depleted for a barrier current of at least 500μA; using some of the data of Fig.6.8 the device area has been selected in each curve of the four graphs in order to ensure this. Obviously, the RC cutoff frequencies will be affected by the different device areas, so the corresponding RC cutoff frequency curve (for r=10Ω) is given with each curve for the transit-time-limited cutoff. Generally, it can be seen that for operation at short wavelengths for which the epilayer can be made thin and, therefore, the transit-time short, the doping can be increased so that the device area necessary for a given current density is reduced, extending the RC cutoff. At longer wavelengths the required depletion width necessitates the use of semiconductor of lower doping in the epilayer; larger area devices are necessary to obtain satisfactory current. However, it can be seen that even with these larger area devices, the RC cutoff frequency may still be higher than the transit-time-limited one. Fig.6.9 illustrates the fact that a careful choice of doping, epilayer width, and device area would have to be made in order to maximise the frequency response of practical optically pumped Mott diode mixers. Fig.6.9(d) suggests that cutoff frequencies of near 100GHz should be obtainable for devices operating at frequency-doubled Nd:YAG laser wavelengths, and Fig.6.9(c) cutoff frequencies of about 50GHz for devices operating at HeNe laser wavelengths. For longer wavelengths, approaching those of GaAs lasers, however, Fig.6.9 suggests cutoff frequencies of barely above 1GHz. This situation may be aided, however, by the fact that large area contacts are being used and so some responsivity could be traded-off by reducing the epilayer thickness; such a proposal would require further investigation with real contacts, since it depends on the quantum efficiency (for example, the transmittance of the Schottky contact) obtainable with the

devices. Some indications of these trade-offs are given in section 6.4.1.

It is apparent from the preceding discussion that more ideal characteristics and higher barrier currents for given diode voltages should be obtainable with narrower epilayers of the higher doping discussed ($1 \times 10^{15} cm^{-3}$). Another reason for selecting higher doping is the fact that the field in the barrier will be higher, and the detrimental effects of the carrier transfer into the metal, as discussed at the end of section 2.1.2, will be minimised. Also it is desirable that the transit-time-limited cutoff does not occur until at least millimetre-wave frequencies (30GHz+); according to Gärtner's equation (2.7), this will require a carrier drift velocity of $2 \times 10^{6} cm/s$ for a 0.25μm wide barrier, and, therefore, fields of over 0.2kV/cm. Punch-through with $1 \times 10^{15} cm^{-3}$ doping is likely to ensure these fields, whereas with $1 \times 10^{14} cm^{-3}$ doping, the fields, and therefore carrier velocities, will be nearly an order of magnitude too low. As the barrier width is constant (defined by the epilayer) the collection volume for photo-carriers will be constant and the bias-independent current generator model is assumed to apply in the predictions of the following sections. This is a simplification as, from the discussions above and at the end of section 2.1.2, the collection efficiency may be bias-dependent. (If photo-carriers are extracted by diffusion the current generator model may still be applicable if this current is approximately illumination-dependent; transit-time limitations will be as for the majority-carrier barrier current.)

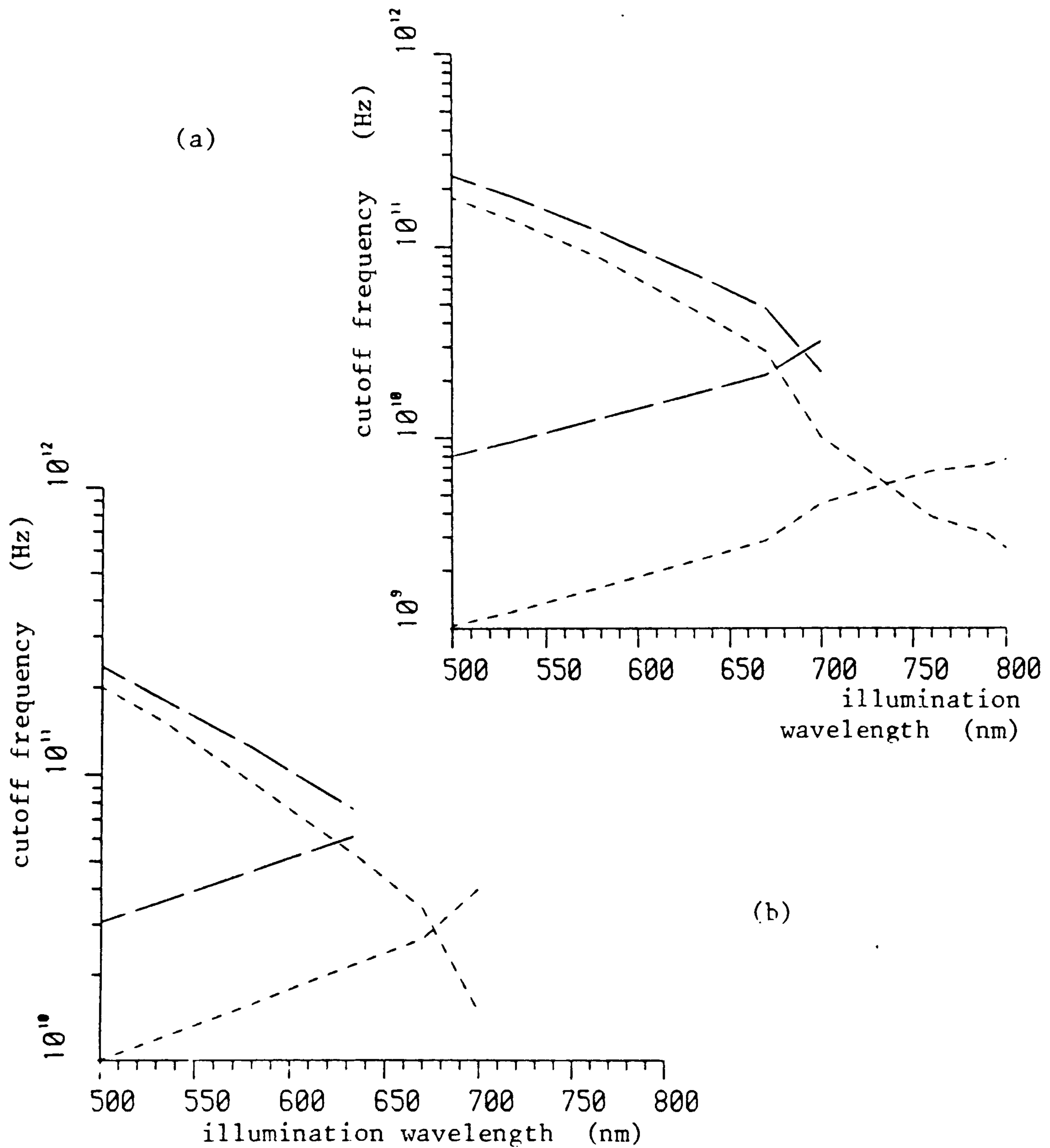

Fig.6.9 Cutoff frequencies for contacts of barrier height 0.8eV and with epilayer widths equal to the absorption length at the corresponding illumination wavelength, under sufficient forward bias to give a barrier current = 500μA. Upward curves are RC limitations, downward curves are transit-time limitations.

(a) $N_D = 1 \times 10^{14} cm^{-3}$: ---- $V - V_{bi} = -0.0814V$, $A \simeq 15\ 000 \mu m^2$

— — $V - V_{bi} = -0.0214V$, $A \simeq 1\ 900 \mu m^2$ A = device area

(b) $N_D = 2 \times 10^{14} cm^{-3}$: ---- $V - V_{bi} = -0.0393V$, $A \simeq 1\ 500 \mu m^2$

— — $V - V_{bi} = -0.0093V$, $A \simeq 450 \mu m^2$

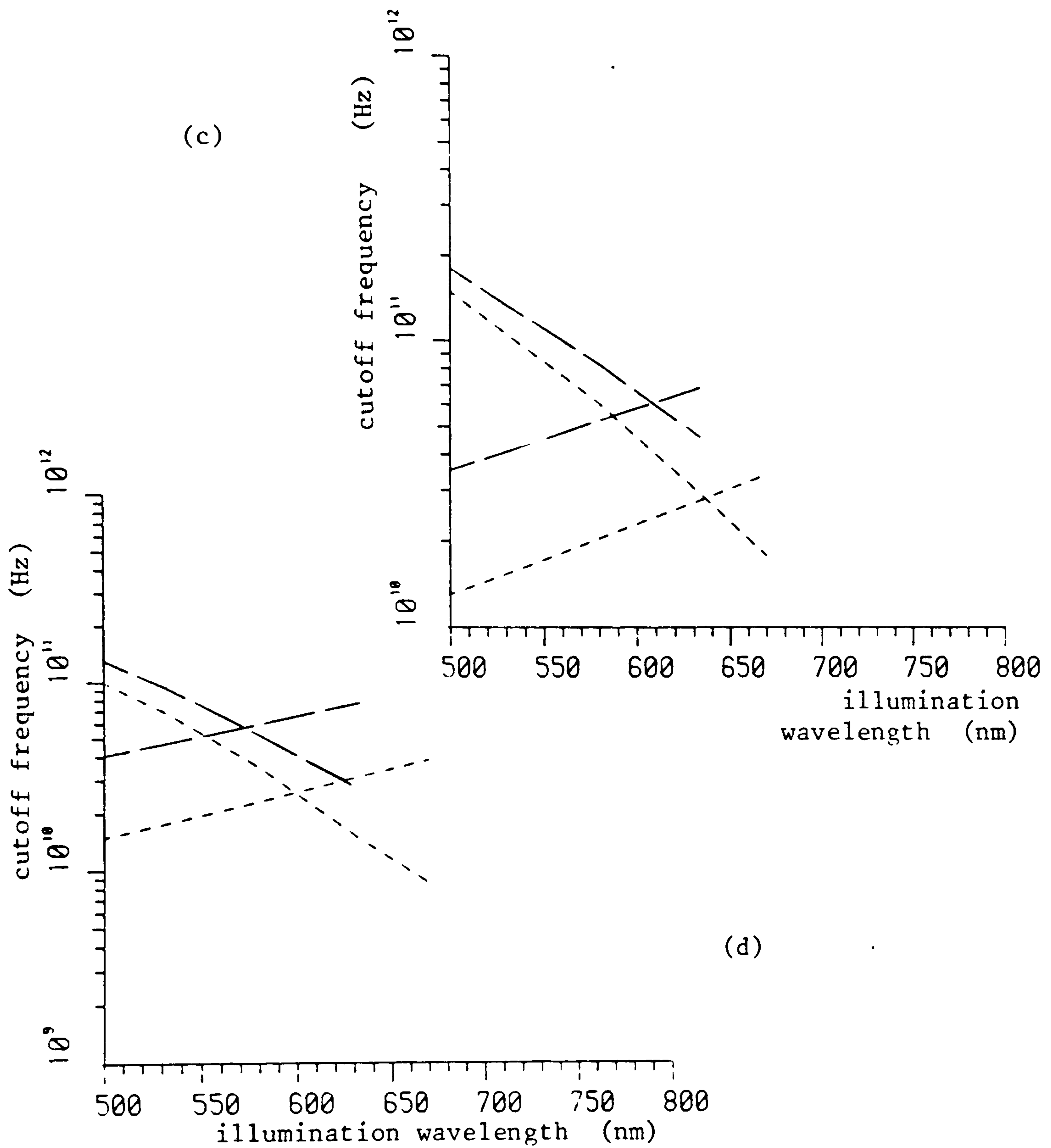

Fig.6.9 Cutoff frequencies for contacts of barrier height 0.8eV and with epilayer widths equal to the absorption length at the corresponding illumination wavelength, under sufficient forward bias to give a barrier current = 500μA. Upward curves are RC limitations, downward curves are transit-time limitations.

(c) $N_D = 5 \times 10^{14} cm^{-3}$: ---- $V - V_{bi} = -0.063V$, $A \simeq 1\ 130 \mu m^2$

—— $V - V_{bi} = -0.033V$, $A \simeq 390 \mu m^2$

(d) $N_D = 1 \times 10^{15} cm^{-3}$: ---- $V - V_{bi} = -0.0809V$, $A \simeq 1\ 000 \mu m^2$

—— $V - V_{bi} = -0.0509$, $A \simeq 330 \mu m^2$

6.4 Predicted performance

6.4.1 Conversion loss

The conversion efficiency obtainable from Mott diode optically pumped mixers can be predicted using the mixer programs described in Chapter 3. As the conversion loss is expected to be lower for these devices, with higher harmonics of the l.o. likely to be of greater influence, the more accurate time domain analysis is employed. It would be impractical to model the I-V characteristics of the Mott diode structures in the mixer program using the combined thermionic emission-diffusion theory; also, the I-V characteristic used in the program needs to be analytic as its derivative is also required. From Figs.6.4 and 6.6, however, it can be seen that the log(current) versus voltage characteristic obtained from the combined theory is approximately linear for applied voltages up to within 30mV of the built-in voltage. The I-V characteristic can therefore be modelled by an expression of the form of eqn.(6.2). It was shown in the last two sections that with some devices it would not be possible to obtain useful forward current while retaining a punched through epilayer. The mixer program will make no allowances for such a situation, in fact the program would operate even if the voltage in eqn.(6.2) were greater than the built-in potential, which is not a physically realisable situation. Such factors have to be considered separately and a judgement must be made on whether any particular mixer program run represents a realisable situation. The judgement will be based not only on the I-V characteristic and the level of current obtainable, but also on the device capacitance, which also depends on the epilayer remaining depleted. In the mixer program the barrier capacitance is assigned a constant value.

Fig.6.10 shows the conversion loss variation with bias for an optically pumped mixer with an I-V characteristic of the form of eqn.(6.2) and with $I_s=I_{sd}=27.4fA$ and $n=1.05$. The value of n is important as it defines the nonlinearity of the I-V characteristic which causes the mixing action. The value of I_s, derived according to the diffusion theory with $\mu_e E$ replaced by $v_d \approx 1.0x10^7 cm/s$ in eqn.(6.10), does not affect the mixing in this way; it is only important in defining the barrier current and conductance at a particular bias. Assuming the pump and circuit conditions and diode ideality factor, n, are the same, the same mixing action (with similar barrier current and conductance) could be achieved with a diode with a different I_s if the quiescent bias is suitably adjusted. Generally, the value of I_s used will be an over-estimate as it does not take into account the effect of thermionic emission which also restricts the current flow. In fact, the thermionic emission 'saturation' current for the same barrier, given by:

$$J_{st} = A^*T^2 \exp(-qE_{BH}/kT)$$

from eqn(6.7) predicts a very similar value of $I_{st}=28.3fA$ to that predicted by the diffusion theory, $I_{sd}=27.4fA$. This suggests that the effective diffusion and recombination velocities are approximately equal and so, from the simple result of the combined theory, eqn.(6.8), the actual 'saturation' current will be approximately half these values, or $I_s \simeq 14fA$. However, this does not take into account the bias dependence of the 'saturation' current because of the approximation involved in using a constant v_d. The complete thermionic emission-diffusion analysis takes into account this bias dependence but, as mentioned previously, is not suitable for use in the mixer program.

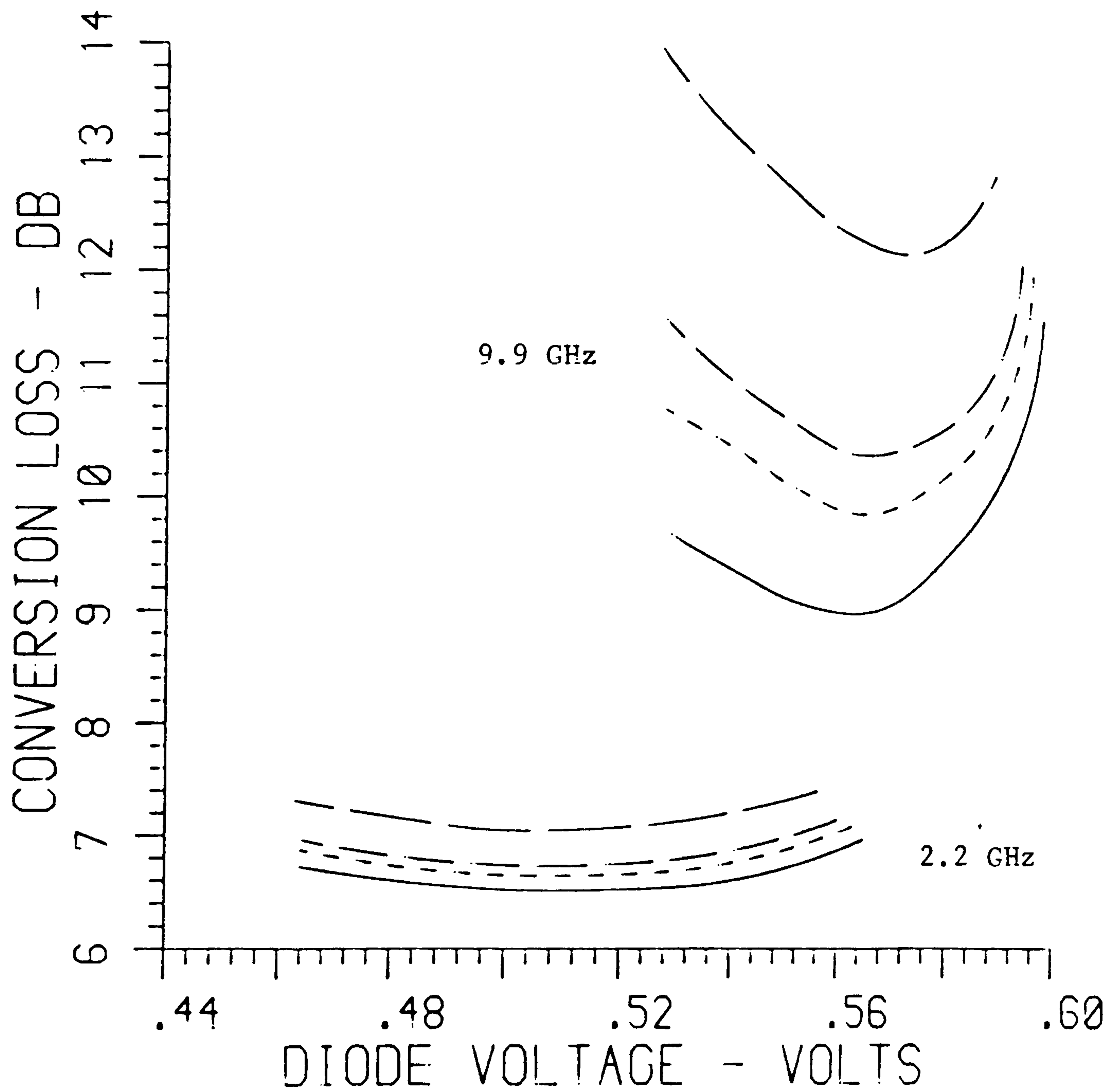

Fig. 6. 10 Conversion loss variation with diode voltage for optically pumped Mott mixer from time domain model predictions. Upper-sideband down-conversion with l.o. frequencies of 2.2GHz (i.f.= 60MHz) and 9.9GHz (i.f.= 270MHz). Parameter: series resistance, r.

———————— r = 0 Ω	- - - - - - - - r = 6 Ω
— — — — r = 10 Ω	—— —— —— r = 25 Ω

500 μA average photocurrent, 100% modulation.

The value of I_s=27.4fA was used, as it does not affect the mixing action; however, the calculation as to whether the epilayer would remain punched through must be made separately using the combined thermionic emission-diffusion theory. For a device of area 10x10μm^2, with epilayer doping 1x10^{15}cm^{-3} and width 0.25μm, from the theory, the epilayer will remain punched through for barrier currents of up to 200μA. For the diode with I_s=27.4fA this corresponds to a punch-through voltage of 0.6165V.

The diode voltage waveforms for the optically pumped Mott mixer at the conversion loss minima at the l.o. frequencies 2.2GHz and 9.9GHz shown in Fig.6.10, are shown in Fig.6.11. The value of the punch-through voltage is also shown. It can be seen that at 2.2GHz the epilayer will remain punched through for practically the whole of the l.o. cycle; at 9.9GHz, the epilayer will not remain punched through for approximately 1/5th of the l.o. cycle and the responsivity can be expected to deteriorate. Under a forward bias of just less than that at the 9.9GHz conversion loss minimum, but still with an intrinsic (r=0Ω) conversion loss of less than 9.5dB, the proportion of the l.o. cycle for which the epilayer will not be punched through can be reduced to approximately 1/6th.

The transit-time-limited cutoff frequency for such a device will be ≃ 30GHz and so transit-time limitations should not have much significance at the frequencies shown in Fig.6.10. As was described in the modelling of the frequency dependence of the tunnelling contact optically pumped mixer performance in section 5.4.4, the effect would be to reduce the a.c. component of the photocurrent (which is the l.o. signal), and hence decrease the conversion efficiency. As both of the above restrictions cause a decrease in the modulated photocurrent, they could be counteracted by an increase in illumination intensity.

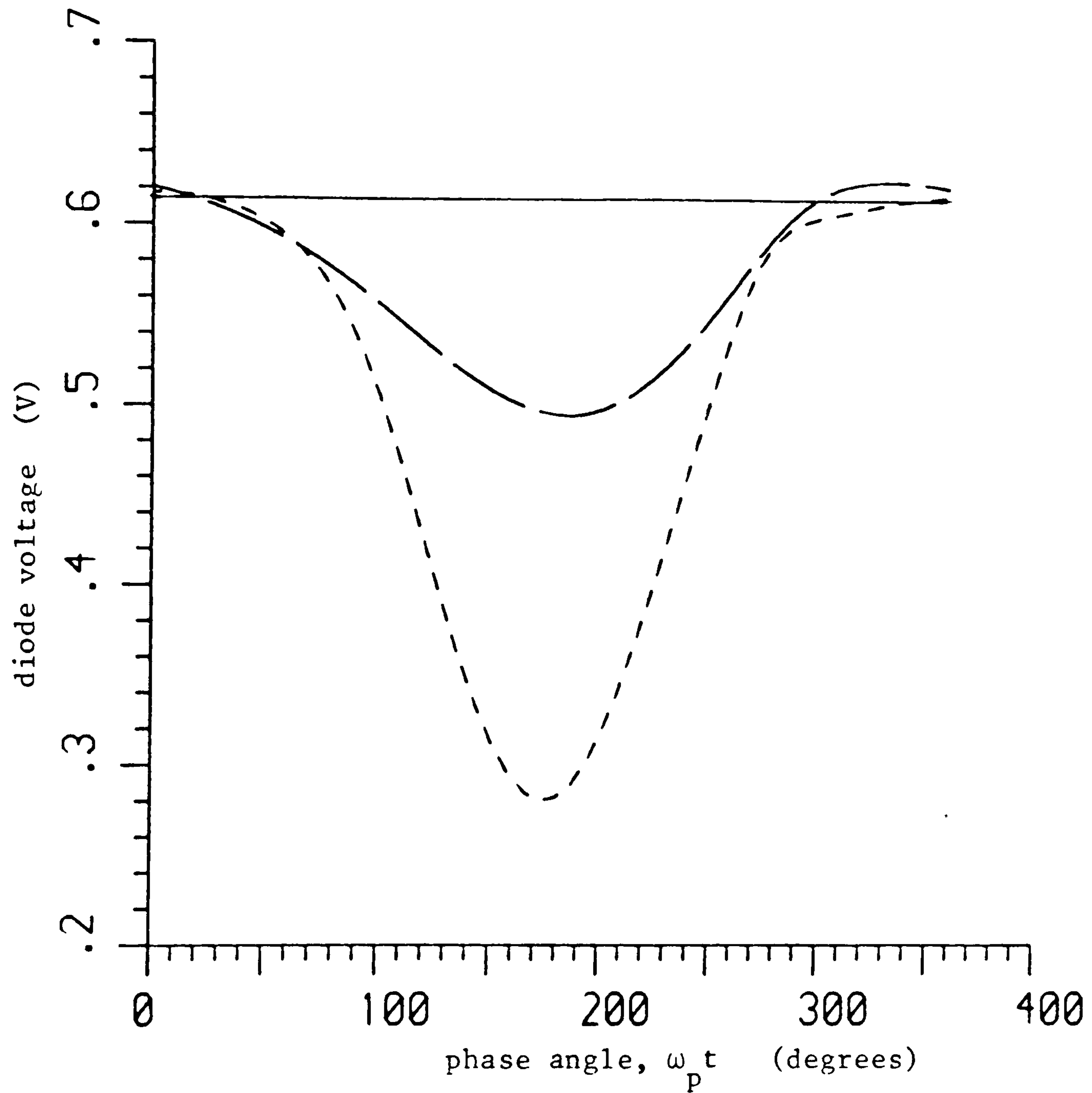

Fig.6.11 Diode voltage waveforms over a l.o. cycle corresponding to the situations at the conversion loss minima shown in Fig.6.10. Negligible series resistance assumed.

l.o. frequency: – – – – – – 2.2GHz, —— —— —— 9.9GHz

Solid line is the punch-through voltage.

A total device capacitance (barrier plus parasitics) has been assigned a value of 0.1pF. Assuming a parasitic capacitance of 50fF, the barrier capacitance should be $\leq$ 50fF; for a device of area $10\times10\mu m^2$ this requires a barrier width $\geq 0.232\mu m$. The predictions, therefore, can be said to adequately represent a device of area $10\times10\mu m^2$ with an epilayer of doping $1\times10^{15}cm^{-3}$ and thickness $0.25\mu m$.

Fig.6.10 shows clearly the effect of diode series resistance on the conversion loss. The diode capacitance causes the performance of the mixer to deteriorate at higher frequencies with the dependence varying as the product of the operating frequency and the diode capacitance - for example, with a diode capacitance of 50fF, the same performance as shown in Fig.6.10 would be obtainable if all of the frequencies were doubled.

An improvement in quantum efficiency leading to average photocurrents higher than the $500\mu A$ used in the predictions of Fig.6.10 would lead to improved performance. For the $0.25\mu m$ barrier structure, high quantum efficiency can be expected at wavelengths $\leq$633nm (HeNe laser emission wavelength), but the responsivity of such a structure may be adequate at longer wavelengths depending on the illumination intensity available.

If it is assumed that all of the available illumination can be utilised, that is if all of the incident photons generate electron-hole pairs and all of the pairs generated in the depletion region contribute to the photocurrent, then using eqn. (2.1) the responsivities of the proposed $0.25\mu m$ epilayer width device will be 0.384, 0.322, 0.222, and 0.168 A/W at wavelengths of 532, 633, 700, and 780nm respectively. The optical power required to generate $500\mu A$ photocurrent using the above responsivities would be 1.3mW at 532nm, 1.6mW at 633nm, 2.3mW at 700nm and 3.0mW at 780nm. However, the

utilisation of 100% of the available illumination will give very optimistic values for the responsivity. From the discussion in previous paragraphs it is apparent that there may be some reduction in responsivity due to the epilayer not being fully depleted during short periods of the l.o. cycle with higher frequency operation, and there may also be some reduction due to the extraction of photo-carriers in the opposing direction, as discussed in sec.2.1.2. Also, there will be losses in the coupling of the optical beam to the device, and due to the reflectance of the metallisation. Responsivities of about half the above values could reasonably be expected and the optical powers required to obtain 500μA photocurrent would then be 2.6mW at 532nm, 3.1mW at 633nm, 4.5mW at 700nm, and 5.9mW at 780nm. The above are average power levels, and for 100% modulation twice these power levels should be available. Of course, it is the a.c. photocurrent that is of importance to the conversion efficiency: at 2.2GHz and 9.9GHz this is likely to be reduced by transit-time limitations to approximately 90% and 85% respectively of its low-frequency value, which will increase the required optical power levels, but not greatly.

Following the same arguments that indicate that efficient operation may be possible with barrier widths less than the absorption length at longer wavelengths, it may also be possible to reduce the barrier width at shorter wavelengths, and hence 'trade-off' some quantum efficiency for an increase in transit-time-limited cutoff frequency. For this to be useful the RC limitations need to be decreased, but it can be seen that another factor, the available illumination intensity, can affect the design considerations for optically pumped mixers.

6.4.2 Other parameters

The noise-temperature ratio of the Mott diode structure will be less than that of the tunnelling contact mixers due to the rectifying nature of its I-V characteristic - this was discussed in section 2.3.3. However, the reduction in the noise-temperature ratio with the proposed structure may not be great, as in both the Mott diode and tunnelling contact cases the shot noise of the optically generated current, especially at higher pump levels, will be the main contribution to the device noise. As the conversion loss is lower for the Mott diode structures, the noise factors of receivers employing these devices will be similarly reduced compared to similar photocurrent levels in the tunnelling contacts. The Mott diode optically pumped mixers will also give far better responsivity.

It was suggested in sec.5.4.3 that lowering the receiver noise factor will reduce the MDS (minimum detectable signal). The higher photocurrent levels which should be obtained with the Mott diode structures, and which are equivalent to stronger pumping, will give higher compression points. The dynamic range of Mott diode optically pumped mixers will thus be much larger than that of the tunnelling contacts described previously.

In section 5.5 the performance of an optically pumped mixer was compared to that of a photodiode-mixer combination. Although the specific example of the tunnelling contact mixer was used to illustrate some points, the arguments in section 5.5 apply to optically pumped mixers generally. In fact, the arguments are more readily applicable to the Mott diode structure, since in order to make the fundamental comparison, similar photocurrent levels and similar conversion efficiencies are assumed in the optically pumped mixer and photodiode-mixer arrangements. The Mott diode optically pumped mixers

should provide both similar photocurrent to fast photodetectors (because of the comparable size of the depleted regions) and similar conversion efficiency to microwave mixers (because of the comparable nonlinearities in the I-V characteristics) - this was not the case for the tunnelling contacts. The conclusion drawn in Chapter 5, that the slightly inferior noise performance with optically pumped mixers compared to a photodetector-mixer combination (and this assuming optimum coupling between the photodiode and mixer) could be more than offset by the simplicity of using a single device, suggests that the proposed Mott diode structures may be of considerable interest for systems in which the l.o. is optically distributed.

The only mixer parameter not so far examined, but which was defined in section 1.4, and described in section 5.4.2 for the tunnelling contact optically pumped mixer, is the diode impedance. Fig.6.12 shows the variation in diode impedance with bias at l.o. frequencies of 2.2GHz and 9.9GHz with intermediate frequencies of 60MHz and 270MHz, respectively, and with the optical l.o. excitation generating 500μA average photocurrent. A diode series resistance of 6Ω has been assumed, and the embedding impedances at the l.o./signal/image frequencies are approximately broadband-matched. At the higher l.o. frequency the real part of the input impedance is in the region of 50Ω, suggesting that good matching could be achieved for a signal source output impedance of 50Ω if the reactive part of the diode impedance (which is in the region of -j100Ω) is effectively resonated. At the lower l.o. frequency the input impedance is higher, as are the output impedances for both cases. To minimise loss, transformer coupling would be required if the source and load impedances are much different to the diode input and output impedances respectively.

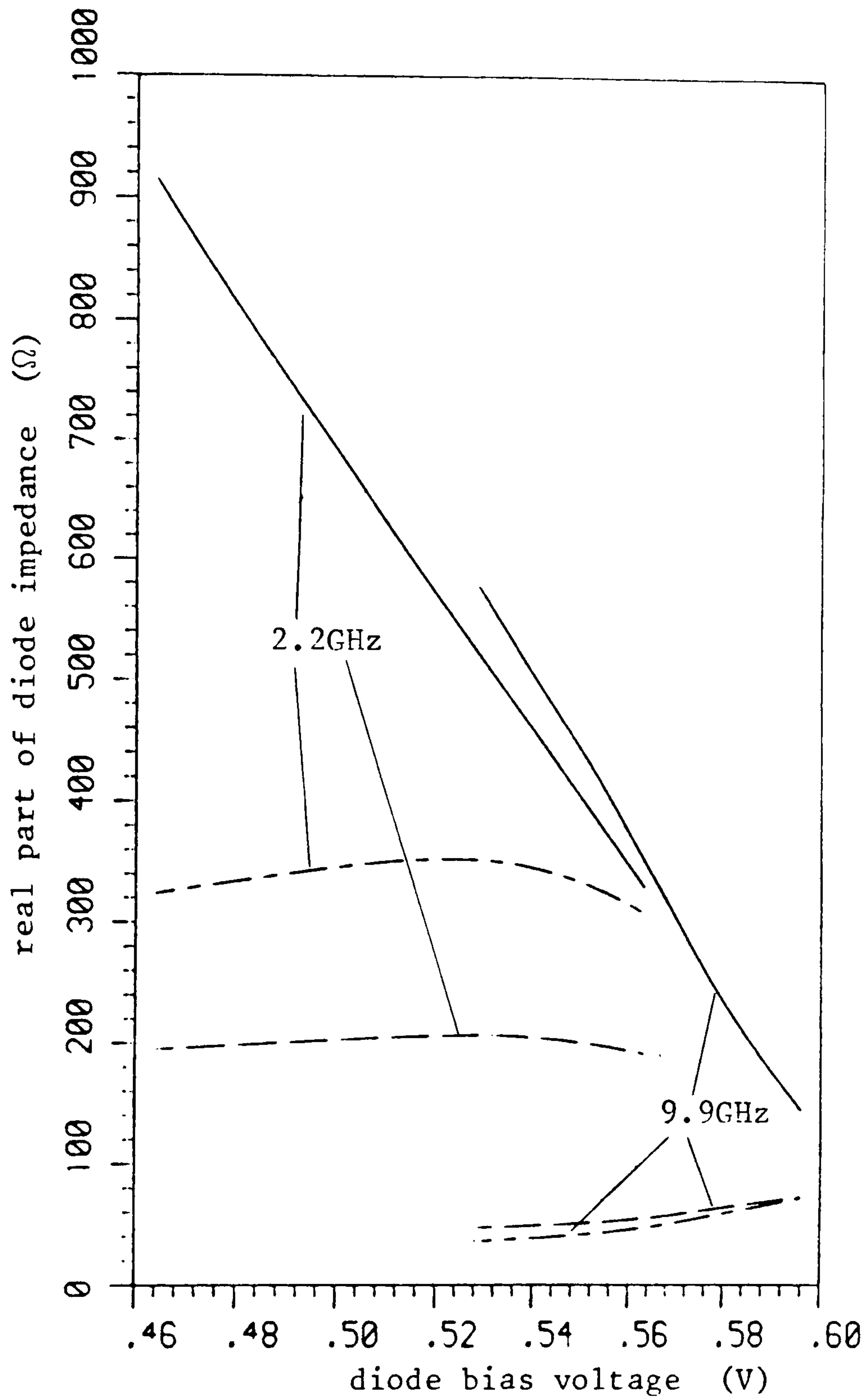

Fig.6.12 Diode impedance with optical l.o. producing 500μA average photocurrent (100% modulation) at l.o. frequencies of 2.2GHz (i.f.= 60MHz) and 9.9GHz (i.f.= 270MHz).

——————— i.f. output impedance

— — — — lower-sideband input impedance

— - — - — upper-sideband input impedance

(a) REAL PART OF IMPEDANCE

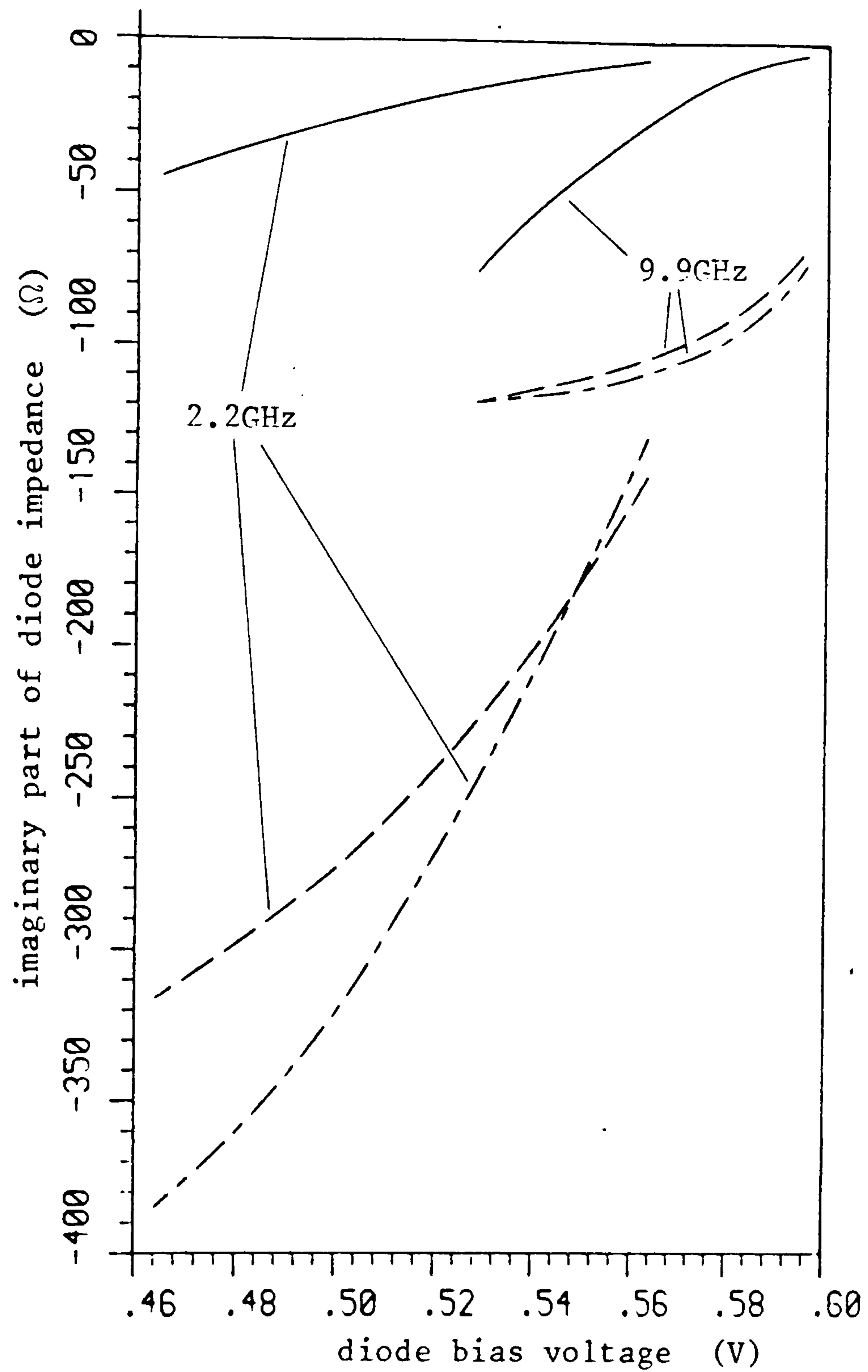

Fig.6.12 Diode impedance with optical l.o. producing 500μA average photocurrent (100% modulation) at l.o. frequencies of 2.2GHz (i.f.= 60MHz) and 9.9GHz (i.f.= 270MHz).

——————— i.f. output impedance

— — — — lower-sideband input impedance

— - — - — upper-sideband input impedance

(b) IMAGINARY PART OF IMPEDANCE

6.5 Chapter summary

A Mott diode structure has been proposed for optically pumped mixers. It consists of a semitransparent metallisation forming a contact to a lightly doped epilayer grown on a heavily doped substrate. This is believed to be the optimum type of structure for simple p-n or metal-semiconductor diode optically pumped mixers. The photodetection in such a device should be as good as that in fast photodiodes, while the resistive nonlinearity and, hence the mixing efficiency, should be as high as that in microwave mixer diodes.

An analysis based on a combined thermionic emission-diffusion theory for the current transport in contacts to lightly to moderately doped semiconductor material has been used to confirm that highly nonlinear characteristics can be obtained with such relatively wide barriers, and that the transit-time limitations of carriers traversing the barrier will be low in suitably designed devices.

Using the time domain optically pumped mixer analysis, conversion loss predictions for the proposed device indicate that efficient frequency conversion (loss, $L_c \leqslant 10dB$) can be achieved at X-band l.o. frequencies with moderate illumination levels (from 1.3mW to 3.0mW average optical power for wavelengths from 532nm to 780nm, assuming 100% external quantum efficiency - i.e., if all of the available light can be effectively coupled into the barrier region contribute to the photocurrent - from 2.6mW to 5.9mW assuming 50%, which is probably more reasonable).

If the quantum efficiency and conversion efficiency of an optically pumped mixer are as good as those of a fast photodiode and microwave mixer diode respectively, which they should be for the Mott diode structure proposed, then the noise factor of the optically pumped mixer will be only slightly inferior, and this assuming optimum coupling in the photodiode-mixer combination. This is likely to be more than compensated for by the simplicity of using a single device.

CHAPTER SEVEN

CONCLUSIONS AND FURTHER WORK

7.1 Summary of major results 259

7.1.1 Summary of theoretical work 259

7.1.2 Performance capabilities of optically pumped mixers 260

7.2 Applications and comparison with alternative approaches 264

7.3 Suggested topics for further work 268

7.3.1 Extensions to theoretical work 268

7.3.2 Further experimental work 269

7.3.2 Alternative structures 271

7.4 Chapter summary 276

7.4.1 Main conclusions 276

7.4.2 Important further work 277

7.1 Summary of major results

In this thesis the results of an investigation into diode mixers with optical local oscillator injection have been presented. Apart from previous publications[36,45-47] containing some of the work presented here, this thesis is the only known study on diode structures as such optically pumped mixers, although optically pumped mixing action in photoconductive devices has been demonstrated[48].

7.1.1 Summary of theoretical work

The mode of operation of optically pumped mixer diodes has been investigated. This has involved a theoretical study of the photocurrent generation which enables the optical local oscillator to provide the admittance modulation necessary for mixing. The carrier generation may occur either in a depleted barrier region or in bulk material, and the resultant photocurrent can have very different characteristics depending on which mechanism is dominant. The influence of material and device parameters on the magnitude and frequency response of the photocurrent has been illustrated.

Using a simplified, voltage-independent and illumination-dependent current generator model for the photocurrent generation, which has been shown to be valid for many practical situations, analytic frequency conversion and noise theory for microwave mixers has been extended to optically pumped action. The excess shot noise contribution of the photocurrent is shown clearly in the noise analysis.

Microwave mixer computer models have also been modified for optically pumped mixers. Two approaches have been used to obtain the solution to the large-signal

problem of finding the nonlinear diode waveforms under optical modulation. In the frequency domain model, the diode capacitance and higher harmonics of the l.o. are ignored and the solution is thus independent of frequency. The predictions give a fair indication of the type of performance that may be achieved; the great advantage is that the computation time is short (this is dependent on the particular problem, but typical compile and run times are less than 20s on an ICL2988 computer at QMC) and the program may be run interactively. In the time domain model the (nonlinear) diode capacitance and higher harmonics of the l.o. are modelled. The program gives very accurate results and can be used to analyse the frequency dependence of the mixer operation. It can also be used to analyse the effects of different embedding circuits. The disadvantage, of course, is that the run times are considerably greater, by almost an order of magnitude, than those of the frequency domain model.

7.1.2 Performance capabilities of optically pumped mixers

Experimental measurements of the conversion loss of heavily doped tunnelling metal-semiconductor contacts with optical pumping have been carried out. Intensity-modulated GaAs/GaAlAs laser diodes and a mode-locked frequency-doubled Nd:YAG laser have been used to provide the optical local oscillator. With the Nd:YAG laser the optical output is very different from that with the semiconductor lasers, in terms of both its wavelength (green region of the spectrum rather than infrared), and its intensity waveform (pulses of FWHM $\leq$ 70ps at 76MHz repetition rate rather than the semiconductor laser output waveforms which are somewhere between sinusoidal and square waves). Using the computer models excellent agreement with the experimental

results has been obtained indicating, that the optically pumped mixer theory is soundly based.

The experimental measurements have been carried out at relatively low frequencies, of the order of 100MHz. With the semiconductor laser illumination, conversion loss minima of 18.5dB and 21.5dB in forward and reverse bias respectively, were obtained. These values are much higher than those predicted with higher levels of photocurrent; for example, with an average photocurrent of 500μA (as opposed to the 120μA generated experimentally) a conversion loss of 10dB was predicted. Predicted minimum incident power levels to generate 500μA photocurrent are 2.2mW at GaAs laser wavelength and 1.4mW at 532nm (frequency-doubled Nd:YAG); however, the devices investigated showed lower than expected responsivity (probably due to reflection and coupling losses, see sections 4.4.1 and 5.1) and would probably require 15mW and 8.5mW at the two above wavelengths respectively. The conversion loss was reduced to a minimum of 15dB in forward bias using Nd:YAG laser illumination (with which approximately 200μA average photocurrent was obtained), but the pulse waveform was not found to be conducive to efficient mixing in reverse bias.

The conversion loss is lower in forward bias due to the greater nonlinearity of the I-V characteristic in this region for the devices investigated. The reverse bias operation was considered important as the cutoff frequency of the tunnelling contacts is greater than in forward bias due to reduced capacitance and reduced dependence on minority-carrier diffusion which is the major transit-time limitation. However, for the particular devices investigated the ratio of the capacitances at the forward and reverse bias conversion loss minima is only approximately 1.2, and taking into account the generation of carriers in the depleted region the transit-time

limited cutoff frequency in reverse bias is not significantly greater than that in forward (⩽4.6GHz as opposed to ⩽4.0GHz for GaAs laser illumination). The RC cutoff frequency is less than 2GHz and this would then be the main frequency limitation. For a $10 \times 10 \mu m^2$ device the RC cutoff frequency may be increased to 11.7GHz, and with GaAs laser illumination transit-times would become more important.

The -3dB frequency for the mixing efficiency will be lower than the device cutoff as the l.o. power coupled into the device will fall as well as the signal power coupled into it. With 500μA average photocurrent the -3dB frequency for the mixers investigated is predicted to be ⩾125MHz, but for a $10 \times 10 \mu m^2$ device it could be in the region of 1GHz for shorter wavelength illumination.

The tunnelling contacts investigated have high noise-temperature ratios and this will limit the performance of receivers employing them as optically pumped mixers. For 120μA average photocurrent it is predicted that $4.2 > t_r > 3.2$ while for 500μA, $10 > t_r > 6.1$.

With similar drive level (≃500μA) microwave mixers will give lower conversion loss (≃7dB). The 500μA photocurrent would be much easier to generate in a fast photodiode, and the carrier transport would not rely on minority-carrier diffusion which is a relatively slow process, as most of the carriers would be generated in a depleted region. (A method of generating more carriers in the depleted region of a tunnelling structure is discussed later in section 7.3.3.) Hence, assuming low-loss coupling between them, a photodetector-mixer combination should give better performance than the tunnelling contact optically pumped mixers. However, low-loss coupling may prove difficult at higher microwave frequencies.

A device as nonlinear as a microwave mixer, but possessing similar responsivity to a fast photodiode, would be more competitive, and it is proposed that a Mott-type structure would fulfil these requirements. In such a structure, a punch-through region of width tailored to the absorption length at the desired operating wavelength could be obtained by fabricating a lightly doped region close to the Schottky contact.

The current transport and, hence current-voltage characteristics for Mott devices have been carefully analysed. Using the accurate time domain model, predictions indicating conversion losses as low as 6.5dB have been obtained using realisable levels of photocurrent (500μA generated in the depletion region). A conversion loss of ≤ 10dB at X-band frequencies has been predicted for a 0.25μm epilayer width ($\approx 1\times10^{15}cm^{-3}$ doped) $10\times10\mu m^2$ contact with theoretical minimum average optical powers of 1.3 to 3.0mW (for illumination wavelengths between 532nm and 780nm). Higher frequency performance could be obtained with modified structures, although this would be at the expense of higher required illumination levels.

With both optically pumped mixer and photodetector-mixer arrangements it is assumed that broadband matching of the l.o., signal and image exists. Photocurrent noise (including laser intensity noise) within the i.f. bandwidth at the l.o. frequency will be converted to the output in both cases. Also, in the optically pumped mixer case, photocurrent noise will be present directly at the i.f. output; as the photodiode and mixer would be coupled at the l.o. frequency, the photocurrent noise at the i.f. will not be present in the photodetector-mixer combination. However, it has been shown (sec. 5.5) that the effect of this is to degrade the noise performance of an optically pumped mixer by only 1→2dB compared with that of a photodetector-mixer combination; this slightly

inferior noise performance may be more than compensated for by the simplicity of using a single device.

Reduced conversion loss could be obtained by employing an amplifier after the photodetector thus increasing the l.o. drive applied to the mixer. However, as discussed in sec. 5.5.2, as the photocurrent noise would also be amplified, this would not improve the noise performance and in many cases may degrade it. If suitable tuned filters were used between the photodetector and amplifier to reduce the noise bandwidth of the photocurrent noise, the noise performance could be improved. It can be seen, though, that this will result in increased system complexity.

7.2 Applications and comparison with alternative approaches

Optically pumped mixers could be employed in a variety of applications in which stabilised laser sources were available. They could, for example, be used in laser frequency measurement where the modulated optical signal would be provided by the beating of a known laser frequency with that of an unknown one. They could also be used as the mixers in optical phase-locked loops such as that described in section 1.5, or as heterodyne detectors in optical communication links. However, in all of these cases there is no necessity for the optical signal to be the large signal, and electrically pumped optoelectronic mixers, for which the l.o. power requirements are more easily met, could be used instead. If high-frequency, intensity-modulated, narrow-optical-linewidth sources could be readily and cheaply found, then optically pumped mixers could replace microwave mixers in many of their applications. Practically, however, optically pumped

mixers are likely to be employed in situations where optical distribution of the l.o. offers some distinct advantage - for example, by making the system lighter and more compact, and free from interference. Such an application could be in a phased-array radar, where the l.o. would have to be distributed to a number of elements and so a significant reduction in bulk would be achieved by using optical fibres rather than waveguides or even coaxial cables.

Fig.7.1 shows the receiver system for a phased-array radar employing optically pumped mixers. The number of elements and the l.o. power requirements of each optically pumped mixer will determine the total required optical l.o. power. From the conclusions drawn in the previous section (7.1.2) at least 3mW would be required for each mixer at GaAs laser wavelengths, although realistically it may be twice this level (sec.6.4.2). These are average powers; for 100% modulation twice these power levels should be available. Assuming intensity-modulated semiconductor lasers are used, output powers of 20mW at X-band have been achieved[117]. This would be sufficient to drive perhaps three optically pumped mixers. With tunnelling contact structures operation would be limited to less than 1GHz, but Mott structures should be useful at X-band and beyond.

In order to drive more elements from a single reference, laser amplifiers could be used before one or more optically pumped mixers after division of the output of the optical reference source. Marshall et al.[118] have described a travelling-wave semiconductor laser amplifier with picosecond pulse response. The amplifier described by Saitoh and Mukai[119] would give a 5mW signal ouput with a signal input ≃0.1mW; this output may be sufficient to drive an optically pumped mixer while the required input is such that a large number of laser amplifiers could be

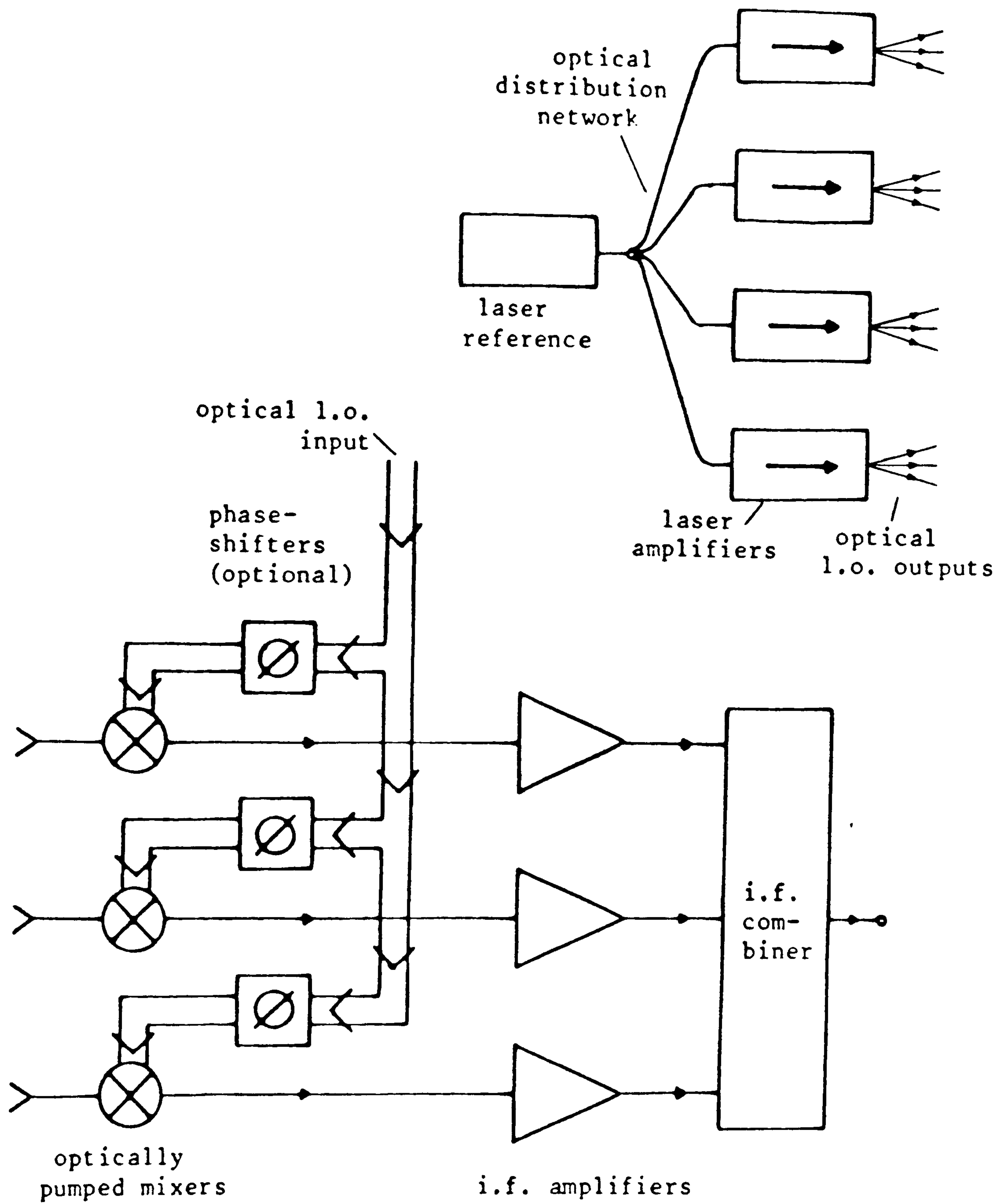

Fig.7.1 Receiver configuration for a phased-array radar employing optically pumped mixers. Possible sub-division of the outputs of laser amplifiers is also shown (top right).

driven by a single laser reference source. To reduce complexity and minimise cost it would be desirable to have each laser amplifier feed more than just one optically pumped mixer; for the device described by Saitoh and Mukai the reduction in gain at higher power levels will limit the total number of mixers that can be driven. However, their device could provide over 10mW output power with less than 1mW input power; each laser amplifier may then be able to feed two mixers while up to 20 amplifiers could be fed from the original reference source; thus this would be sufficient for an array of up to 40 elements. Further improvements in laser amplifier performance would increase the number of possible array elements and/or decrease the number of required laser amplifiers. However, problems caused by the intensity noise of laser amplifiers will arise and these need to be investigated.

Alternatively, high-power lasers could be used and schemes such as mode-locking employed to obtain the intensity-modulation. Very high powers are obtainable from solid-state and dye lasers (typical commercially available systems give over 1W average power in mode-locked operation). High-power semiconductor lasers with CW outputs of 0.2W have also been demonstrated[120]; such devices might also be useful l.o. sources when mode-locked. Other schemes were discussed in section 1.5.

The alternative approaches of using photodetector-mixer or photodetector-amplifier-mixer combinations need to be briefly discussed. In the first case, with the assumption that the responsivity of the optically pumped mixer is similar to that of a fast photodetector, the optical power requirements will not be reduced. If the photocurrent is amplified, however, less optical power will be required per element, but this approach may suffer from some disadvantages also. The amplifiers which will be required at each element and have to operate at the

relatively high l.o. frequency, would now have to be of higher gain than discussed previously in section 5.5 where it was assumed that large photocurrents were being generated. Following this discussion, to prevent significant photocurrent noise (including laser intensity noise) being converted to the output, due to the high amplification of the l.o., the l.o. filters which reduce the l.o. noise bandwidth would have to be even more narrow-band.

7.3 Suggested topics for further work

7.3.1 Extensions to theoretical work

The frequency response of an optically pumped mixer is one of its most important parameters, and one of the fundamental limitations to this response is carrier transit-times. For the tunnelling contacts, the solution to the continuity equation for the minority-carrier diffusion in an illuminated device, including the time-dependent terms, would be useful in confirming the validity of the analysis presented in sections 2.1.3 and 4.4.2. In sections 6.2 and 6.3 a detailed analysis of the carrier transport and its transit-time limitations in Schottky structures was extended to Mott diodes by using a few simplifying assumptions. An analysis of the Mott structure along the same lines as that for the Schottky one would be useful in confirming the validity (or otherwise) of these assumptions. Such an analysis could also be employed to determine the effect of the Fermi level shift due to illumination, and the recombination of photo-carriers at interface states, on the collection efficiency of the diodes. Both of the above analyses of electronic processes within semiconductor devices would be aided by a time domain computer simulation employing

phenomenological descriptions of the carrier generation, transport, etc.

At present, the characterisation of the devices, including the transport processes and frequency limitations, and the predictions of their performance as optically pumped mixers are done separately. Combining the two may be useful, and may give important insights into device behaviour, but is likely to be a considerable mathematical and programming task.

The time domain model for optically pumped mixing used in this thesis is accurate, but relatively slow. The extension of Schüppert's model[83] to optically pumped mixing will give much faster performance (the computing time may be reduced by an order of magnitude) without any cost in accuracy.

Finally, the noise analysis for optically pumped mixers needs to be extended along the lines of those of Dragone[79] and Held and Kerr[86] (see Appendix C), to take into account correlated shot noise.

7.3.2 Further experimental work

Significant work has gone into characterising the tunnelling contacts. However, a number of measurements could be performed in order to verify some of the predictions that have been made. For example, the transit-time limitations could be further studied by using shorter, dye laser pulses and examining the effects of the pulse spreading by comparison with predictions from the time domain mixer model. The dye laser could also be tuned to examine the wavelength dependence over a limited range.

Experimental measurements at present have been performed at relatively low frequencies (≃100MHz) beyond which it is predicted device limitations will degrade the

conversion efficiency. These predictions could be verified by performing measurements at higher frequencies; of course, the mixer embedding circuits would have to be redesigned.

The noise figure of the tunnelling contact optically pumped mixers is expected to be approximately 25→30dB with the conversion efficiencies obtained experimentally. Measurement of this noise figure could be performed using a high level noise diode source (of excess noise ratio, ENR ≈ 30dB); with typical noise diode sources (ENR ≈ 15dB) a more elaborate system would be required. Measurement would be much simpler if the noise figure of the mixer was significantly lower.

Experimental work is needed to verify the predicted performance of the Mott diode mixers. The work should consist of a detailed characterisation of the devices (as has been done for the tunnelling contacts in Chapter 4) and measurement of the conversion loss and noise performance. Performance at a range of frequencies should be measured in order to study the freqency limitations of the devices. A problem is that such structures have not been fabricated; until such time as they are available, preliminary work could be performed with fast photodiode structures such as those of Wang and Bloom[103] or Parker and Say[104]. Modelling of the performance of these fast photodetectors as optically pumped mixers will need to take into account the fact that the epilayers will not remain fully depleted in the nonlinear forward bias regime due to their being too heavily doped and/or too wide.

Comparisons have been made with the theoretically attainable performance of a fast photodetector-mixer combination; experimental verification of this performance would be useful and may also serve to highlight any difficulties in designing such an arrangement.

7.3.3 Alternative structures

The tunnelling contacts discussed in Chapters 4 and 5 are limited by their relatively low quantum efficiency and their dependence on minority-carrier diffusion as the main current transport mechanism. This is primarily caused by their narrow depletion widths. An obvious way to overcome this would be to stack a number of junctions together; a schematic for such a layered structure of the p-n junction type is shown in Fig.7.2. As has already been mentioned, the parasitic series resistance of the contacts used in this work is primarily due to the metallisation, and therefore the series resistance will not be significantly increased with a layered structure. The capacitance, on the other hand, will be reduced approximately by a factor n, where n is the number of junctions. The RC-limited cutoff frequency can thus be dramatically improved.

In fact, the effect of stacking the junctions would not be as straightforward as outlined above. An adverse effect would arise due to all of the barriers being in series and limiting the current; voltage would be dropped across each of them. In order to obtain similar current variation larger voltage variation would be required than with a solitary barrier. Increasing the doping would decrease the barrier resistance and alleviate the above situation but it will also result in narrower barriers; for a given depleted width more barriers would then be required. The depletion width of an individual barrier is proportional to $1/\sqrt{N_D}$ where N_D is the doping level. The current-voltage characteristic is dependent on a number of material and barrier parameters, such as the built-in potential. At low to moderate doping levels the conductance is almost independent of doping, but as tunnelling becomes significant the dependence tends towards ~ $\exp(\sqrt{N_D})$[53]. Theoretically then, a large number of closely spaced barriers on heavily doped material would

give high barrier conductance; however, practical limitations to the fabrication of such a structure would limit the spacing. The limitation would not be serious, as even if there were undepleted material between the barriers, as long as the thickness of the undepleted material were significantly less than the minority-carrier diffusion length, the responsivity and transit-time-limited cutoff frequency would not be adversely affected.

Fabrication would obviously be a problem, especially if a metal-semiconductor structure with alternating layers of metal and heavily doped semiconductor were required. The metal layers would have to show good adherence and chemical stability as well as being suitable for forming good electrical junctions. Also, crystal growth would be affected by the intervening metal layers. Similar electrical characteristics could be obtained with a p^+-n^+ structure (shown in Fig.7.2), and processes such as molecular-beam-epitaxy could be used to achieve the high definition required between the different regions.

The only other reported instance of optically pumped mixing is that of Foyt et al.[48] with their photoconductive mixer. At the present state of the art (minimum size of interdigitated contacts, minimum photoconductive lifetimes observed) Foyt et al. predict a maximum operating frequency of 3.2GHz for their optically pumped photoconductive mixers, although their experiments were carried out at similar frequencies to those used in this work (≈100MHz). No clear indication of the conversion efficiency is given either. The power levels projected to be necessary are theoretical minima and considerably higher power levels have been used in their experiment. Even if the photoconductive lifetime could be reduced, the power levels required would probably preclude operation at frequencies above those predicted for the Mott diode structures.

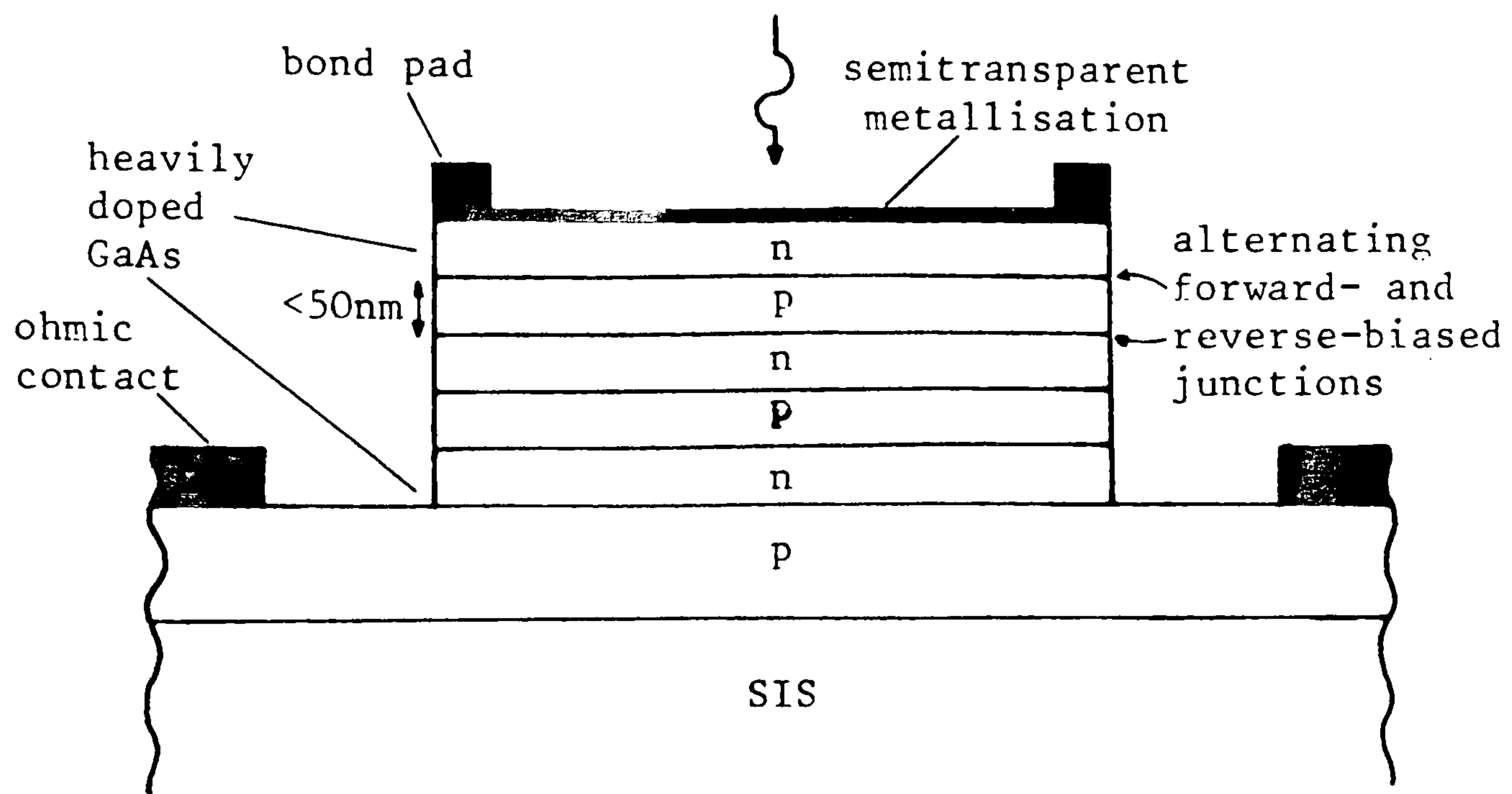

Fig.7.2 Stacked tunnelling junction structure: alternating layers of heavily doped n- and p-type semiconductor.

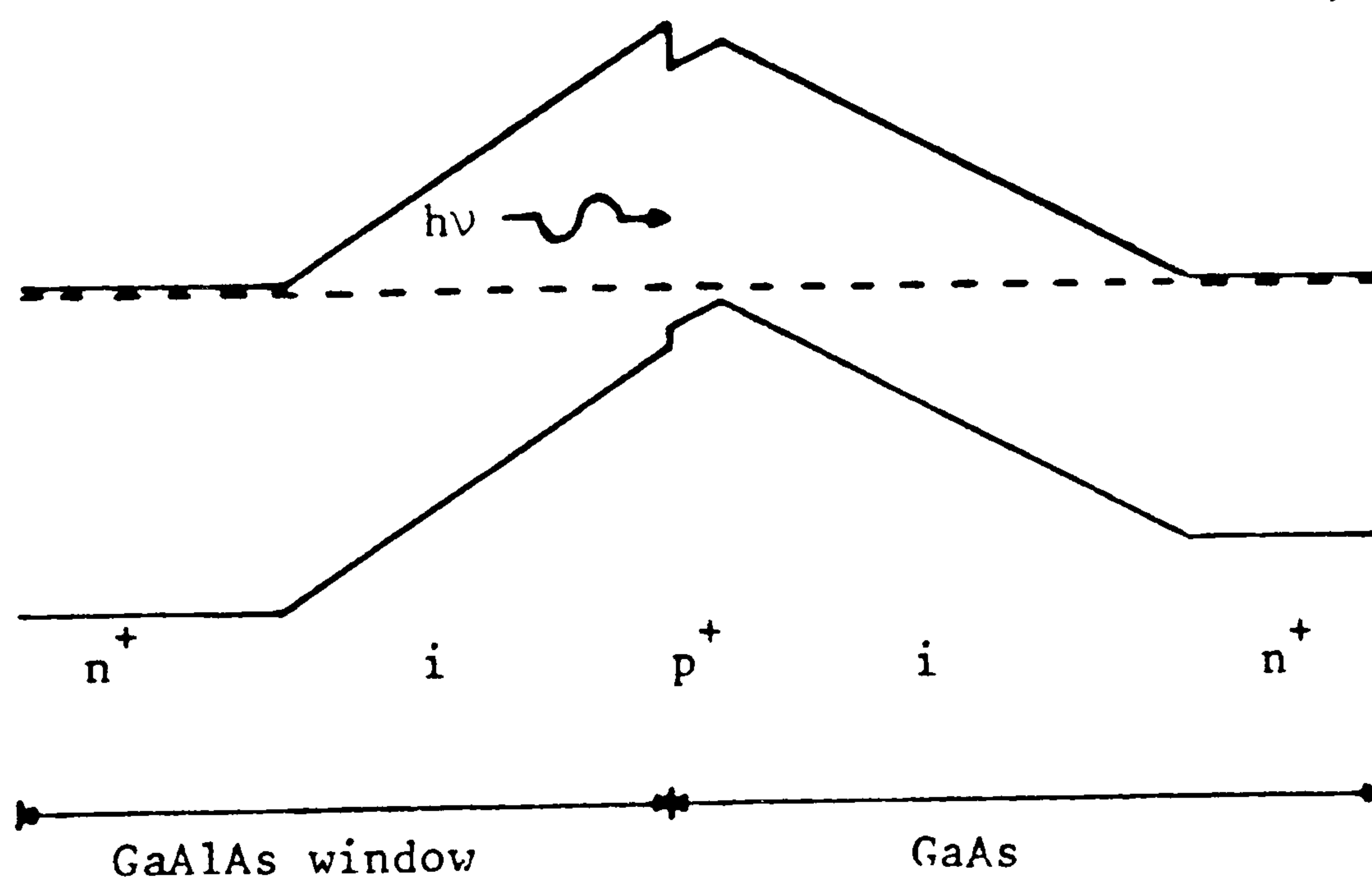

Fig.7.3 Schematic diagram of band profiles in modulated barrier photodiode (after ref.[124]).

It may be interesting, therefore, to examine the potential of other photodetector structures. Wei et al. have obtained fast photoconductive-like behaviour in GaAs by fully depleting the region between two contacts, and hence forming a back-to-back, or symmetrical Mott barrier[121]. The gap between the contacts is very small (≈3μm) so the focussing requirements are considerable. A high bias voltage, 10→20V, would be required to operate the device in a nonlinear region, but if the photocurrent can modulate the voltage, mixing may be achievable in this region. However, the degree of nonlinearity in this region is not known. McCleer and Haddad have predicted that punch-through structures like the above, operated near the transit-time frequency, or in the BARITT mode, can then be employed to give low-noise, negative-resistance, reflection-type amplification of a detected photocurrent[122]. This has been demonstrated by Jager et al.[26]. However, this type of operation is more akin to the optical injection locking of microwave oscillators mentioned in section 1.1, and does not seem promising for optically pumped mixing, as the gain is circuit- and frequency-dependent, and not (directly) photocurrent-dependent.

Another type of photodetector which has received considerable interest, mainly for its sensitivity to low level signals, is the modulated barrier photodiode[123,124] (or triangular barrier photodiode[125]). The current flow is majority-carrier as in metal-semiconductor diodes, but the barrier is formed within the semiconductor by a thin heavily doped layer sandwiched between two very lightly doped or intrinsic regions, all of which is between regions doped with impurities of the opposite polarity. The doping concentrations and thicknesses of the regions are such that the central layer and lightly doped regions are fully depleted at any bias condition. Heterostructures can be used to enable the carrier generation to be

concentrated around the barrier peak[124]. The structure of such a device is shown in Fig.7.3. The barrier is modulated by minority-carriers at the barrier peak, so response speeds are then limited by the minority-carrier lifetime; this gives relatively long fall times with pulse modulation[123]. If the response times can be reduced, the devices may prove useful optically pumped mixers, as Chen et al. have observed a dependence of the differential conductance on illumination[123].

Illumination could be used to modulate the barrier width of a diode, and hence achieve optically pumped capacitive mixing. With a resistive image termination conversion gain may be achievable in down-conversion[52] although this will probably require very high pump powers to obtain the necessary modulation of the diode capacitance. Optically distributed local oscillators may not be able to deliver sufficiently high pump powers.

Finally, moving away from diode structures, MESFETs could prove efficient optically pumped mixers. The high-frequency performance of MESFETs as electrically pumped optoelectronic mixers[27,126] and the high sensitivity of many of the parameters of MESFET devices to illumination[11] suggests that optically pumped action could be achievable. The most obvious mechanism for achieving optically pumped mixing would be the illumination of the gate region of the MESFET thereby varying the channel conductance. Further work is necessary to determine how effective the modulation of the channel conductance can be, but this was the mechanism used by Chu et al.[27] and Rauscher et al.[126] for electrically pumped action. Again, the power requirements may be a limiting factor; Chu et al. required (electrical) l.o. powers ≈200mW. However, relatively low levels of optical power may be required if an arrangement similar to that of Rauscher et al. is employed. In this arrangement the self-oscillation of a MESFET circuit was

used to provide the l.o. signal for down-conversion of an optical signal within the same MESFET. For an optically pumped mixer it may be possible to optically injection-lock a MESFET oscillator for down-conversion of an electrical signal.

7.4 Chapter summary

7.4.1 Main conclusions

1. Analytic theories have been developed which illustrate the photocurrent generation, frequency conversion and the effects of noise mechanisms in optically pumped mixers.

2. Computer models of optically pumped mixing have been developed and these show very good agreement with experimental results.

3. Conversion loss measurements have been carried out at low frequencies (≈100MHz) on a tunnelling metal-semiconductor contact. The minimum conversion losses achieved have been relatively high (≈20dB with several milliwatts optical power). However, the low conversion efficiency and the need to operate at low frequencies are both caused by the construction of the prototype device used and not by any fundamental limitation of optically pumped mixing.

4. An improved diode structure has been proposed for an optically pumped mixer, and the characteristics of the proposed structure analysed. Predictions from the time domain computer model for one particular Mott device indicate efficient operation (loss $\leqslant$ 10dB) should be achievable at X-band frequencies even with GaAs laser wavelength illumination (of power $\geqslant$ 3mW). With shorter wavelength illumination such performance should be

achieved at lower laser power levels, or with a modified structure, at higher frequencies.

5. The noise performance of the Mott diode optically pumped mixers is expected to be only slightly inferior (1→2dB) to that of a photodetector-mixer combination (and this assuming optimum coupling between the two). The simplicity of using a single device may be of considerable advantage in many complex microwave systems.

7.4.2 Important further work

1. A phenomenological model of the carrier generation and transport in metal-semiconductor barriers with epitaxial layers would be useful in determining the performance of the proposed Mott mixers. Such a model should take into account the effect of illumination on the majority-carrier quasi-Fermi level, and the effect of recombination at interface states. It should also be a time domain model so that frequency-dependent effects are accurately modelled.

2. Improving the time domain mixer computer model by using Schüppert's analysis[83] would give much faster operation. Also a noise analysis incorporating correlated shot noise could be incorporated into the computer model.

3. An experimental investigation to characterise and measure the performance of Mott diode optically pumped mixers would be of importance as these devices are predicted to give superior performance.

4. The use of alternative structures could be investigated. Interesting structures may be variable capacitance diodes, modulated barrier photodiodes, or, moving away from diode structures, MESFETs.

REFERENCES

1. Forrest, J.R.; and de Salles, A.A: 'Optics controls microwaves', Microwave System News, June 1981, 112-22, (1981)

2. Kiehl, R.A.: 'Novel optical control techniques for solid-state radar transmitters', IEEE Trans. Microwave Theory Tech., MTT-28, 409-13, (1980)

3. Esdale, D.J.; and Houlton, M.R.: 'Optical elements in the MAST phased array radar demonstrator at RSRE', IEE Colloq. on *Optical control and generation of microwave signals*, digest no. 1986/4, 4/1-7, (1986)

4. Seeds, A.J.; Blanchflower, I.D.; Gomes, N.J.; King, G.; and Flynn, S.J.: 'New developments in optical control techniques for phased array radar'. To be presented at 1988 IEEE - MTT-S International Microwave Symposium, New York, May 25-27(1988)

5. Pengelly, R.S.: 'GaAs monolithic microwave circuits for phased-array applications', IEE Proc., Part F - Communications, Radar, and Signal Processing, 127, 301-11, (1980)

6. Leonberger, F.J.; and Moulton, P.F.: 'High speed InP optoelectronic switch', Appl. Phys. Lett., 35, 712-4, (1979)

7. MacDonald, R.I.; Hara, E.H.; and Hum, R.H.: 'Fast photoconductor optoelectronic broadband switch with low control voltage', Electron. Lett., 17, 611-2, (1981)

8. Herczfeld, P.R.; Daryoush, A.S.; Rosen, A.; Stabile, P.; and Contarino, V.M.: 'Optically controlled microwave devices and circuits', RCA Review, 46, 528-51, (1985)

9. Kiehl, R.A.: 'Behaviour and dynamics of optically controlled TRAPATT oscillators', IEEE Trans. Electron Dev., ED-25, 703-10, (1978)

10. Forrest, J.R.; and Seeds, A.J.: 'Analysis of the optically controlled impatt (Opcad) oscillator', IEE J. Solid-State and Electron Dev., 3, 161-9, (1979)

11. de Salles, A.A.: 'Optical control of GaAs MESFETs', IEEE Trans. Microwave Theory Tech., MTT-31, 812-20, (1983)

12. Wahi, P.; Turski, Z.; Daryoush, A.S.; and Herczfeld, P.R.: 'Comparison of indirect optical injection locking techniques of multiple X-band oscillators', 1986 IEEE MTT Symposium Digest, 615-8, (1986)

13. Seeds, A.J.; and Forrest, J.R.: 'Initial observations of optical injection locking of an X-band impatt oscillator', Electron. Lett., 14, 829-30, (1978)

14. de Salles, A.A.; and Forrest, J.R.: 'Initial observations of optical injection locking of GaAs MESFET oscillators', Appl. Phys. Lett., 38, 392-4, (1981)

15. Goldberg, L.; Rauscher, C.; Weller, J.F.; and Taylor, H.F.: 'Optical injection locking of X-band FET oscillator using coherent mixing of GaAlAs lasers', Electron. Lett., 19, 848-50, (1983)

16. Patel, C.K.N.; and Sharpless, W.M.: 'Optical heterodyning using point contact germanium diodes', Proc. IEEE (Corresp.), 52, 107-8, (1964)

17. Hall, J.L.; and Morey, W.W.: 'Optical heterodyne measurement of neon laser's millimeter-wave difference frequency', Appl. Phys. Lett., 10, 152-5, (1967)

18. Daniel, H.-U.; Maurer, B.; Steiner, M.; and Walther, H.: 'Schottky diode mixer for visible laser light and microwave harmonics up to 0.43THz', Appl. Phys. Lett., 41, 313-5, (1982)

19. Donald, D.K.; Bloom, D.M.; and David, F.K.: 'Efficient simple optical heterodyne receiver; d.c. to 80GHz', Proc. SPIE Int. Soc. Opt. Eng., 545, 29-34, (1985)

20. Malyon, D.J.; Hodgkinson, T.G.; Smith, D.W.; and Wyatt, R.: 'A practical comparison of heterodyne and homodyne detection', IEE Colloq. on *Advanced optical transmission systems*, digest no. 1984/111, 7/1-4, (1984)

21. Kasper, B.L.; Burrus, C.A.; Talman, J.R.; and Hall, K.L.: 'Balanced dual-detector receiver for optical heterodyne communication at Gbit/s rates', Electron. Lett., 22, 413-5, (1986)

22. Bachus, E.-J.; Böhnke, F.; Braun, R.-P.; Eutin, W.; Foisel, H.; Heimes, K.; and Streibel, B.: 'Two channel heterodyne-type experiment', Electron. Lett., 21, 35-6, (1985)

23. Liddell, W.: 'Optical phase-locked loop', IEE Colloq. on *Advances in Coherent Optic Devices and Technologies*, digest no. 1985/30, 9/1-4, (1985)

24. Burghardt, B.; Hoeffgen, H.; Meisel, G.; Reinert, W.; and Vowinkel, B.: 'Beat frequency generation between visible lasers with frequency differences in the 80-GHz band', Appl. Phys. Lett., 35, 498-500, (1979)

25. Drullinger, R.E.; Evenson, K.M.; Jennings, D.A.; Petersen, F.R.; Bergquist, J.C.; Burkins, L.; and Daniel, H.-U.: '2.5THz frequency difference measurements in the visible using metal-insulator-metal diodes', Appl. Phys. Lett., 42, 137-8, (1983)

26. Jager, D.; Paulus, P.; and Heidemann, R.: 'The BARITT diode - a low noise heterodyne photodetector with high internal gain', Physica B+C, 129B+C, 501-5, (1985)

27. Chu, A.; Fetterman, H.R.; Peck, D.D; and Tannenwald, P.E.: 'Heterodyne experiments from millimeter wave to optical frequencies using GaAs MESFETs above f_T', *IEEE*

1982 Microwave and Millimeter-Wave Monolithic Circuits, Dallas, TX, Symp. Digest, 25-7, (New York: IEEE 1982)

28. Yariv, A.: *Optical electronics*, 3rd edn., Holt, Rinehart and Winston, New York, (1985)

29. Knight, D.J.E.; and Woods, P.T.: 'Application of nonlinear devices to optical frequency measurement', Journal of Physics E: Scientific Instruments, 9, 898-916, (1976)

30. Bay, Z.; and Luther, G.G.: 'Locking a laser frequency to the time standard', Appl. Phys. Lett., 13, 303-4, (1968)

31. Kaminow, I.P.; Bridges, T.J.; and Pollack, M.A.: 'A 964-GHz travelling-wave electro-optic light modulator', Appl. Phys. Lett., 16, 416-8, (1970)

32. Midwinter, J.E.; and Warner, J.: 'Up-conversion of near infrared to visible radiation in lithium-meta-niobate', J. Appl. Phys., 38, 519-23, (1967)

33. Hulme, K.F.; Jones, O.; Davies, P.H.; and Hobden, M.V.: 'Synthetic proustite (Ag_3AsS_3): a new crystal for optical mixing', Appl. Phys. Lett., 10, 133-5, (1967)

34. Baird, K.M.; Riccius, H.D.; and Siemsen, K.J.: 'CO_2 wavelengths and the velocity of light', Optics Commun., 6, 91-5, (1972)

35. Warner, J.: 'Photomultiplier detection of 10.6μm radiation using optical up-conversion in proustite', Appl. Phys. Lett., 12, 222-4, (1968)

36. Seeds, A.J.; Esdale, D.J.; Gomes, N.J.; Lenoir, B.; and Wight, D.R.: 'Opto-electronic mixers', IEE Colloq. on *Optical control and generation of microwave signals*, digest no. 1986/4, 8/1-5, (1986)

37. Davis, Q.V.; and Kulczyk, W.K.: 'Optical and electronic mixing in an avalanche photodiode', Electron. Lett., 6, 25-6, (1970)

38. MacDonald, R.I.; and Hill, K.O.: 'Avalanche opto-electronic downconverter', Opt. Lett., 7, 83-5, (1982)

39. Yakovlev, V.V.: 'Conversion of the radiation modulation frequency in SHF-biased avalanche photodiodes', Sov. J. Opt. Technol., 49, 681-3, (1982)

40. Seeds, A.J.; and Gomes, N.J.: 'Avalanche diode harmonic opto-electronic down-converter', Proc. 10th Biennial IEEE/Cornell Elec. Eng. Conf., Ithaca, NY, 331-40, (1985)

41. Seeds, A.J.; and Lenoir, B.: 'Avalanche diode harmonic optoelectronic mixer', IEE Proc. Part J - Optoelectronics, 133, 353-7, (1986)

42. Lam, D.K.W.; and MacDonald, R.I.: 'GaAs optoelectronic mixer operation at 4.5GHz', IEEE Trans. Electron Dev., ED-31, 1766-8, (1984)

43. Müller, J.E.; and Hanke, C.: 'Noise performance of microwave-biased photoconductive detectors', Infrared Phys., 19, 533-40, (1979)

44. Roulston, D.J.: 'Low-noise photoparametric up-converter', IEEE J. Solid-State Circuits, SC-3, 431-40, (1968)

45. Seeds, A.J.; Esdale, D.J.; Gomes, N.J.; and Wight, D.R.: 'Optically pumped tunnelling millimetre-wave mixer', Proc. 10th Biennial IEEE/Cornell Elec. Eng. Conf., Ithaca, NY, 319-30, (1985)

46. Gomes, N.J.; and Seeds, A.J.: 'Optically-pumped electronic mixer', (abstract only) . Paper presented at *Semiconductor and Integrated Optoelectronics* - SIOE'87, UWIST, Cardiff, (1987)

47. Gomes, N.J.; and Seeds, A.J.: 'Novel optically pumped electronic mixer using a Mott diode structure', Electron. Lett., 23, 1084-5, (1987)

48. Foyt, A.G.; Leonberger, F.J.; and Williamson, R.C.: 'InP optoelectronic mixers', Proc. SPIE Int. Soc. Opt. Eng., 269, 109-14, (1981)

49. Torrey, H.C.; and Whitmer, C.A.: *Crystal rectifiers*, MIT Radiation Lab. Series 15, McGraw-Hill, New York, (1948)

50. Oxley, T.H.: 'Backward diodes as mixers at microwave frequencies', J. Electron. Control, 17, 1-17, (1964)

51. Penfield, P.; and Rafuse, R.P.: *Varactor applications*, MIT Press, Cambridge , MA, (1962)

52. Geissler, R.: 'Microwave parametric upper-sideband down-convertor with conversion gain', Electron. Lett., 18, 428-9, (1982)

53. Sze, S.M.: *Physics of semiconductor devices*, 2nd edn., Wiley, New York, (1981)

54. Mortenson, K.E.: *Variable capacitance diodes*, Artech House, Dedham, MA, (1974)

55. Olshansky, R.; Lanzisera, V.; Su, C.B.; Powazinki, W.; and Lauer, R.B.: 'Frequency response of an InGaAsP vapor phase regrown buried heterostructure laser with 18GHz bandwidth', Appl. Phys. Lett., 49, 128-30, (1986)

56. Bowers, J.E.; Hemenway, B.R.; Bridges, T.J.; Burkhardt, E.G.; and Witt, D.P.: '26.5GHz bandwidth InGaAsP lasers with tight optical confinement', Electron. Lett., 21, 1090-1, (1985)

57. Gee, C.M.; Thormond, C.M.; and Yen, H.M.: '17GHz bandwidth electro-optic modulator', Appl. Phys. Lett., 43, 998-1000, (1983)

58. Wight, D.R.; Allen, P.C.; Trussler, J.W.A.; Cooper, D.P.; Esdale, D.J.; and Oliver, P.E.: 'Ultra high speed micro-optical modulators in GaAs: the TEAM and the LEAM', Proc. 12th Int. Symp. *GaAs and Related Compounds 1985*, Karuizawa, Japan, pp667-72, (1985)

59. Lau, K.Y.; and Yariv, A.: 'Intermodulation distortion in a directly modulated semiconductor injection laser', Appl. Phys. Lett., 45, 1034-6, (1984)

60. Steele, R.C.: 'Optical phase-locked loop using semiconductor laser diodes', Electron. Lett., 19, 69-71, (1983)

61. Goldberg, L.; Taylor, H.F.; and Weller, J.F.: 'FM sideband injection locking of diode lasers', Electron. Lett., 18, 1019-20, (1982)

62. Goldberg, L.; Taylor, H.F.; Weller, J.F.; and Bloom, D.M.: 'Microwave signal generation with injection-locked laser diodes', Electron. Lett., 19, 491-3, (1983)

63. Braun, R.-P.; and Streibel, B.: 'Coherent optical fibre transmission using injection locked lasers', IEE Colloq. on *Advances in Coherent Optic Devices and Technologies*, digest no. 1985/30, 12/1-2, (1985)

64. Goldberg, L.; Yurek, A.M.; Taylor, H.F.; and Weller, J.F.: '35GHz microwave signal generation with an injection-locked laser diode', Electron. Lett., 21, 814-5, (1985)

65. Heasell, E.L.: 'The influence of illumination on the majority-carrier quasi-Fermi-level in the Schottky barrier diode', Solid-State Electron., 24, 889-95, (1981)

66. Lavagna, M.; Pique, J.P.; and Marfaing, Y.: 'Theoretical analysis of the quantum yield in Schottky diodes', Solid-State Electron., 20, 235-40, (1977)

67. Gartner, W.W.: 'Depletion-layer photo-effects in semiconductors', Phys. Rev., 116, 84-7, (1959)

68. Bar-Lev, A.: *Semiconductors and electronic devices*, 2nd edn., see pp 185-9, 408, Prentice-Hall, Englewood Cliffs, NJ, (1984)

69. Sawyer, D.E.; and Rediker, R.H.: 'Narrow-base germanium photodiodes', Proc. IRE, 46, 1122-30, (1958)

70. see, e.g., the analysis in Shurmer, H.V.: *Microwave semiconductor devices*, Pitman (Electronic Eng. Series), London, (1971)

71. Saleh, A.A.M.: *Theory of resistive mixers*, MIT Press, Cambridge, MA, (1971)

72. Buckingham, M.J.: *Noise in electronic devices and systems*, Ellis Horwood, Chichester, (1983)

73. Pettai, R.: *Noise in receiving systems*, Wiley, New York, (1984)

74. Robins, W.P.: *Phase noise in signal sources*, IEE Telecommunications Series 9, Peter Peregrinus, London, (1982)

75. 'IRE standards on electron tubes: definitions of terms, 1957', Proc. IRE, 45, 983-1010, (1957)

76. Friis, H.T.: 'Noise figures of radio receivers', Proc. IRE, 32, 419-22, (1944)

77. van der Ziel, A.: *Fluctuation phenomena in semi-conductors*, Butterworths, London, (1959)

78. Schneider, M.V.: 'Metal-semiconductor junctions as frequency converters', in Button, K.J. (ed.), *Infrared and millimeter waves*, vol.6, Academic Press, New York, (1982)

79. Dragone, C.: 'Analysis of thermal and shot noise in pumped resistive diodes', Bell Syst. Tech. J., 47, 1883-902, (1968)

80. van der Ziel, A.: *Noise: sources, characterization, and measurement*, Prentice-Hall, Englewood Cliffs, NJ, (1970)

81. Egami, S.: 'Nonlinear-linear analysis and computer-aided design of resistive mixers', IEEE Trans. Microwave Theory Tech., MTT-22, 270-5, (1974)

82. Gwarek, W.K.: Nonlinear analysis of microwave mixers, M.S. Thesis, MIT, Cambridge, MA, (1974)

83. Schüppert, B.: 'A fast and reliable method for computer analysis of microwave mixers', IEEE Trans. Microwave Theory Tech., MTT-34, 110-9, (1986)

84. Kerr, A.R.: 'A technique for determining the local oscillator waveforms in a microwave mixer', IEEE Trans. Microwave Theory Tech., MTT-23, 828-31, (1975)

85. Hicks, R.G.; and Khan, P.J.: 'Numerical technique for determining pumped nonlinear device waveforms', Electron. Lett., 16, 375-6, (1980)

86. Held, D.N.; and Kerr, A.R.: 'Conversion loss and noise of microwave and millimeter-wave mixers: Part 1 - Theory', IEEE Trans. Microwave Theory Tech., MTT-26, 49-55, (1978)

87. see, e.g., Kreyszig, E.: *Advanced engineering mathematics*, 4th edn., Wiley, New York, p.765, (1979)

88. Siegel, P.H.; and Kerr, A.R.: 'A user oriented program for the analysis of microwave mixers...', NASA Tech. Memo, TM80324, Goddard Space Flight Center, Greenbelt, MD, (1979)

89. Rhoderick, E.H.: *Metal-semiconductor contacts*, Clarendon Press, Oxford, (1978)

90. Padovani, F.A.; and Stratton, R.: 'Field and thermionic-field emission in Schottky barriers', Solid-State Electron., 9, 695-707, (1966)

91. Padovani, F.A.: 'The voltage-current characteristic of metal-semiconductor contacts', in Willardson, R.K., and Beer, A.C. (eds.), *Semiconductors and semi-metals*, vol. 7A, Academic Press, New York, (1971)

92. see, e.g., Schiff, L.I.: *Quantum mechanics*, 3rd edn., McGraw-Hill, New York, (1968)

93. Rideout, V.L.; and Crowell, C.R.: 'Effects of image-force and tunneling on current transport in metal-semiconductor (Schottky-barrier) contacts', Solid-State Electron., 13, 993-1009, (1970)

94. Sinha, A.K.; and Poate, J.M.: 'Effect of alloying behaviour on the electrical characteristics of n-GaAs Schottky diodes metallized with W, Au and Pt', Appl. Phys. Lett., 23, 666-8, (1973)

95. Henisch, H.K.: *Semiconductor contacts: an approach to ideas and models*, Clarendon Press, Oxford, (1984)

96. Macdonald, J.R.: 'Accurate solution of an idealized one-carrier metal-semiconductor junction problem', Solid-State Electron., 5, 11-37, (1962)

97. Casey, H.C., Jr.; Sell, D.D.; and Wecht, K.W.: 'Concentration dependence of the absorption coefficient for n- and p-type GaAs between 1.3 and 1.6eV', J. Appl. Phys., 46, 250-7, (1975)

98. Hwang, C.J.: 'Quantum efficiency and radiative lifetime of the band-to-band recombination in heavily doped n-type GaAs', Phys. Rev. B, 6, 1355-9, (1972)

99. Hwang, C.J.: 'Optical properties of n-type GaAs. I. Determination of hole diffusion length from optical absorption and photoluminescence measurements', J. Appl. Phys., 40, 3731-9, (1969)

100. Oxley, T.H.: 'Mixers and detectors', in Morgan, D.V. and Howes, M.J., (eds.), *Microwave solid-state devices and applications*, Peter Peregrinus, Stevenage, (1980)

101. Anand, Y.: 'Microwave Schottky-barrier diodes', in Sharma, B.L. (ed.), *Metal-semiconductor Schottky barrier junctions and their applications*, Plenum Press, New York, (1984)

102. Shurmer, H.V.: *Microwave semiconductor devices*, Pitman, London, (1971). (see ref.[70])

103. Wang, S.Y.,; and Bloom, D.M.: '100GHz bandwidth planar GaAs Schottky photodiode', Electron. Lett., 19, 554-5, (1983)

104. Parker, D.G.; and Say, P.G.: 'Indium tin oxide/GaAs photodiodes for millimetric-wave applications', Electron. Lett., 22, 1266-7, (1986)

105. Parker, D.G.: 'Use of indium tin oxide to form a highly effeicient 20GHz Schottky barrier photodiode', Electron. Lett., 21, 778, (1985)

106. Parker, D.G.: 'On the formation of near ideal quasi-Schottky barriers between indium tin oxide and gallium arsenide', GEC J. Res., 5, 116-23, (1987)

107. Ball, P.R.; and Culshaw, B.: 'Semiconductor laser sources for coherent optical-fibre systems', IEE J. Solid-State and Electron Dev., 3, 242-5, (1979)

108. McColl, M.; and Millea, M.F.: 'Advantages of Mott barrier mixer diodes', Proc. IEEE, 61, 499-500, (1973)

109. Nagle, J.P.; Hing, L.A.; Kerr, T.M.; and Summers, J.G.: 'A Mott mixer diode', J. Vac. Sci. & Technol. B, 4, 631-2, (1986)

110. Schottky, W.: 'Halbleitertheorie der Sperrschicht', Naturwissenschaften, 26, 843, (1938)

111. Bethe, H.A.: 'Theory of the boundary layer of crystal rectifiers', MIT Rad. Lab. Rep. 43-12, (1942)

112. Crowell, C.R.; and Sze, S.M.: 'Current transport in metal-semiconductor barriers', Solid-State Electron., 9, 1035-48, (1966)

113. Kao, C.W.; Anderson, C.L.; and Crowell, C.R.: 'Photoelectron injection at metal-semiconductor interfaces', 95, 321-39, (1980)

114. Chang, C.Y.; and Sze, S.M.: 'Carrier transport across metal-semiconductor barriers', Solid-State Electron., 13, 727-40, (1970)

115. Crowell, C.R.; and Beguwala, M.: 'Recombination velocity effects on current diffusion and imref in Schottky barriers', Solid-State Electron., 14, 1149-57, (1971)

116. Miller, W.L.; and Gordon, A.R.: 'Numerical evaluation of infinite series and integrals which arise in certain problems of linear heat flow, electrochemical diffusion, etc.', J. Phys. Chem., 35, 2785-884, (1931)

117. Ng, W.; Craig, R.; and Yen, H.W.: '11.5GHz modulation bandwidth p-substrate GaInAsP buried crescent laser with high output power', Electron. Lett., 24, 43-5, (1988)

118. Marshall, I.W.; Spirit, D.M.; and O'Mahony, M.J.: 'Picosecond pulse response of a travelling-wave semiconductor laser amplifier', Electron. Lett., 23, 818-9, (1987)

119. Saitoh, T.; and Mukai, T.: 'Broadband 1.5μm GaInAsP travelling-wave laser amplifier with high-saturation output power', Electron. Lett., 23, 218-9, (1987)

120. Hamada, K.; Wada, M.; Shimizu, H.; Kune, M.; Susa, F.; Shibutani, T.; Yoshikawa, N.; Itoh, K.; Kano, G.; and Teramoto, I.: 'A 0.2W CW laser with buried twin-ridge

substrate structure', IEEE J. Quantum Electron., QE-21, 623-8, (1985)

121. Wei, C.J.; Klein, H.-J.; and Beneking, H.: 'Symmetrical MOTT barrier as a fast photodetector', Electron. Lett., 17, 688-90, (1981)

122. McCleer, P.J.; and Haddad, G.I.: 'A proposed new hogh-speed optical detector', IEEE Trans. Electron Dev., ED-25, 389-92, (1978)

123. Chen, C.Y.; Cho, A.Y.; Garbinski, P.A.; Bethea, C.G.; and Levine, B.F.: 'A new majority-carrier photodetector', Appl. Phys. Lett., 39, 340-2, (1981)

124. Chen, C.Y.: 'Theory of a modulated barrier photodiode', Appl. Phys. Lett., 39, 979-81, (1981)

125. Barnard, J.A.; Najjar, F.E.; and Eastman, L.F.: 'The steady-state optical response of the homojunction triangular barrier photodiode', IEEE Trans. Electron Dev., ED-29, 1396-403, (1982)

126. Rauscher, C.; Goldberg, L.; and Yurek, A.M.: 'GaAs FET demodulator and down-convertor for optical-microwave links', Electron. Lett., 22, 705-6, (1986)

APPENDIX A

THE PHOTOCURRENT CONTRIBUTION OF CARRIERS GENERATED OUTSIDE THE DEPLETION REGION

When a semiconductor is illuminated, if the incoming photons have energies greater than the bandgap in the material, then it can be assumed that each photon will produce an electron-hole pair. If these pairs are generated in a barrier (or depleted) region then it can be further assumed that the pairs will be separated by the electric field and will contribute to the external current as they traverse the barrier. Carriers generated outside the barrier region, however, may recombine without contributing to the external current; to contribute to the external current they must reach the barrier where they can then be swept across by the electric field. As the illumination creates excess carriers, the carriers generated outside the barrier will contribute to the external current by diffusing to it; as the excess carrier concentration is important, it is the minority-carriers which dominate the current flow. The photocurrent generated in this way will depend on the diffusion length of the minority-carriers, and on the absorption length in the material. The diffusion current density can be found from the one-dimensional continuity equation which gives (using the terminology employed in sec.2.1):

$$D_p \frac{\partial^2 p_1}{\partial x^2} - \frac{p_1}{\tau_p} = -\Phi \, \alpha \, \exp(-\alpha x) \qquad \text{(A1)}$$

where p_1 is the excess hole concentration, $p_1 = p_n - p_{n0}$.

In deriving the above, it is assumed that the electric field in the bulk is negligibly small.

The general solution to the homogeneous equation of the above is of the form:

$$p_1 = A.\exp(x/L_p) + B.\exp(-x/L_p) \qquad (A2)$$

where $L_p = \surd(D_p/\tau_p)$

A particular solution of the form p_1=Cexp(−αx) is chosen; this yields the full solution:

$$p_1 = A.\exp(x/L_p) + B.\exp(-x/L_p) + C.\exp(-\alpha x) \qquad (A3)$$

where $C = \Phi\alpha L_p^2 / D_p(1 - \alpha^2 L_p^2)$

The first boundary condition is that for $x\rightarrow\infty$, $p_n=p_{n0}$, or $p_1=0$. This gives A=0.

The second boundary condition is that there are negligibly few holes in the barrier since they are removed by the electric field; that is, $p_n=0$ for x=w, which is equivalent to $p_1(w)=-p_{n0}$. This gives:

$$-p_{n0} = B.\exp(-w/L_p) + C.\exp(-\alpha w)$$

$$\text{or} \quad B = -(p_{n0} + C.\exp(-\alpha w)).\exp(w/L_p) \qquad (A4)$$

The solution for the hole concentration is therefore:

$$p_1 = -(p_{n0} + C.\exp(-\alpha w)).\exp[(w-x)/L_p] + C.\exp(-\alpha x) \qquad (A5)$$

The diffusion current density can be found from the above by using the relation,

$$J_{diff}(x) = -qD_p \frac{dp_1(x)}{dx} \tag{A6}$$

This gives,

$$J_{diff}(x) = -qD_p\{[(p_{n0} + C.\exp(-\alpha w))/L_p].\exp((w-x)/L_p) - \alpha C.\exp(-\alpha x)\} \tag{A7}$$

The contribution of diffusing carriers to the external current will be the value of the diffusion current at the barrier, that is:

$$J_{diff}(w) = -qD_p \frac{\alpha L_p}{1+\alpha L_p} \exp(-\alpha w) - qD \frac{p_{n0}}{L_p} \tag{A8}$$

APPENDIX B

MIXER LINEAR ANALYSIS

The small-signal analysis of an optoelectronic mixer with optical l.o. excitation need be no different from that for ordinary mixers. All that is required is to form the complex admittance matrix of the mixer from the diode conductance and capacitance Fourier coefficients found in the large-signal analysis. The small-signal analysis used is based on that of Held and Kerr[B1]. The subscript notation for the sideband frequencies, which leads to a considerable simplification of the mixer theory, is that proposed by Saleh[B2]:

$$\omega_n = \omega_0 + \omega_p \qquad n = 0, \pm 1, \pm 2, \pm 3, \ldots \qquad \text{(B1)}$$

Hence the upper-sideband, i.f. and lower-sideband are, $\omega_{+1}=\omega_0+\omega_p$, ω_0, and $\omega_{-1}=\omega_0-\omega_p$, and will have voltage components V_{+1}, V_0, V_{-1}.

A brief summary of the equations used in the linear analysis will now be given; for a fuller explanation the reader is referred to Held and Kerr's original paper[B1].

If $\mathbf{\delta I}$ and $\mathbf{\delta V}$ are the vectors of small-signal currents and voltages, they are related by the conversion admittance matrix, $\mathbf{Y}$:

$$\mathbf{\delta I} = \mathbf{Y}\ \mathbf{\delta V} \qquad \text{(B2)}$$

where $\mathbf{\delta I} = [\ \ldots\ ,\ \delta I_1\ ,\ \delta I_0\ ,\ \delta I_{-1}\ ,\ \ldots\ ]^T$

$$\mathbf{\delta V} = [\ \ldots\ ,\ \delta V_1\ ,\ \delta V_0\ ,\ \delta V_{-1}\ ,\ \ldots\ ]^T$$

and

$$\mathbf{Y} = \begin{bmatrix} & \cdot & \cdot & \cdot & \\ & \cdot & \cdot & \cdot & \\ & \cdot & \cdot & \cdot & \\ \cdots & Y_{11} & Y_{10} & Y_{1-1} & \cdots \\ \cdots & Y_{01} & Y_{00} & Y_{0-1} & \cdots \\ \cdots & Y_{-11} & Y_{-10} & Y_{-1-1} & \cdots \\ & \cdot & \cdot & \cdot & \\ & \cdot & \cdot & \cdot & \\ & \cdot & \cdot & \cdot & \end{bmatrix}$$

with the element values given by:

$$Y_{mn} = G_{m-n} + j(\omega_0 + m\omega_p)C_{m-n}$$

G_{m-n} and C_{m-n} are the (m-n)th Fourier coefficients of the diode conductance and capacitance waveforms, $g_j(t)$ and $c_j(t)$, defined by the transformation:

$$G_{m-n} = 1/T \int_{-T/2}^{T/2} g_j(t) \exp(-j(m-n)\omega_p t)\, dt$$

$$C_{m-n} = 1/T \int_{-T/2}^{T/2} c_j(t) \exp(-j(m-n)\omega_p t)\, dt$$

where T is the l.o. period.

The above admittance matrix is for the intrinsic diode; to take into account the diode series resistance and embedding network an augmented admittance matrix, **Y'**, is required, where the elements will be given by

$$Y'_{mn} = Y_{mn} \qquad , \; m \neq n \qquad (B3)$$

$$Y'_{mn} = Y_{mn} + [\, Z_{e,m} + R_s \,]^{-1} \qquad , \; m = n$$

Inverting the admittance matrix we have:

$$\mathbf{Z'} = (\mathbf{Y'})^{-1}$$

From the impedance matrix **Z'** the conversion loss and input and output impedances of the mixer can be calculated. First the conjugate-matched i.f. load impedance is found by open-circuiting the i.f. port and finding its impedance. The i.f. load impedance is given by:

$$Z_{e0} = Z^{*}_{IFout} = (Z'_{e0,\infty} + R_s)^{*} = Z'^{*}_{00,\infty} + R_s \qquad (B4)$$

where $Z'_{00,\infty}$ is the centre element of the **Z'** matrix with $Z_{e0}=\infty$. Mixer input impedances are found from:

$$Z_{inm} = R_s + \frac{(Z_{em} + R_s).Z'_{mm}}{(Z_{em} + R_s) - Z'_{mm}} \qquad (B5)$$

where Z'_{mm} is the mm-th element of the mixer impedance matrix with the i.f. load conjugate-matched.

Finally, the loss of the mixer in converting from sideband j to sideband i, taking into account the loss in the diode series resistance, is given by:

$$L_{ij} = \frac{|\, Z_{ei} + R_s \,| \; |\, Z_{ej} + R_s \,|}{4 \,|\, Z'_{ij} \,|\; Re[Z_{ej}]\; Re[Z_{ei}]} \qquad (B6)$$

where Z'_{ij} is the ij-th element of the Z' matrix with the load conjugate-matched.

References

B1. Held, D.N.; and Kerr, A.R.: 'Conversion loss and noise of microwave and millimeter-wave mixers: Part 1 - Theory', IEEE Trans. Microwave Theory Tech., MTT-26, 49-55, (1978)

B2. Saleh, A.A.M. : *Theory of resistive mixers*, MIT Press, Cambridge, MA, (1971)

APPENDIX C

MIXER NOISE ANALYSIS INCLUDING CORRELATED SHOT NOISE

In the noise analysis considered here, the noise components at the various sideband frequencies, which are modulated and therefore converted to other sideband frequencies, are related. Since the noise components can be considered to be small, they may be related using the linear analysis of Appendix B by assuming the noise to consist of pseudo-sinusoidal components, of which those components at the sideband frequencies will affect the mixer performance. As with the linear analysis presented in Appendix B, the noise analysis follows that of Held and Kerr[C1].

If the complex amplitude of the pseudo-sinusoidal shot noise current at sideband m is $\delta I'_{sm}$, then the output noise voltage at the i.f. is

$$\delta V_{s0} = \mathbf{Z'_0} \, \delta \mathbf{I'_s} \qquad \text{(C1)}$$

where $\delta \mathbf{I'_s}$ is the vector $[\ldots, \delta I'_{s1}, \delta I'_{s0}, \delta I'_{s-1}, \ldots]$ and $\mathbf{Z'_0}$ is the zero-th row of the square mixer impedance matrix $\mathbf{Z'}$. The ensemble average of the square of the mean noise voltage is

$$\langle |\delta V_{s0}|^2 \rangle = \mathbf{Z'_0} \langle \delta \mathbf{I'_s} \, \delta \mathbf{I'_s}^{\dagger} \rangle \mathbf{Z'_0}^{\dagger} \qquad \text{(C2)}$$

where the superscript $\dagger$ denotes the complex conjugate transpose. The square matrix $\langle \delta \mathbf{I'_s} \, \delta \mathbf{I'_s}^{\dagger} \rangle$ is the correlation matrix for the mixer shot noise. This matrix has been evaluated by Dragone[C2], who obtained:

$$\langle \delta I'_{sm} \; \delta I'^{*}_{sn} \rangle = 2\, q\, I_{m-n}\, \Delta f \tag{C3}$$

In a similar fashion the ensemble average of the mean-square output noise voltage due to thermal noise can be defined:

$$\langle |\, \delta V_{t0} \,|^{2} \rangle = \mathbf{Z'_0} \langle \mathbf{\delta I'_t} \; \mathbf{\delta I'^{\dagger}_t} \rangle \mathbf{Z'^{\dagger}_0} \tag{C4}$$

The square matrix is the correlation matrix for thermal noise; however, since $\delta I'_{tm}$ and $\delta I'_{tn}$ are assumed uncorrelated, it is a diagonal matrix with no elements for $m \neq n$ and the elements

$$\langle \delta I'_{tm} \;\; \delta I'^{*}_{tm} \rangle = \frac{4kT_d R_s \Delta f}{|Z_{em} + R_s|^{2}} \qquad m \neq 0 \tag{C5a}$$

$$= \frac{4kT_d R_s \Delta f}{|Z_0|^{2}} \qquad m = 0 \tag{C5b}$$

By combining eqns. (C2) and (C4) the total output ensemble average mean-square noise voltage can be written:

$$\langle \delta V_{NO}^{2} \rangle = \mathbf{Z'_0} \{ \langle \mathbf{\delta I'_s} \; \mathbf{\delta I'^{\dagger}_s} \rangle + \langle \mathbf{\delta I'_t} \; \mathbf{\delta I'^{\dagger}_t} \rangle \} \mathbf{Z'^{\dagger}_0} \tag{C6}$$

Held and Kerr use the value of $\langle \delta V_{NO}^{2} \rangle$ evaluated from the above expression to define an effective input noise temperature and a single-sideband noise figure for the mixer. However, from the discussion in sec.2.3.2, the noise-temperature ratio of the mixer is a more useful parameter since it can be used to calculate the receiver overall noise factor, which is the most important performance specification.

The total output noise power is

$$N_0 = \frac{\langle \delta V_{NO}^2 \rangle}{Re[Z_{e0} + R_s]} \cdot \Delta f \qquad (C7)$$

The noise-temperature ratio of the mixer is then simply:

$$t_r = \frac{\langle \delta V_{NO}^2 \rangle}{Re[Z_{e0} + R_s]\ kT_0} \qquad (C8)$$

For an optically pumped mixer there will be additional shot noise due to the photocurrent. This could be modelled by taking the shot noise current component at sideband m, $\delta I'_{sm}$, to be composed of both the shot noise current component due to the barrier conductance and that due to the photocurrent generation:

$$\delta I'_{sm} = |\delta I'_{smg}| + |\delta I'_{smph}|$$

The use of such a formulation, however, would require a re-interpretation of eqn. (C3) which is used to evaluate the components of the correlation matrix.

The shot noise due to the photocurrent will be modulated in the same way as the shot noise due to the current through the barrier conductance; it will therefore have correlated components as discussed above. The correlation between noise components at different sidebands can cause an apparent reduction in the output noise compared to a simple summation of the contributions of all of the individual components to the output[C3]. Since the barrier current modulation is caused by the

photocurrent modulation, there must be some correlation between their shot noise components. It is interesting to speculate, therefore, that the optically pumped mixer may be less noisy than the application of the simple analysis of secs.2.3.3 - 2.3.6 will predict. A more detailed investigation of these effects is required to confirm or deny this.

References

C1. Held, D.N.; and Kerr, A.R.: 'Conversion loss and noise of microwave and millimeter-wave mixers: Part 1 -Theory', IEEE Trans. Microwave Theory Tech., MTT-26, 49-55, (1978)

C2. Dragone, C.: 'Analysis of thermal and shot noise in pumped resistive diodes', Bell Syst. Tech. J., 47, 1883-902, (1968)

C3. van der Ziel, A.: *Noise: sources, characterization, and measurement*, Prentice-Hall, Englewood Cliffs, NJ, (1970)